EFFECT OF MICROSCOPIC DEFECTS ON SUPERCONDUCTING PROPERTIES OF HIGH PURITY NIOBIUM USED FOR SRF CAVITIES

By

Mingmin Wang

A DISSERTATION

Submitted to
Michigan State University
in partial fulfillment of the requirements
for the degree of

Material Science and Engineering—Doctor of Philosophy

2020

ABSTRACT

EFFECT OF MICROSCOPIC DEFECTS ON SUPERCONDUCTING PROPERTIES OF HIGH PURITY NIOBIUM USED FOR SRF CAVITIES

By

Mingmin Wang

High purity niobium has been used to fabricate superconducting radio-frequency (SRF) cavities for linear particle accelerator applications for decades due to its high critical temperature (9.3 K) and critical magnetic field. Great progress has been made in achieving high accelerating gradients and quality factors (a measure of efficiency). However, the performance of Nb cavities still suffers from the variability of the material such that high quality factors and accelerating gradients cannot be consistently produced.

Trapped magnetic flux is well known for causing significant radio-frequency losses. Both local flux penetration and flux trapping indicate the local suppression of superconductivity. Magnetic flux from both unshielded earth field and thermoelectric currents can be trapped when a cavity is cooled through its superconducting transition temperature. Microstructural defects including hydrogen, grain boundaries, and dislocations are possible causes for flux trapping. However, the details of magnetic flux trapping mechanisms and conditions that enable it are still not clear. Research on this topic has been very active in the SRF community. Cavity studies on flux expulsion after different heat treatments and cooldown procedures have been performed in recent years, but the study of flux trapping mechanisms at the microscopic level is still lacking.

In order to study the effect of microscopic defects on flux trapping, single crystal and bicrystal samples were designed with strategically chosen tensile axes to intentionally introduce defects by a 5% tensile strain. Magneto-Optical (MO) Imaging was used to visualize locations

where magnetic flux was trapped, and the dislocation substructures were studied using Electron Channeling Contrast Imaging (ECCI).

The results show that high angle grain boundaries (HAGB) and low angle grain boundaries (LAGBs) have different flux penetration behaviors. LAGBS could be hydrogen segregation sites leading to precipitation of normal conducting hydrides along LAGBs at ~100–130 K during cooling. In hydrogen contaminated single-crystal samples, large hydride scars (locations where a hydride formed and then dissolved during heating) were observed both at the LAGBs and within the grain after MO cooling; however, only hydrides at the LAGBs appeared to cause premature flux penetration. Flux trapping related to LAGBs could still be observed after the heat treatment removed most of the hydrogen. By contrast, the flux penetration along a HAGB could be turned off by heat treatment that removed hydrogen and restored by reintroducing hydrogen into the sample. This work suggests that HAGBs are not as effective at causing flux penetration or trapping as hydrides and LAGBs.

Some deformed bi-crystal samples show correlations between a larger amount of deformation or a higher density of dislocations and more trapped flux. Deformation led to the development of dislocation substructures; however, the effect of dislocation arrangements on flux penetration could not be observed in the current work. Further study with flux measurement techniques of a higher resolution and sensitivity is necessary to understand what kinds of dislocation substructures are most likely to cause flux penetration.

To my parents and my sister, who always believe in me.

ACKNOWLEDGMENTS

I would like to express my deepest appreciation to my advisor, Dr. Thomas Bieler, whose knowledge and support guided me through the past six years. His enthusiasm for research and dedication to education inspires me to pursue my dream of becoming a researcher in materials science and to help others.

I am also extremely grateful to my committee members Dr. Carl Boehlert, Dr. Martin Crimp, and Dr. Elias Strangas for their constructive advice and guidance. This dissertation would not have been possible without their support and encouragement. Special thanks to Dr. Martin Crimp for his help with ECCI.

I am also deeply indebted to my collaborators Dr. Peter Lee, Dr. Anatolii Polyanskii, Dr. Shreyas Balachandran, Mr. Santosh Chetri, and Dr. Zuhawn Sung at National High Magnetic Field Lab/Applied Superconductivity Center for their deep insights into superconductivity theories and help with MO experiments. Thanks should also go to Chris Compton at Facility for Rare Isotope Beams (FRIB) at Michigan State University for his help with Nb sample processing.

Last and certainly not least, I would like to extend my sincere thanks to my fellow graduate students in the Metals Group for their support, encouragement, and friendship. Special thanks to my friends Lijiang Xu, Yifan Men, Yifeng Tian, Wu Zhou, Wu Pan, Pei Chen, Zeyang Yu, Yuanchao Liu, Yuxi Ma, Jialin Liu for their invaluable friendship.

This work was financially supported by the U.S. Department of Energy, Office of High Energy Physics, through award DE-SC0009962.

TABLE OF CONTENTS

LIST OF TABLES

LIST OF FIGURES

KEY TO ABBREVIATIONS

SRF Superconducting radio-frequency

SEM Scanning electron microscopy

AFM Atomic force microscopy

TEM Transmission electron microscopy

ECCI Electron channeling contrast imaging

EBSD Electron backscattered diffraction

OIM Orientation imaging microscopy

MO imaging Magneto-optical imaging

LAGB Low angle grain boundary

HAGB High angle grain boundary

GND Geometrically necessary dislocations

SSD Statistically stored dislocations

GNB Geometrically necessary boundary

IDB Incidental dislocation boundary

IPF Inverse pole figure

IQ Image quality

KAM Kernel average misorientation

LAM Local average misorientation

GROD Grain reference orientation deviation

Chapter I. INTRODUCTION

A. SRF cavities and limitations

Particle accelerators are used in various fields from particle physics, atomic physics, materials science, to cancer therapy and the semiconductor industry [1]–[3], with nearly 200,000 particle accelerators in operation worldwide. The development of high-performance accelerators relies on superconducting radio-frequency (SRF) technology, which uses elliptical niobium (Nb) cavities and radio-frequency induction to generate oscillating electromagnetic fields to accelerate charged particles such as electrons and positrons at ~2 K [4]. Ion accelerators require larger cavities with more complex shapes [4].

SRF cavities are usually made from high purity (RRR[1] > 300) Nb because of its high critical temperature ($T_c = 9.3$ K) among elemental superconductors, good formability (easily machined and deep-drawn), reliable chemical stability, and sufficient availability on the market [4]–[7]. During the past decades, pushing the limits of high accelerating electric fields (E) and quality factors Q[2] has provided the motivation for continuing research and development of Nb cavities. Improvements in the fabrication process have enabled the theoretical limit (~52 MV/m) of accelerating field and ultra-high quality factors (Q~10^{11}) to be occasionally achieved [8], [9].

However, this high performance cannot be consistently reproduced and the performance of Nb cavities varies even when the same manufacturing processes are used, suggesting that variability of the material properties could account for the variability in performance. One big source of material variability comes from the microscopic defects in Nb, including impurity atoms, voids, inclusions, hydrides, dislocations, and grain boundaries. These defects may limit SRF

[1] Residual Resistivity Ratio: the ratio of the electric resistivity measured at 273 K to that at 4.2 K.
[2] Quality factor Q is a measure of energy efficiency defined as the ratio of stored energy in a cavity to the dissipated energy.

cavity performance and are inevitably and heterogeneously introduced along the fabrication path from forging, rolling, deep drawing, and welding. Such defects can trap magnetic flux from the earth field or thermocurrent-generated field during cavity cooldown through the superconducting transition temperature (9.3 K); the trapped flux is well-known for causing significant radio-frequency (RF) losses[3] and thus degrades the performance during the operation of Nb cavities [10], [11], [20]–[22], [12]–[19].

B. Flux pinning by dislocations and grain boundaries

Dislocations are one-dimensional crystal defects that are generated during plastic deformation to accommodate strains, and heavy deformation leads to a high density of dislocations and dislocation substructures. Dislocations can assist flux entry at lower surface magnetic fields and are capable of trapping magnetic flux, resulting in RF losses due to oscillatory motion of trapped flux under the RF fields [10], [11], [13], [23]. Since the size of individual dislocations is too small compared to the coherence length of Nb (38 nm), it is hypothesized that dislocation substructures and entanglements (instead of individual dislocations), with sizes comparable to the coherence length, are causing flux penetration and trapping [23].

Much effort has been made to improve the flux expulsion property of Nb cavities. A recent study suggested that a 900–1000 ℃ heat treatment could significantly improve the flux expulsion property[4] of high purity niobium cavities, and EBSD (electron backscattered diffraction) analysis showed grain growth and a decrease in the local average misorientation as a result of the heat treatment [24]. Grain boundaries and dislocations were considered as possible defects causing flux trapping in that study; however, it was not clear which one is dominant. Another study by the

[3] Significant energy losses such as high field Q slope (abnormal Q drop) when surface field is larger than 100 mT.
[4] Measured by fluxgate magnetometers on the equator of the cavity surface

same group suggested that cold work, which created dislocations, was a strong determinant of flux expulsion behavior, and the cavity made from rolled Nb material showed a much higher level of flux trapping compared with the cavity made from as-received material (less cold work) [25].

Grain boundaries (interfaces dividing grains with different orientations) play a critical role in defining Nb cavity performance because they are both sources and sinks for microstructural defects. There have been reports that grain boundaries with special orientations with respect to the external magnetic fields could cause preferential flux penetration at superconducting temperatures [26]–[28]. Flux penetration at some low angle grain boundaries (LAGBs) was also observed in deformed single-crystal Nb samples [16], [29]. As not all high angle or low angle grain boundaries show flux penetration, further studies are necessary to fully understand the effect of grain boundaries.

C. The motivation of the current work

Recent studies of flux trapping focused on optimization of processing methods for performance improvement using real size Nb cavities; however, the study of flux trapping mechanisms at the microscopic level is still lacking. This current study was performed by strategically introducing microstructural defects (including dislocations, low angle grain boundaries, and hydrogen) into bulk Nb samples and investigating their effect on the magnetic flux trapping/penetration. Magneto-optical (MO) imaging was used to directly observe magnetic flux in Nb samples. Preferential flux penetration or flux trapping indicates the suppression of the superconductivity of Nb. Electron channeling contrast imaging (ECCI), combined with electron backscattered electron diffraction (EBSD), was performed to characterize dislocations and grain boundaries.

The goal is to understand the effect of microstructural defects on superconducting properties (in terms of flux penetration and trapping) of Nb by evaluating the relationships between dislocation content, low angle and high angle grain boundaries, hydrogen, heat treatment, cryogenic cooling, and flux penetration and trapping. The results of this research will identify what is responsible for the performance variability of Nb cavities and provide guidance for cavity processing strategies that can optimize the final microstructural defects and therefore enable consistent enhancement of the performance of Nb cavities.

Chapter II. LITERATURE REVIEW

A. Superconducting radio frequency cavity

SRF science and technology is widely used in particle accelerators that can accelerate particles such as protons to a speed close to the speed of light. It can be used to make the particles with opposite moving directions collide against each other, revealing information relevant to the history of the universe [1], [4].

This technology is realized in SRF cavities (metallic chamber structure) made of superconducting materials in which high electromagnetic fields are generated periodically by radio-frequency oscillations (from 50 MHz to 10 GHz) [30] that generate resonating superconducting currents in the cavity walls [4], [31].

The charged particles injected into the cavities feel the electric force pushing them forward, and the timing is carefully controlled so that the particles can pick up speed in each single cavity cell. Depending on the resonating frequency, resonating mode, and ratio (β) of the desired final speed to the light speed, SRF cavities can take different geometries. Figure 1 shows an example of a 9-cell Nb cavity used as the baseline cavity for the International Linear Collider [32]. New machines being built such as the Linac Coherent Light Source-II (LCLS-II) project at SLAC National Accelerator Laboratory use a similar cavity geometry [33].

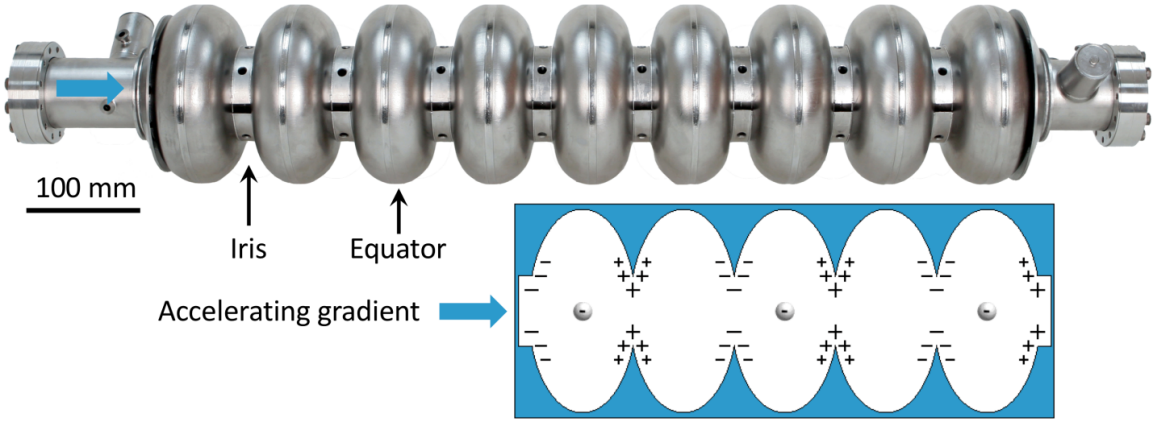

Figure 1. A TESLA 9-cell 1.3-GHz superconducting Nb cavity for the International Linear Collider [32] (top image). The black arrows indicate the locations of the iris and the equator. The blue arrows indicate the direction of the accelerating gradient that accelerates the electrons down the beam tube. The schematic illustration (bottom image) reveals the inner arrangement of electrons at one point in time during oscillating electric fields timed to accelerate electrons in each cell (Image Courtesy: Jefferson Lab).

Since superconducting currents flow in the ~100 nm subsurface, SRF cavity performance is very sensitive to the cavity surface quality [34]. Therefore any imperfections within the material or on the surface of the cavities are intolerable and should be removed by processing procedures including buffered chemical polishing (BCP), electro-polishing (EP), ultra-pure water rinsing, followed by clean-room assembly [34], [35].

Compared to normal conducting cavities, SRF cavities have the advantage of low electric resistance. Nb cavities are housed in cryomodules filled with liquid helium to keep the temperature below the critical temperature ($T_c = 9.3$ K) and the cost of cryogenic cooling is a major cost driver. Performance of a Nb cavity is measured by the quality factor (Q) and the accelerating electric field (E). Therefore, a Nb cavity needs to have a high Q so that the operation of the accelerators can be economically feasible. Theoretically, 100% of the input energy can be converted to the speed of the accelerated beam. However, the system generates heat due to residual electrical resistance and needs this dissipated energy to be removed to maintain the cryomodules in the superconducting

state. One major source of RF losses and residual resistance is the trapped magnetic flux during cooldown through the superconducting transition temperature. The magnetic flux can arise from either the earth's filed or the thermoelectric currents.

New linear accelerators, such as LCLS-II at SLAC National Accelerator Laboratory, have even higher quality factor requirements ($Q = 2.7 \times 10^{10}$) [33], [36]. With a quality factor larger than 10^{10}, RF losses caused by trapped magnetic flux may be what limits Q values. The effect of microstructural defects on flux trapping in Nb is the focus of this dissertation.

B. Superconductivity theories

1. Some fundamental definitions

Superconductivity was discovered by Kamerlingh Onnes in 1911 [37], [38], which opened a totally new field of low-temperature physics. This phenomenon is characterized by zero electrical resistance of a material below the critical temperature (T_C) [12]. Another important feature is perfect diamagnetism, i.e., materials in the superconducting state (also known as the Meissner state) ($T < T_C$) completely expel a magnetic field below the critical magnetic field (H_C).

According to the magnetization properties, superconductors can be classified into type-I and type-II superconductors. There is only one critical magnetic field for type-I superconductors, which shows a perfect diamagnetism (Meissner state) below the critical filed H_C, but will be fully normal-conducting above H_C. For type-II superconductors (such as Nb), there are two critical fields, H_{C1} and H_{C2}. A type-II superconductor is in superconducting state (Meissner state) below H_{C1}, mixed state for $H_{C1} < H < H_{C2}$, and normal state when $H > H_{C2}$. The mixed state is a partially diamagnetic state and part of the magnetic flux, quantized in a form of vortices (Abrisokov vortices), can penetrate the superconductor [12]. Figure 2 shows phase diagrams of type-I (a) and type-II (b) superconductors.

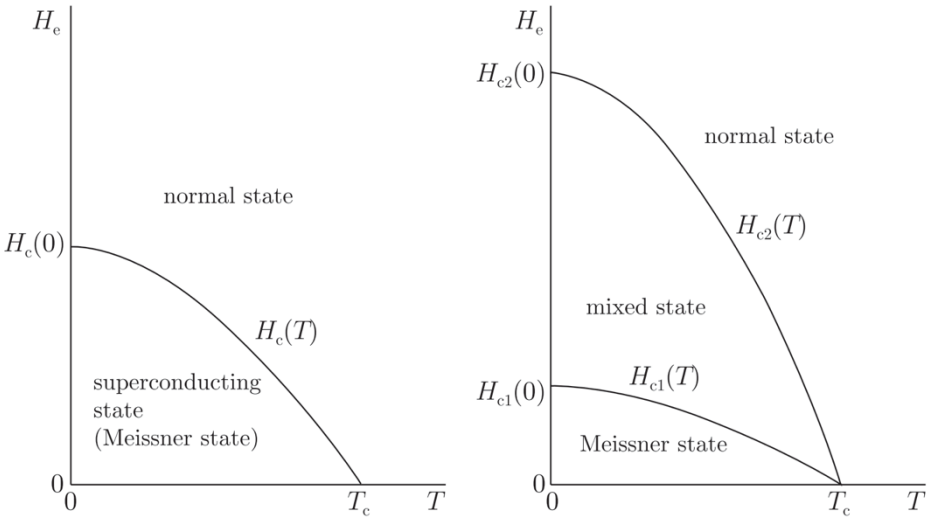

Figure 2. Phase diagrams of the magnetic field versus temperature for type-I (a) and type-II (b) superconductors [12].

2. London theory

The London theory was put forward by the London brothers in 1935 before the discovery of type-II superconductors [12]. It explains the Meissner effect and describes the superconducting state.

The London theory equations are [12]:

$$\boldsymbol{E} = \frac{m^*}{n_s e^{*2}} \cdot \frac{d\boldsymbol{j}}{dt} \tag{1}$$

$$\boldsymbol{b} + \frac{m^*}{\mu_0 n_s e^{*2}} \nabla \times \nabla \times \boldsymbol{b} = 0 \tag{2}$$

where $\boldsymbol{E}$, $\boldsymbol{b}$ and $\boldsymbol{j}$ are the electric field, the magnetic flux density, and the current density; m^*, e^* and n_s are the mass, electric charge, and number density of superconducting electrons; μ_0

is the permeability of vacuum and t is the time. Electromagnetic relations are described by these two equations that provide characteristic parameters from which the penetration depth can be derived (see Equation (3)).

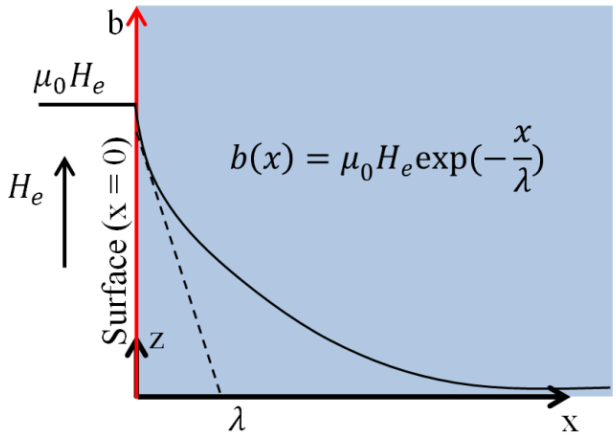

Figure 3. Magnetic flux distribution near the surface of a superconductor in the Meissner state [12].

Consider a superconductor with a semi-infinite dimension in the x-axis direction and infinite dimensions in the y- and z-axis directions with a surface defined as x = 0 (Figure 3). An external magnetic field H_e is applied parallel to the z-axis and it is assumed that the magnetic flux density varies only along the x-axis. Then, Equation (2) reduces to

$$\frac{\mathrm{d}^2 b}{\mathrm{d}x^2} - \frac{b}{\lambda^2} = 0 \tag{3}$$

where b is the magnetic flux density and λ is the penetration depth, which is written as

$$\lambda = \sqrt{\frac{m^*}{\mu_0 n_s e^{*2}}} \tag{4}$$

Solving equation (3) by applying conditions of $b = \mu_0 H_e$ at $x = 0$ and $b = 0$ at infinity gives

$$b(x) = \mu_0 H_e \exp\left(-\frac{x}{\lambda}\right) \tag{5}$$

The function $b(x)$ is plotted in Figure 3. A tangent line at $(0, \mu_0 H_e)$ intercepts the x-axis at $(\lambda, 0)$. λ is defined as the penetration depth, which is a measure of how deep the external magnetic field can penetrate into a superconductor in the Meissner state. The penetration depth of Nb is 39 nm [39].

3. Ginzburg-Landau theory

Although the London theory can successfully explain the Meissner effect, it only describes the situation in the superconducting state. For the mixed state ($H_{c1} < H < H_{c2}$), the Ginzburg-Landau (G-L) theory [40], [41] is more applicable. In the G-L theory, the order parameter Ψ is introduced, with $|\Psi|^2$ denoting the number density of superconducting electrons, and the free energy of a superconductor depends on $|\Psi|^2$, which has a non-zero value for the superconducting state and becomes zero for the normal conducting state (loss of superconductivity).

The electromagnetic properties in a superconductor are determined by two characteristic lengths, i.e. the penetration depth λ, and the coherence length ξ [40], [41]. These two parameters can be derived from the G-L theory, as shown in Equations (6) and (7).

$$\lambda = \sqrt{\frac{m^*}{4\mu_0 e^2 |\Psi_\infty|^2}} \tag{6}$$

where $|\Psi_\infty|^2$ is the equilibrium value of $|\Psi|^2$ when the derivative of the free energy density is zero.

$$\xi = \frac{h_p}{4\pi\sqrt{2} e \mu_0 H_c \lambda} \tag{7}$$

where h_p is the Planck's constant and the coherence length, ξ, is the spatial extent of the wave function of electrons [12]. The coherence length of Nb is 38 nm and it describes the spatial distance needed for the transition from the superconducting state to the normal state. In the mixed state of type-II superconductors, the coherence length is the radius of the normal core of a flux line (see Section C), where the superconductivity is lost due to the penetration of quantized magnetic flux.

London theory and Ginzburg-Landau theory are well established theories of superconductivity and provide the fundamentals for understanding mechanisms of magnetic flux trapping by defects in Nb.

C. Magnetic flux trapping

1. Magnetic flux penetration in the mixed state

As an external magnetic field, H_e, increases to just above H_{c1}, Nb transitions to mixed state and the external magnetic flux can penetrate the superconductor according to the phase diagram shown in Figure 2b, but the magnetic flux is quantized on a macroscopic scale [12], [41]. The quantized flux is called a flux line or vortex, which is isolated from each other when the external field is just above H_{c1} [12]. The spatial variation of the magnitude of order parameter $|\Psi|$ and magnetic flux density *b* near a flux line is shown in the schematic plot in Figure 4. The radius of a vortex is equal to the penetration depth λ (~39nm), and the superconductivity is lost ($|\Psi| = 0$) within a radius of ξ (coherence length, ~38 nm). This central region with a diameter of 2ξ is almost in the normal state and thus is called the normal core.

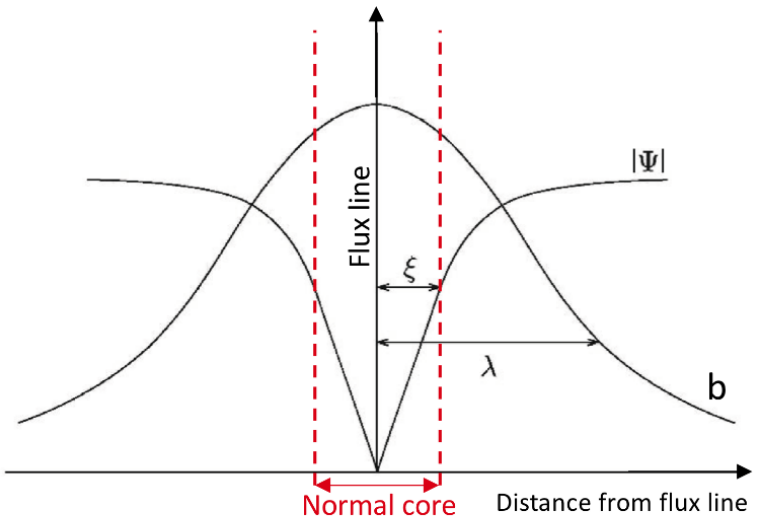

Figure 4. Schematic plot of spatial variations of the order parameter ($|\Psi|$) and the magnetic flux density (b) near an isolated flux line at mixed state of the superconductor; the flux line is parallel to the vertical axis, which shows the magnitude of the order parameter and the flux density. Penetration depth λ is the radius of the vortex, while coherence length ξ is the radius of the normal core [12].

2. Losses caused by magnetic flux trapping

Magnetic flux, resulting from the earth's field or thermoelectric currents generated as the cavity is cooled through T_C, can be trapped in Nb, leading to anomalous RF loses (high field Q-slope, Figure 5a) and local overheated regions (hot spots) in the equator areas where the RF magnetic field is at its maximum [11], [13], [42], [43]. A study [13] was performed to map the hot spots on the cavity surface during an RF test, as shown in Figure 5b. A comparison between Figure 5b and Figure 5c shows that the temperature difference of hot spots decreased, especially at locations of the red dots, where local heaters were used to apply the local thermal gradient known for depinning trapped flux. This is evidence that the hot spots are caused by trapped vortices.

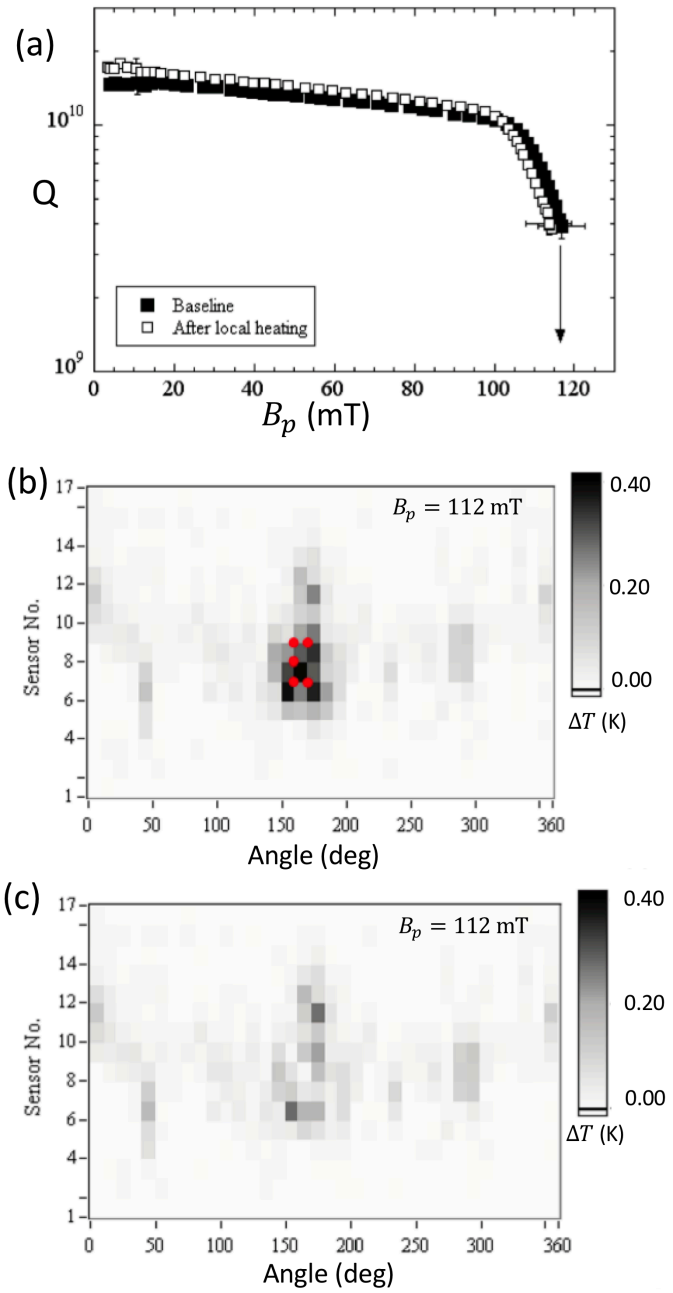

Figure 5. RF test results at 1.7 K shows a high field Q slope at a peak surface magnetic field of about 112 mT before (black square) and after (white square) local heating (a), and the corresponding unfolded temperature maps at $B_p = 112$ mT, T = 1.7 K before (b) and after (c) local heating [13].

3. Mechanisms of magnetic flux trapping

The mechanisms of magnetic flux trapping by microstructural defects such as grain boundaries, hydrides, dislocations, and voids have been studied for many decades [14], [16], [44]–[48]. In the 1950s, Pippard studied the effect of surface roughness, anneal, polycrystallinity, and insoluble impurities on the magnetic flux pinning in Sn [44]. Flux trapping could be reduced by improving Nb purity, electropolishing, and anneal, indicating a correlation between the flux trapping and the presence of defects in superconductors. Mechanisms of flux pinning by grain boundaries and dislocations will be discussed in this section.

a. Flux pinning by grain boundaries

In recent years, large grain Nb has been used to fabricate SRF cavities that have demonstrated higher quality factors with lower fabrication costs due to the elimination of forging and rolling processes, compared to the traditional fine grain Nb cavities [5]. One of the hypotheses for the improved performance is that large grain Nb has fewer grain boundaries and therefore traps less magnetic flux when cooled through the critical temperature.

Zerweck [15] first proposed an electron scattering mechanism at grain boundaries to explain flux pinning by grain boundaries. Electron scattering occurs when electrons travel across grain boundaries. As a result, the mean free path[5] of the electrons becomes shorter at grain boundaries, leading to shorter coherence length, which means the energy of the normal core of a flux line becomes smaller when a flux line approaches a grain boundary. This lower energy enables the flux lines to be pinned by the grain boundaries, and the strength of flux pinning is

[5] The average distance traveled by electrons between collisions.

proportional to the variation rate of the coherence length, where the elementary pinning force can be expressed as [12]

$$f_P = \frac{\pi}{2}\xi_b \mu_0 H_c^2 \left(\frac{d\xi}{dx}\right)_m \tag{8}$$

where ξ_b is the bulk coherence length, and $\left(\frac{d\xi}{dx}\right)_m$ is the maximum value of the coherence length variation rate [12]. Experiments have been carried out to prove the mechanism of grain boundary pinning. Figure 6 is from a study by Dasgupta [14]. There is a peak of critical current when the magnetic field is parallel to the grain boundary, indicating the existence of the flux pinning force due to the grain boundary, which is proportional to the critical current of superconductors.

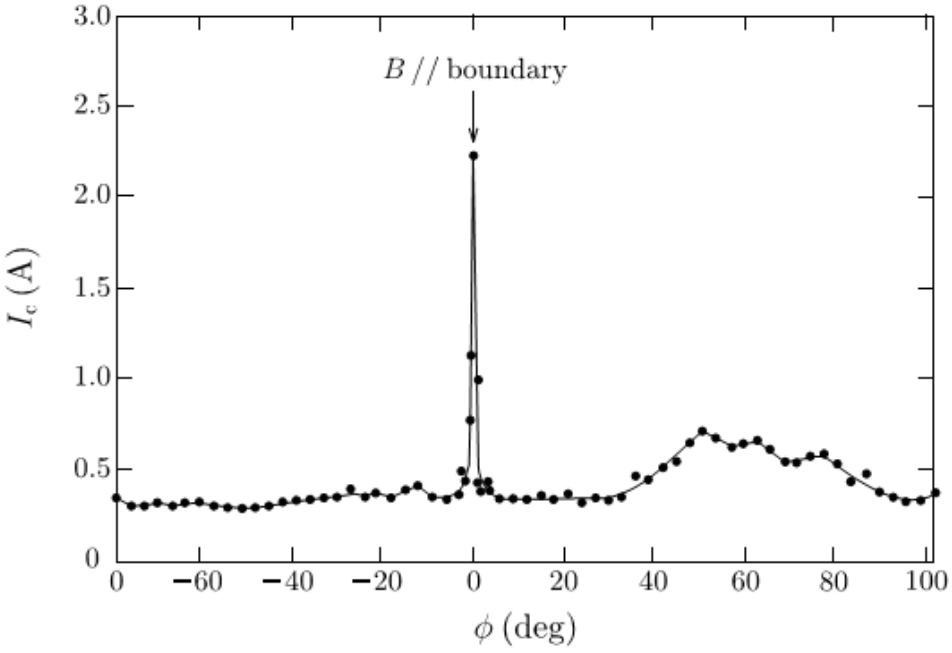

Figure 6. The relationship between the critical current density and the angle between the magnetic field and the grain boundary. The critical current peak at **B** // boundary indicates a pinning force jump when the grain boundaries are parallel to the applied magnetic field [14].

b. Flux pinning by dislocations

Dislocations are introduced during the SRF cavity fabrication and can act as pinning centers of magnetic flux. While the pinning force of grain boundaries is due to the electron scattering mechanism, the pinning force from dislocations arises from the elastic energy interaction between a dislocation and a flux line. Small changes in the specific volume (of the order of 10^{-7}) and elastic constant (of the order of 10^{-4}) occur when a material becomes superconducting, resulting in a stress field surrounding the normal core of a flux line [49]. Therefore, forces between a dislocation and a flux line act on each other can be calculated using the Peach-Koehler equation [50].

Consider an edge dislocation parallel to a flux line, as shown in Figure 7. In cylindrical coordinates with z-axis lying in the center of a flux line (pointing out of the page), the stress tensor of the normal core of a flux line is given by [49]

$$\boldsymbol{\sigma} = \frac{\Gamma \xi^2}{r^2} \begin{bmatrix} 1 & 0 & 0 \\ 0 & -1 & 0 \\ 0 & 0 & 0 \end{bmatrix} \tag{9}$$

where ξ is the radius of the normal core of an isolated flux line, $\Gamma = -\frac{\epsilon_{v0}\mu(1+\upsilon)}{3(1-\upsilon)}$, ϵ_{v0} is the ratio of dilation in the normal core to that of the surrounding superconducting region, μ is the shear modulus, υ is the Poisson's ratio, and r the distance between the flux line and the dislocation line.

With a Burgers vector $\boldsymbol{b} = b_0(-\cos\phi_0, \sin\phi_0, 0)$ in the (x', y', z) coordinates ($\boldsymbol{b} = b_0(1,0,0)$ in the original coordinate system), and a dislocation line vector $\boldsymbol{t} = (0,0,1)$, the Peach-Koehler equation $\boldsymbol{f} = -(\boldsymbol{\sigma} \cdot \boldsymbol{b}) \times \boldsymbol{t}$ can be applied:

$$\boldsymbol{f} = \frac{\Gamma \xi^2 b_0}{r^2}(-\sin\phi_0, \cos\phi_0, 0) \tag{10}$$

where $\boldsymbol{f}$ is the force acting on the dislocation in the stress field of the flux line, which is equal to the force acting on the flux line by the dislocation stress filed, but in an opposite direction. When r is equal to its lower limit ξ, the maximum elementary pinning force $f_p = \Gamma b_0$.

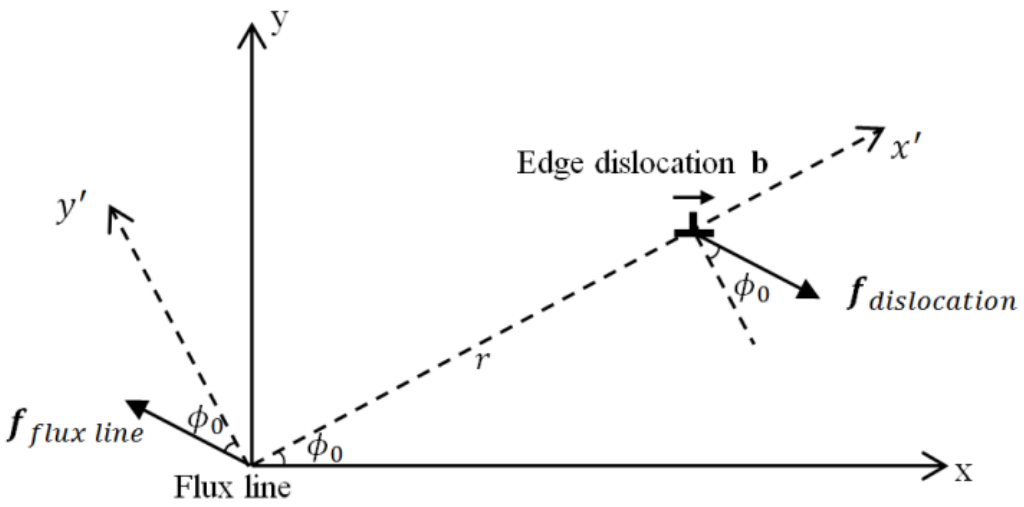

Figure 7. Flux line at the origin and a parallel edge dislocation with the repulsive forces on both the flux line and the dislocation [49].

Some studies indicate the flux pinning force due to dislocations is considerably weaker than that of voids [45] or normal precipitates [12]. However, in heavily worked materials, dislocations could form substructures that have sizes comparable to the coherence length and thus may be more effective at trapping magnetic flux than individual dislocations.

D. Dislocation structures and slip systems in Nb (BCC crystal structure)

1. Dislocation basics

Dislocations are one dimensional or linear crystal defects dividing the slipped part and unslipped part of a crystal lattice that has been through plastic deformation [51], [52] (Figure 8). Dislocation slip is one of the mechanisms enabling the formability of metals [53]–[55]. The magnitude and direction of shear of a dislocation is defined by its Burgers vector, denoted by $\boldsymbol{b}$, and the plane the dislocation glides on is called the slip plane. One slip direction and a slip plane compose a slip system, and multiple slip systems can be simultaneously activated during plastic deformation.

Dislocations can be categorized into pure screw, pure edge, and mixed characters. An edge dislocation has a line direction perpendicular to the Burgers vector, while a screw dislocation line is parallel to the Burgers vector. Dislocations with line directions between edge and screw on the slip plane have a mixed character. A schematic illustration of a curved dislocation is shown in Figure 8, where the left end of the dislocation is a pure screw and the right end a pure edge. The curved part in the middle has a mixed dislocation character.

Screw dislocations in BCC[6] metals are parallel to the <111> Burgers vectors with no defined slip planes, while the edge dislocation line direction is most commonly a <112> or <110> direction on a {110} or {112} slip plane, with <111> Burgers vectors.

[6] Body-centered cubic.

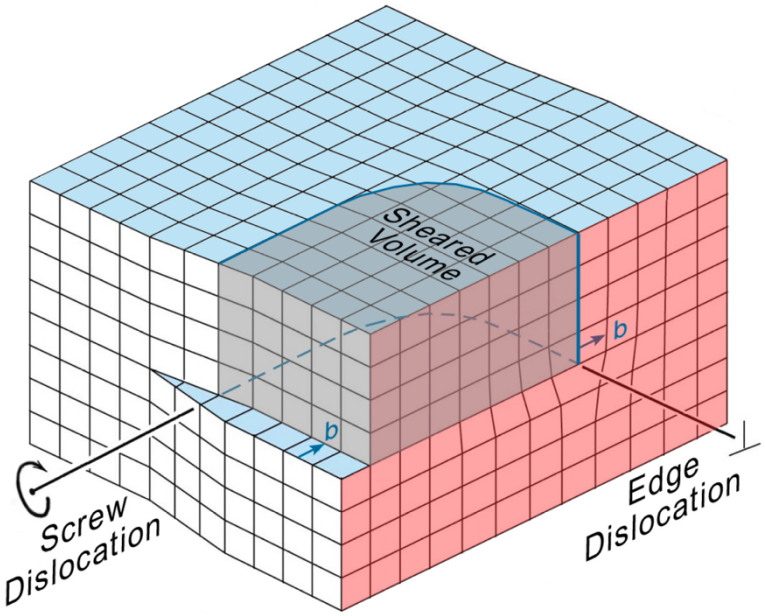

Figure 8. A curved dislocation having pure screw character (left end) and pure edge character (right end), and mixed character in the middle where the dislocation line is neither perpendicular nor parallel to the Burgers vector **b.** The dislocation line separates the sheared volume and the un-sheared volume of the crystal lattice [10].

For simplicity, the slip of dislocations can be illustrated using the model of an edge dislocation, which can be thought of as an extra half atom plane (plane B in Figure 9b) [56] inserted into an otherwise perfect crystal lattice (Figure 9a). Under shear stress parallel to slip plane A (Figure 9b), an edge dislocation is generated by breaking the atom bonds and starts to glide on the slip plane along the Burgers vector direction. This moving edge dislocation separates the slipped and un-slipped parts of the crystal (blue shadows in Figure 9b) and will slip through the whole slip plane and exit from the other surface, resulting in a step on the surface with a displacement equal to the magnitude of the Burgers vector (Figure 9c). The upside-down "T" symbol indicates the edge dislocation with its line direction perpendicular to the page.

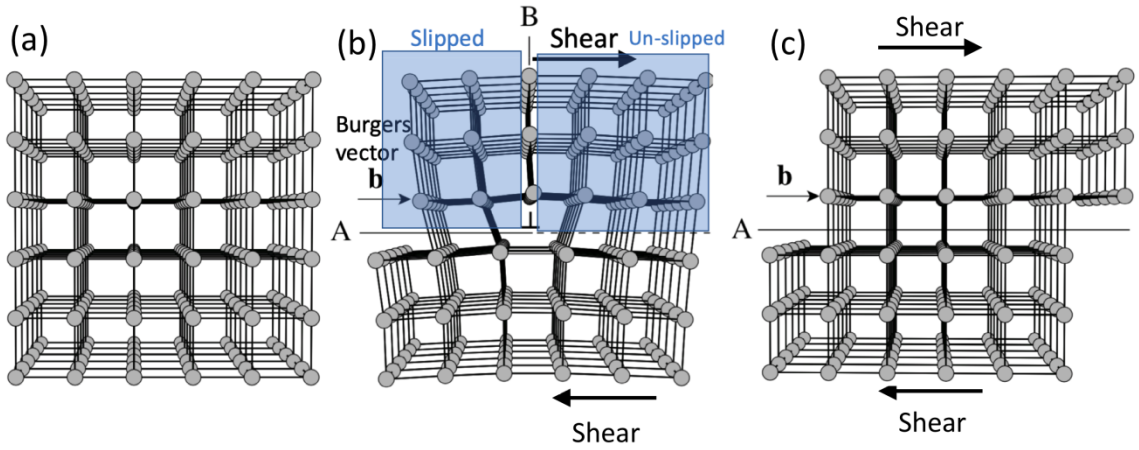

Figure 9. A perfect crystal lattice (a) generates dislocations under shear stress, which is an extra plane of atoms separating slipped and un-slipped parts of the crystal lattice, and moves along the direction of the Burgers vector (b); the edge dislocation slips through the whole slip plane and exit from the other surface, resulting in a step on the surface (c).(redrawn in [56] based on classic works of [53]–[55]).

2. Slip systems in BCC metals

Nb is the most elastically compliant of BCC metals [57] and has a high stacking fault energy that enables cross slip, so the slip of dislocations is the main mechanism of deformation. For BCC metals, slip occurs in close-packed <111> directions [58] on {110}, {112}, and {123} crystallographic slip planes [59], which intersect with each other along a common <111> direction, as shown in Figure 10. Consequently, it is easy for screw dislocations to cross slip between {110} planes and {112} planes, resulting in wavy and ill-defined slip lines [59], [60]. In single-crystal Nb with pre-existing dislocations, the heat treatment affects the dominant slip system activation [20], [29], [31].

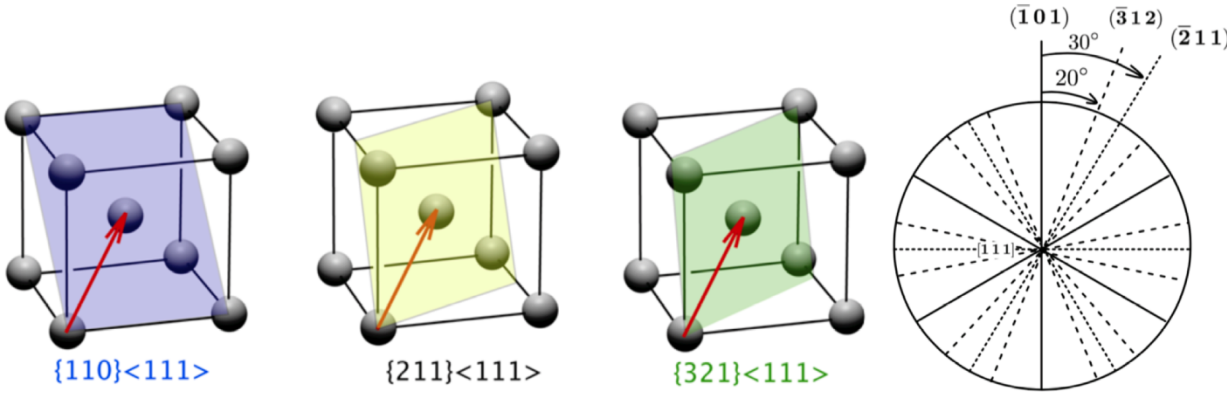

Figure 10. Three potential slip systems in BCC metals and the corresponding [111] direction stereographic projection [61].

Screw dislocations are more frequently observed than edge dislocations in BCC metals, which indicates a higher mobility of edge dislocations [60], [62], [63]. Dislocations in BCC metals reside in deep energy wells, and a large percentage of the energy needed for dislocation slip is provided by thermal vibration [64]. Like other BCC metals, Nb has a high strength at cryogenic temperatures, which is the operating environment of Nb cavities.

3. Dislocation substructures in BCC metals after deformation

After deformation, Nb samples show macroscopic shape changes as a result of the slip of dislocations. Tangled networks of dislocations and dislocation substructures can be very complicated even in a single grain. They tend to divide and subdivide a crystal grain into smaller volumes with different slip systems dominating the deformation process [65]–[68]. Dislocation groups remaining within deformed metals are categorized into two types: statistically stored dislocations (SSDs) and geometrically necessary dislocations (GNDs). The SSDs exist as nearby pairs with opposite Burgers vectors and they can be annihilated when diffusion enables them to move and meet each other and annihilate. The local strain caused by the SSDs cancels, while the strain from the GNDs contributes to the final shape change of the crystal [65].

A deformed grain tends to divide and subdivide into volume elements [66], [67]. Equiaxed dislocation cells constitute the smallest volume elements [68] and the blocks of these cells are divided by dense dislocation walls, which may evolve into microbands with increasing deformation [66], [67]. Cell walls are incidental dislocation boundaries that develop due to the statistical mutual trapping of glide dislocations [65], while dense dislocation walls contain geometrically necessary dislocation boundaries, which are necessary for lattice rotations [65].

4. Schmid law and non-Schmid effect in BCC metals

a. Schmid law

It has been established that metals deform by dislocation slip on multiple different slip planes along specific directions. Multiple slip systems are often activated to achieve macroscopic deformation. This collective slip of dislocations does not necessarily happen simultaneously. Rather, dislocation slip usually starts on a specific plane when the shear stress resolved on this plane reaches a critical value, called the critical resolved shear stress (CRSS), before slip on multiple slip systems is activated.

Consider a uniaxial tensile test of a cylindrical sample with an applied force *F* along the axis, as shown in Figure 11. The Schmid law [69] defines the relationship between the tensile load, resolved shear stress, and the orientation of the slip system, given in Equation (11):

$$\tau_r = \sigma \cos\psi \cos\lambda \tag{11}$$

where τ_r is the resolved shear stress, σ is the applied stress along the tensile axis, ψ is the angle between the tensile axis and the slip plane normal, and λ the angle between the tensile axis and the slip direction, as defined in the schematic illustration in Figure 11.

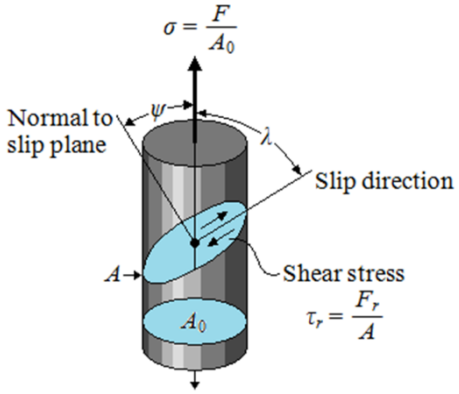

Figure 11. Schematic illustration of the Schmid law showing the relationship of the applied force, resolved sheared stress, and slip system orientation. (Image credit: engineeringarchives.com, based on [69]).

When the applied force F reaches a value such that the resolved shear stress $\tau_r = \text{CRSS}$, the slip system described in Figure 11 will be activated. The Schmid factor is defined as $m = \cos\psi \cos\lambda$, and it describes the likelihood of the activation of a slip system based on uniaxial deformation and the crystal orientation [69]. A slip system in uniaxial loading has a Schmid factor varying from 0 to 0.5, with 0.5 representing the most highly stressed slip system, hence the highest likelihood of activation. A slip system with $m = 0.5$ represents a soft orientation where the resolved shear stress on the slip system is as high as it can be.

The Schmid factor is a very useful tool to determine possible active slip systems when the material is subjected to stress and will be used in this study for tensile sample design and slip system analysis. The non-Schmid effect of BCC systems will be discussed next.

b. Non-Schmid effect of BCC metals

BCC metals are known to have a high temperature and strain rate dependence of yield and flow stress even in pure metals, due to the intrinsic characteristics of the BCC structure [70]. As early as 1928, Taylor [71] found that slipping on a given plane showed different gliding resistance for opposite slipping directions in some BCC metals, indicating the breaking of the Schmid law,

which is also known as the non-Schmid effect of BCC metals. Many investigations in the following decades substantiated Taylor's discovery by showing that the resistance to dislocation glide on {112} planes is lower for applied shear stress in the twinning sense compared to shear stress in the anti-twinning sense [72]–[76]. This is called the twinning/anti-twinning asymmetry of {112} slip in BCC metals. Studies of tensile deformation of Nb at 150 K show dominant straight slip traces belonging to low-stressed planes [77]. This phenomenon is evidence of anomalous slip and indicates a breakdown of the Schmid law of critical resolved stress at low temperatures. According to the Schmid law, the operative slip system should have the highest resolved shear stress.

Figure 12 shows measured values of CRSS in compression tests for three different temperatures for a BCC metal, as an example of the non-Schmid effect. The horizontal axis χ is the angle between [-101] direction and the normal of the maximum resolved shear stress plane (MRSSP). This orientation of the MRSSP has been commonly used in earlier theoretical and experimental studies [70], [78]. Due to the crystal symmetry, it is sufficient to consider $-30° < \chi < 30°$. The MRSSP is the (-1-12) plane for $\chi = -30°$, and then becomes the (-211) plane when $\chi = 30°$ [79]. In Figure 12, the asymmetry at 20 K is so large that CRSS for twinning (-211) shear is only 80% of the anti-twinning (-1-12) shear. This asymmetry becomes less evident at higher temperatures (77 K), and essentially invisible at room temperature (293 K).

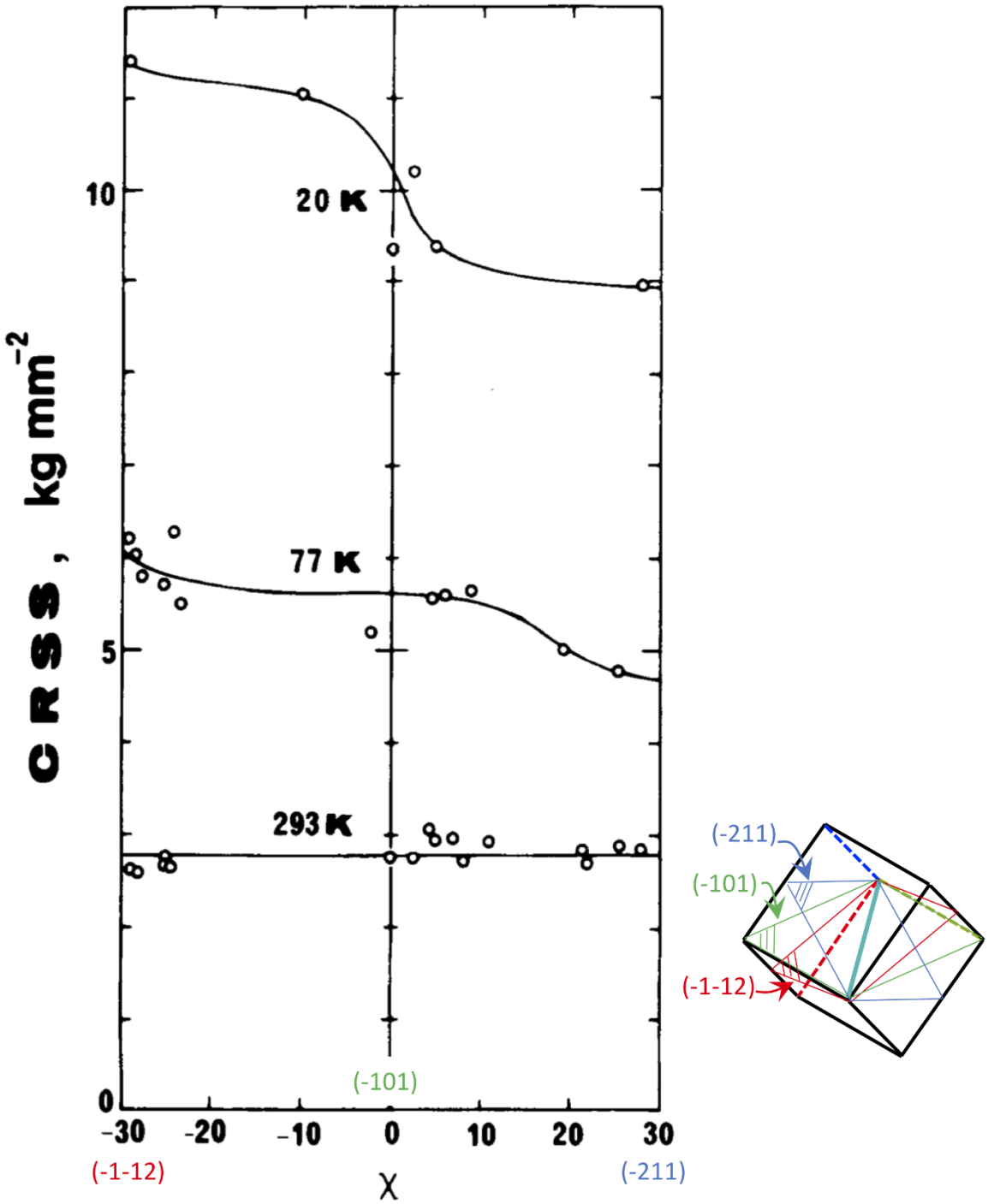

Figure 12. Curves of the measured critical resolved shear stress (CRSS) versus the angle (χ) between [-101] and the maximum resolved shear stress plane (MRSSP) normal at three different temperatures show the twinning-antitwinning asymmetry of a BCC metal (Li-65 at. pct. Mg) at low temperatures. The unit cell at the lower right corner shows three possible MRSSPs sharing the same [-1-1-1] Burgers vector (turquoise line). $\chi = 30°$, 0°, and $-30°$ for planes (-211), (-101), and (-1-12), respectively. The red, blue, and green dashed lines represent the crystal x, y, and z axes. This plot was reconstructed based on [80].

In spite of the non-Schmid effect of BCC systems, the Schmid factor is used as the major criterion to evaluate the likelihood of slip system activation in this dissertation, and the argument for this is given below.

Mapar [81] carried out studies to fit non-Schmid crystal plasticity models to predict the tensile test results of single-crystal Nb, but it was not successful. Instead, Mapar's work suggested that the Schmid model could predict the tensile deformation of Nb more effectively than the non-Schmid model. It was pointed out that it is possible that Nb shows a more evident non-Schmid effect in compression stress states [81]. Also, the non-Schmid effect is affected by the temperature, as shown in Figure 12. Christian [70] reported that the tension-compression asymmetry of Nb was not evident at room temperature and only became considerable at 77 K. Therefore, it is reasonable to assume that the Schmid's law still holds for uniaxial tensile deformation at room temperature, such as the tensile tests in this dissertation.

Using the Schmid factor as a criterion for the likelihood of slip activation requires an assumption that {110} and {112} planes of Nb have the same CRSS. Although there is a difference between the CRSS values of the two planes, the work by a former PhD student Kang [82] suggests that this difference is minor. Kang performed single crystal Nb tensile tests and slip system analyses. It was found that the preferred slip systems are dependent on the pre-existing dislocation substructures. In as-received samples with pre-existing dislocation content, the preferred slip planes were observed to be {112} planes, while in annealed samples of the same orientation the preferred slip planes changed to {110} planes, due to a low pre-existing dislocation density. This suggests that the CRSS difference of the {110} and {112} is not significant and hence is assumed to be the same in this dissertation.

Slip systems of Nb during tensile deformation have been systemically studied by former PhD students working on the Nb project [82], [83]. There is still a lack of study on the compression tests of single crystal Nb samples. Also, the previous work was only focused on the deformation behavior itself, without correlating the dislocations structures with superconductivity. In the current dissertation, dislocations and their effect on superconductivity of Nb were both studied by combining electron microscopy and magnetic flux characterization techniques, with a focus on their effect on flux trapping behavior.

E. Hydrogen contamination in Nb

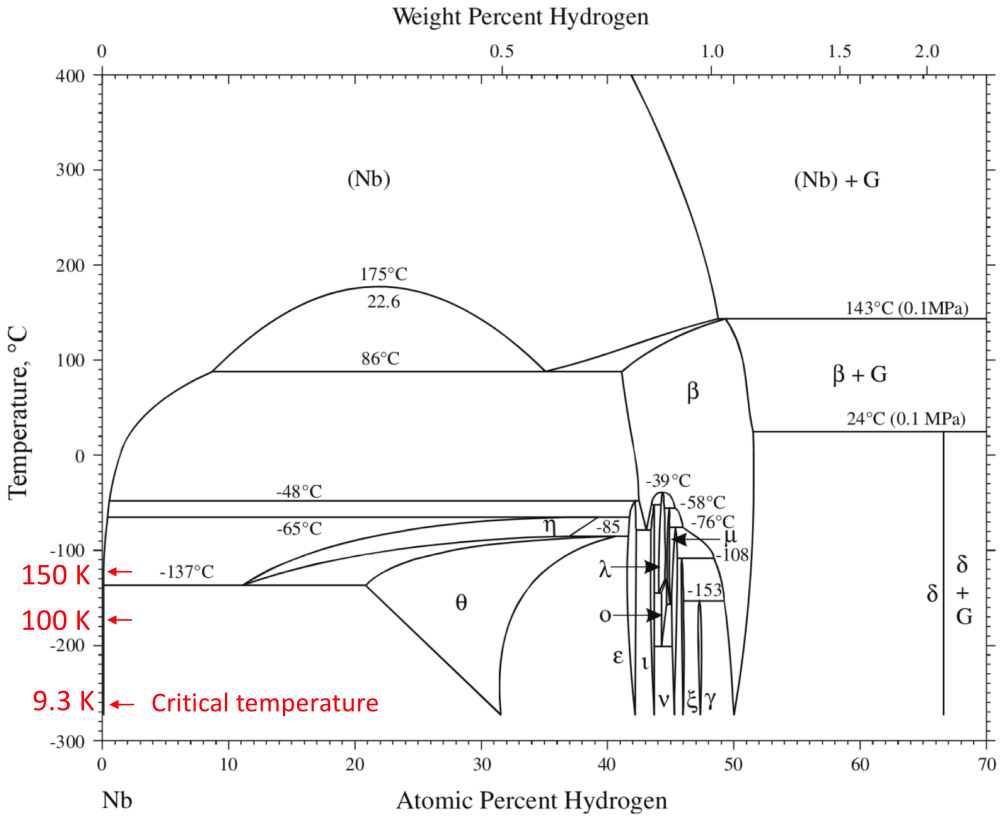

Figure 13. Nb-H phase diagram [84].

Hydrogen can be trapped in vacancies, dislocation cores, and solid-solid interfaces and it is well-known for causing embrittlement in metals [85]–[87]. The Nb-H phase diagram, Figure

13, shows that hydrides can form when there is a small concentration of hydrogen. In Nb, hydrogen can combine with vacancies to form vacancy-hydrogen complexes due to the fact that the complex has lower formation energy than vacancies in hydrogen contaminated Nb [88]. These vacancy-hydrogen complexes act as hydride nucleation sites and facilitate precipitation of normal-conducting hydrides during Nb cavity cooldown through 100–150 K. Hydrides cause Q-disease and high field Q-slope in Nb cavities which are characterized by an abnormal increase of residual resistance and RF losses during the RF test [89], [90]. To eliminate the high field Q-slope, Nb cavities are usually processed using electropolishing followed by a 90–145 ℃ heat treatment in vacuum [90]. This low temperature baking is believed to break down the vacancy-hydrogen complexes, and thus suppress the precipitation of hydrides [23], [90]. The cure for Q-disease is a 600–800 ℃ anneal, which reduces the bulk hydrogen concentration, although the subsurface H concentration is only slightly affected by a 600–800 ℃ heat treatment [91], [92]. The subsurface hydride precipitation is suppressed due to the breakdown of vacancy-hydrogen complexes after heat treatments in spite of a high hydrogen concentration.

Due to its small volume, hydrogen can easily enter Nb during electro-polishing and buffered chemical polishing when the surface pentoxide layer is broken and fresh Nb surface exposed [90]. Oxide layers can effectively protect Nb from hydrogen contamination [93]. The concentration of hydrogen inside Nb is the highest near the surface and can be 1–20 at.% within several tens of nanometers beneath the surface, while it is much lower in the bulk (~10^{-4} at.%) [91], [94], [95]. During cooldown to the superconducting temperature (~9.3 K), normal-conducting Nb hydride precipitation can lead to a ~12% local volume increase, which is accommodated by both elastic deformation and formation of interstitial dislocation loops in the Nb matrix that transport material away from the hydrides [96]–[99]. When warming up, Nb

hydride reversion (dissolution) leads to a local volume decrease, which is accommodated by a reduction of elastic strain and reverse plastic deformation near the precipitate. This leaves scars with a locally high density of dislocations in regions where hydrides were present [96], [97].

Hydrogen has a high mobility in Nb and can interact with other defects such as grain boundaries and dislocations, which could be both trapping/segregation sites and transport channels for hydrogen atoms [85], [100]. The interaction between hydrogen and defects and how this interaction affects flux trapping in Nb is a primary focus in the present work.

F. Experimental techniques to characterize dislocations and trapped flux

Electron channeling contrast imaging (ECCI) was used to characterize dislocations, while magneto-optical (MO) imaging was used to observe the magnetic flux behavior in Nb samples below the superconducting transition temperature. A short review of these two techniques is presented in this section.

1. ECCI

The scanning electron microscope (SEM) based ECCI technique enables the direct observation of dislocations in bulk samples [101]–[107]. In contrast to transmission electron microscopy (TEM), the ECCI technique allows for direct observation of dislocations on a bulk sample with a much larger observation area without destroying the sample, and the technique is more suitable for in-situ observations and dislocation density measurement [105]–[108].

An SEM equipped with scanning coils that can rock the electron beam around a point by about 5° enables the collection of selected area channeling patterns (SACPs), which serves as an orientation map of the crystal. Based upon the SACP, the sample can be tilted and rotated to reach the desired channeling conditions, similar to a two-beam condition in TEM, where dislocations

locally distort the crystal lattice of an otherwise perfect crystal, leading to a higher backscattered electron (BSE) yield near the dislocation than the ideal channeling condition for the perfect crystal. The BSE yield is collected by a detector and used to construct an image that shows the spatial locations of defects.

Usually, a region is observed under several different channeling conditions in order to perform $\boldsymbol{g} \cdot \boldsymbol{b}$ analysis to determine the Burgers vectors and slip planes of the dislocations, based on the $\boldsymbol{g} \cdot \boldsymbol{b} = 0$ [102], [103], [105] and the $\boldsymbol{g} \cdot \boldsymbol{b} \times \boldsymbol{u} = \boldsymbol{0}$ [109] invisibility criteria, where $\boldsymbol{g}$ is the diffraction vector, $\boldsymbol{b}$ the Burgers vector, and $\boldsymbol{u}$ the dislocation line direction.

An enabling tool to conduct ECCI observations is TOCA[7] [110], [111], which can simulate SACP bands needed to determine $\boldsymbol{g}$ vectors. This tool provides tilts and rotations to reach the desired imaging conditions. Figure 14 [107] shows the meaning of the dimensionless deviation parameter w, which describes how much the crystal orientation with respect to the incident beam ($\boldsymbol{k_0}$) deviates from the Bragg condition. Figure 14a shows the incident electron beam with a wave vector $\boldsymbol{k_0}$ and the excited lattice planes (hkl) represented by five parallel solid lines. (b)–(d) show the simulated SACPs of three different conditions with an overlaid white cross that represents the electron beam. By tilting and rotating, the crystal orientation with respect to the incident beam can be changed to reach different deviation parameters. The electron beam center is located outside of the corresponding channeling band (vertical in (b)) for $w > 0$, and moves inside the channeling band for $w < 0$. When $w = 0$, the beam center is right at the edge of the channeling band, corresponding to the exact Brag condition and the angle between the incident beam and the

[7] Tools for Orientation determination and Crystallographic Analysis.

lattice planes is equal to the Brag angle θ. Electron channeling contrast (ECC) images are taken using a small positive deviation parameter to obtain a good contrast of dislocations [112].

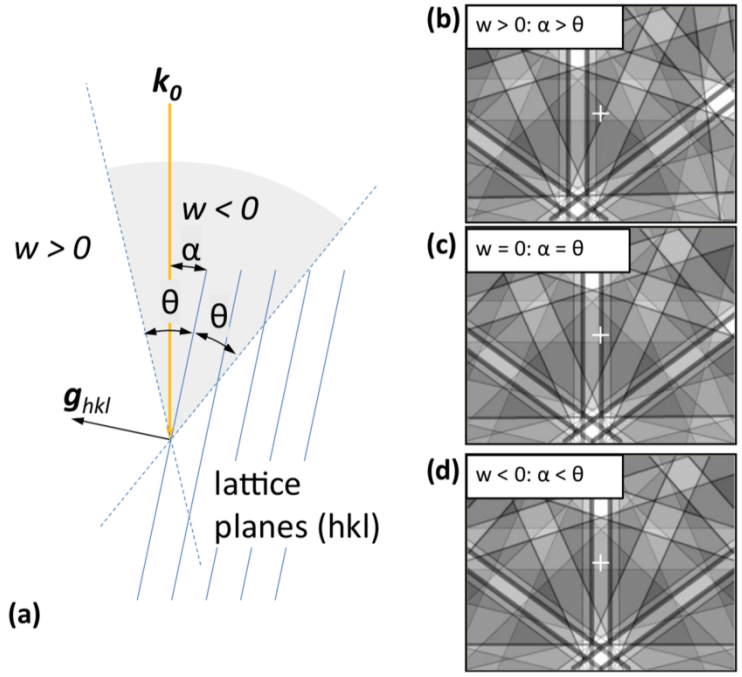

Figure 14. Schematic representation showing the meaning of the deviation parameter w. (a) shows the orientation of the crystal lattice (parallel solid lines) with respect to the incident beam ($\boldsymbol{k_0}$). θ is the Bragg angle, α is the angle between the incident beam and the lattice plane, and $\boldsymbol{g_{hkl}}$ the reciprocal lattice vector. (b)–(d) are the simulated SACPs of three slightly different orientations overlaid with a white cross representing the beam center [107].

BSE yield $\Delta\eta$ is a function of the crystal orientation with respect to the incident beam. The dependence of BSE yield $\Delta\eta$ on the deviation parameter is provided in Equation (12). Only the part of the total BSE intensity due to orientation variation is considered in this equation.

$$\Delta\eta = \frac{N\sigma_B}{2\pi}\xi_0'\left(-\frac{\left(w+\xi_0'/\xi_g'\right)}{1+w^2-\left(\xi_0'/\xi_g'\right)^2}+\frac{w}{1+w^2+\left[(1+w)\left(\xi_0'/\xi_g'\right)\right]^2}\right) \tag{12}$$

where N is the number of atoms per unit volume, σ_B is the cross-section for backscattering, and ξ_0' and ξ_g' are the absorption distances of electrons determined based on quantum mechanical calculations.

This dependence of BSE yield on the deviation parameter based on Equation (12) is plotted in Figure 15 [107]. Intensive backscattering occurs for $w < 0$ and a bright band is formed in the SACP (within the channeling band). The BSE intensity drops rapidly to the minimum when $w = w_C$, forming the dark Kikuchi line in the SACP. This rapid change of BSE yield with respect to the deviation parameter at values close to zero forms the electron channeling contrast [107].

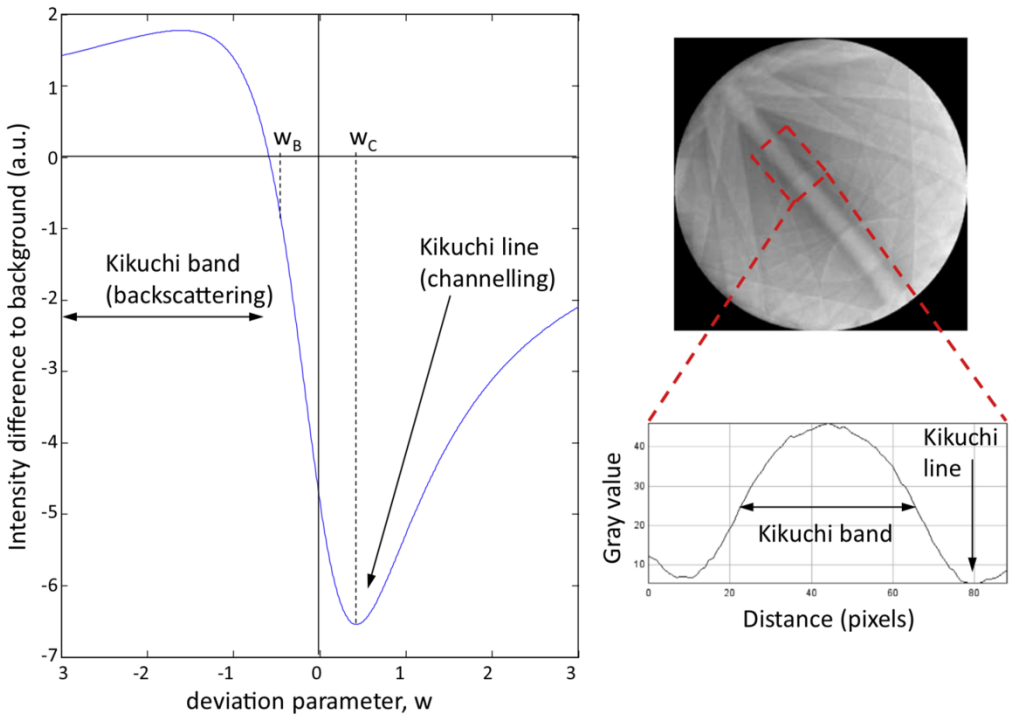

Figure 15. The plot of the BSE yield dependence on the deviation parameter w (left) and an SACP with an intensity profile across the selected band (red dashed line box) (right). $w = w_B$ indicates the backscattering condition with a high BSE yield, and $w = w_C$ indicates the channeling condition, with a low BSE yield. Note that the position of the exact Bragg condition ($w = 0$) is different from the position of the channeling condition [107].

ECCI is the main method for crystal defect characterization in deformed Nb samples in this study. With a resolution comparable to the bright field transmission electron microscopy, ECCI enables studies of dislocation arrangement, low angle grain boundaries, and dislocation densities.

2. Cryogenic magneto-optical (MO) imaging

MO imaging uses the strong Faraday effect in bismuth-doped yttrium iron garnet (B-YIG) to measure the change of the vertical magnetic field component ($\boldsymbol{H_z}$) above a superconducting sample using a standard polarized light microscope. The light polarization can be rotated by a magnetic field [27], [113], [114], as shown in the schematic illustration in Figure 16. Therefore, the magnetic flux that penetrates the MO sample can be related to the rotation of the light polarization, and hence, visualized. The collected MO images are grey-scale, and a brighter intensity indicates a higher density of magnetic flux. The technique is able to resolve magnetic fields of the order of 1 mT with ~5–10 μm spatial resolution [27], [114], [115].

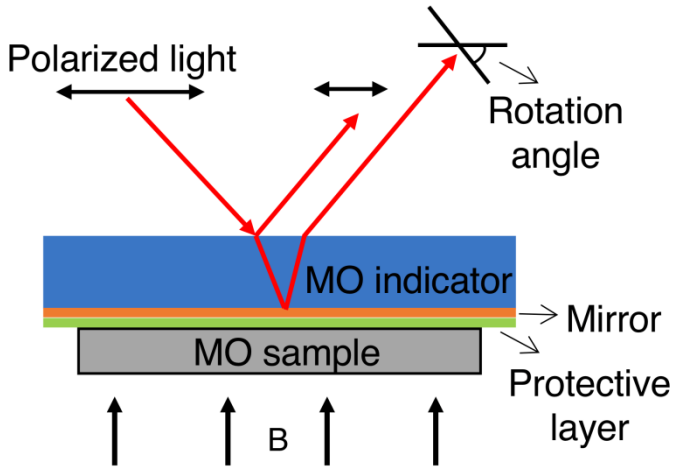

Figure 16. Schematic drawing of the side view of the MO imaging technique. The applied magnetic field (**B**) is perpendicular to the MO sample overlaid with a protective layer, a mirror, and a MO indicator (after Polyanskii [115]).

There are three imaging modes for the MO technique: zero-field-cooling (ZFC) mode, remnant field (RF) mode, and field-cooling (FC) mode [16], [27]. For the ZFC mode, a sample is cooled in a zero-field environment below the critical temperature ($T_c = 9.3$ K) at a rate of 8–10 K/min, then an increasing external field is applied perpendicular to the sample surface (Figure 16). Flux penetration into the sample is revealed as a brighter contrast compared to dark flux free regions in MO images. ZFC is sensitive to surface superconducting properties. For the RF mode, the external field applied following the ZFC mode is removed to show the remnant field within the sample. In the FC mode, the sample is cooled in an external field, which is later removed when the temperature is below the critical temperature, to take the FC MO images. Since the sample has been fully penetrated before it reaches the superconducting state, FC MO images taken after external field removal show bulk flux pinning properties.

An MO imaging study on high-purity Nb samples was carried out and it was observed that flux penetration along grain boundaries occurred when the grain boundary plane is close to parallel to the applied magnetic field [27]. This is consistent with Figure 6.

G. A review of studies on magnetic flux penetration and trapping

Trapped magnetic flux by defects is one of the main sources for RF losses in Nb cavities. Trapped flux with a flux density of 1 μT can lead to an increase of 3.5 nΩ in surface resistance [116]. There has been much research on this topic in the past decades. Microstructural defects including dislocations, hydrides, and grain boundaries were investigated to evaluate their effect on flux penetration and superconductivity of Nb.

Narlikar [117] investigated the effect of dislocation configuration on the superconductivity of Nb using magnetization measurements in annealed and cold worked polycrystalline Nb samples, respectively. In Narlikar's work, it was observed that cold work created dislocation cell structures

that became more organized regular dislocation networks after a 1200 ℃ anneal. The former dislocation structure caused more trapped flux compared with the regular dislocation networks. It pointed out that flux lines were trapped by their interactions with dislocation tangles, and dislocation tangles with large local variations in dislocation density were more effective flux trapping centers than uniformly distributed dislocations in cold worked Nb. However, the magnetization measurement in Narlikar's study only represented an overall effect of defects in the samples and was not able to show the spatial distribution of the trapped flux. As a result, the effect of dislocations and grain boundaries on flux trapping could not be separated. Habermeier [118] and coworkers carried out a magneto-optical study of a deformed single crystal Nb rod orientated for single slip, which showed locations of flux penetration into Nb samples. Their study suggested anisotropic flux penetration, which was attributed to the formation of dislocation cell structures along special directions leading to anisotropic flux pinning forces [118]. It was observed that the flux pinning force was the largest when flux lines were parallel to the dislocations. Habermeier's work linked the distribution of flux penetration with dislocation arrangement using MO and sample orientation design for single slip, but no characterization of dislocation structures was carried out. There could be a deviation between the designed dislocation arrangements and the dislocations structures that were actually present. A dislocation imaging method, such as ECCI, with a large enough observation area, is valuable to study details of the dislocation arrangement.

Köszegi [119] studied polycrystalline Nb samples extracted from a large-grain high-purity Nb slice using quantitative magneto-optical imaging and found that 1400 ℃ heat treatment led to significantly reduced trapped flux, from 100% trapping to 30% trapping. Köszegi's work enabled direct observation of flux trapping by hydrides. Flux trapping by individual ~10 μm hydrides, which formed during cooldown, were resolved as local maxima in magneto-optical imaging.

Neither the grain boundary nor the crystal orientation was observed to play major roles in the amount of trapped flux.

Preferential flux penetration along grain boundaries indicates suppression of local superconductivity at grain boundaries. Multiple magneto-optical studies [27], [28] showed that preferential flux penetration occurred when the external field was parallel to the boundary planes, suggesting the weakness of grain boundaries in expelling flux. Grain boundaries are segregation sites for hydrogen atoms, and hydrogen trapped in the grain boundaries can precipitate as hydrides during cooldown. It is not clear whether the grain boundary flux penetration observed in references [27], [28] was caused by the normal conducting hydrides[8] in the grain boundary, or the intrinsic characteristics of the grain boundary itself. It is not clear which one is dominant if both factors are affecting flux penetration.

The performance of SRF Nb cavities strongly depends on the cavity preparation process, including 120 ℃/48 h, 600 ℃/10 h, and 800 ℃/2 h heat treatments and nitrogen doping, which suggests that the diffusion and redistribution of light elements, such as hydrogen, oxygen, and nitrogen, play important roles in superconducting properties of dislocations, vacancies, and grain boundaries [120]. Hydrogen is highly mobile in Nb and can get trapped in vacancies, dislocation cores or grain boundaries, which may also serve as transport channels for hydrogen atoms and hence provide precipitation sites for hydrides. Therefore, the effect of dislocations, hydrides, and grain boundaries cannot be viewed in isolation from each other; instead, the interactions between them should be understood. These interactions between hydrogen, dislocations and grain boundaries, and how they affect flux trapping will be discussed in this dissertation.

[8] Hydrides have a much lower critical temperature (1.5 K) than Nb (9.25 K).

H. The opportunity for research

Achieving minimum possible residual resistance and a high quality factor ($Q > 10^{10}$) is critical for new superconducting linear accelerators that are being built, such as LCLS-II at SLAC [33]. LCLS-II is an upgrade of LCLS, the world's first hard X-ray free-electron laser source built in 2006. The performance goal of LCLS-II is to reach a quality factor higher than 2.7×10^{10} and an accelerating electric field of 16 MV/m. Trapped flux can cause significant RF losses in Nb cavities with such a high quality factor; however, understanding of the mechanisms of flux trapping and expulsion in Nb cavities during cooldown is still not clear enough to consistently achieve reproducible high performance. To achieve the performance goal of the new accelerators, researchers in several accelerator-focused national labs have carried out many investigations to improve the performance of Nb cavities by optimizing the processing methods, including heat treatments and cooling procedures [9], [23]–[25], [36], [90]. Real size Nb cavities were used in these investigations.

One important manifestation of RF losses due to trapped flux is the high field Q slope, which can be eliminated by a 120 ℃/48 h vacuum heat treatment (also known as mild baking). An explanation of the mechanism of mild baking was proposed in studies carried out by Romanenko and coworkers [23], [90]. It was suggested that mild baking can cause dissociation of vacancy-hydrogen complexes, which exist in the near-surface layer in a large concentration, and hence suppress the precipitation of hydrides during cooldown and lead to the decrease of the dislocation density. Recent research on magnetic flux expulsion showed that nearly full flux expulsion and ultra-high quality factors (~10^{11}) could be achieved by high temperature heat treatments and spatial thermal gradients at the normal/superconducting phase front during cooling [9], [24], [121]. A spatial thermal gradient is known to lead to depinning forces [122], while high temperature heat

treatments are believed to reduce dislocation densities, dissociate vacancy-hydrogen complexes, and cause grain growth. Flux expulsion studies by Romanenko suggested that in order for efficient magnetic flux expulsion during cavity cooldown, the thermal gradient needs to be larger than 0.1–0.2 K/cm and the cooling rate through the superconducting transition temperature needs to be larger than 30 mK/s [9], [123]. Posen's study [25] also suggested that cold work plays an important role in flux trapping. Cavities made from heavily deformed material showed much more trapped flux during cooldown compared with another cavity made from as-received material. The sensitivity of RF losses to trapped flux depends on the cavity preparation methods such as nitrogen doping, which change the electron mean free paths of the material [36].

Recent studies on flux trapping and expulsion reviewed above are all based on real Nb cavities and therefore have the advantage of being close to practical situations. However, these studies only focused on different processing methods (thermal gradient, heat treatments) and the resulting improvement in performance including quality factors and flux expulsion properties, without systematically studying flux trapping mechanisms on the microscopic level, such as flux trapping by hydrides, dislocations, grain boundaries, and low angle grain boundaries. It would be strategic to design these microscopic material defects with special structures to evaluate their effect on flux trapping in Nb samples.

In this dissertation, Nb samples were designed with chosen grain boundaries and tensile axes based on crystal orientation and Schmid factor analysis to strategically introduce desired dislocations by nominal 5% tensile deformation, such that the effect of these dislocations, grain boundaries, and hydrides on flux penetration and flux trapping can be evaluated. The ECCI technique enables comprehensive imaging and characterization of microscopic defects including dislocations and low angle grain boundary structures in bulk samples, while MO imaging

technique is useful to observe the magnetic flux behavior in the Nb samples. The combination of these two techniques can illuminate the correlation between the crystal defects and the resulting local superconductivity suppression and flux trapping.

Several hypotheses can be proposed based on the literature review in this chapter. These hypotheses guide experimental design and analysis and motivate research opportunities on flux trapping and expulsion in Nb cavities:

1. High angle grain boundaries are transport channels, while low angle grain boundaries and dislocation substructures are traps, for hydrogen.
2. Hydride precipitation may be favored at grain boundaries and dislocation substructures along specific crystallographic directions related to dislocation arrangements.
3. Hydrides and dislocation substructures (including LAGBs) are the main sources of flux trapping or premature flux penetration, while the effect of grain boundaries on flux trapping/penetration is not as significant.
4. Patterns of flux penetration are related to the arrangements of dislocation substructures.
5. The amount of trapped flux is proportional to the density of dislocations in cold worked Nb samples. Compared with randomly distributed dislocations, more organized dislocation substructures (such as LAGBs) are more effective at trapping magnetic flux.

I. Structure of the dissertation

Chapters I and II provide an introduction and a literature review about the background of the current work. Chapter III describes the material and the experimental procedures.

Chapter IV is a magneto-optical study of a deformed single crystal Nb sample to understand the relationships between hydrides, dislocation arrangements, LAGBs, and flux penetration. Flux penetration at LAGBs was observed, and the reasons for the flux penetration, the interaction between hydrogen and LAGBs, and the LAGB development due to cold work are discussed.

Chapter V is part of a continuing effort, based on the previous work [82], to investigate the evolution of dislocation structures during the deformation of single crystal Nb tensile samples. Different deformation mechanisms of the annealed and as-extracted samples are discussed, and dislocation entanglements were observed in 40% strained single crystal Nb using ECCI.

Chapter VI presents an investigation of flux penetration in undeformed bicrystal Nb samples with different grain boundaries using MO imaging and ECCI, to identify relationships between grain boundaries, dislocation substructures, hydrides, heat treatment, and flux trapping. The effect of intrinsic characteristics of grain boundaries on flux penetration is discussed, and the dislocations generated due to hydride precipitation were characterized and their possible effect is speculated.

Chapter VII shows a study on deformed bicrystal Nb tensile samples that were designed to cause focused shear near grain boundaries or with different orientation hardness values in the two adjacent grains during tensile deformation. The 5% deformed samples were investigated using MO and ECCI to evaluate the effect of dislocation content and substructures on flux trapping. The

relationship between amounts of deformation or dislocation densities and amounts of trapped flux is discussed.

A general discussion integrating topics in Chapter IV, V, VI, and VII is presented in Chapter VIII, followed by the conclusion and future work in Chapter IX.

Chapter III. MATERIALS AND METHODS

A. Nb disks, Laue X-ray diffraction, and ECCI characterization

1. Nb disks

All samples were extracted from two Nb disks, with diameters of ~270 mm and thicknesses of ~3 mm, provided by Chris Compton at the Facility for Rare Isotope Beams. The Nb disks were sliced from large-grain Nb ingots and the material had a high purity with RRR larger than 300. The two Nb disks are identified as the Tokyo-Denkai (TD) disk and the Ningxia (NX) disk. The chemical compositions are listed in Table 1. Low magnification photographs of the TD and Ningxia Nb disks, with visible large grains, are shown in Figure 17a and c, respectively.

Table 1. The maximum allowed impurity amounts specified by the manufacturers.

Impurity	Maximum allowed impurity amounts (at ppm)	
	TD Nb ingot	Ningxia Nb ingot
Tantalum	93	51
Tungsten	5	8
Titanium	19	10
Iron	17	8
Silicon	33	33
Molybdenum	9.7	10
Nickle	16	8
Oxygen	58	29
Nitrogen	66	33
Hydrogen	460	276
Carbon	77	77

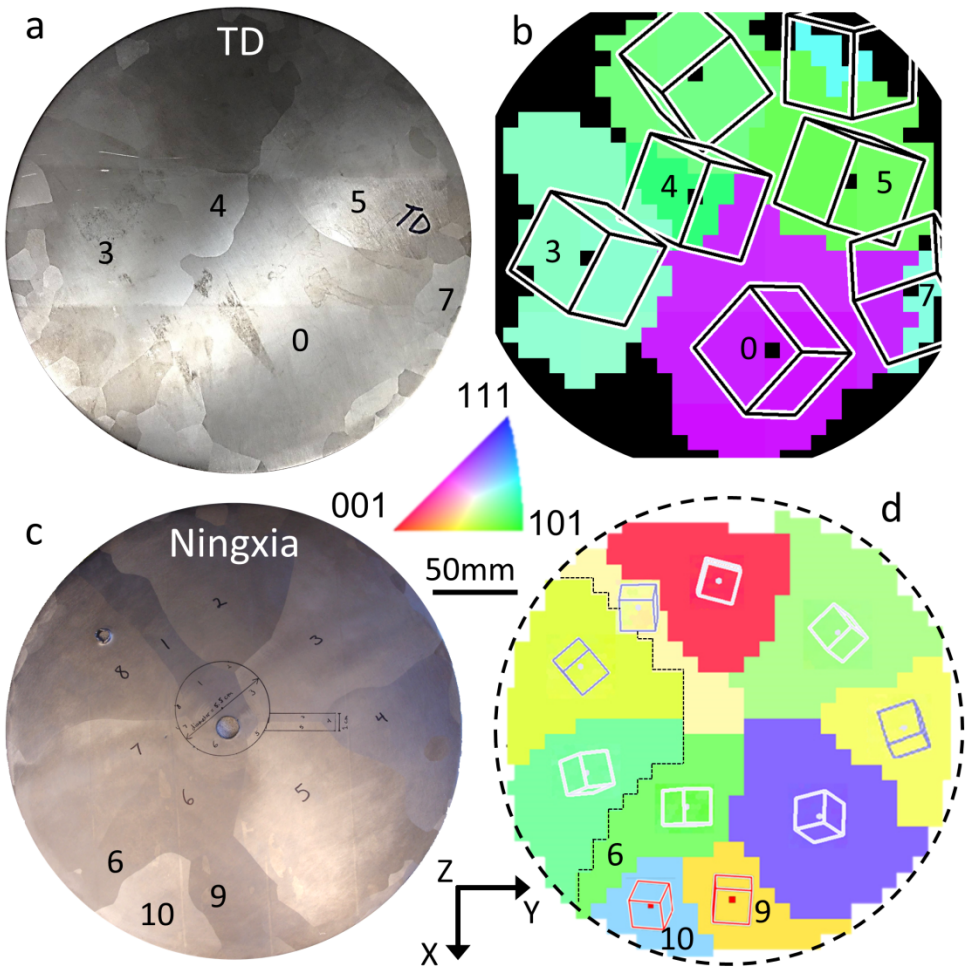

Figure 17. Large-grain Nb TD (a–b) and Ningxia (c–d) disks sliced from ingots and corresponding surface normal direction orientation maps measured using Laue X-ray diffraction (b and d, respectively). The prisms overlaid on the orientation maps represent the visualization of BCC crystal orientations. The black arrows at the bottom indicate the global coordinate system (reconstructed from reference [82]).

2. Laue X-ray diffraction

Bunge Euler angles (φ_1, Φ, φ_2) are used to describe the orientation of crystals with respect to the global (sample) coordinate system. Due to the high degree of symmetry of the BCC crystal structure, there are 48 equivalent Euler angle triplets that describe the same crystallographic orientation. Therefore, it is important to discern between the global (sample) coordinate system and the crystal (local) coordinate system. The global coordinate system with the X-axis pointing

down, Y-axis to the right, and Z-axis pointing out of the page is used throughout this dissertation (black arrows at the bottom of Figure 17).

Before any tensile samples were extracted, the grain orientations in the two Nb disks were measured using Laue X-ray backscattered diffraction technique. A Laue X-ray diffraction setup was built by our group with an open sample stage (Figure 18) that is large enough to hold the Nb disks, which are too large to fit into an SEM chamber. The recorded diffraction patterns were analyzed and indexed using OrientExpress software 3.4, based on information of the BCC structure, the distance of the sample from the Laue camera, and dimensions of the area detector [82]. The Laue method lacks the spatial resolution compared with the electron backscattered diffraction (EBSD). Grains smaller than 1 mm cannot be characterized as 1 mm is the illumination area of the X-ray. According to reference [124], the angular accuracy of the Laue method is about 0.2°, which is comparable to EBSD measurement. The major source of error comes from the mounting uncertainty.

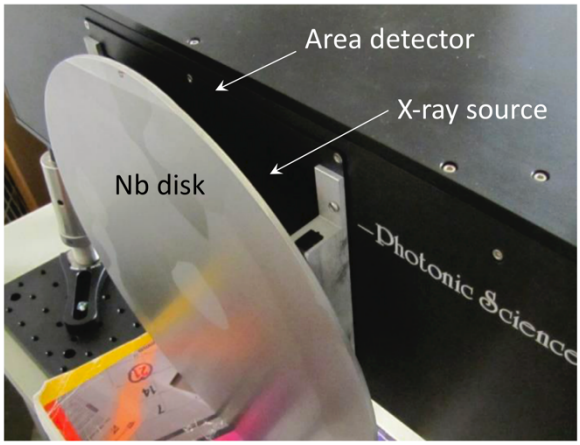

Figure 18. Setup of Laue X-ray measurement of the Nb disks (image remade from reference [124]).

The Laue X-ray diffraction characterization was mostly performed by a former Ph.D. student Di Kang. For more details of this technique, the readers are referred to reference [82]. Orientation maps generated from the orientation measurements are shown in Figure 17b (TD Nb disk) and Figure 17d (Ningxia Nb disk). The crystal orientation data are very useful for tensile axis design based on the Schmid law to make samples with favored slip systems during tensile deformation along chosen tensile axes.

3. ECCI characterization and sample preparation

ECCI is the main technique used in the current study to characterize dislocation structures in the Nb samples. The general procedures for performing ECCI and the sample preparation methods are described in this part, while the details of sample preparation are presented in APPENDIX A.

Sample preparation is of great importance for the success of ECCI characterization. A sample with a very smooth and damage free surface that shows sharp selected area channeling patterns (SACPs) under the channeling mode of SEM (Figure 19) is a prerequisite for ECCI. In order to achieve this surface condition, bulk Nb samples were first ground using sandpapers (Grit 600, 800, and 1200), followed by polishing on cloth using 9 μm, 3 μm, and 1 μm diamond suspensions, and a final polishing using 0.05 μm OP-S (colloidal silica suspension). To remove the surface damage layer due to mechanical grinding and polishing, the samples were then prepared by chemically removing about 20 μm to 150 μm surface material using BCP. The recipe consists of 25 vol.% nitric acid, 25 vol.% hydrofluoric acid, and 50 vol.% phosphoric acid. The BCP was carried out in a plastic beaker with a rotating stir bar to keep the solution flowing during polishing to avoid etching pits.

Figure 19 shows a low-magnification secondary electron (SE) image of a well prepared single crystal Nb sample with clear channeling bands (left) and the corresponding selected area channeling patterns in the channeling mode (right). The channeling bands are visible in the resolution mode SE image, collected by an Everhart-Thornley [125] detector, because the crystal orientation with respect to the incident beam changes significantly over the field of view at low magnifications [107].

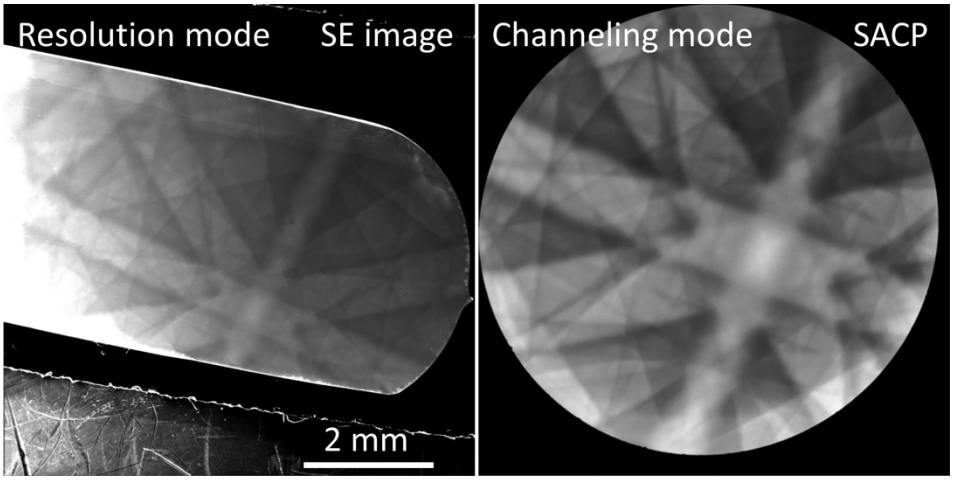

Figure 19. Clear channeling bands on the prepared surface of a single crystal Nb in resolution mode (left) and the selected area channeling patterns collected in the channeling mode (right) using a Tescan Mira SEM.

ECCI was conducted in a Tescan MIRA SEM equipped with a selected area channeling mode, where the primary electron beam can be rocked around a small area (~20 μm) on the sample surface to collect selected area channeling patterns (SACPs). The SACPs were indexed with the assistance of TOCA based on the measured orientation of the sample using EBSD, to determine the $\boldsymbol{g}$ vectors of the main channeling bands, as shown in Figure 20. The Euler angles were measured using EBSD and entered into the TOCA software to generate the simulated channeling

patterns, which can be compared with the collected SACPs (center of Figure 20) to index the main channeling bands (in blue shadows).

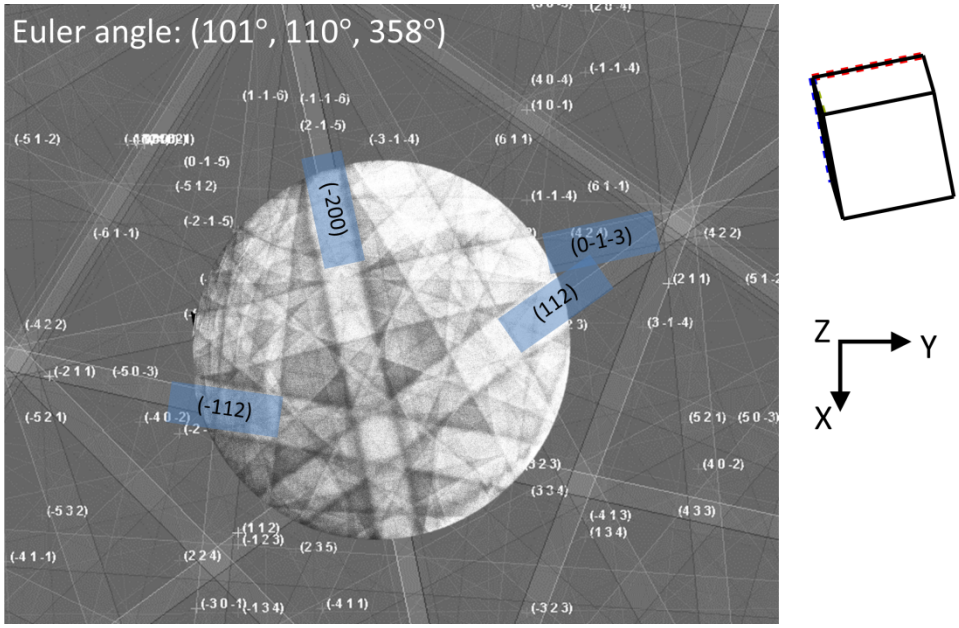

Figure 20. Indexing of the collected selected area channeling patterns by overlaying it on the simulated channeling patterns. The prism at the top right corner shows the orientation of the sample, with red and blue dashed lines representing the x and z axes of the crystal coordinate system. The global coordinate system is indicated by the black arrows below the prism.

The indexed SACPs were used to identify tilt and rotate angles of the sample to reach the desired channeling conditions by aligning the electron beam center with the edge of a channeling band. The mostly used ***g*** vectors are (200), (110), and (112) channeling bands, which have the sharpest contrast. A voltage of 30 kV, a working distance of 9 mm, and a spot size of 20 nm were used to collect the ECC images.

B. MO study of deformed single crystal Nb samples (Chapter IV)

This section summarizes the experimental procedures of the MO study of deformed single crystal Nb samples in Chapter IV reproduced from reference [16].

1. Tensile sample design

A tensile sample with the geometry shown in Figure 23 was extracted from grain 3 in the TD Nb disk using electron discharge machining (EDM). Schmid factors for 360 possible tensile directions were calculated based on the measured orientation of grain 3 in the TD ingot (Figure 17b) in order to find a tensile direction that would lead to one or two favored slip systems. Theoretically, at the beginning of the deformation along the chosen tensile axes, only these one or two favored slip systems will operate and generate dislocations.

In order to realize this, a MATLAB code was built by our group to carry out the Schmid factor calculations. This code assumes a horizontal tensile direction (global Y-axis) and takes the crystal orientation (the second and third Euler angles of grain 3: $\Phi = 141°, \varphi_3 = 108°$) as input to calculate Schmid factors (m) of all 24 slip systems ({110} and {112} slips systems) in BCC over a 360° rotation of the crystal orientation around the sample normal (Z) direction, by changing the angle φ_1 from 0 to 360° with a step size of 1°. The generated curves of the absolute values of Schmid factors for all 24 slip systems in BCC based on grain 3 orientation are shown in Figure 21 over a range of φ_1 from 60° to 240°. The vertical red solid line marks the angle $\varphi_1 = 167°$ (original orientation), and the red dashed line indicates the desired orientation that favors <111> slips on (121) and (110) planes, which is about 37° rotation from the original orientation. The favored slip systems are marked using red rectangles in the legend and the Schmid factors of the two highly favored slip systems are indicated next to the vertical red dashed line in Figure 21. At the desired orientation, there are only two favored slip systems with Schmid factors much higher than other slip systems. Based on Figure 21, the chosen tensile axis is shown in Figure 22 with a red outline of a tensile sample drawing on top of the TD Nb disk image. The deformation along

this tensile axis will lead to generation of dislocations of the two most favored slip systems (red rectangles in Figure 21).

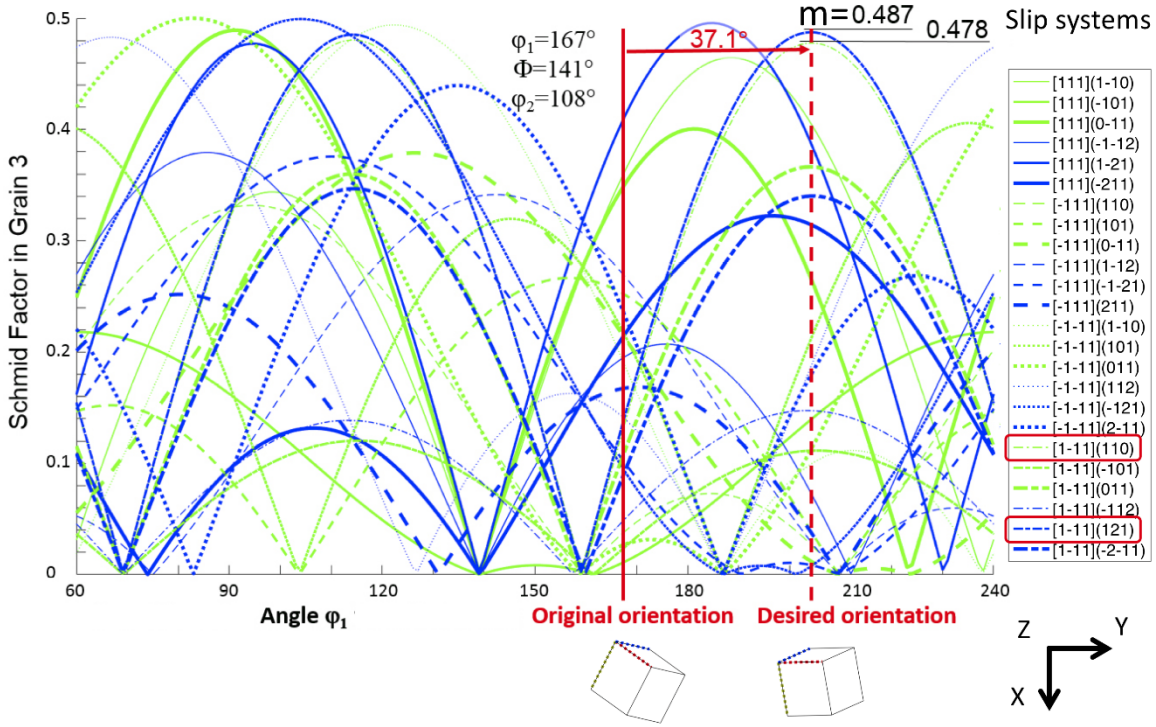

Figure 21. Curves of the absolute value Schmid factors calculated for all 24 slip systems in grain 3 in TD Nb disk over a 360° orientation rotation (by changing the angle φ_1) about the sample normal direction. The vertical red solid and dashed lines represent the original orientation (Figure 17b) and the desired orientation to favor the <111> slip systems on the (121) and (110) planes, respectively. Favored slip systems of new orientation are indicated by red rectangles, the prisms show the orientation (the dotted red, green, and blue lines represent the x-axis, y-axis, and z-axis of the crystal coordinate system), and the black arrows at the lower right corner indicate the sample (global) coordinate system. The Schmid factor calculation assumes a tensile direction along the Y-axis.

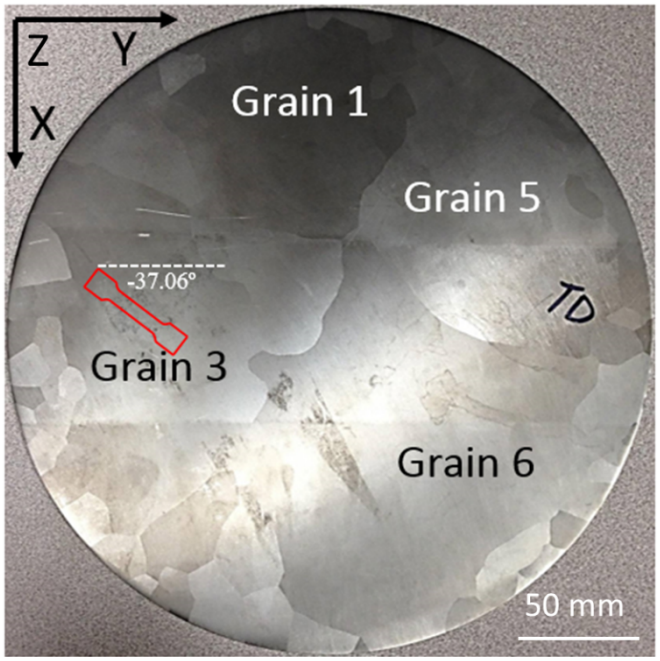

Figure 22. The chosen tensile axis represented using a red outline of the tensile sample about 37° rotated clockwise from the horizontal direction.

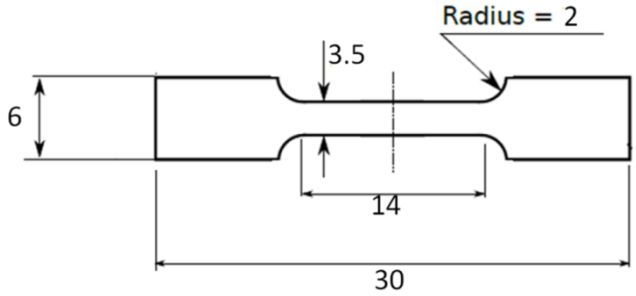

Figure 23. Geometry and dimensions (mm) of Nb tensile samples.

2. 5% deformation and MO sample extraction

The tensile sample was uniaxially strained to reach 5% tensile strain using a cross-head speed of 0.5 inch per minute, after which the deformed sample was cut into four small slices (MO samples A, B, C, and D) with dimensions of 3 × 3 × 1.5 mm, as shown in the photo of the sliced sample in Figure 24(a) and a schematic illustration in Figure 24(b). In Figure 24(b), the yellow dashed line indicates the slip trace of the favored (121)[1-11] slip system, the green dashed-line rectangle shows where the TEM sample was extracted, and the overlaid prims on the shoulders

represent the favored slip system (121)[1-11], with the shaded plane representing the slip plane and the turquoise line the Burgers vector.

The MO samples were sliced along a direction about 45° from the horizontal or vertical direction such that the Burgers vector of the favored slip system (121)[1-11] is approximately parallel to the MO imaged surface (red arrows) of Samples C and D, and perpendicular to the surface of Samples A and B. Therefore, if (121)[1-11] slip is dominant during deformation, the dislocation line orientations on the MO imaged surface can be depicted by the schematic illustration in Figure 24(c), with the screw dislocations (red) parallel to the surface of the left two slices (C and D), and perpendicular to the surface of the right two slices (A and B). The edge dislocations (blue) will be parallel to the surface for all slices. The slip system (110)[1-11], with the same Burgers vector, is also highly favored with Schmid factor $m = 0.48$m and will be very likely to operate during deformation. With this designed dislocation orientation with respect to the surface that is imaged using MO, it is more convenient to study the possible correlation between dislocation arrangements and the flux penetration, or to show the lack of correlation.

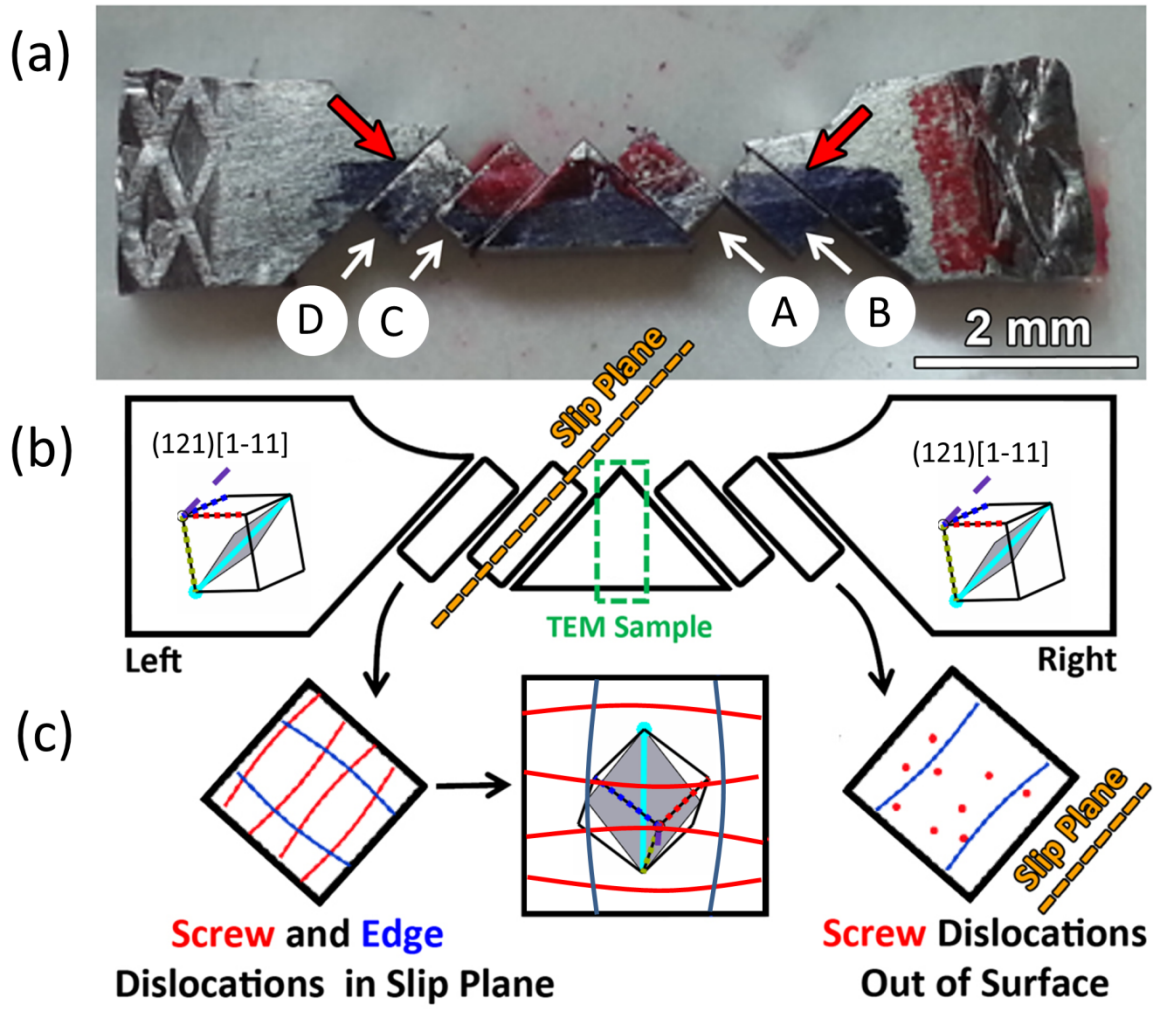

Figure 24. (a) Photo of the deformed tensile sample after EDM slicing with four 45° tilted slices (sample A, B on the right, and C, D on the left). Red paint was used to mark the surface before cutting. The red arrows indicate the directions of MO imaging, with an external magnetic field applied along the opposite directions. (b) A schematic illustration showing the estimated slip plane trace (gold dashed line), the location of TEM sample extraction (green dashed line box), and prisms showing the orientation of Grain 3 and the most favored slip system. (c) The slices (A, B, C, and D) rotated 90° revealing the arrangement of dislocations on the surface imaged using MO. The screw dislocation lines (red) are parallel to the surface in the left two slices, and perpendicular to the surface in the right slices. Edge dislocation lines (blue) are parallel to the surface for all slices.

3. MO imaging

All MO imaging work in this dissertation was performed by Dr. Anatolii Polyanskii at the National High Magnetic Field Laboratory/Applied Superconductivity Center.

The as-extracted MO samples (B and D) were mechanically polished and processed using BCP for 30 minutes to prepare the surface for MO imaging. The BCP recipe consists of 25 vol.% nitric acid, 25 vol.% hydrofluoric acid, and 50 vol.% phosphoric acid.

Three MO imaging modes, ZFC, remnant field (RF), and FC, were used to study MO samples. For the ZFC mode, the MO samples were cooled in a zero-field environment to 7–8 K (below T_c), followed by the application of an external field of 50–60 mT ($<H_{c1}$) perpendicular to the sample surface. ZFC MO images were collected with different field strengths. After this, the external field was removed, and the RF MO images were taken that showed trapped flux. To collect the FC MO images, the same sample was heated up to just above the critical temperature (to ~10–15 K), so that the sample returned to the normal conducting state. The samples were then cooled again in an external magnetic field of 120 mT ($>H_{c1}$) to 7–8K, and the 120 mT external field was removed to form the FC image.

4. TEM and EBSD analysis

This part of the work was carried out by Dr. Zuhawn Sung at the National High Magnetic Field Laboratory/Applied Superconductivity Center in Tallahassee, Florida.

The microstructure of the 5% deformed sample was characterized using a JEOL ARM200F transmission electron microscope (TEM). TEM thin foils were prepared by slicing the remaining central part (green dashed-line rectangle in Figure 24b) of the deformed sample, with a precision diamond saw so that the TEM sample normal was parallel to the tensile axis. Sliced samples were initially mechanically thinned to ~150–200 μm thickness by diamond lapping and then subsequently reduced to ~80–100 μm in central thickness by a dimple grinder. To observe pristine cold-work deformed structure, thinned specimens were finalized for electron transparency using a Struers Tenupol-5 Twin-Jet polishing system with a solution of 6–8 vol. % H_2SO_4 in methanol.

This jet electropolishing is preferred over the focused ion beam (FIB) technique in TEM sample preparation for observation of dislocation morphology in soft metals like Nb because the heavy Ga ions of the FIB can easily disturb the lattice structures of the soft metal surface, which leaves point defects on the TEM sample surface.

Electron backscattered diffraction (EBSD)-orientation imaging microscopy (OIM) was used to characterize the micro-crystallographic features on the sample surface. The OIM was performed in a Zeiss 1540 EsB field emission scanning electron microscope (FESEM) equipped with an EDAX-Hikari high-speed OIM camera. 15 keV electron beam energy and a step size of 50–100 nm were used.

The angular accuracy of EBSD technique is in the range of 0.5° to 2° [126]–[129], and the spatial resolution can be as good as 30–60 nm [128], [130]. The EBSD patterns were collected with the sample at a 70° tilt to maximize the BSE yield. Sample mounting errors can lead to an orientation variation of ~1–2°.

5. 800 ℃ *anneal*

After the first MO cryogenic cycles, the MO samples (B and D) were annealed at 800 ℃ for 2 hours under ultrahigh vacuum (10^{-6} Torr) and then analyzed using MO for the second time. It is empirically known that 600–800 ℃ anneal can remove most of the hydrogen atoms from the bulk of Nb, and therefore, this is a standardized heat treatment procedure to control hydrogen contamination in Nb cavities [91], [92], [131].

C. Dislocation evolution in single crystal Nb samples (Chapter V)

This section summarizes the experimental procedures of the study of dislocation evolution in single crystal Nb samples in Chapter V, which was reproduced from reference [20].

1. Sample preparation

Four single crystal niobium samples with the same orientation (Euler angler: 170°, 67°, 179°) were extracted from the Ningxia Nb disk with a residual resistivity ratio (RRR) > 300, and then different processing methods were applied. Undeformed Sample U-ex was as-extracted, Sample U-an was extracted and annealed, deformed Sample D-ex was extracted and deformed in tension to 40% engineering strain, and Sample D-an was extracted, annealed at 800 ℃ for 2 hours, and then deformed in tension to 40% engineering strain. The sample preparation is summarized in Table 2. Details of characterization using EBSD and the deformation history of these samples (orientation T) are found in references [82]. This orientation has maximum shear stress on a $\{110\}\langle 111\rangle$ slip system and a 9% lower resolved shear stress for shear on a $\{112\}$ plane in the same $\langle 111\rangle$ direction [10].

Table 2. Sample preparation.

Sample ID	Preparation
U-ex	As extracted
U-an	Extracted and then annealed at 800 ℃ for 2 hours
D-ex	Extracted and then deformed to 40% engineering strain
D-an	Extracted, annealed at 800 ℃, and then deformed to 40% engineering strain

2. Atomic force microscopy

Surface topography of the deformed samples with slip traces was measured with atomic force microscopy (AFM) using a VEECO Dimension 3100 scanning probe microscope operating in tapping mode over an area of $40 \times 40\ \mu m^2$. The Gwyddion open source software was used for data processing and visualization.

3. Slip trace analysis

Dislocations with a high resolved shear stress acting on them, represented by a high Schmid factor *m*, can pass through the material, leaving slip traces on the surface, which can be analyzed to identify the active slip system during deformation. Slip trace analysis was performed on the two deformed samples, D-ex and D-an, by comparing slip traces calculated based on the crystal structure and local orientation (using a MATLAB script) with the slip traces observed in SE images.

4. Electro-polishing

The samples were electro-polished in an electrolyte of 90 vol. % sulfuric acid and 10 vol. % hydrofluoric acid using a tungsten cathode while the electrolyte temperature was controlled at minus 30 ℃ with liquid nitrogen. Electro-polishing was done for 8 minutes under a voltage of 15V, resulting in a mirror-like and damage-free surface that provided the surface quality necessary for ECCI observations. Details of electro-polishing is presented in APPENDIX A.

D. Undeformed bicrystal Nb samples (Chapter VI)

This section summarizes the experimental procedures of MO and ECCI study of undeformed bicrystal Nb samples in Chapter VI.

1. MO sample extraction

Three cylindrical bicrystal MO samples, with a thickness of ~1.5 mm and a diameter of 3 mm, were extracted using EDM with chosen grain boundaries from the Nb disks shown in Figure 17. The cylinder axes were parallel to the Nb disk surface normal, and the top surfaces were vibration polished, as shown in Figure 25. The grain boundary traces on the top surface are visible and the bottom ones are marked by black dashed lines. Samples I and II were extracted from the Ningxia Nb disk, while Sample III was cut from the TD Nb disk. The grain boundary

misorientations were 53°, 24°, and 11° for Samples I, II, and III, respectively. The tilt angle of the grain boundary is defined as the angle between the grain boundary plane and the magnetic field applied during MO imaging, which was perpendicular to the sample surface. In Sample I the grain boundary tilt angle was uniformly 10°, in Sample II it varied from 0° (right 2/3 boundary) to about 8° (left 1/3 boundary), and in Sample III the tilt angle varied from 0°–6°, and the boundary showed a twist. Note that both Sample II and Sample III had a boundary that had a partial segment perpendicular to the sample surface (parallel to the magnetic field), while the sample I grain boundary was not perpendicular to the surface along the whole boundary length.

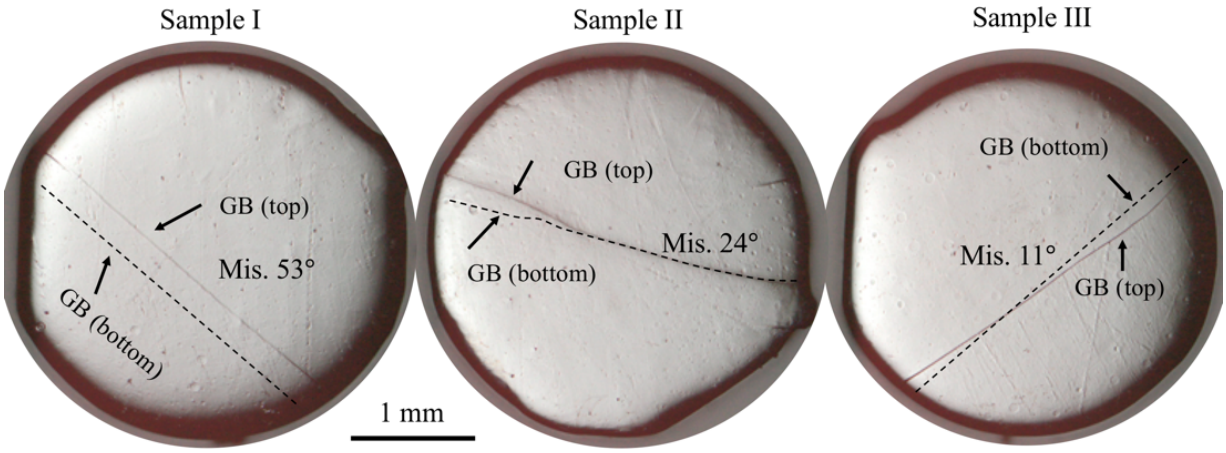

Figure 25. Top surface optical images of three bicrystal MO samples with top surface GB traces visible and bottom GB traces marked by black dashed lines to show the GB tilt; Samples II and III have GBs with a segment perpendicular to the surface, Sample I has a grain boundary with a uniform tilt of 10°, and Sample III has a continuous twist.

2. MO imaging, heat treatment, EBSD, and ECCI

The as-extracted samples were vibration polished, followed by a 30-minute BCP before they were cooled for MO imaging. No heat treatment was done for the three samples before the first MO imaging; therefore, all samples were contaminated with hydrogen. MO imaging for the

three samples was performed at 7–8 K at different fields (15–60 mT) perpendicular to the sample surface, and the results of the first MO imaging are shown in Figure 44.

a. Sample I

After the first MO imaging (cryogenic cycle), the surface of Sample I was prepared by BCP to remove 100–150 μm surface material and then analyzed using ECCI (results shown in Figure 51). In order to evaluate the effect of heat treatment on the evolution of dislocation structures of hydride scars in Sample I, an 800 ℃ 3-hour heat treatment was carried out, followed by a brief BCP etch to improve the surface quality. Again, ECCI analysis was performed on Sample I after the heat treatment (results shown in Figure 52).

b. Sample II

After the first MO imaging, the hydride scars on the surface of Sample II were examined using EBSD, as shown in Figure 45. The EBSD scans were performed on a Tescan Mira field emission gun (FEG)-SEM equipped with an EDAX Hikari EBSD camera (480×480 pixel resolution) and OIM software, using step sizes less than 1 μm. A voltage of 25 kV, working distances of 20–25 mm, and an exposure time of 0.1 s were used. Inverse pole figures (IPF), image quality (IQ), Kernel average misorientation (KAM), and grain reference orientation deviation (GROD) maps were generated from the EBSD scans using OIM analysis software v. 7.3.1. Surface topography of a hydride scar was measured using AFM with a scanning area of $27 \times 29\ \mu m^2$. The Gwyddion open source software was used for data processing and visualization (Figure 47).

Sample II was then heat treated at 800 ℃ for 3 hours to degas hydrogen, followed by a 140 ℃ 48-hour nitrogen doping in an ultra-high vacuum furnace, after which a second MO imaging was carried on Sample II (MO results shown in Figure 49). A subsequent mechanical polishing

was performed on Sample II to reintroduce hydrogen, and a third MO imaging was carried out (Figure 49). Finally, the surface of Sample II was characterized using ECCI after a 150 μmsurface removal by BCP (results shown in Figure 53 and Figure 54). The sample preparation history with the chronology of MO and ECCI observations is shown in Figure 26.

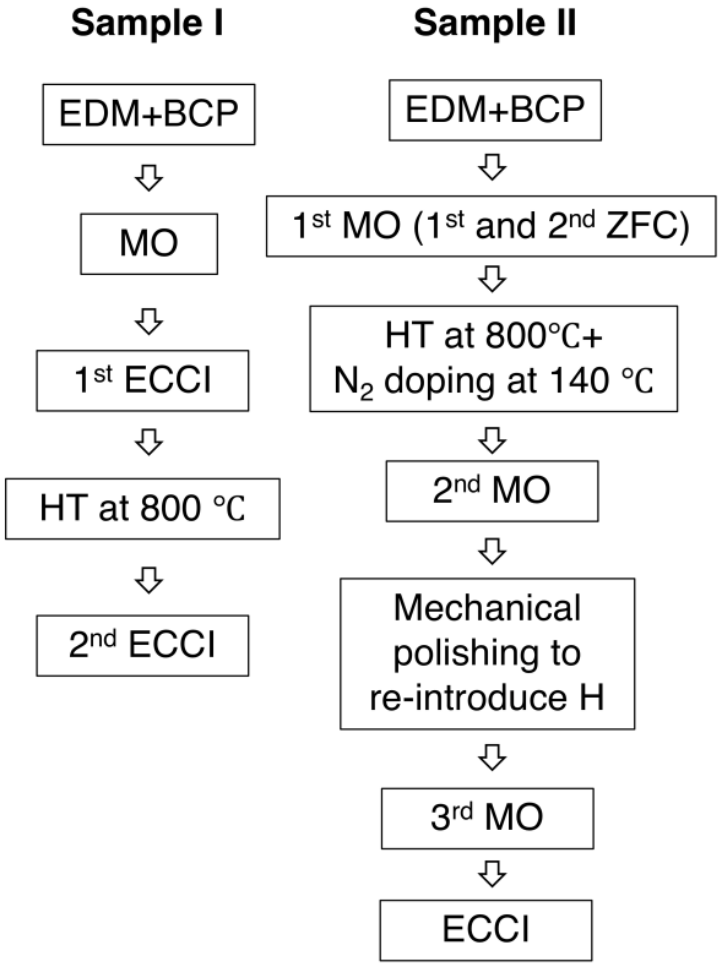

Figure 26. Sample processing history with the chronology of MO and ECCI observations indicated. Only one MO experiment (cryogenic cycle) was carried out for sample I, followed by two ECCI observations before and after 800 ℃ heat treatment (HT). Three MO experiments (three cryogenic cycles) were performed for sample II after BCP, after 800 ℃ HT + N_2 doping, and after mechanical polishing, respectively, followed by ECCI observation.

E. Deformed bicrystal Nb samples (Chapter VII)

This section summarizes the experimental procedures of the MO and ECCI study of the deformed bicrystal Nb samples in Chapter VII.

1. Bicrystal tensile sample extraction

Bicrystal tensile samples were designed based on Schmid factor analysis and extracted from the Ningxia and TD Nb disk shown in Figure 17. The Schmid factor is used as an indicator of orientation "hardness" of the two grains in a bicrystal. For a given tensile axis, a "soft" orientation has favored slip systems with high Schmid factors (>0.45), while a "hard" orientation has slip systems with low Schmid factors (<0.40).

In the TD disk, tensile axes were chosen to generate different combinations of hard and soft orientations of the two adjacent grains when the bicrystals were deformed along the chosen axes, while for NX disk, the tensile axes were chosen to have favored slip system parallel to the grain boundaries to cause focused shear deformation near the grain boundaries.

Portions of Nb disks and tensile axis choosing results are shown in Figure 27, with two tensile samples extracted from each grain boundary. Tensile axes are represented by blue drawings of tensile samples overlaid on the grain boundaries (black dashed lines) on both TD and NX disks. Grains are numbered using "G" followed by the grain number. Bicrystals are named using "TD" or "NX" followed by the grain numbers of the two adjacent grains. One bicrystal sample from each boundary in the TD ingot was studied in an as-extracted state. Two bicrystal samples from each grain boundary in the NX ingot were studied, with one in an as-extracted state, and another one in a heat-treated state (800℃ 2-hour annealed after extraction).

The four most favored slip systems of each bicrystal are listed in Table 3 for the chosen tensile axes shown in Figure 27. Schmid factors larger than 0.45 (soft orientations) are marked in

red. Table 3 also shows that both Grain 6 in NX6-10 and grain 9 in NX10-9 have a highly favored slip system parallel to the grain boundaries, so that focused shear along grain boundaries is highly likely under tensile stress along the chosen axes. The grain boundary tilt angles were measured by overlapping the bottom grain boundaries trace on top of the top boundaries.

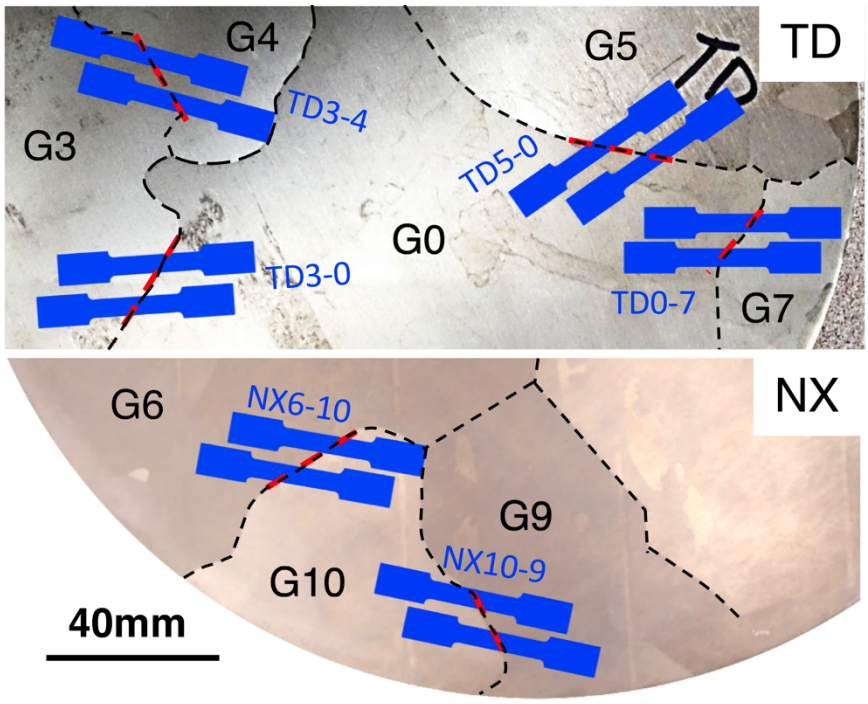

Figure 27. Portions of the TD and NX Nb disks overlaid with blue drawings of tensile samples with chosen tensile axes and black dashed lines representing GBs. Grains are marked by "G" followed by the grain number. Red dashed lines mark the GB segments, where bicrystal samples were extracted.

Table 3. GB misorientation, GB tilt angle, and Schmid factors (for the four most favored slip systems in each grain along chosen tensile axes) of Nb bicrystals.

Bicrystal ID	GB misorien-tation (°)	GB tilt angle (°)	Grain#	Top four Schmid factors
TD3-4 (Soft-soft)	11	0–13	G3	0.48, 0.43, 0.40, 0.29
			G4	0.50, 0.43, 0.43, 0.37
TD3-0 (Hard-hard)	20	N/A	G3	0.39, 0.34, 0.33, 0.28
			G0	0.35, 0.34, 0.32, 0.31
TD5-0 (Soft-soft)	36	0–4	G5	0.46, 0.45, 0.35, 0.35
			G0	0.49, 0.49, 0.44, 0.44

Table 3 (cont'd)

TD0-7 (Hard-soft)	47	N/A	G0	0.34, 0.32, 0.30, 0.29
			G7	0.50, 0.49, 0.45, 0.45
NX6-10 (Soft-soft)	43	AE: 7	G6	0.50 (// GB), 0.43, 0.43, 0.36
		HT: N/A	G10	0.48, 0.47, 0.44, 0.44
NX10-9 (Soft-soft)	23	AE: 14	G10	0.48, 0.48, 0.45, 0.45
		HT: 0–8	G9	0.50 (// GB), 0.48, 0.46, 0.45

AE: as-extracted, HT: heat treated

2. Tensile test, heat treatment, MO imaging, and microscopic analysis

Tensile deformation of ~5% was carried out for all samples, which were characterized using ECCI and EBSD to evaluate the dislocation density and substructures. MO imaging was performed on smaller MO samples (circular pieces with a thickness of ~1.5 mm and a diameter of 3 mm), which were extracted from the deformed bicrystal samples. A 600 ℃ 10-hour heat treatment was performed to remove hydrogen from MO samples before MO imaging. Therefore, the effect of hydrogen contamination is not significant and will not be considered in this chapter.

Dislocation density was measured in five areas in each grain near the grain boundary of sample NX10-9HT. A correction factor of $1/\cos 60°$ was multiplied by the measured dislocation density values, assuming that the dislocations were at random orientations. The length of LAGBs per area was measured using ImageJ (https://imagej.nih.gov/ij/) in the same regions. The results are shown in Figure 64.

Chapter IV. MO STUDY OF DEFORMED SINGLE-CRYSTAL NB SAMPLES

The main content of this chapter is extracted from a published work [16] in which Mingmin Wang is the second author and contributed to the experimental and sample design, MO sample extraction, result analyses, and discussion.

A single crystal Nb tensile sample was designed with a strategically chosen tensile axis, based on orientation analysis and the Schmid law, to introduce desired dislocation arrangements by a nominal 5% tensile deformation. MO imaging was used to observe the magnetic flux behavior in deformed samples at superconducting temperatures. Defects (LAGBs, hydrides, and dislocations) that might be favorable for hydride segregation and flux penetration were investigated using TEM and EBSD. This chapter seeks to clarify the relationships between hydrides, dislocation arrangements, LAGBs, and flux penetration and trapping in Nb. A summary of major observations and discussion is given below, and the original publication is provided in the Appendix C.

A. LAGBs are traps for hydrogen atoms

Room temperature observation of the hydrogen contaminated samples showed numerous hydride scars on the surface after MO cooling, which can be attributed to hydride precipitation during cooling. EBSD analysis (Figure 28) showed a ~20–60 μm wide hydride scar free zone on either side of the LAGBs after the cryogenic cooling cycle. Hydride scars are present all along the LAGB. This suggests that a substantial amount of hydrogen migration toward the LAGB occurred during the cooling. According to grain boundary segregation models in alloys [132], [133], grain boundary segregation is known to be the result of dragging solute atoms to the grain boundary in the form of vacancy-complexes. When plastic deformation is applied, non-equilibrium vacancy concentrations can be produced in the metal by dragging jogs of screw dislocations. The

supersaturated vacancies can interact with hydrogen atoms, creating supersaturated vacancy-solute complexes. The propensity of vacancies to migrate to grain boundaries gives rise to non-equilibrium grain boundary segregation of the solute atoms [134]. Typical cool down between 150 K and 2 K during SRF Nb cavity operation allows hydrogen atoms to diffuse up to a length of ~30 μm [135]. This diffusion distance is comparable to the width of the observed hydride scar free zone (~20–60 μm).

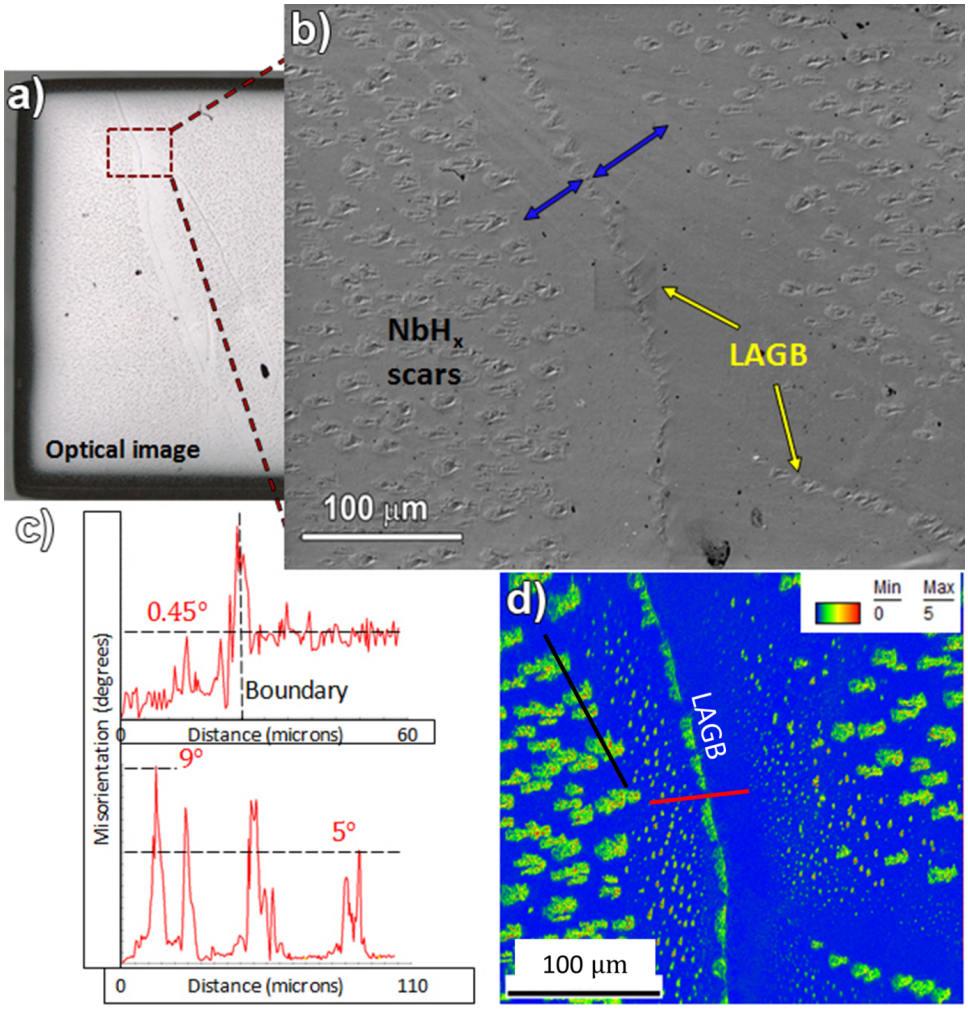

Figure 28. (a) Optical microscopy image of the LAGBs where premature magnetic flux penetration occurred (Figure 29, Sample D); (b) SE image of the area marked in the dashed-line box in (a) showing hydride scars and hydride free zones near the LAGB; (d) local average misorientation map with misorientation profiles (c) across the LAGB (red) and across several hydride scars (black). (This figure was reconstructed from Figure 8 in reference [16]).

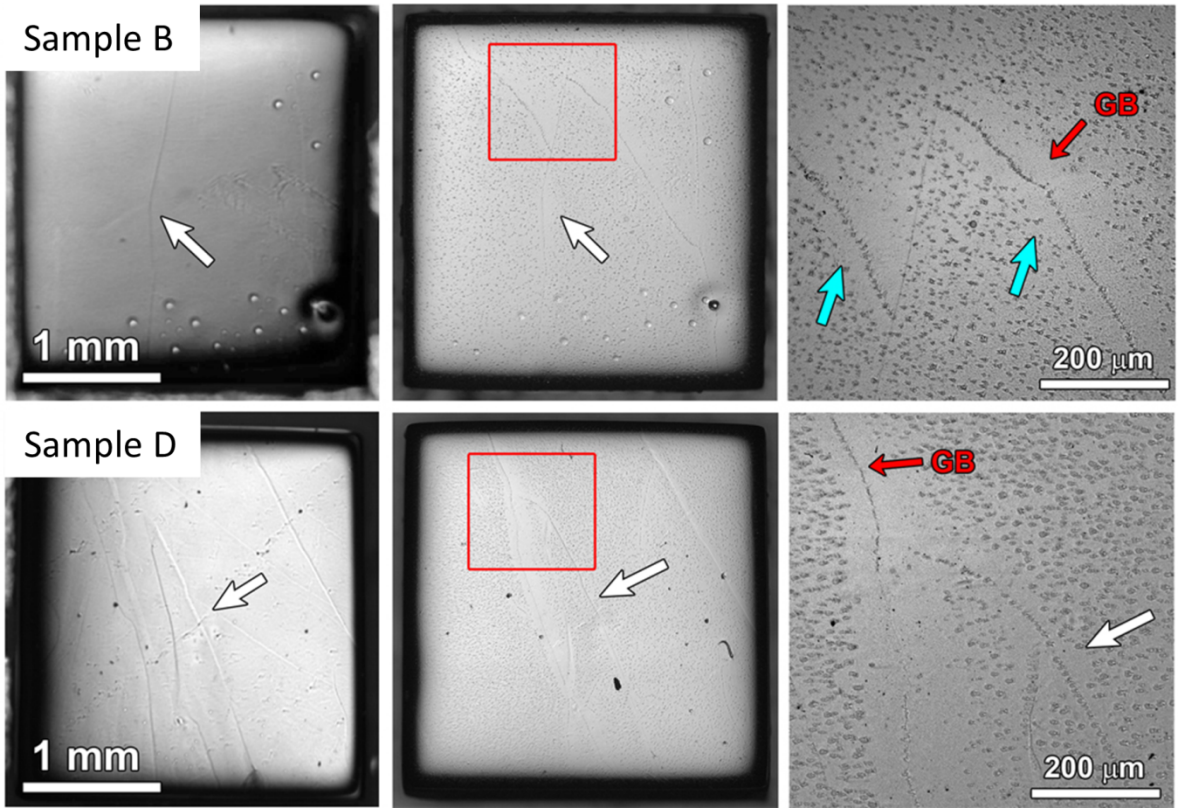

Figure 29. Surface optical images of Sample B (upper) and Sample D (lower) before (the leftmost) and after (the middle) cryogenic cooling during MO imaging. The rightmost images show enlarged areas in the vicinity of LAGBs (red rectangles). (From Figure 7 in reference [16]).

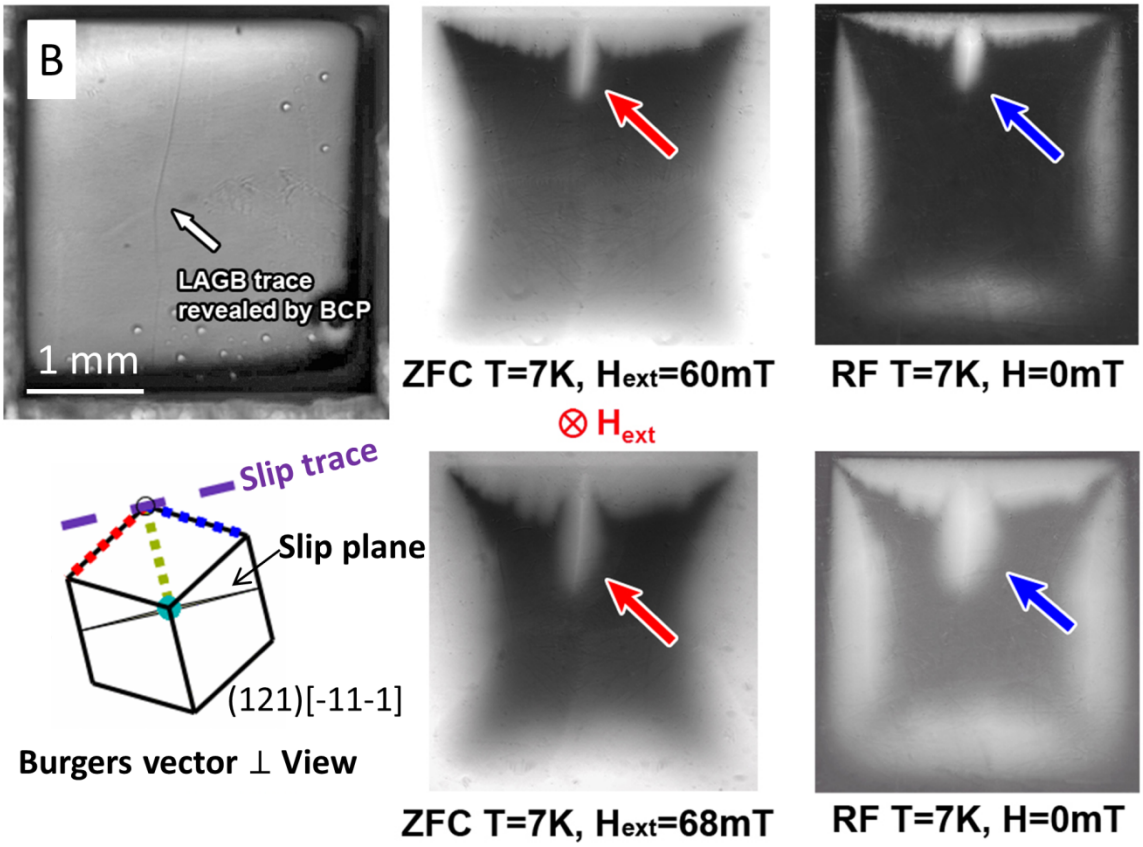

Figure 30. ZFC and RF mode MO images of Sample B, with the highly favored slip plane parallel to the external magnetic field H_{ext} (perpendicular to the page). The white arrow marks the location of the LAGB, and red and blue arrows mark the location of preferential magnetic flux penetration and trapped flux (bright contrast in MO images). (Reconstructed from Figure 4 in reference [16]).

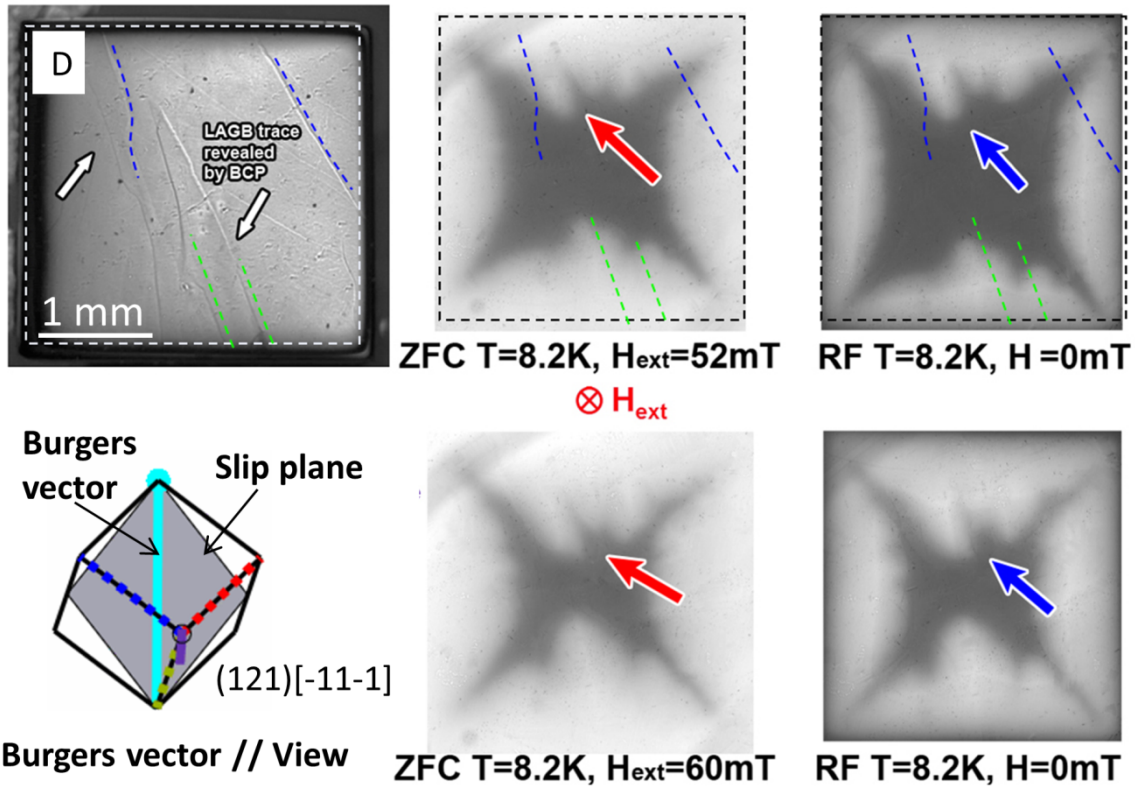

Figure 31. ZFC and RF mode MO images of Sample D, with the highly favored slip plane and the Burgers vector nearly perpendicular to the external magnetic field H_{ext}. The white arrows mark the locations of the LAGBs, and red and blue arrows mark the location of preferential magnetic flux penetration and trapped flux (bright contrast in MO images). The locations of LAGBs are also indicated with blue and green dashed lines in both the optical image the MO images. (Reconstructed from Figure 5 in reference [16]).

B. LAGBs cause premature magnetic flux penetration

MO investigations suggested that magnetic flux preferentially penetrated LAGBs, which also showed preferential hydride precipitation. Although hydrides were also distributed in the grain interior (Figure 29), they apparently did not have the same effect on flux penetration as LAGBs did (see MO images in Figure 30 and Figure 31). This suggests that Nb hydrides combined with dislocation networks in LAGBs locally reduce the superconducting order parameter at LAGBs, thereby leading to the breakdown of superconductivity and hence the premature flux

penetration. However, not all LAGBs trapped flux (as evident in Figure 31), suggesting that the orientation and possibly the size of the LAGB with respect to the magnetic field is also important.

C. Remaining flux trapping at LAGBs was still present after heat treatment

After the 800 °C/2-hour anneal, the pattern of flux penetration into the sample was substantially altered. While still showing some residual weakness at the LAGBs, the bulk properties were mostly recovered, indicated by the rooftop pattern in the FC MO images (Figure 32). A plausible explanation for the residual LAGB weakness is that residual nanoscale hydrides at LAGBs beyond the resolution of MO perturbed the circulating superconducting currents and produced very different magnetic flux penetration patterns that appeared to be initiated from the surface.

The 800 °C/2-hour anneal may be insufficient to remove all hydrogen atoms segregated at the LAGBs and the resulting formation of hydrides at LAGBs during cool-down may still locally degrade superconductivity; this would be consistent with a surface susceptibility study described in [136].

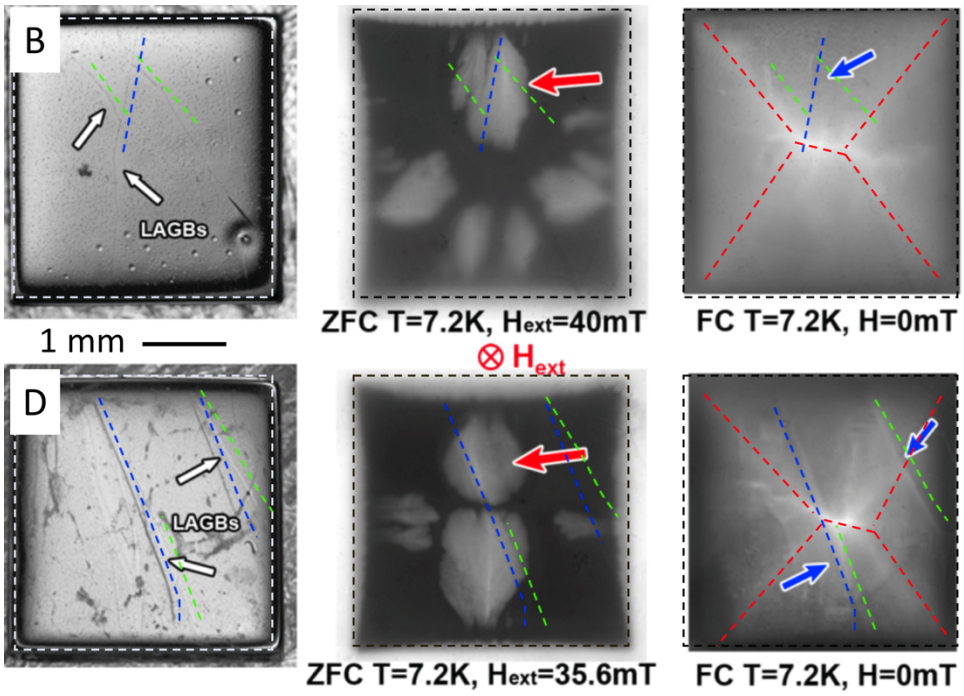

Figure 32. ZFC and FC mode MO images of Sample B (upper images) and Sample D (lower images) after 800 °C/2 hour anneal under ultrahigh vacuum (≥ 10^{-6} torr). Although trapped flux by LAGBs was still observed (blue and green dashed lines), the bulk superconductivity is mostly restored as indicated by the rooftop pattern (red dashed lines) in the FC images. (Reconstructed from Figure 9 in reference [16]).

D. Effect of dislocation arrangements on flux penetration

Although tensile samples were designed to favor the production of special dislocation arrangements, the effect of this design on magnetic field penetration was not evident in Figure 30 and Figure 31, possibly due to the resolution limit of the techniques used in this study. High resolution and more sensitive superconducting characterization methods including AC susceptibility [136], superconducting quantum interface device (SQUID), and vibrating sample magnetometer (VSM) [137] would be necessary to clearly understand the effect of dislocation structural morphology.

Chapter V. DISLOCATION EVOLUTION IN SINGLE-CRYSTAL NB SAMPLES

The content of this chapter is extracted from a published work in which Mingmin Wang was the lead author [20]. The design of the bi-crystal samples and the tensile tests were performed by Di Kang.

A. Introduction

The mechanism of plastic deformation by operation of slip systems in BCC metals is complicated, a deep understanding of which is necessary to build physics-based crystal plasticity models to predict the behavior of the material under stress throughout the fabrication path of SRF Nb cavities. Studies of slip systems during the deformation of single crystal Nb [138], [139] suggested that stress-strain behavior depended strongly on the initial grain orientations. The stress-strain behavior also changes due to anneal, which changes hardening behavior resulting from the operation of preferred slip systems during the tensile deformation.

This chapter is a continuing effort, based on Di Kang's work [82], to investigate the evolution of dislocations and slip system activation during the deformation of single crystal Nb tensile samples subjected to different deformation and heat treatment processes. Direct observation of dislocations using ECCI on single crystal tensile samples was carried out to enable identification of dislocation characters (screw-mixed-edge) and the activity of slip systems underlying the highly orientation dependent stress-strain behavior of single crystal niobium.

B. Results and discussion

1. Selected area channeling patterns (SACPs)

A prior electron backscattered diffraction (EBSD) scan was used to obtain the Euler angle triplets, which were used to plot the stereographic projection and to generate simulated SACPs,

with the assistance of TOCA. Various tilt and rotate angles were identified to enable the $\boldsymbol{g} \cdot \boldsymbol{b}$ visibility analysis to identify dislocation Burgers vectors as commonly used in TEM analysis.

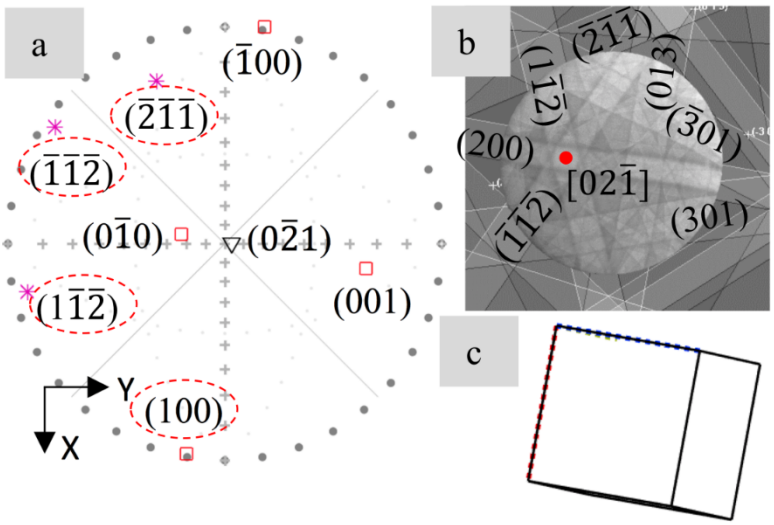

Figure 33. Stereographic projection (a) and SACP indexing of undeformed Sample U-ex (b) prior to tilting and rotating (Euler angles: 170°, 67°, 179°) by overlaying the collected SACP on top of the simulated pattern; the $[02\bar{1}]$ zone axis is evidently to the left of the center of SACP, which has an inverted perspective compared with the stereographic projection. Indices in parentheses indicated in (b) are $\boldsymbol{g}$ vectors associated with the observed channeling bands; the four plane normal directions near the edge of the stereographic projection in (a) marked by dashed ellipses correspond to four of the indexed bands in (b). This orientation is visualized with the unit cell (c), with red and blue dotted edges representing the x- and z-axes of the crystal coordinate system, respectively.

Figure 33 shows the stereographic projection for the sample prior to tilting to optimal dislocation imaging conditions as well as the indexed SACP of Sample U-ex. The measured SACP is overlaid on the simulated SACP in Figure 33b, to enable identification of the indices of the channeling bands. The stereographic projection can be used to verify the indexing results by TOCA. Figure 33c shows the orientation of a unit cell with the red and blue dashed lines representing x- and z-axis; the y-axis points into the page and is not evident. This is the crystal coordinate system used throughout this chapter.

Various tilts and rotations were determined to put the electron beam along a channeling band from a particular plane to provide high contrast on either side of the band, typically a couple of degrees from a zone axis. After collecting an SACP, finer adjustments were made to put the primary electron beam center at the edge of a channeling band to activate an optimal channeling condition, in which the backscattered electron (BSE) image, or ECC image, shows enhanced contrast of lattice distortions caused by dislocations.

2. ECCI observations

a. Sample U-ex

Figure 34(a, b, and c) show three ECC images of U-ex in the same region taken under different channeling conditions for the application of $\boldsymbol{g} \cdot \boldsymbol{b}$ analysis. In Table 4, the four possible Burgers vectors in BCC structures are listed and the dot products between $\boldsymbol{b}$ and $\boldsymbol{g}$ vectors are calculated with "+" representing non-zero values and "0" representing zero values. Screw dislocations are invisible when $\boldsymbol{g} \cdot \boldsymbol{b} = \boldsymbol{0}$, while for edge dislocations, both $\boldsymbol{g} \cdot \boldsymbol{b} = \boldsymbol{0}$ and $\boldsymbol{g} \cdot (\boldsymbol{b} \times \boldsymbol{u}) = \boldsymbol{0}$ need to be satisfied for invisibility, where $\boldsymbol{u}$ is the dislocation line direction.

The dot-like features of dislocation A with dark-light contrast adjacent to each other have dislocation lines nearly perpendicular to the sample surface. For threading (perpendicular to the surface) dislocations, the contrast vector is defined as the direction from the dark end to the light end. Dislocation A has contrast vectors (red arrows) perpendicular to the $\boldsymbol{g}$ vectors (white arrows) under different channeling conditions, indicating that A is a screw dislocation and it has a Burgers vector parallel to its line direction [140]. Therefore, the Burgers vector of dislocation A is most likely to be $\boldsymbol{b}$ = [1-11], which is close to perpendicular to the sample surface and matches the observation (all visible) under three imaging conditions (Table 4). [-1-11] was ruled out because its $\boldsymbol{g} \cdot \boldsymbol{b}$ values did not match the observations.

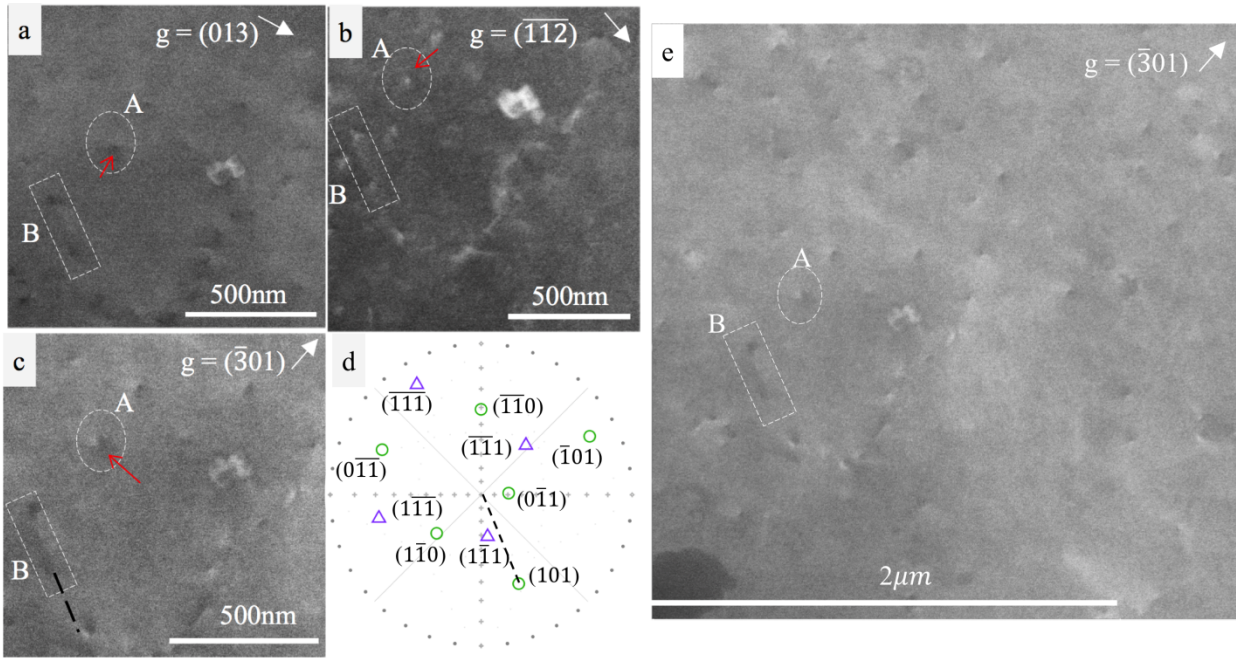

Figure 34. ECC images of Sample U-ex under three different channeling conditions (***g*** vectors, a,b,c) and the stereographic projection after tilting and rotating for the ***g*** = (-301) image (d), and (e) a low magnification image of (c) that shows a dislocation density of 9×10^{12} m^{-2}.

Table 4. $\boldsymbol{g} \cdot \boldsymbol{b}$ analysis of sample U-ex. The visible conditions are represented using "+", and invisible conditions represented using "0". Dislocation A is identified as a screw with ***b*** = [1-11].

$\boldsymbol{g} \cdot \boldsymbol{b}$		***g*** vector		
		(013)	(-1-1-2)	(-301)
b	[-1-1-1]	+	+	+
	[1-1-1]	+	+	+
	[1-11]=A	+	+	+
	[-1-11]	+	0	+
Observation of dislocation A		Visible	Visible	Visible

Dislocation B appears as a line segment and is visible under all three channeling conditions. The line direction is indicated by a black dashed line in Figure 34c, which lines up with the [101] direction in the stereographic projection in Figure 34d, suggesting that B is an edge dislocation with a line direction $\boldsymbol{u} = [101]$ on a {112} plane (because edge dislocations in BCC have either <110> or <112> line directions on {112} or {110} planes, respectively). The values of $\boldsymbol{g} \cdot (\boldsymbol{b} \times \boldsymbol{u})$

for the two possible Burgers vectors of dislocation B perpendicular to [101] are listed in Table 5, which shows visible conditions for both Burgers vectors for all $\boldsymbol{g}$ vectors. Therefore, the Burgers vector of dislocation B could not be determined between the two possibilities.

Table 5. Values of $\boldsymbol{g} \cdot (\boldsymbol{b} \times \boldsymbol{u})$ for two possible Burgers vectors of dislocation B.

$\boldsymbol{g} \cdot (\boldsymbol{b} \times \boldsymbol{u})$		$\boldsymbol{g}$ vector		
		(013)	$(\bar{1}\bar{1}\bar{2})$	$(\bar{3}01)$
$\boldsymbol{u} = [101]$	$\boldsymbol{b}$ = [1-1-1]	+	+	+
$\boldsymbol{u} = [101]$	$\boldsymbol{b}$ = [-1-11]	+	+	+
Observation of dislocation B		Visible	Visible	Visible

By counting the number of dislocations in Figure 34e, a lower magnification view that contains the area in Figure 34c, and dividing it by the area of observation, the pre-existing dislocation density is estimated to be $9 \times 10^{12}\ m^{-2}$, assuming all dislocations are perpendicular to the sample surface. Therefore, no geometry correction was performed. Note that this is always a lower bound estimation of the dislocation density because not all dislocations are visible, and the dislocation line directions are not exactly perpendicular to the surface.

b. Sample U-an

Figure 35 shows an ECC image of Sample U-an, which was annealed after being extracted. The anneal removed many pre-existing dislocations, resulting in a lower dislocation density than sample U-ex. This is consistent with observations in the previous research that suggested that anneal lowered the flow stress due to the removal of pre-existing dislocations [31].

Due to the lack of images from other channeling conditions, $\boldsymbol{g} \cdot \boldsymbol{b}$ analysis was not able to identify the Burgers vectors of the observed dislocations. The dislocations marked by the boxes in Figure 35 are nearly parallel to the sample surface. Dislocations B has a line direction that is lined up with the [101] direction.

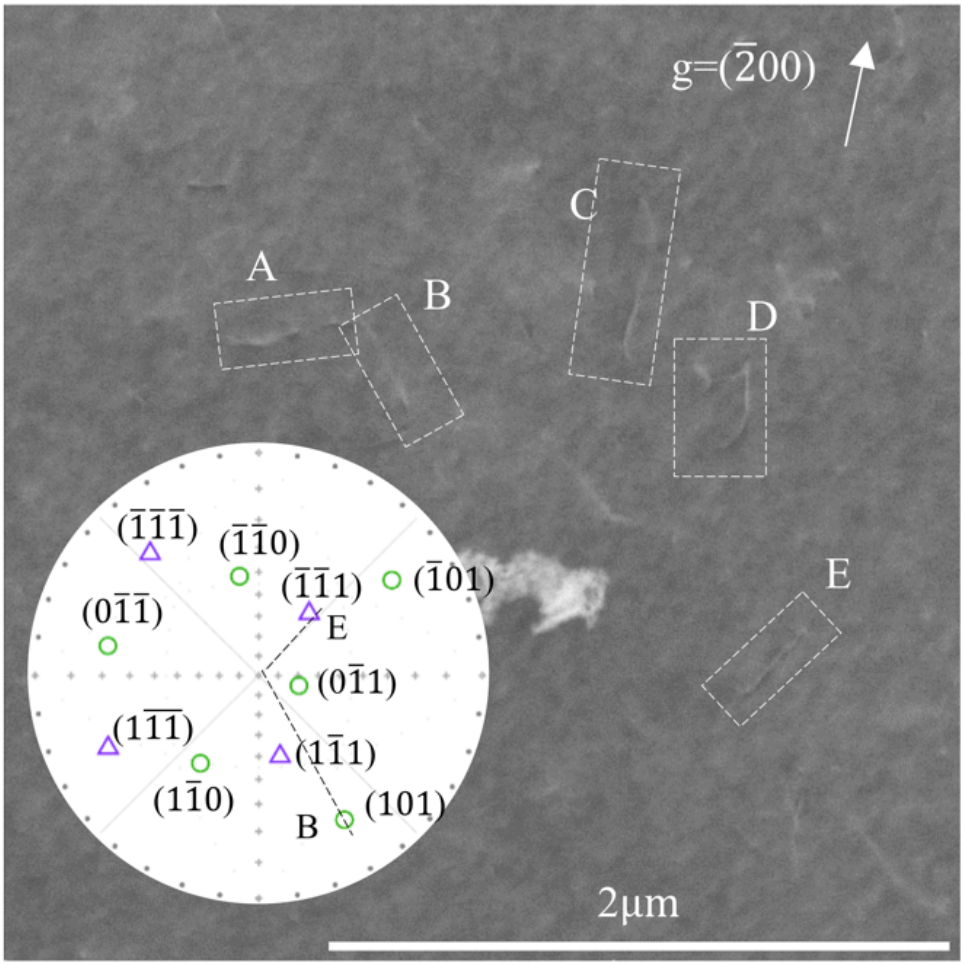

Figure 35. Dislocation image of annealed Sample U-an. The line directions of dislocations B and E are marked in the stereographic projection (after tilting and rotating) with black dashed lines.

c. Sample D-ex

ECC images of sample D-ex in Figure 36 show tangled dislocation structures as a result of the 40% tensile strain imposed on the as-extracted sample. This makes dislocation density estimation very difficult, although some of them can be isolated and analyzed (white arrows and dashed boxes).

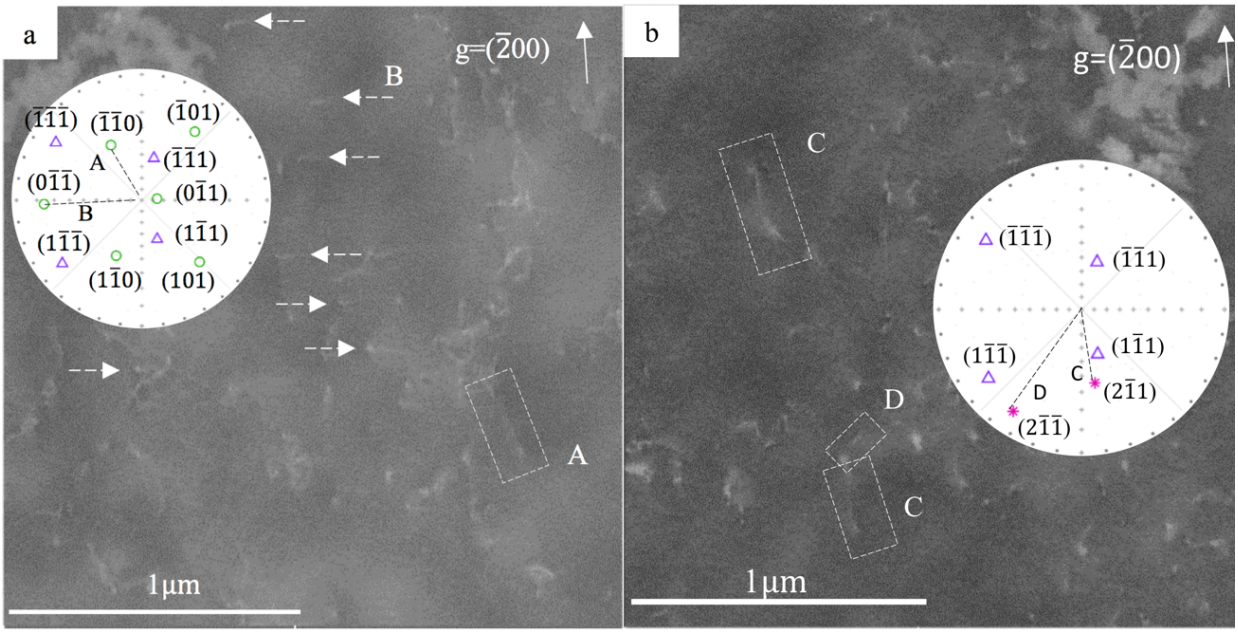

Figure 36. ECC images of two regions of sample D-ex under the same channeling condition. Dislocation contrast is marked by arrows (a) and boxes (a and b) and the line directions are marked in the stereographic projections (after tilting and rotating) by black dashed lines.

$\boldsymbol{g} \cdot \boldsymbol{b}$ analysis was tried for both regions in Figure 36, but unambiguous conclusions could not be obtained due to poor image qualities from other channeling conditions. Since dislocation line directions can be identified from ECC images and the stereographic projections, the possible slip systems that generated these dislocations can be determined by applying the geometry relationships between Burgers vectors, line directions, and slip plane normals.

Dislocation A in Figure 36a has a line direction parallel to direction [-1-10] indicated by a black dashed line in the stereographic projection. Therefore, A could be an edge dislocation generated by the (-11-2)[1-1-1] or the (1-1-2)[1-11] slip system. Dislocation B in Figure 36a includes a series of dislocations with a line direction parallel to [0-1-1], which are edge dislocations and could be generated by either the (2-11)[-1-11] or the (21-1)[1-11] slip system. Figure 36b shows ECC images of another region of sample D-ex. Dislocations C and D have line directions parallel to [2-11] and [2-1-1] respectively, suggesting that they are both edge dislocations

generated on {110} slip systems. Therefore, the slip systems that generated C and D could be (011)[$\bar{1}\bar{1}$1] and (01-1)[111], respectively.

d. Sample D-an

Sample D-an was deformed to 40% strain after being annealed at 800℃ for 2 hours and an ECC image is shown in Figure 36a. Tangled dislocation structures are also observed for D-an, and dislocations of type A and B are marked with white dashed arrows and boxes respectively. Type A includes a series of dislocations with line direction parallel to [0-1-1] as shown in the stereographic projection, which is likely an edge dislocation on a {112} slip system and the Burgers vector could be either [-1-11] or [1-11]. The slip system could be either (2-11)[-1-11] or (21-1)[1-11]. The $\boldsymbol{g} \cdot \boldsymbol{b}$ analysis could not be used to identify the Burgers vectors due to lack of images of other channeling conditions. Figure 36b shows an ECC image of another region of D-an. Dislocations are almost all tangled together, and individual dislocation analysis is difficult. This reflects the 40% tensile deformation that created many dislocation entanglements.

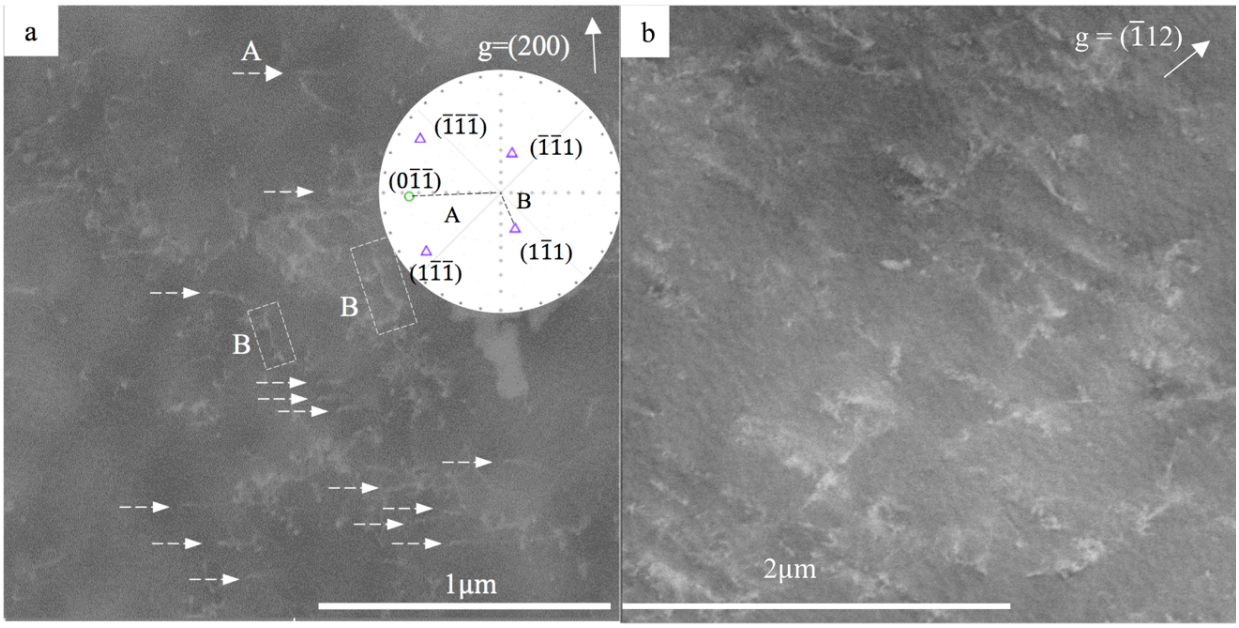

Figure 37. ECC images of two regions of sample D-an with dislocations marked by boxes and arrows. The dislocation line directions are marked in the stereographic projections (after tilting and rotating) by black dashed lines.

3. Schmid factor calculation

Assuming that activation of slip systems follows the Schmid law, which states that with the same stress applied, slip systems with a higher resolved shear stress (higher Schmid factor) have a higher probability of activation and generating dislocations. High dislocation density observed in the as-extracted sample U-ex might come from prior deformation caused by thermal contraction during cooling of the Nb ingot. This prior deformation, as well as the tensile deformation, were considered next in a Schmid factor analysis to assess where the observed dislocations might have come from. The Schmid factors of all observed slip systems were calculated and compared in Table 6.

Three possible deformation directions, defined in Figure 38, were evaluated in a MATLAB code that calculates the Schmid factors of slip systems based on a given crystal orientation (for this crystal, the Bunge Euler angles are 170°, 67°, 179°), measured with tensile direction parallel to the Y-axis of the global coordinate system.

The tensile sample was deformed by 40% in the sample Y-axis direction. The corresponding stress tensor is given in Equation (13).

$$\sigma_Y = \begin{bmatrix} 0 & 0 & 0 \\ 0 & 1 & 0 \\ 0 & 0 & 0 \end{bmatrix} \tag{13}$$

$$\sigma_Z = \begin{bmatrix} 0 & 0 & 0 \\ 0 & 0 & 0 \\ 0 & 0 & 1 \end{bmatrix} \tag{14}$$

The Z-axis direction (normal to the Nb disk surface) is a possible prior deformation direction and a potential extension or contraction direction associated with thermal strains during ingot cooling. The corresponding stress tensor associated with thermal stresses in Z-axis direction is given in Equation (14). Another possible prior deformation direction is the radial direction of the Nb disk, the contraction direction during ingot cooling. The range of possible radial directions is identified in Figure 38 based on the gauge length of the tensile sample. Therefore, adjusted Euler angles of (93°–111°, 67°, 179°) were used to calculate the value range of radial direction Schmid factors for edge dislocations, using the stress tensor of Equation (13) (while screw dislocations are not constrained to a slip plane, mixed or edge dislocations are). High Schmid factor values are shown in bold font in Table 6.

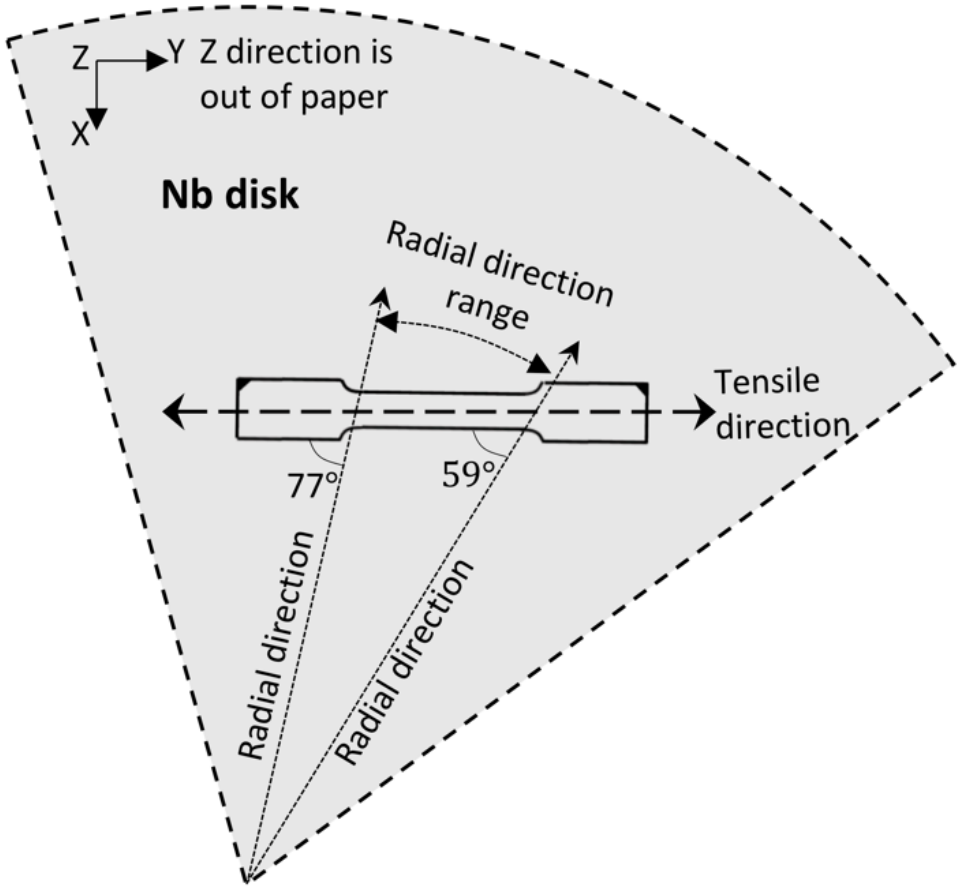

Figure 38. Three deformation directions of interest are defined for the tensile sample in its original location on the Nb disk; the global coordinate system XYZ is indicated at the upper left corner. The tensile direction is parallel to Y-axis, and the orientation is measured as (170°, 67°, 179°) for this configuration.

Schmid factor calculations (Table 6) suggest that some observed dislocations, such as (2-11)[-1-11] or (21-1)[1-11], are associated with slip systems that have low Schmid factors for the tensile direction deformation but much higher Schmid factors for Z-axis or radial deformation directions. This suggests that these dislocations were very likely pre-existing and generated during ingot cooling. On the other hand, slip system $(\bar{1}01)[111]$, with a high tensile direction Schmid factor, was identified by slip trace analysis (see next section), although it was not observed by ECCI. Table 6 shows that this slip system has a high Schmid factor of 0.49 during tensile deformation, indicating high mobility. Therefore, it is possible that dislocations on slip system

$(\bar{1}01)[111]$ passed through the material and exited the material, leaving predominant slip traces and relatively few dislocations remaining within the material. If so, the observed dislocations were dislocations that formed obstacles for the primary slip system, rather than indicators of active slip systems.

Table 6. Schmid factors (*m*) of observed slip systems in different deformation conditions (high values are bold).

Sample	**Observed slip systems**	**Calculated Schmid factor (*m*)**		
		Tensile direction	Z direction	Radial direction
U-ex	**b**= [1-11]	Screw	Screw	Screw
	(-1-21)[1-1-1] or (-121)[-1-11]	0.11 or 0.31	0.29 or **0.45**	0.26~0.33 or 0.25~**0.40**
D-ex	(-11-2)[1-1-1] or (1-1-2)[1-11]	**0.43** or 0.19	0.22 or 0.05	0.13~0.22 or 0.24~0.29
	(2-11)[-1-11] or (21-1)[1-11]	0.03 or 0.07	**0.41** or **0.4**	**0.45~0.48** or 0.36~**0.46**
	(011)[-1-11]	0.37	0.28	0.02~0.21
	(01-1)[111]	0.24	0.27	0.02~0.04
	(-101)[111][a]	**0.49**	0.08	0.25~**0.41**
D-an	(2-11)[-1-11] or (21-1)[1-11]	0.03 or 0.07	**0.41** or **0.4**	**0.45~0.48** or 0.36~**0.46**
	(-101)[111][a]	**0.49**	0.08	0.25~**0.41**

[a]These are slip systems identified using slip trace analysis, while others were observed using ECCI.

4. Slip trace analysis of D-ex and D-an

Figure 39 shows the SE images of slip traces after 40% tensile deformation with wavy slip traces for both samples, but the predominant slip traces could be matched with the $(\bar{1}01)[111]$ slip system, with a high Schmid factor of 0.49, as calculated in Table 6, indicating that it was a highly favored slip system. This slip system is represented by a unit cell overlaid on the SE images in Figure 39, with a turquoise line representing the slip direction, or Burgers vector, on the shaded slip plane, and a dashed line indicating the calculated slip trace. The crystal coordinate system is indicated using red, green, and blue dotted lines, corresponding to x, y, and z directions, respectively.

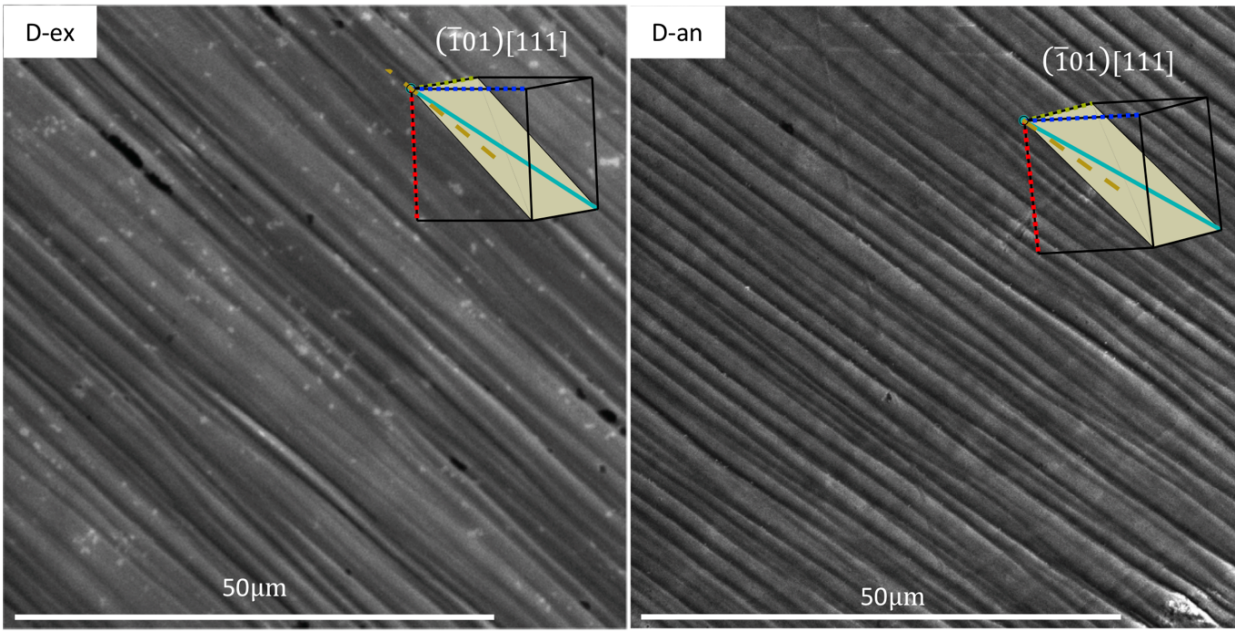

Figure 39. Secondary electron (SE) images of slip traces on the surfaces of D-ex and D-an after deformation, overlapped with calculated slip traces (dashed lines) based on the locally collected orientation data; each unit cell represents the matching slip system with a turquoise line indicating the Burgers vector on a shaded slip plane; red, green, and blue dotted lines are the x, y, and z directions of the crystal coordinate system.

By comparing the morphology of the slip traces of the extracted sample (D-ex) and the annealed sample (D-an), it is apparent that the annealed sample has a more uniform distribution of slip traces than the extracted sample, indicating differences in the deformation processes on the same slip system in the two samples. This difference was quantified using AFM measurements and assessment of stress-strain behavior, which will be discussed later.

Figure 40 and Figure 41 show AFM topographic maps and the corresponding surface profiles of sample D-ex and D-an after deformation. The AFM maps clearly show different slip trace morphologies of the two samples. The extracted sample (D-ex) showed big steps with smaller steps in between, while the annealed sample (D-an) showed a more uniformly spaced distribution of slip traces, consistent with the SEM observation in Figure 39.

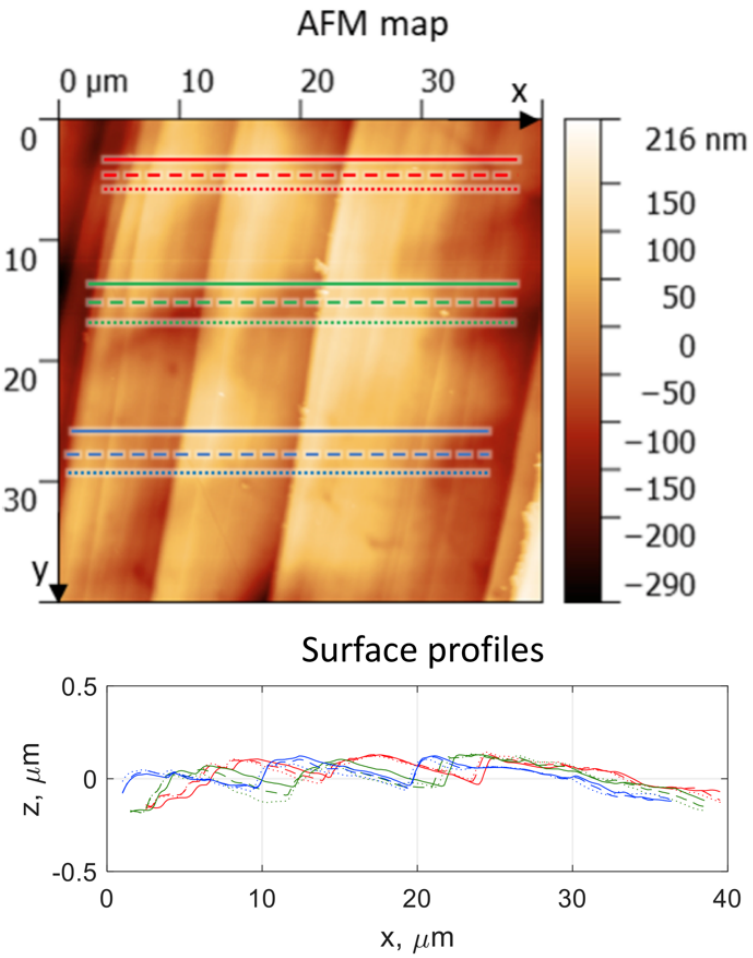

Figure 40. Sample D-ex AFM topographic map (top) and surface profiles (bottom) corresponding to the 9 colored lines overlaid on the AFM map, showing widely spaced slip steps.

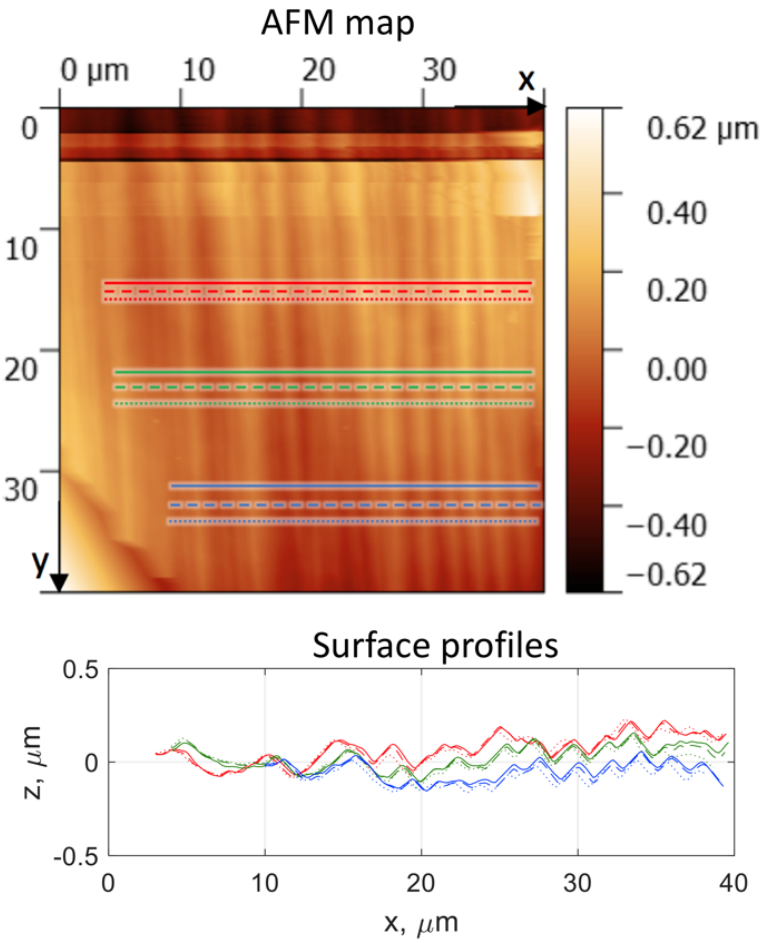

Figure 41. Sample D-an AFM topographic map (top) and surface profiles (bottom) corresponding to the 9 colored lines overlaid on the AFM map, showing regularly spaced topography along both horizontal and vertical directions.

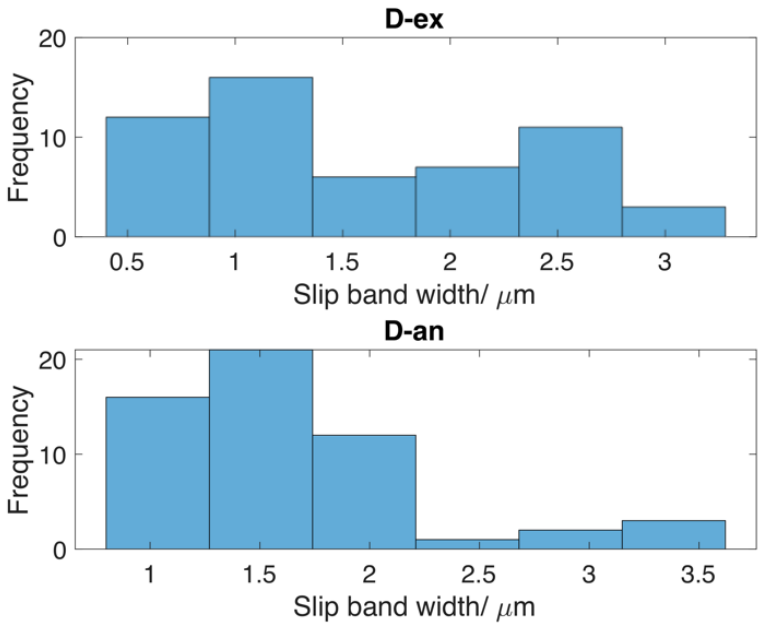

Figure 42. Histograms of slip band width with 55 measurements on each SE image (Figure 39) of Samples D-ex and D-an.

The slip band width could be directly measured using ImageJ [141] software from Figure 39, and the histograms based on 55 measurements for each sample are shown in Figure 42. The slip band width distribution of D-an was more concentrated, with most values in the range of 0.8–2.2 μm, while the band width values for sample D-ex were distributed throughout the whole range of 0.4–3.3 μm. This again suggests that the annealed sample has more uniform slip traces than the extracted sample after deformation.

5. Assessment of the stress-strain behavior

Both {110} and {112} slip systems were observed in the ECC images of D-ex that was deformed without anneal, and of D-an that was deformed after anneal. Previous research [31] (deformation of samples with different orientations) indicated that based upon analysis of crystal rotation due to tensile deformation, many of the as-extracted samples with different orientations showed stronger evidence for the slip on {112} planes than {110} planes, but for this specific set

of samples with the same orientation studied in this work, there was no evidence for significant slip on {112} planes. The Schmid factor analysis in Table 6 shows that the Schmid factors of the observed {112} slip systems are much higher if the crystal was deformed along the ingot radial direction or Z direction, suggesting that the observed {112} dislocations might be pre-existing dislocations generated due to thermal strains that occurred during cooling of the 270 mm diameter ingot. The fact that {112} dislocations were observed for the annealed sample indicates that the anneal was not able to remove these pre-existing dislocations, which act as forest dislocations and interact with newly generated dislocations by tensile deformation.

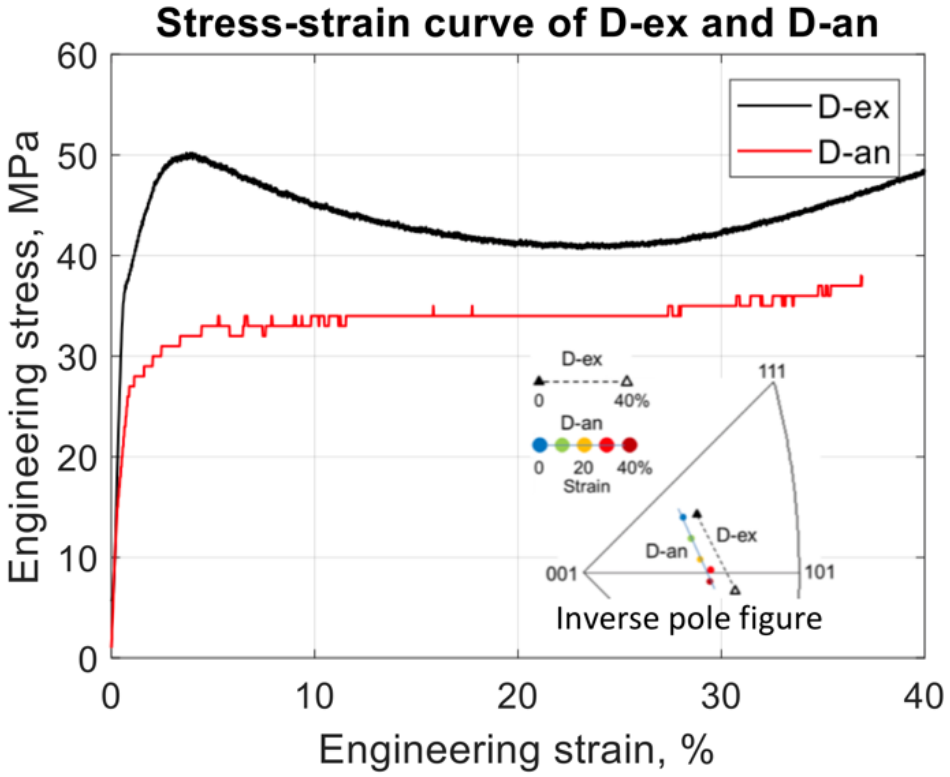

Figure 43. The stress-strain behavior of the extracted sample D-ex shows much greater yield stress and work hardening than the annealed sample D-an(reproduced from reference [31]). The inverse pole figure (inset) shows the orientation evolution of the tensile axis with deformation, which is roughly parallel for both Samples D-ex and D-an.

Figure 43 shows the difference in the stress-strain behavior of Samples D-ex and D-an. Sample D-ex has a 0.2% offset yield stress of 36 MPa, followed by distinct hardening and then a flow stress decrease between 4% and 20% strain. On the other hand, D-an shows a 30% lower 0.2% offset yield strength of about 25 MPa, with less hardening just after yield. This difference indicates that some of the pre-existing dislocations were removed from D-an by anneal. The difference in this initial dislocation population played an important role in the initial hardening process of D-ex [138]. The pre-existing dislocations with a low resolved shear stress (low Schmid factors) acting on them were not mobile, and they created forest dislocation barriers, leading to dislocation multiplication of mobile dislocations, which increased the flow stress. By contrast, there were fewer forest dislocations in the annealed sample U-an, so that U-an showed lower flow stress with no significant hardening. The inset in Figure 43 shows the evolution of the tensile axis orientation with deformation is roughly parallel for both extracted and annealed samples. This indicates similar slip system activation in both samples, which is consistent with slip trace analysis of sample T in reference [31], as well as the observed dominant slip traces of $(\bar{1}01)[111]$ for both D-ex and D-an in Figure 39.

Both SEM observation (Figure 39) and AFM characterization (Figure 40 and Figure 41) of the slip traces of D-ex and D-an clearly show that the two samples have different slip trace morphology, indicating that a different deformation resistance was responsible for the different stress-strain behavior shown in Figure 43. For D-ex, there are significant areas of small steps between bigger slip steps. This appearance of irregularly spaced slip bands with differing amounts of slip displacement is evidence of more heterogeneous slip and development of preferred (or limited) pathways where dislocations moved through the crystal. By contrast, the lower flow stress shown in Figure 43 of D-an may represent the response to forming more channels where mobile

dislocations could freely move, due to far fewer barriers for dislocation motion. This suggests that the fewer initially present dislocations in the annealed sample were more easily overcome by dislocations with high Schmid factors, and the higher initial dislocation density in D-ex resulted in barriers that require sufficiently higher stress to overcome. Once these barriers were overcome, this led to avalanche behavior, where large shear displacements took place and the flow stress dropped after yield.

Both modeling and experimental work on dislocation slip avalanches have been carried out for nanoscale single crystals [142]–[144]. In these studies, compression tests of Nb single crystal nanopillars showed stress-strain curves with a saw-like or staircase shape, indicating dislocation avalanches, accompanied by the formation of slip lines on the sample surface. Statistical studies showed that the slip sizes (total axial displacement during an avalanche) of dislocation slip avalanches followed a power-law probability distribution [144], in which the event frequency decreased with increasing slip sizes of dislocation avalanches. Slip avalanche behavior was also affected by stress level and strain rate [145]. During avalanches, trapped dislocations overcome pinning centers before they exit the sample at the surface.

Relatively few dislocations with b = [111] were observed using ECCI. Because these dislocations were the most mobile and contributed to the strain, they were more likely to have passed through the crystal, such that what were visible were the less mobile dislocations and entanglements resulting from interactions with immobile dislocations, as shown in Figure 36 and Figure 37. This is consistent with the slip trace analysis in Figure 39, where the slip system (-101)[111] was identified, with a high Schmid factor of m=0.49 according to Table 6.

C. Summary

Dislocation structures were characterized using ECCI on four single crystal Nb samples with the same orientation but different heat treatment and deformation histories, to identify the relationship between stress-strain behavior and the evolution of dislocation structures.

For the undeformed samples U-ex and U-an, ECCI observations suggested that the pre-existing dislocation had a high density ($\sim 9 \times 10^{12}$ m^{-2}) and an apparently much lower density after the 800℃ 2-hour anneal, consistent with the flow stress decrease after anneal that was reported in the previous research.

Both {110} and {112} slip systems were observed for samples deformed to 40% strain, but Schmid factor calculations suggested that some of the dislocations associated with {112} slip systems were pre-existing dislocations that anneal did not remove.

Slip trace observations of D-ex and D-an using AFM suggested that the two deformed samples experienced different deformation mechanisms. The distribution of slip traces of D-an was more regularly spaced, suggesting a more uniform deformation of the annealed sample. For D-ex, the flow stress increase was due to the pre-existing dislocations that had a low mobility and created forest dislocation barriers. The later flow stress drop could be explained by the development of irregularly spaced dislocation pathways resulting from overcoming dislocation entanglement barriers that enabled much more highly localized slip behavior (avalanches) between obstacles. This is consistent with the slip trace analysis and AFM characterization.

Direct observations of dislocation evolution in this chapter provide information that can explain observations regarding deformation mechanisms and will be useful for building constitutive models for computational cavity design.

Chapter VI. UNDEFORMED BICRYSTAL NB SAMPLES

A. Introduction

In this chapter, flux penetration was investigated in three bicrystal Nb samples with different grain boundaries using cryogenic MO imaging. The dislocation structures associated with hydride precipitation before and after heat treatment were characterized using ECCI. The goal is to identify relationships between grain boundaries, dislocation substructures, hydrides, heat treatment, and flux trapping.

B. Results

1. MO, EBSD, and AFM analysis

The results of the first MO imaging of the three samples are shown in Figure 44. Sample I showed no apparent preferential flux penetration related to the grain boundary.

Sample II showed a "fork" shaped preferential flux penetration along the grain boundary (Figure 44f), with one tine of the fork corresponding to the high angle grain boundary (HAGB, with misorientation > 15°) and the lower tine corresponding to a low angle grain boundary. The remnant field MO image (Figure 44g) shows trapped flux by the GBs, with the same fork shape. Sample II was then reheated above *Tc* and cooled a second time with zero fields to 7.8 K, and then a magnetic field of 56 mT was applied, resulting in a less amount of flux penetration (2nd ZFC in Figure 44h) than the prior condition, where the temperature was higher and the external field lower. The location of the fork flux is marked using red dashed lines.

Sample III (Figure 44k) showed preferential grain boundary magnetic flux penetration at $T = 8.7$ K after application of $H = 16.8$ mT along the part of the boundary that was nearly parallel to the field (compare with Figure 25), and there was also a little bit of flux penetration along the tilted boundary near the right edge.

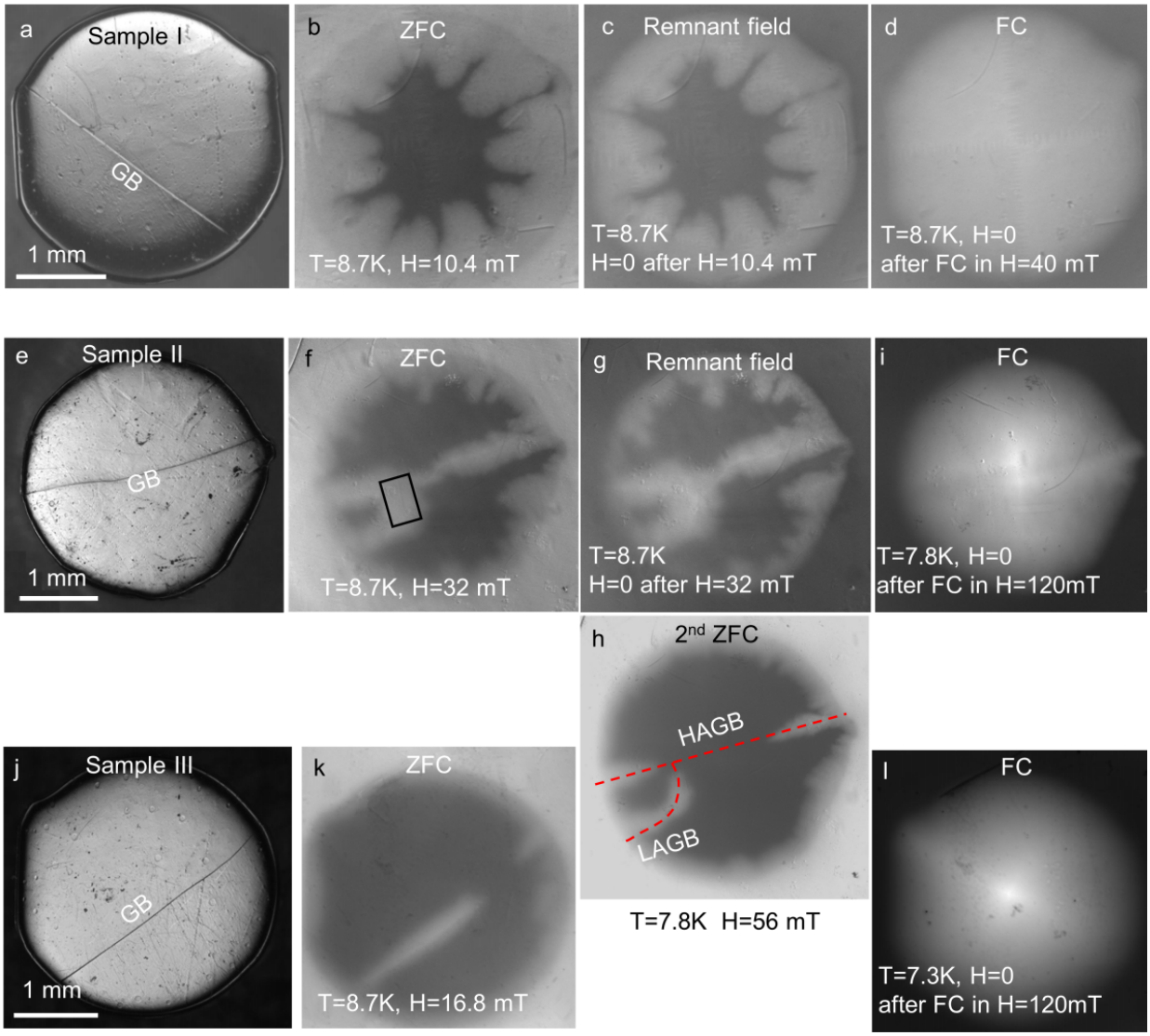

Figure 44. MO results of the three bicrystal samples with each row showing the top surface optical image (column 1) and MO images in ZFC, remnant field, and FC modes (columns 2, 3, and 4) for each bicrystal sample. Surface optical images show visible grain boundaries and the mounting position is consistent between the optical image and MO images for each sample.

After MO imaging, further EBSD analysis of the lower tine of the flux fork of Sample II (black outline in Figure 44f) revealed an LAGB shown in Figure 45. The EBSD data collected from the fork flux penetration region (black outline in Figure 44f) was reconstructed using four maps. The sample normal direction inverse pole figure (IPF) map overlaid with the image quality

(IQ) map (IPF+IQ in Figure 45) shows the orientation of the two grains on either side of the HAGB, with the lower grain showing a faint low angle grain boundary, which is marked with white lines with a nearly vertical direction. This LAGB runs downward from the HAGB and then to the left (below the outlined area) until it meets the edge of the sample, corresponding to the lower tine of the flux fork observed in the MO image (Figure 44f). The LAGB was prominent and marked using white lines in the Kernel average misorientation (KAM) map and the grain reference orientation deviation (GROD) angle and axis maps in Figure 45. The GROD-angle map shows multiple sub-grains separated by LAGBs (white lines) in the lower grain. The GROD-axis map was color-coded according to the rotation axis direction between each pixel and the average grain orientation. This map reveals that each sub-grain had a particular rotation axis from the average orientation, implying that different LAGBs consisted of dislocations operating on different slip systems. Table 7 summarizes the misorientation angles and rotation axes of boundaries marked as "AB", "CD", "ED", and "DF" in the GROD-angle map, which shows that the misorientations are about 22° for the HAGB, and 2–3° for the LAGBs.

Another feature revealed by EBSD maps were the dark scars with low image quality in the IPF+IQ map in Figure 45, which are shown with more detail in Figure 46. These are typical hydride scars resulting from deformation accommodation due to hydride precipitation during cooling. This hydride precipitation during cooling and subsequent dissolution during reheating represent one MO cryogenic cycle. Exemplary hydride scars after the first MO cryogenic cycle on sample II in Figure 46 illustrate their typical "chevron" shape morphology; they were more evident in the overlaid image quality (IQ) map generated from the EBSD scan of the fork flux penetration area (black outline in Figure 44f). These nominally 50 μm hydride scars were evident in all EBSD maps, causing local ~3° misorientations as shown in the KAM map in Figure 45.

They were frequently lined up along features that appeared to be scratches (most evident in the IQ map in Figure 46), and along the HAGB, but they were not apparent along the LAGBs in the KAM and GROD maps in Figure 45. Some of the hydride scars did not appear to be correlated with either a scratch or the HAGB.

Table 7. Misorientations and rotation axes of boundaries marked in the GROD-angle map in Figure 45.

GB ID	GB type	Misorientation angle	Rotation axis
AB	HAGB	21.9°	[-21,17,-9]
CD	LAGB	3.1°	[27,-8,-9]
ED	LAGB	2°	[26,1,10]
DF	LAGB	2.1°	[14,-13,-23]

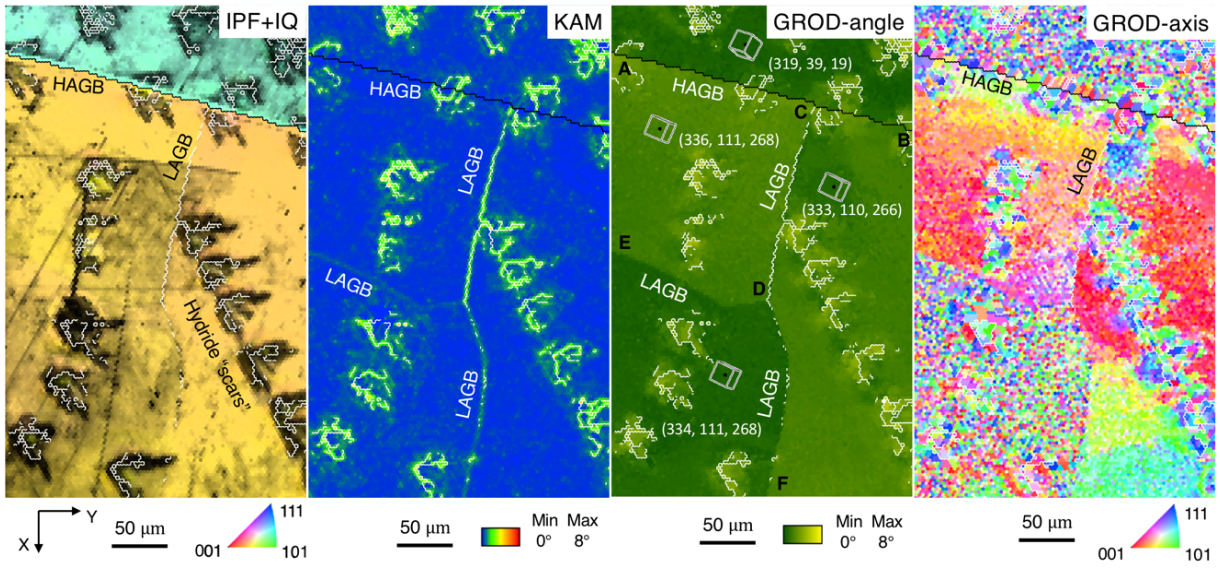

Figure 45. EBSD scan of the fork flux penetration area of sample II. IPF+IQ: Sample normal direction inverse pole figure (IPF) map with overlaid image quality (IQ) shows the high angle grain boundary (HAGB) and hydride scars (black); KAM: Kernel average misorientation map shows low angle grain boundaries (LAGBs) (white lines) and hydride scars causing 2–3° misorientations; GROD-angle: Grain reference orientation deviation angle map with the average grain orientation as the reference, overlaid with prisms and Euler angles (in degrees) representing the crystal orientation of each grain or sub-grain; GROD-axis: GROD axis map shows the local crystal rotation axes with respect to the average grain orientation.

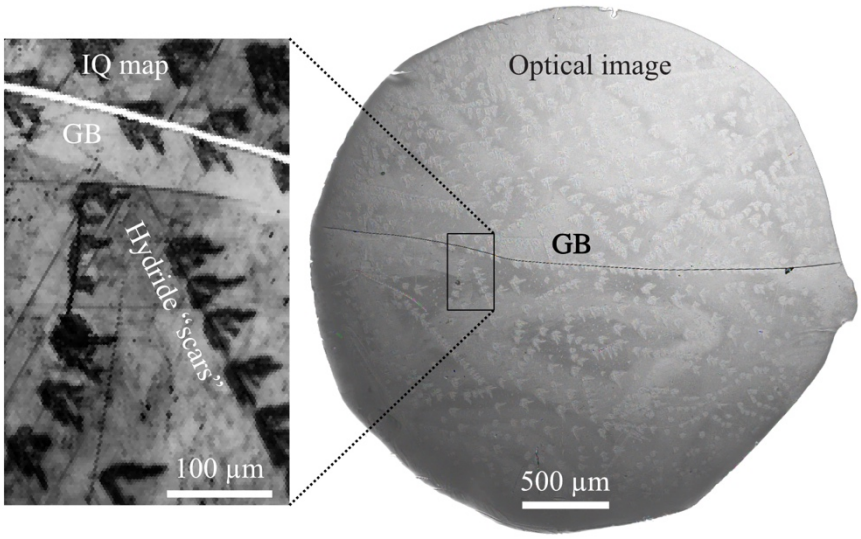

Figure 46. BSE image of the surface (right) of sample II after the first MO cryogenic cycle shows a large number of hydride scars with a size of about 50 µm, arranged along scratches and the high angle grain boundary, which is also shown with more detail in the image quality (IQ) map (left) generated from the EBSD scan of the black outline area in Figure 44f.

Atomic force microscopy (AFM) was performed on a single hydride scar on the surface of sample II to reveal the surface topography of the accommodation deformation region where a hydride precipitate existed. The AFM maps in Figure 47 clearly show that there were remaining features of the plastic deformation of the scar region, with a height difference of about 200 nm. The "chevron" shape of the hydride is apparent as a low elevation region surrounded by pushed up regions (by about 100 nm) surrounding it. The very low (dark) region (-100 nm) is consistent with the necessary shrinkage resulting from hydride dissolution. This topography illustrates the strain history from hydride formation and dissolution.

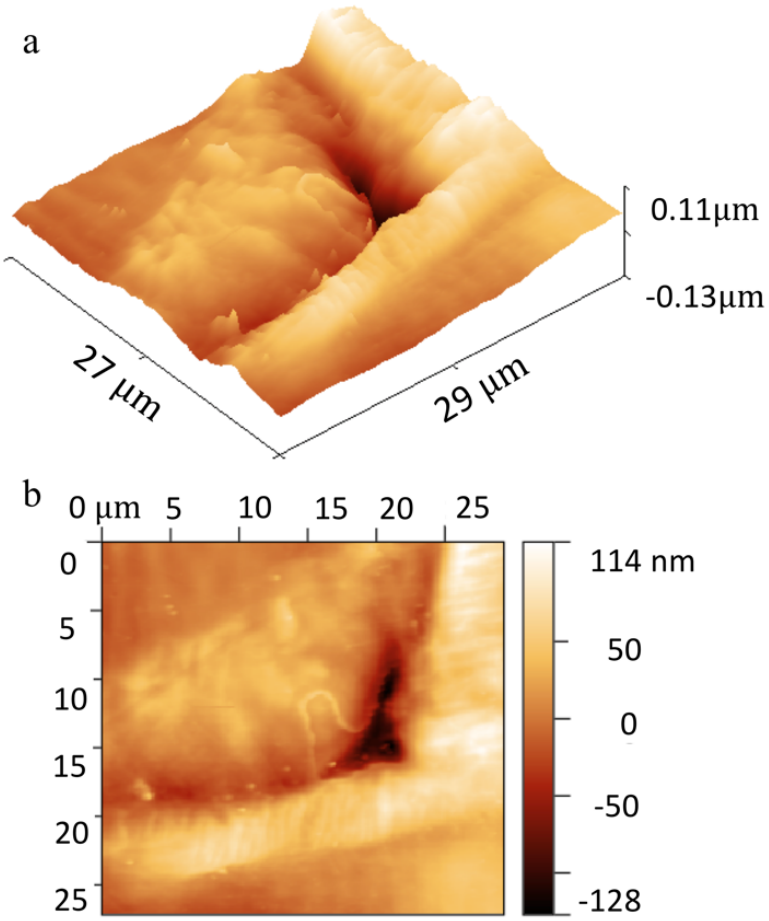

Figure 47. 3D (a) and 2D (b) maps constructed from an atomic force microscopy scan of a single hydride scar on the surface of sample II after MO (the first cryo-cycle) show a surface height difference of about 200 nm.

Because sample II showed a variety of defect phenomena (preferential GB flux penetration, LAGBs, and hydride scars) that can affect cavity performance, this sample was used to investigate how heat treatment (HT) and nitrogen doping affect LAGB and HAGB defects that could trap flux. To follow a path similar to that currently used for cavity processing, an 800 ℃ 3-hour heat treatment was done to remove hydrogen, followed by a 140 ℃ 48-hour N_2 doping treatment. A subsequent ZFC MO image (second cryo-cycle) is shown in Figure 49a, where in contrast to Figure 44f-h, it did not show the previously observed fork shaped flux penetration (marked with red dashed lines in Figure 49a and b). Rather, there was a uniform flux penetration at 70% of the

magnetic field (H = 22 mT) that was used to observe flux penetration in Figure 44f before the heat treatment. This indicates that removal of hydrogen decreased the preferential vulnerability along grain boundaries, but the overall material was less resistant to the magnetic field after the heat treatment and nitrogen doping.

To determine whether the introduction of hydrogen caused grain boundary flux penetration, sample II was then mechanically polished again to reintroduce hydrogen and a third MO measurement (third cryo-cycle) was done. The ZFC MO image in Figure 49b reveals a partially restored fork shaped flux penetration (but penetration along the left 2/3 of the HAGB was not observed) at T = 6.4 K, H = 44 mT, which is at a lower temperature and with a field similar in strength to the first MO measurement. Although heat treatment made flux penetration disappear for both HAGB and LAGB in Figure 49a, the LAGB flux penetration was restored more than the HAGB flux penetration in Figure 49b. This suggests that LAGBs, which are composed of dislocation substructures, are more effective at causing flux penetration than HAGBs.

The repeated cryogenic cycles of sample II with MO imaging show that the flux penetration along the HAGB and LAGB could be turned on and off by introducing and removing hydrogen. This difference in flux penetration resistance (compared with Figure 44f) is correlated with the hydride formation. However, a direct correlation of flux trapping by hydrides could be proved from this current work, due to the lower resolution of the MO technique. Direct observation of flux trapping caused by hydrides was achieved in a recent MO study of SRF cavity Nb [119].

Given that the MO measurement reflects more of a bulk effect than a surface effect, a decision was made to examine the subsurface region (as the surface was covered with hydride scars again as in Figure 46), so about 150 μm was chemically removed from the surface, and an additional EBSD scan was made as shown in Figure 48. This figure shows that the low angle

boundary was in the same place, indicating that the boundary is nominally perpendicular to the surface, except for the 50 µm closest to the high angle grain boundary, where there were a number of low angle boundaries. Evidence of hydride scars is apparent in a number of locations along LAGBs, as shown by arrows in Figure 48. The BSE image shows three ~30 µm hydride scars along the nearly vertical LAGB, and two along the high angle grain boundary (HAGB), which were also evident in the local average misorientation (LAM) map and the IQ map. There were ~3° misorientation regions in the LAM map associated with these scars, consistent with the EBSD scan of the original surface hydride scars in Figure 45. The hydride scars along the LAGB are smaller than the original 50 µm surface scars (Figure 45) but larger than the 10 µm in-grain hydride scars on the same subsurface that are shown and discussed in more detail below.

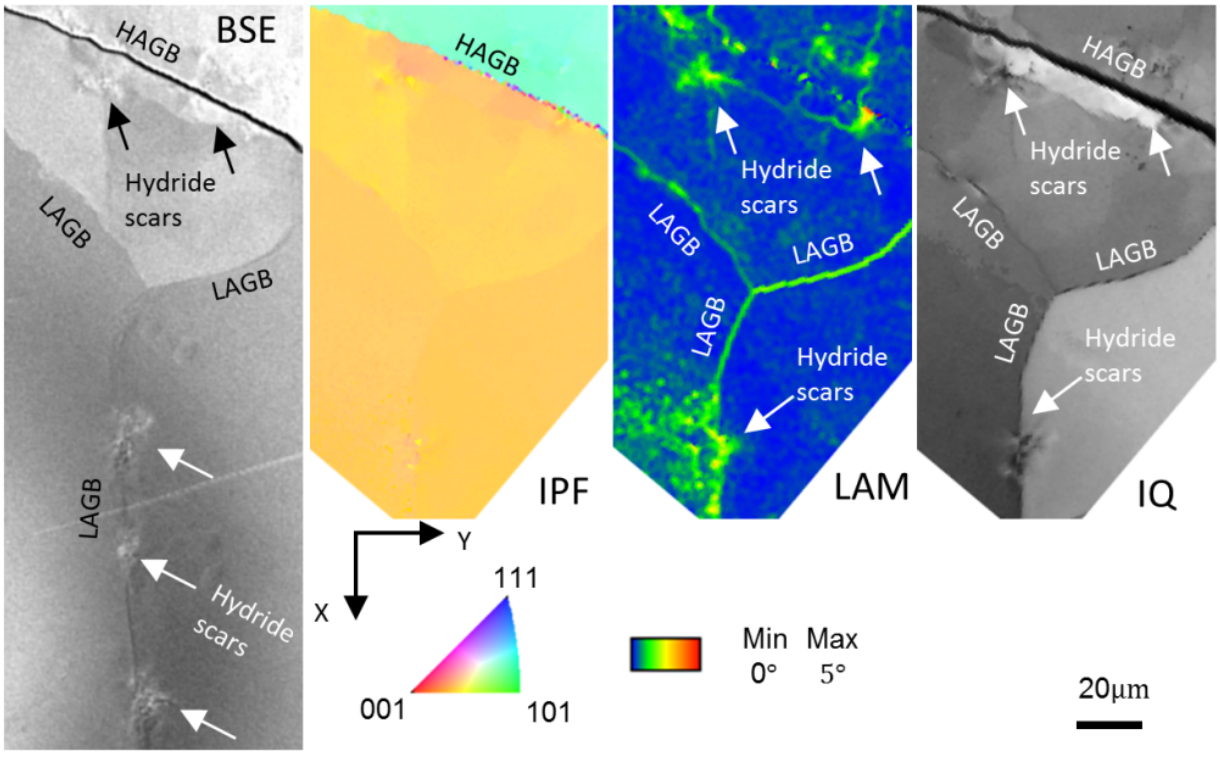

Figure 48. Subsurface beneath the fork flux penetration area (black outline in Figure 44f) after removal of about 150 µm showed hydride scars along both HAGB and LAGBs in the BSE image, IPF, LAM (local average misorientation), and IQ maps.

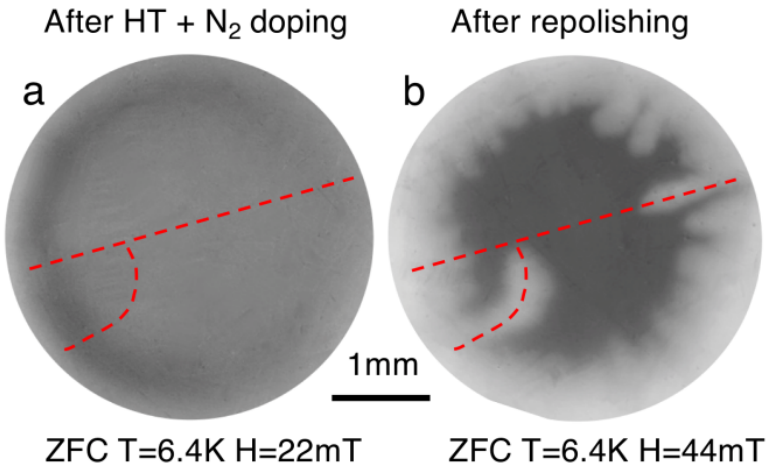

Figure 49. ZFC MO images of sample II after 800°C heat treatment (to remove hydrogen) and nitrogen doping (a) and after subsequent mechanical polishing to reintroduce hydrogen (b) suggest that preferential magnetic flux penetration along grain boundaries can be turned off by heat treatment and partly restored by mechanical polishing. The location of the previous fork flux penetration is marked using red dashed lines.

2. Microscopic analysis

Although flux penetration and hydride scars were correlated in the MO analysis just described, flux penetration could be related to either the structure of the hydrides or damage done by the formation of the hydrides, as the material was not strongly resistant to flux penetration after the heat treatment. Consequently, the effect of internal strain resulting from the hydride deformation accommodation (regions surrounding normal-conducting hydrides) was investigated to identify the dislocation structures using ECCI within and near the deformed regions surrounding the hydrides and how the 800 ℃ heat treatment, a standard processing method for real SRF cavities, affect these regions.

a. Sample I

The surface quality of Sample I after the first MO cryogenic cycle is not sufficient for ECCI, therefore, BCP was used to prepare the surface before ECCI observations, which removes

100–150 μm surface material and still conserves hydride scar structures. Sample I was twice examined using ECCI, first after hydride scars were formed from the first MO experiment (cryogenic cycle), then after the heat treatment.

After 100–150 μm material removal, the surface of Sample I was still observed to be covered with a large number of hydride scars with a smaller size of several micrometers, as shown in Figure 50a. These scars are about 20% the size of the ~50 μm scars on the original surface as shown in Figure 46.

EBSD-OIM analysis was performed on the surface of sample I after MO and the results are shown in Figure 50b and c. For the scar indicated by the red arrow in Figure 50a, the IQ map (Figure 50b) shows that the scar has a lower image quality, or darker contrast, compared to the surrounding regions that show a higher image quality, or a brighter IQ map contrast. This is consistent with the significant plastic deformation and orientation gradients resulting from hydride precipitation, which led to a distorted crystal lattice, and hence less sharp EBSD patterns (lower image quality). The KAM map in Figure 50c shows that the scar caused about a 3° misorientation, consistent with the hydride scars observed in Sample II (Figure 45).

ECC images of the scar indicated by a red arrow in Figure 50a are shown in Figure 51 at two different channeling conditions. In Figure 51a, with **g** = (00-2), high density individual dislocations are most clearly resolved in regions surrounding the scar and appear to be moving towards or emitted from the scar, with evident dislocation pile-ups (red arrows), which is consistent with the plastic deformation due to the hydride precipitation and dissolution. Dislocation B is visible for both imaging conditions, while dislocation A with a “V” shape is only visible for **g** = (00-2), suggesting that A and B have different Burgers vectors. This suggests that dislocations of different Burgers vectors were generated to accommodate the plastic deformation

during the precipitation and dissolution of hydrides. On the other hand, the center of the scar has the brightest contrast, where individual dislocations cannot be identified possibly due to varying channeling conditions throughout the scar as a result of plastic deformation that caused crystal rotations. This is evident by various regions showing different contrast inversions with different predominant channeling conditions. The regions with bright or dark contrast inversions in the middle of the scar are irregular, with poorly defined edges, and their shapes are not consistent between the two images with different imaging directions.

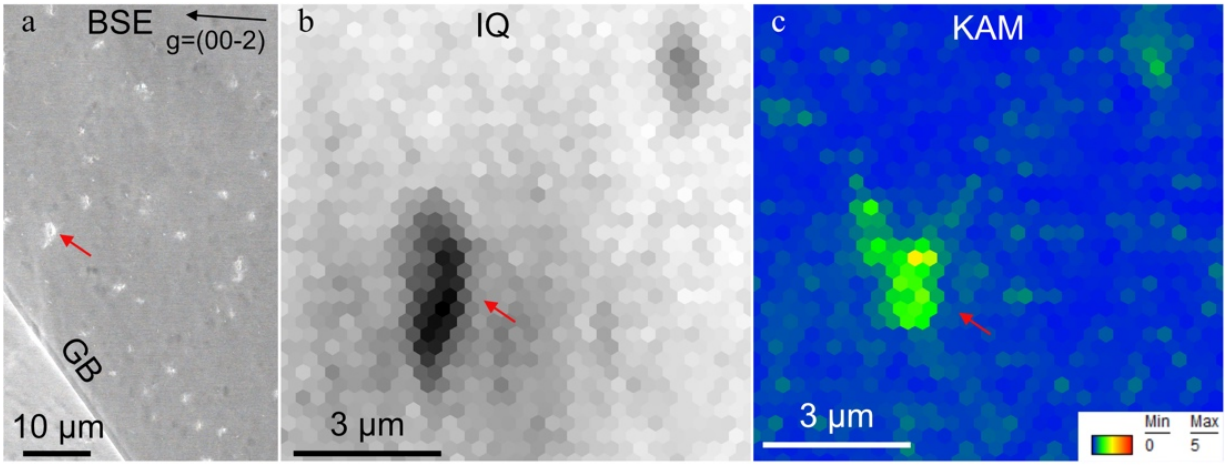

Figure 50. (a) Low magnification BSE image under condition ***g*** = (00-2) of hydride scars on the sub-surface of Sample I after MO; (b) the IQ map showing a low image quality of the scar observed in Figure 51, indicated by a red arrow; (c) the KAM map showing about a 3° misorientation of the same scar.

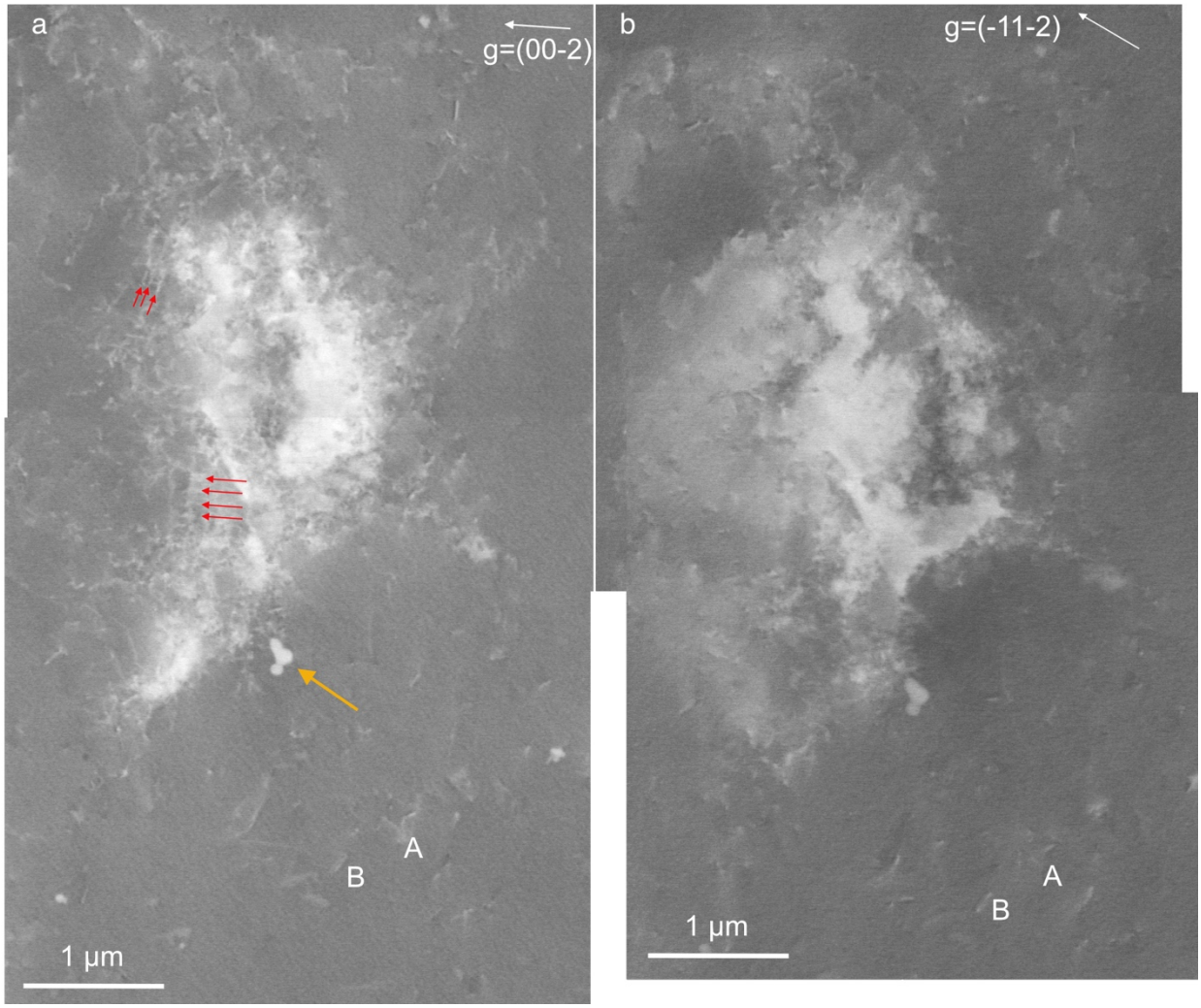

Figure 51. Sample I ECCI images under two different channeling conditions (**g** vectors represented by white arrows) of a scar on the surface of sample I after MO, before heat treatment. The orange arrow indicates a speck of dust used as a landmark.

In order to evaluate the effect of heat treatment on the evolution of dislocation structures of hydride scars in Sample I, an 800 ℃ 3-hour heat treatment was carried out followed by a brief BCP etch to improve the surface quality. The ECC images in Figure 52 of a representative scar show that after heat treatment, the hydride scars appeared to have fewer dislocations and LAGBs were developed, in contrast to Figure 51 (before HT). Well defined ~1 μm subgrains with sharp boundaries that are apparent in the same location in multiple images suggest dislocation recovery

processes during the heat treatment (dislocations with opposite sign meet with the aid of diffusion, and mutually annihilate, with many remaining dislocations accumulating to form low angle boundaries).

The curvatures of the dislocations i and ii in Figure 52a have bowing directions towards the scar center, indicating internal stress that would move the dislocations toward the center of the scar, consistent with a reverse flow of material toward the center of the hydride as it dissolved. Similar to Figure 51, dislocations of different Burgers vectors and dislocations pile-ups are evident near the scar, as a result of the plastic deformation. Dislocation i is visible for both imaging conditions in Figure 52a and b, while iii is invisible in Figure 52b, suggesting different Burgers vectors of i and iii.

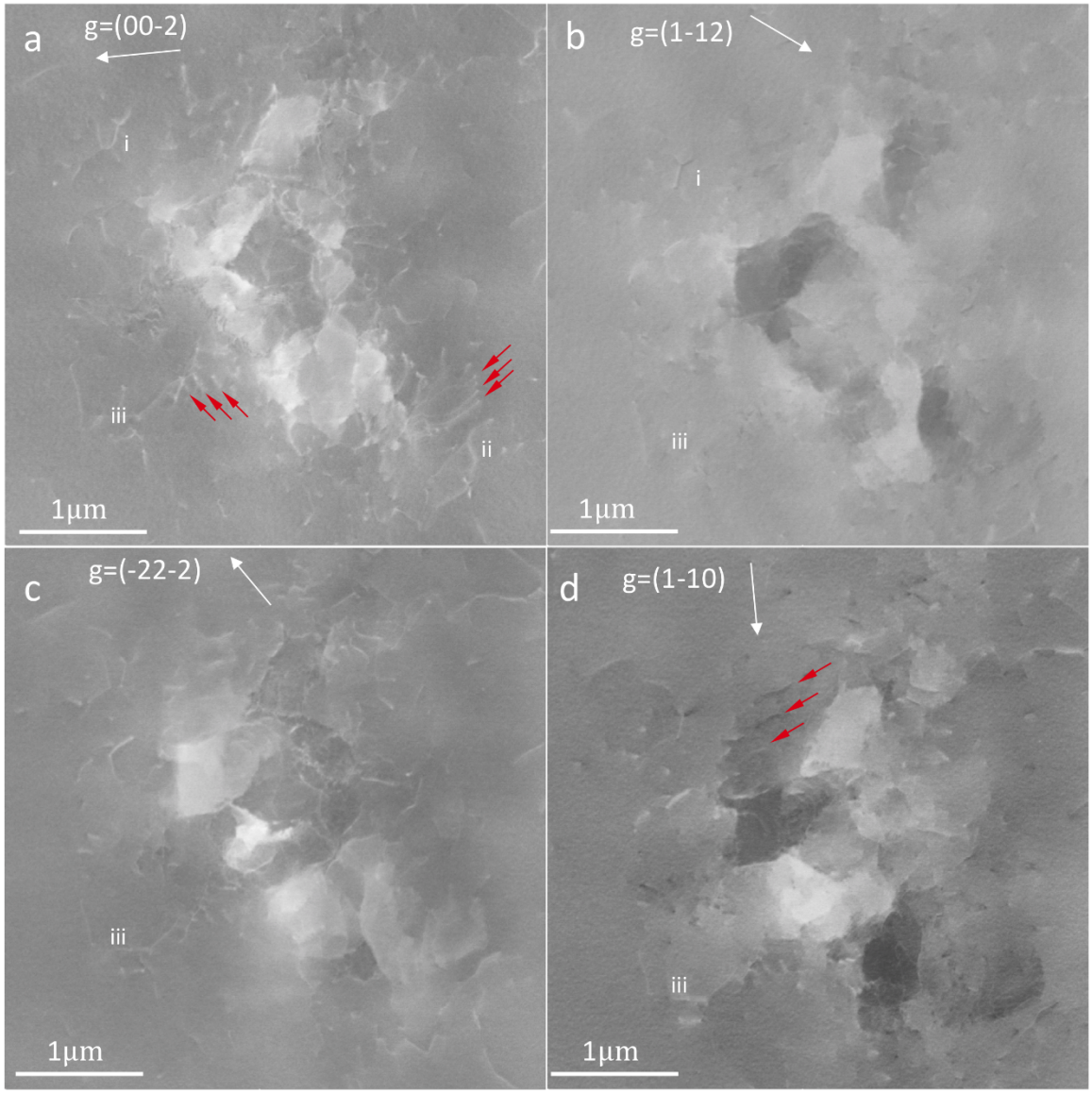

Figure 52. Sample I ECCI images of a specific scar after 800℃ 3-hour heat treatment under four different channeling conditions (**g** vectors) show development of sub-grains with apparently fewer dislocations HT.

b. Sample II

Sample II experienced the first MO cycle (Figure 44), followed by an 800 ℃, 3-hour heat treatment and 140 ℃ 48-hour nitrogen doping, and a second MO cycle (Figure 49), and then repolishing followed by a third MO cycle, after which ECCI analysis was performed after

removing 150 μm by chemical polishing. A low magnification BSE image in Figure 53a shows numerous scars with decreasing size with distance from the grain boundary, but these scars are smaller (~10–20 μm) than the ~50 μm scars on the original surface after the first MO cryo-cycle (Figure 46), and smaller than nearby hydride scars adjacent to LAGBs evident in Figure 48.

Figure 53b shows an ECC image of the scar identified by the arrow in Figure 53a under the channeling condition of $\boldsymbol{g}$ = (-200), with three numbered areas (marked 1, 2, and 3) in white dashed-line boxes enlarged using the same channeling condition. This scar contains regions with very different dark and bright contrast, resulting from different local crystal orientations that provide different backscattered electron yields. The KAM map in Figure 54 shows that the range of orientations present in a scar varies by a few degrees, indicating that the different subgrain orientations are separated by low angle boundaries. These different orientations in different regions are the outcome of subgrain formation during the heat treatment following the deformation caused by the hydride precipitation during the MO cryogenic cycles. In Figure 53b. the regions surrounding the scar show many dislocations, which appear as bright dots or lines that can be observed individually at high magnifications in areas 1, 2, and 3. Hence, the surrounding regions were affected by the accommodation deformation during volume change from precipitation and dissolution of hydrides, and dislocations are necessary to transport material away from or towards the precipitation area. Compared to the annealed condition of Sample I (Figure 52), the subgrain structures in Sample II are smaller and more irregular, and the dislocation density appears to be greater.

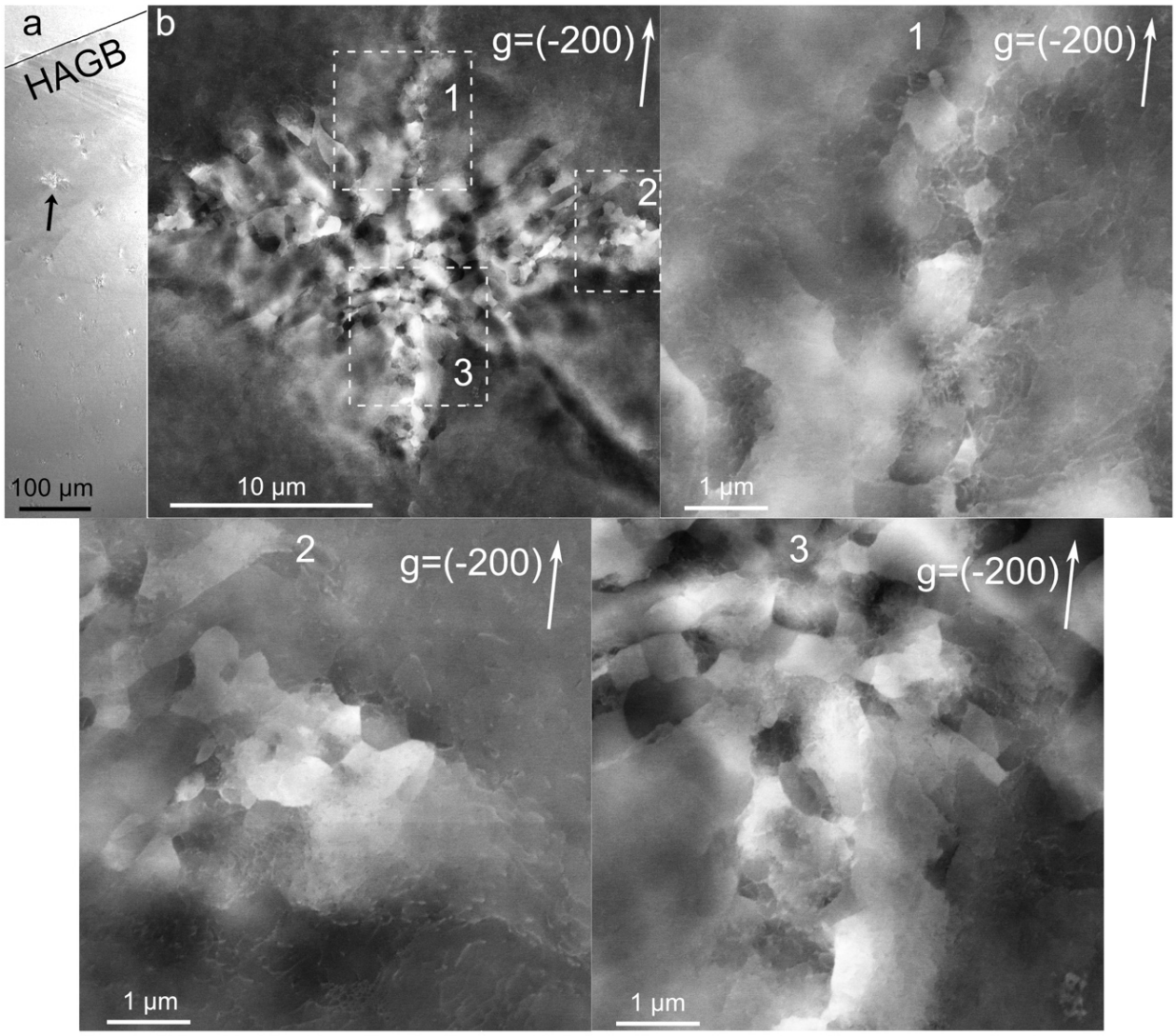

Figure 53. Sample II ECC image of a specific scar under the channeling condition ***g*** = (-200), with three numbered areas in white dashed-line boxes viewed at a higher magnification under the same channeling condition.

The scar in Figure 53b was also characterized using EBSD-OIM analysis and the maps generated are shown in Figure 54, where the IPF map shows orientation gradients within the scar with the LAGBs marked by white lines. The KAM map in Figure 54 shows about a 3° misorientation of the LAGBs, with some similarly high misorientations in the regions surrounding the scar, which is consistent with the high dislocation content observed in ECCI analysis. It is significant that there are regions of low KAM within and immediately surrounding the scar, which

suggests the possibility of a highly recovered region. The GROD-angle map in Figure 54 reveals the local orientation deviation with respect to the average grain orientation Consistent with the regions of low KAM values (blue), the image quality is higher within the scar and lower in the surrounding regions, as shown in the IQ map.

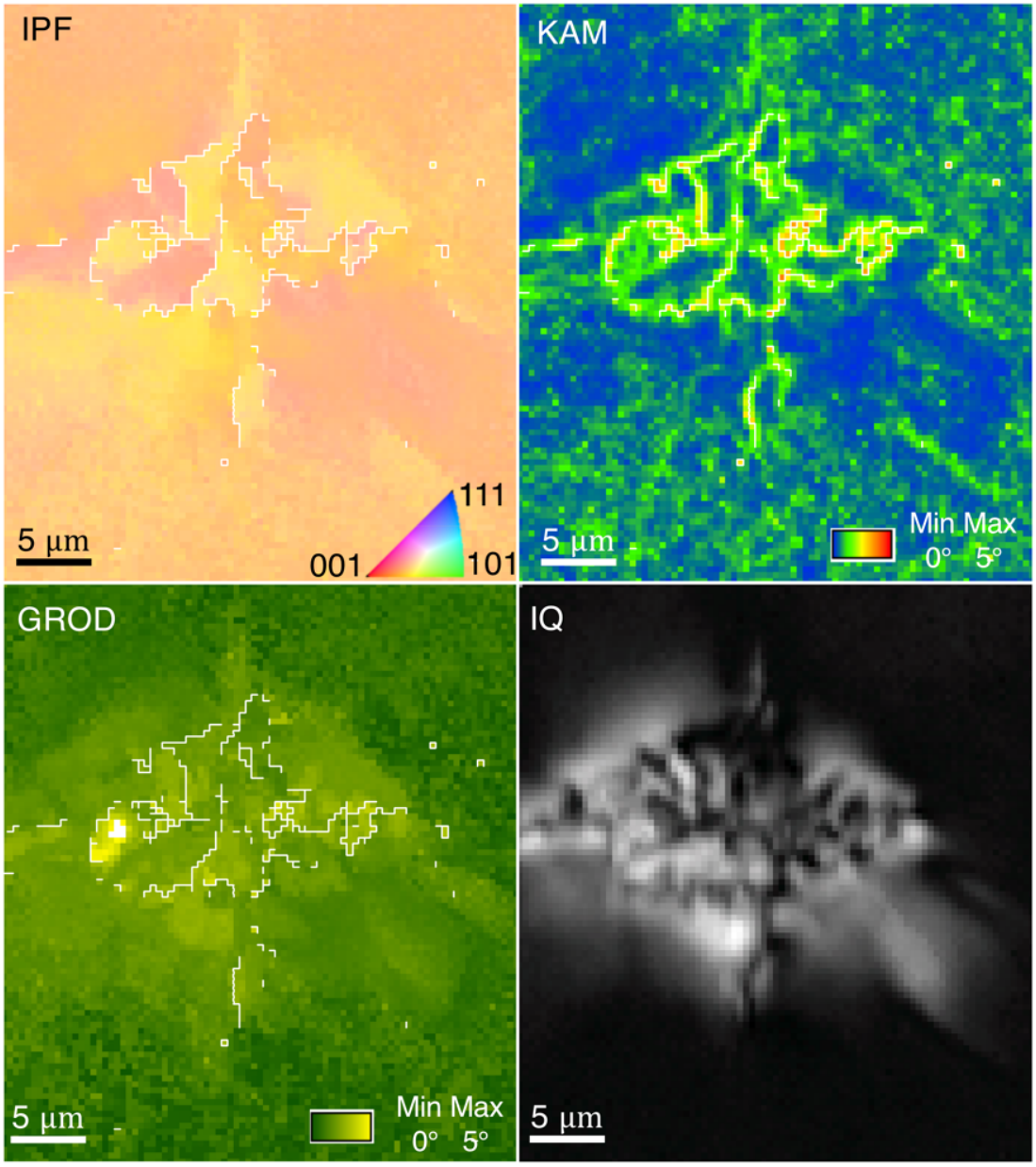

Figure 54. EBSD maps of the scar shown in Figure 53b reconstructed from an EBSD scan with a step size of 0.4 µm. LAGBs are marked using white lines in the IPF, KAM, and GROD-angle

Figure 54 (cont'd)
maps. The IPF map reveals the orientation gradient around the hydride scar, which caused a misorientation of about 3° as shown in the KAM and GROD angle maps. The IQ map shows higher image quality in the scar in contrast to the surrounding area.

D. Discussion

1. Grain boundary flux penetration and hydrides

The three bicrystal samples (Figure 25) observed using MO imaging have different grain boundary characters that could influence magnetic flux penetration and trapping behavior. The grain boundary characters and corresponding MO results are summarized in Table 8. Preferential HAGB flux penetration was observed in both Samples II and III (marked in red in Table 8), which have part of the boundary with 0° tilt angles (parallel to the magnetic field), and relatively low misorientations (24° and 11° respectively). Sample I, with a higher tilt angle (HAGB plane not parallel to the magnetic field) and misorientation (53°), did not show HAGB flux penetration. However, the reason for the lower field flux penetration in Samples I and III in the first MO cycle than Sample II is unclear. Previous studies revealed preferential HAGB flux penetration at $T = 6$ K, $H = 32$ mT for boundaries that are parallel to the magnetic field [27], and partial LAGB flux penetration at $T = 7$ K, $H = 60$ mT [16].

Grain boundaries are segregation sites for hydrogen atoms, resulting in a large number of hydrides at grain boundaries during MO imaging. Flux trapping by hydrides has been observed by other researchers [119]. Therefore, it is possible that these normal-conducting hydrides caused flux penetration along grain boundaries. If so, this flux penetration due to hydrides appeared to be most effective when the grain boundaries occupied by hydrides were aligned with the applied magnetic field.

Table 8. Grain boundary characters of three MO samples.

Sample	Tilt angle	Misorientation	GB flux penetration
I	~10°	53°	No
II	~0°	24°	Yes
III	Twist that includes ~0°	11°	Partial, where ~0°

The MO imaging of the hydrogen-containing sample II (as shown in Figure 44f) showed fork shaped preferential flux penetration along both HAGB and LAGB, which disappeared after the heat treatment that removed most of the hydrogen (Figure 49a). This suggests that hydrides could be the dominant reason for the grain boundary flux penetration. If so, bringing back hydrogen to the sample would cause the grain boundary flux penetration to reappear. This was confirmed by a subsequent MO imaging after a mechanical polish that reintroduced hydrogen (Figure 49b). Therefore, the grain boundary itself might not have a significant effect on flux penetration.

After the heat treatment, a uniform flux penetration at a lower field (6.4K, 22 mT) occurred compared to Figure 44f, indicating a weaker overall resistance to flux penetration. A similar flux penetration at 8.4K, 29 mT was observed in a 5% strained bicrystal sample with the same grain boundary after the same heat treatment (Figure 61). The fact that flux penetrates uniformly at a lower field with low hydrogen concentration and recovered hydride scars (and with recovered dislocation substructure after heat treatment following deformation) suggests the possibility that internal damage from hydride scars (or mechanically imposed strain) that are uniformly scattered within the grains may facilitate flux penetration.

After the subsequent reintroduction of hydrogen via mechanical polish of sample II, the resulting MO image (Figure 49b) shows incomplete restoration of the original fork flux penetration. It is not clear why flux penetration along the left side of the high angle grain boundary did not

occur in Figure 49b, as there was no measurable change in the high angle grain boundary position. This result suggests that hydrogen may be more likely to segregate in higher concentration along dislocations and low angle grain boundaries, but the evidence presented suggests that hydrides nucleated preferentially and grew larger along both low and high angle boundaries.

2. Dislocation structures around hydride scars

There were substantial dislocation structures and high dislocation densities in the areas within and near the hydride scars (Figure 50-Figure 54), with different histories of MO cycles, heat treatments (HT), and buffered chemical polishing (BCP, 150 μm surface removal). Observed features of hydride scars are summarized in Table 9.

Table 9. Observation of hydride scars after different histories of MO cycles and heat treatments.

History	Sample I (tilted GB)	Sample II ('fork')	Sample III (twisted GB)
1st MO (cryo-cycle)	No preferential flux penetration ZFC 8.7K, 10.4 mT	LA, HA GB flux penetration ZFC 8.7K, 32 mT, repeated at 7.8K, 56 mT, slightly less penetration	Partial GB penetration ZFC 8.7K, 16.8 mT in GB oriented || field
Surface SEM after 1st MO	Numerous hydride scars (~50μm)	Numerous hydride scars (~50 μm)	Numerous hydride scars (~50 μm)
2nd MO after 800℃ HT+N_2 doping (H removed)	N/A	Fork flux penetration not observed; uniform penetration at lower field (ZFC 6.4 K, 22 mT)	N/A
3rd MO after mechanical polishing (H reintroduced)	N/A	Fork flux penetration restored (ZFC 6.4K, 44 mT)	N/A
1st ECCI after 150 μm BCP	Small hydride scars (~3 μm); high density dislocations in scars, no LAGB	Smaller scars (~20 μm); High density dislocations + many LAGBs in and near scar (recovery)	N/A
2nd ECCI after HT, 20 μm BCP	LAGBs and dislocations	N/A	N/A

Table 9 (cont'd)

	observed in scar (recovery)		

After the first MO experiment, large hydride scars (~50 μm) (Figure 46) were observed to be distributed along the HAGB and scratches, which are preferred sites for hydrogen segregation and hydride nucleation. The hydride scars observed in sample II, with three MO cryogenic cycles, are much larger than the scars in sample I (Figure 50a, where 150 μm was removed from the surface), which experienced only one cryogenic cycle. Repeated MO cycles may lead to locally complex hysteresis strain loops, especially if scars are nucleation sites for new hydrides. The higher dislocation density observed after reintroduction of hydrogen into sample II along with well-defined subgrain boundaries suggests that hydrides formed where they had formed before, which could be facilitated by the low angle boundary networks already present, where hydrogen could preferentially reside. The smaller hydride scars observed after surface removal indicates that the hydrogen concentration decreases with depth into the bulk niobium, which could account for the smaller hydride scars in the subsurface. Alternatively, the 3-D constraint (lack of a free surface) may have led to smaller hydrides in Sample I and Sample II after surface removal, than on the free surface of Sample II.

The dislocations near the scars were generated to transport the material away from or towards the precipitates and are evidence of the required accommodation deformation. Previous studies [96], [97] showed prismatic dislocation loops formed near the hydride scars, which, however, were not observed in the current study, perhaps due to the hydrides in current work being much larger. An elasto-plastic model of hysteresis was proposed to describe the precipitation and dissolution of hydrides in niobium that considered both elastic and plastic deformation [98]. Another similar study suggested that the hydride precipitates were coherent to the Nb matrix when

the hydrides were smaller than a critical size, and semi-coherent for larger hydride sizes [99]. Both elastic energy stored in hydrides and the energy needed to form dislocations come into play to determine this critical size [99].

The ECCI analysis of these scars after heat treatment showed sub-grain development in the scars due to recovery during heat treatment. This is clear by comparing the ECC images of the scars in Sample I before (Figure 51) and after (Figure 52) the 800 ℃ heat treatment. The EBSD analysis in Figure 54 showed LAGBs within the scar (IPF map), as well as regions of possible recrystallization nuclei, though there were no high angle grain boundaries adjacent to highly recovered regions with low densities of dislocations. Note that the IQ map showed higher image quality (brighter contrast) interweaved with some low image quality spots within the scar, in contrast to the surrounding area with lower image quality (darker contrast). The scar area was heavily deformed during the hydride precipitation and therefore had a larger driving force for recovery or recrystallization during the following 800 ℃ heat treatment, which could lead to a higher level of recovery, or higher image quality.

3. Relationships between hydrides, dislocation networks, and flux penetration

The observations of flux penetration in bicrystal niobium samples in this study suggested that hydrogen played a key role in preferential grain boundary flux penetration and trapping. Grain boundaries tend to have a higher concentration of hydrogen, which could precipitate as normal-conducting hydrides and trap magnetic flux during cryogenic cooling, making grain boundaries weak spots for flux penetration.

Although no direct observation of hydride flux trapping was observed by MO imaging in the current work, these results indicate that higher concentration of hydrogen and the resulting hydrides in grain boundaries could facilitate the early entry and subsequent trapping of magnetic

flux along HAGBs and LAGBs. Hydride decorated LAGBs and hydrogen depleted zones immediately next to LAGBs that cause preferential flux penetration [16] have also been observed in single crystal niobium, suggesting diffusion of hydrogen into the LAGBs from within the grain. In contrast, there was a decreasing hydride scar size with distance from the high angle grain boundary in Figure 53a, suggesting that high angle boundaries are a source of hydrogen that diffuses into the grain. This indicates that high angle boundaries are not traps for hydrogen in the same way that low angle boundaries are. Instead, high angle grain boundaries could be a transport channel for hydrogen atoms. The presence of a high dislocation density within heat treated hydride scars indicates that hydride precipitation is preferable in dislocation networks that served as traps for hydrogen atoms. Therefore, the relationship between hydrides, dislocation networks, and flux pinning may be inseparable. Advanced flux characterization methods with a micrometer to nanometer level resolution would enable further exploration of the influence of dislocations.

E. Summary

Preferential grain boundary flux penetration was observed in bicrystal samples with relatively low misorientations and the boundary planes nearly parallel to the applied magnetic field. Hydrogen and the resulting hydrides could be the dominant sources causing the grain boundary flux penetration, while the intrinsic characteristics of grain boundary itself might be insignificant.

MO cycles led to hydride precipitation that generated a large number of dislocations to accommodate the volume change. These dislocation networks generated during MO cycles and the heat treatment are scattered in the grains and might cause the observed lower resistance to flux penetration. The development of LAGBs was observed in and around the hydride scars after the 800 ℃, 3-hour heat treatment, indicating recovery or even partial recrystallization of the scars.

Chapter VII. DEFORMED BICRYSTAL NB SAMPLES

A. Introduction

Grain boundaries can act as barriers for dislocation slip, and hence, cause heterogeneous deformation near grain boundaries with dislocation pileup and local stress concentration [146]. Depending on the grain boundary characteristics, it can also be transparent to dislocations on specific systems [146]. Since both grain boundaries and dislocations are of interest in terms of flux trapping, Nb samples with grain boundaries along with dislocation structures near them are desired to investigate the effect of grain boundaries and plastic deformation on the flux penetration or trapping behavior, and hence the effect on superconductivity of Nb.

In this chapter, one set of bicrystals (extracted from Ningxia ingot) were designed to have favored slip system parallel to the grain boundary so that these slip systems can be activated and cause focused deformation near grain boundaries. Another set of bicrystals (extracted from TD ingot) were designed to have different combinations of soft and hard orientations, so that the two grains experience different amounts of deformation, which was examined for the effect of deformation on flux trapping. These bicrystals with different orientation relationships between the two grains and grain boundary types provide a good sample pool to evaluate conditions when flux penetration or trapping occurs.

B. Results

1. Tensile test results

Figure 55 shows the engineering stress-strain curves of the tensile tests. The yield strength and orientation hardness (based on Schmid factor analysis) are summarized in Table 10. It suggests that the yield strength and hardening are orientation dependent. TD3-0 and TD0-7, with hard orientations, showed the highest hardening and yield strengths (43 MPa and 40 MPa

respectively), while TD3-4 had the lowest hardening and yield strength, corresponding to its soft orientations. These results are consistent with the sample design based on Schmid factor analysis to favor specific slip systems. Sample NX10-9HT showed a strength drop compared to NX10-9AE possibly due to the decrease of pre-existing dislocation density during the pre-deformation heat treatment. However, the heat-treated Sample NX6-10HT showed a higher yield strength than the as-extracted Sample NX6-10AE. ECCI, EBSD and MO characterization methods were performed on all bicrystal samples as organized in Table 10, which lists the characterization methods used for each bicrystal sample in this chapter.

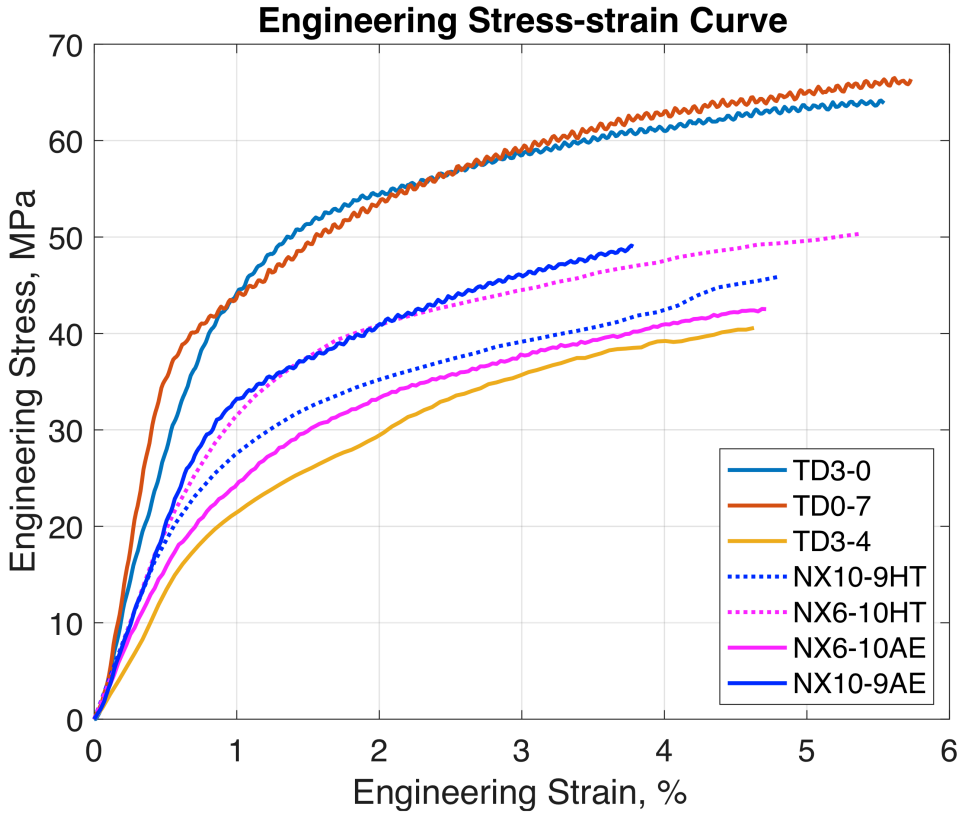

Figure 55. Engineering stress-strain curves of all tensile samples extracted from two Nb disks except for Sample TD5-0.

Table 10. Yield strength and orientation hardness of bicrystal tensile samples and characterization methods used.

Bicrystal Sample ID	Yield strength (MPa)	Orientation hardness (Schmid factor)	Characterization methods		
			MO	ECCI	EBSD
NX6-10AE	26	Soft (0.50)-soft (0.48)	Yes	Yes	N/A
NX6-10HT	32		Yes	Yes	Yes
NX10-9AE	33	Soft (0.48)-soft (0.50)	Yes	N/A	N/A
NX10-9HT	28		Yes	Yes	Yes
TD3-0	43	Hard (0.39)-hard (0.35)	N/A	N/A	Yes
TD0-7	40	Hard (0.34)-soft (0.50)	N/A	N/A	Yes
TD3-4	22	Soft (0.48)-soft (0.50)	Yes	Yes	N/A
TD5-0	N/A	N/A	Yes	Yes	N/A

2. ECCI, EBSD, and MO analysis of NX6-10 and NX10-9

This section describes the MO, ECCI, and EBSD results of Samples NX6-10AE, NX6-10HT, NX10-9AE, and NX10-9HT. MO imaging results will be shown first, followed by further study of the microstructure using ECCI and EBSD analysis.

a. Sample NX6-10AE: MO and ECCI results

As-extracted Sample NX6-10AE was strained to ~5% engineering strain (Figure 55), followed by the extraction of a cylindrical MO sample that was used for MO imaging. The optical image and MO images of Sample NX6-10AE is shown in Figure 56a with a red dashed line indicating the location of the grain boundary. At H = 48 mT, the sample showed central flux penetration, with no preferential grain boundary flux penetration observed. The FC MO image in Figure 56 shows more trapped flux (bright contrast) in Grain 6 compared to Grain 10, suggesting different flux trapping characteristics of the two grains in deformed NX6-10AE. The grain boundary is 7° tilted from being perpendicular to the surface (Table 3).

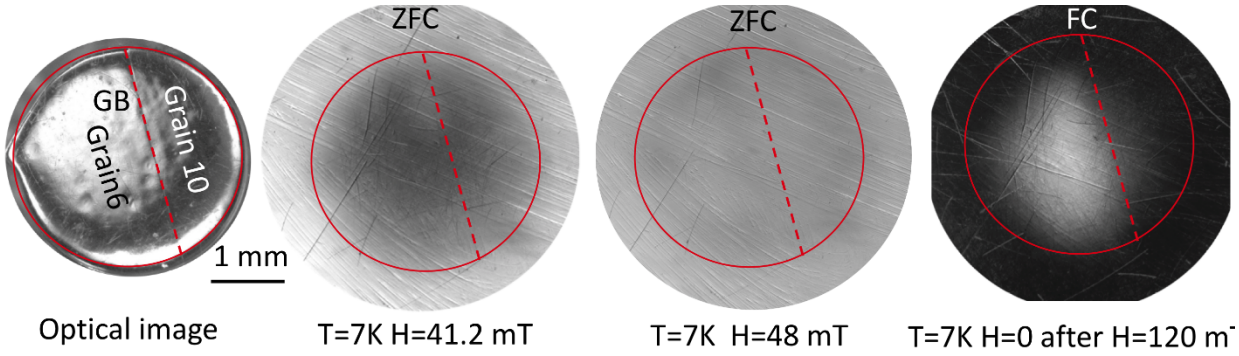

Figure 56. Sample NX6-10AE showed central flux penetration (ZFC at H = 48 mT) and more trapped flux in Grain 6 than Grain 10 (FC). The red dashed line indicates the location of the grain boundary, and the red circle indicates the location of the MO sample edge (compare with the optical image).

In order to investigate whether there is a correlation between flux trapping and dislocation content in the two grains, ECCI observation was performed in both grains of NX6-10AE. Figure 57 shows two representative ECC images of two different areas in Grain 6 after 5% deformation using channeling conditions $\boldsymbol{g}$ = (1-12) or $\boldsymbol{g}$ = (002). Most of the dislocations have line directions nearly perpendicular to the surface. Some of the dislocations have orientations that are nearly parallel to the sample surface, and hence have contrast as short lines, such as dislocation C and D (Figure 57(left)).

However, no good contrast of dislocations in Grain 10 was obtained under several different channeling conditions, while dislocations were easily observed in multiple areas in Grain 6. This may suggest that Grain 10 had a much lower dislocation density than Grain 6. If so, this would be consistent with Grain 6 showing more flux trapping in the FC MO image in Figure 56.

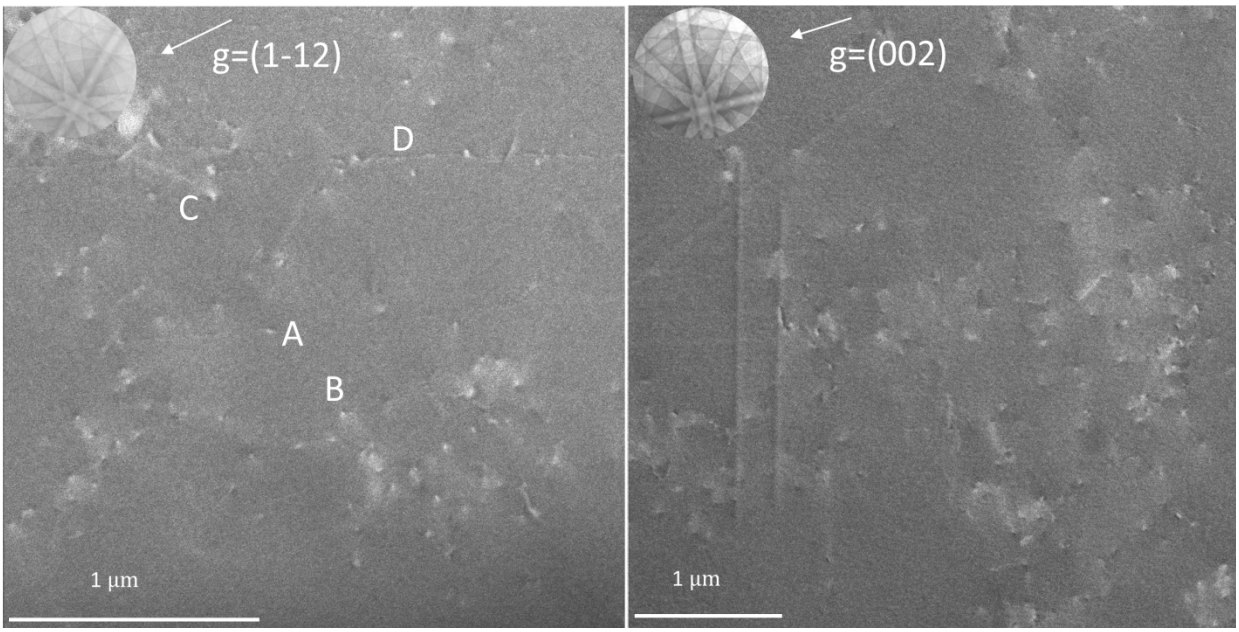

Figure 57. Representative ECC images overlaid with selective area channeling patterns (SACPs) of two different areas in Grain 6 of NX6-10AE after 5% strain show a high density of dislocations (mostly perpendicular to the sample surface).

b. Sample NX6-10HT: microstructure evolution before and after 5% deformation

An 800 ℃ heat treatment was performed for NX6-10HT before deformation to remove pre-existing dislocations. Multiple areas near the grain boundary were observed using different channeling conditions to and the representative ECC images are shown in Figure 58. Two ECC images of the same region (near GB) in Grain 6 using $\boldsymbol{g}$ = (-112) (Figure 58a) and $\boldsymbol{g}$ = (1-12) conditions (Figure 58b) show pre-existing dislocations and LAGBs that were not removed by the 800 ℃ heat treatment This is most obvious in Figure 58b with different contrast in Subgrain A and Subgrain B due to the two subgrains being in very different orientations. Pre-existing dislocations and LAGBs were also observed in Grain 10 (near the HAGB) (Figure 58c and d). These dislocations are probably introduced during the cooling of the Nb ingot that causes thermal strains. By counting the number of dislocations in an ECC image and dividing it by the area, the dislocation density of that area can be estimated. Most dislocations in Figure 58a and c are dot-

like, suggesting they are nearly perpendicular to the surface. An estimated dislocation density is $\rho = 3 \times 10^{12} \mathrm{m}^{-2}$ (Figure 58c). This is always a lower bound of the dislocation density since not all dislocations are visible under a given channeling condition and the dislocations are not necessarily exactly perpendicular to the surface.

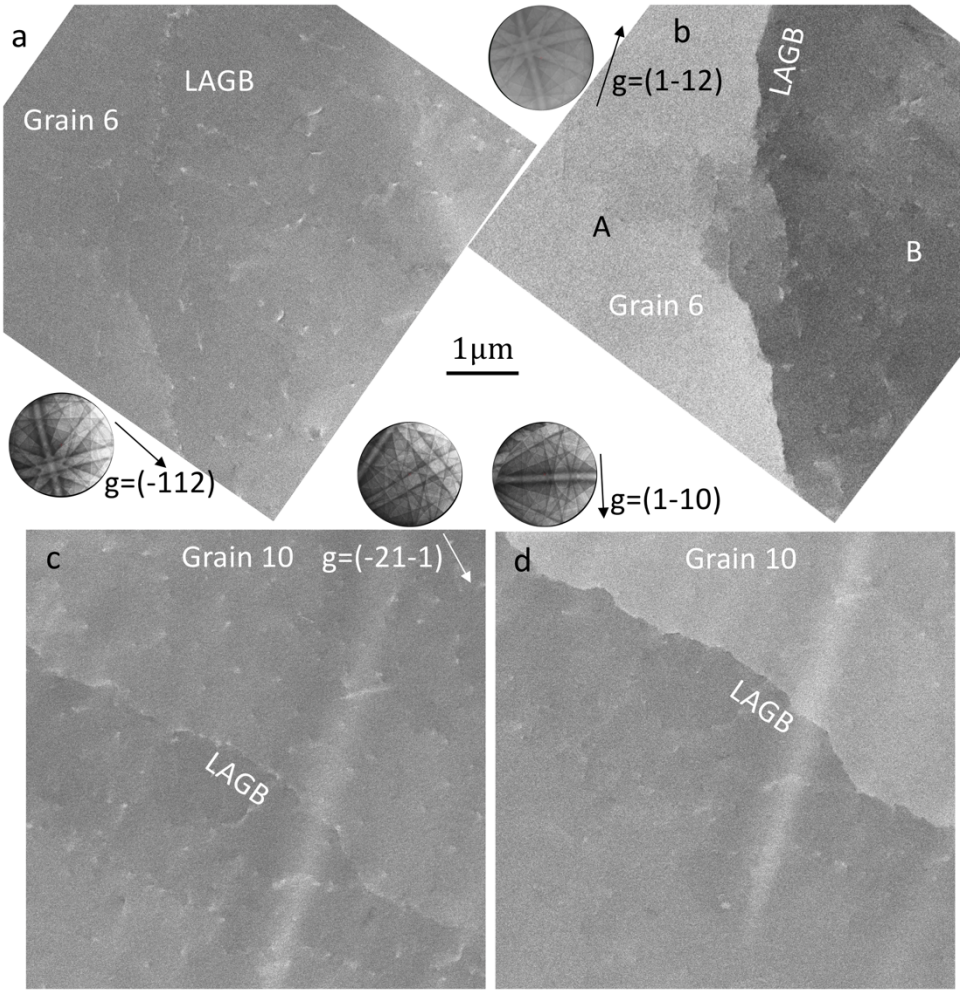

Figure 58. ECC images of both Grain 6 (a and b) and Grain 10 (c and d) of NX6-10HT before deformation show pre-existing dislocations and low angle grain boundaries (LAGBs) using two channeling conditions for each grain. Selected area channeling patterns (SACPs) are attached to show the channeling conditions.

After the tensile deformation of NX6-10HT (soft orientation in both grains), ECCI observations were carried out after some surface removal (~150 μm BCP). The ECC image

(Figure 59a) shows a region with many subgrains in Grain 6 adjacent to the grain boundary after deformation. The white arrow indicates the tension direction. This suggests the development of LAGBs near the grain boundary during the deformation. Three local regions marked with colored boxes were numbered as 1, 2, and 3 and observed using a higher magnification. Region 1 shows multiple LAGBs and a high density of dislocation in Grain 6 close to the grain boundary, and Region 2 and 3 show a high density of dislocation, as well as LAGBs. Dislocation density from Regions 2 and 3 was measured to be $\rho = 8 \times 10^{12}\ m^{-2}$, which is about three times the density prior to deformation (Figure 58).

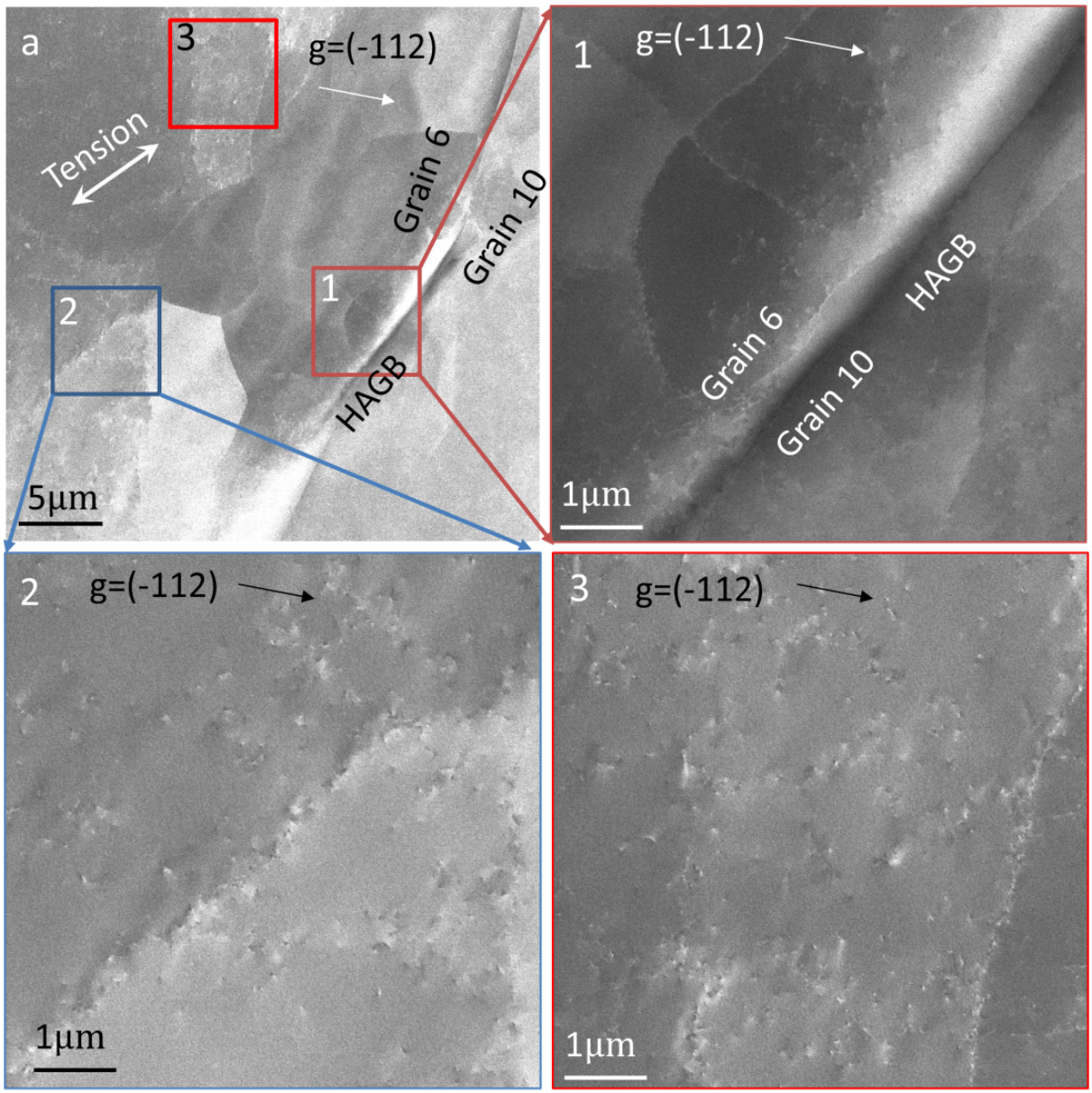

Figure 59. NX6-10HT ECC image (a) of Grain 6 after deformation using g = (-112) condition. The numbered local regions (color boxes), with higher magnification, showed development of LAGBs and a high density of dislocations. Both grain orientations are soft, and the tension direction is marked using a white double-arrow (a).

The region observed in Figure 59a was further studied using EBSD analysis to reveal the orientation gradients and the results are shown in Figure 60. The BSE image shows many subgrains in the region adjacent to the grain boundaries, as well as another LAGB in Grain 10. The IPF map overlaid with a gray-scale IQ map shows the orientation gradients near the HAGB,

where the orientation gradients are consistent with the subgrains observed in the BSE image. The KAM map clearly shows high KAM values near the grain boundary in both grains, suggesting heterogeneous deformation in areas near the HAGB. Interestingly, there were two local regions with low KAM in Grain 6 near the boundary. The GROD angle map reveals that the subgrains in Grain 6, had less than 5° orientation deviations from the grain average orientation. The GROD-axis map shows regions with particular rotation axes near the grain boundary, consistent with observed subgrains in the BSE image.

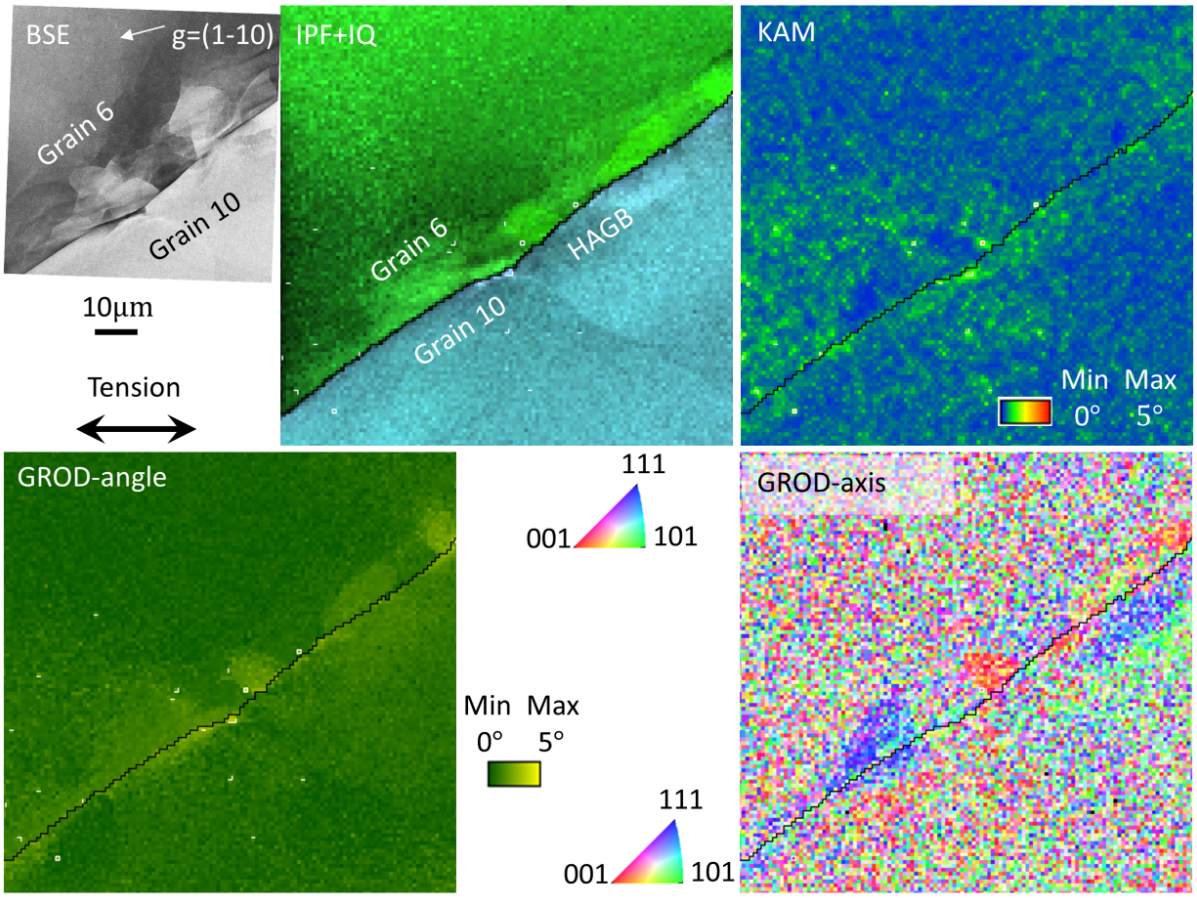

Figure 60. EBSD maps of the same area that was shown in Figure 59a. The BSE image (top left) shows subgrain structures and LAGBs in Grain 6 as well as a LAGB in Grain 10. The IPF map overlaid with IQ shows the orientation gradients near the HAGB. The KAM map shows misorientation (~3°) near the HAGB than within the grains. The GROD angle map shows the orientation difference of each pixel compared with the grain average orientation. The GROD-axis map shows regions near the HAGB have particular rotation axes (color) from the grain

Figure 60 (cont'd)

average orientation, suggesting subgrain development. All maps and images are of the same magnification.

Compared to the as-extracted Sample NX6-10AE, the 800 ℃ heat treated Sample NX6-10HT showed a clear trend of subgrain development and heterogeneous deformation near the grain boundary. It is also surprising to note that the annealed NX6-10HT showed a higher yield strength and hardening than NX6-10AE according to the tensile test results in Figure 55. This implies that dislocation nucleation was difficult to achieve.

c. Sample NX10-9AE: MO results

MO imaging was performed on the MO sample extracted from deformed NX10-9AE. Figure 61a shows an SE image of the MO sample, with the red solid line and the white dashed line representing the top and bottom grain boundaries, respectively. The grain boundary is consistently tilted 14° from being parallel to the applied magnetic field (Table 3). MO images in Figure 61b and c show no difference in flux trapping in the two grains, except for a uniform central flux penetration at T = 8.4 K, H = 37 mT. There was no observed preferential GB flux penetration either. Grains 10 and 9 are both in soft orientations according to Table 3 and are expected to have a similar amount of deformation.

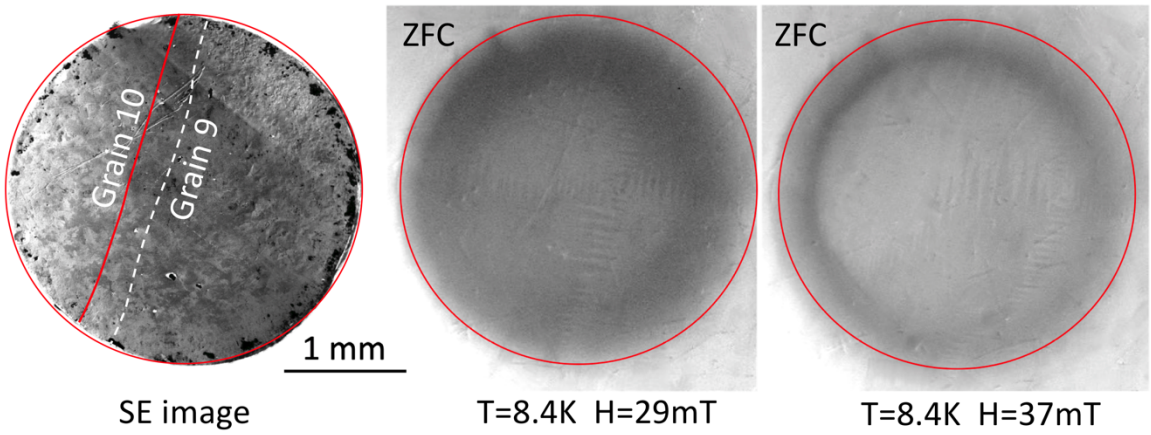

Figure 61. Second electron image of Sample NX10-9AE with the top (red line) and bottom (white dashed line) grain boundaries indicated. The ZFC MO images show central flux penetration at $T = 8.4$ K, $H = 29$, 37 mT. The red circle indicates the location of the edge of the MO sample.

d. Sample NX10-9HT: MO and ECCI results

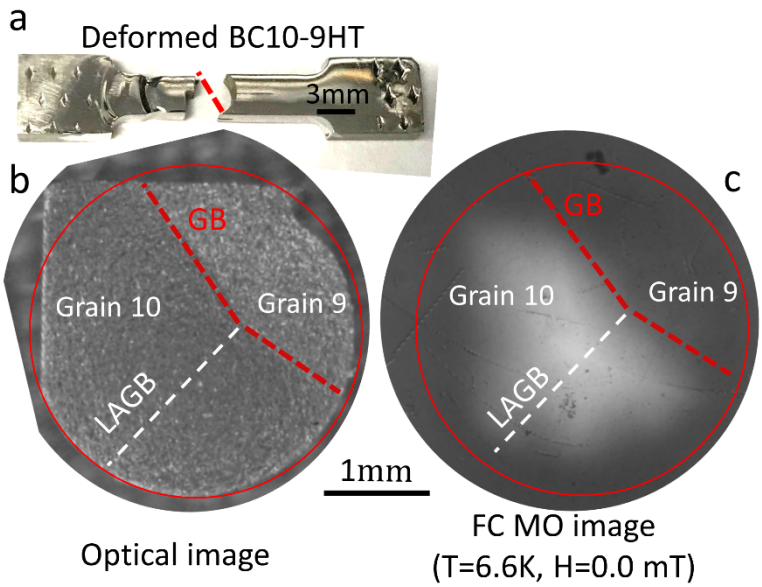

Figure 62. MO sample extracted from the deformed Sample NX10-9HT (a) and its optical image (b) and field cooled MO image (c) show that Grain 10 trapped more magnetic flux than Grain 9. The red dashed line indicates the location of the HAGB and the white dashed line marks the pre-existing LAGB that existed before deformation.

NX10-9HT was heat treated at 800 ℃ before deformation to remove pre-existing dislocations. The FC MO image in Figure 62c was taken at $H = 0$ mT after the sample was cooled in a magnetic field of 120 mT, which was removed when the temperature reached 6.6 K (below T_c). More trapped flux (brighter contrast) was apparent in Grain 10, although no GB flux penetration was observed. The GB tilt angle is ~0–8° (Table 3). In Figure 62, the red and white dashed lines indicate the location of the HAGB and the pre-existing LAGB, respectively. The pre-existing LAGB is stable and was not removed by the 800 ℃ heat treatment.

In order to identify the microstructure effect on flux trapping, ECCI was performed in both grains of the NX10-9HT and the representative ECC images of two different regions in each grain are shown in Figure 63, where the white or dark features are dislocations with dislocation lines at different angles from the sample surface. By counting these features (excluding dislocations in low angle grain boundaries) and dividing this number by the area, the density of dislocations can be estimated. The geometry correction method proposed in ref [147] was used to make a better estimate of the measured dislocation density, assuming that the dislocations were at random orientations. A correction factor of 1/cos(60◦) was multiplied by the measured dislocation density values.

Five regions were observed using ECCI and the dislocation density measurements are shown in Figure 64 (top), which suggests that Grain 10 had a higher density of dislocations after 5% strain, suggesting a correlation between dislocations and flux trapping.

In the same five regions, the lengths of LAGB traces per area were measured using ImageJ, and the results in Figure 64 (bottom) show an opposite trend compared with the dislocation density measurements. Two regions measured in Grain 10 contain no LAGBs. Grain 9 shows a larger

LAGB trace length than Grain 10 after deformation. It is possible that dislocations rearrange into LAGBs during deformation, leading to the decrease in dislocation density in Grain 9.

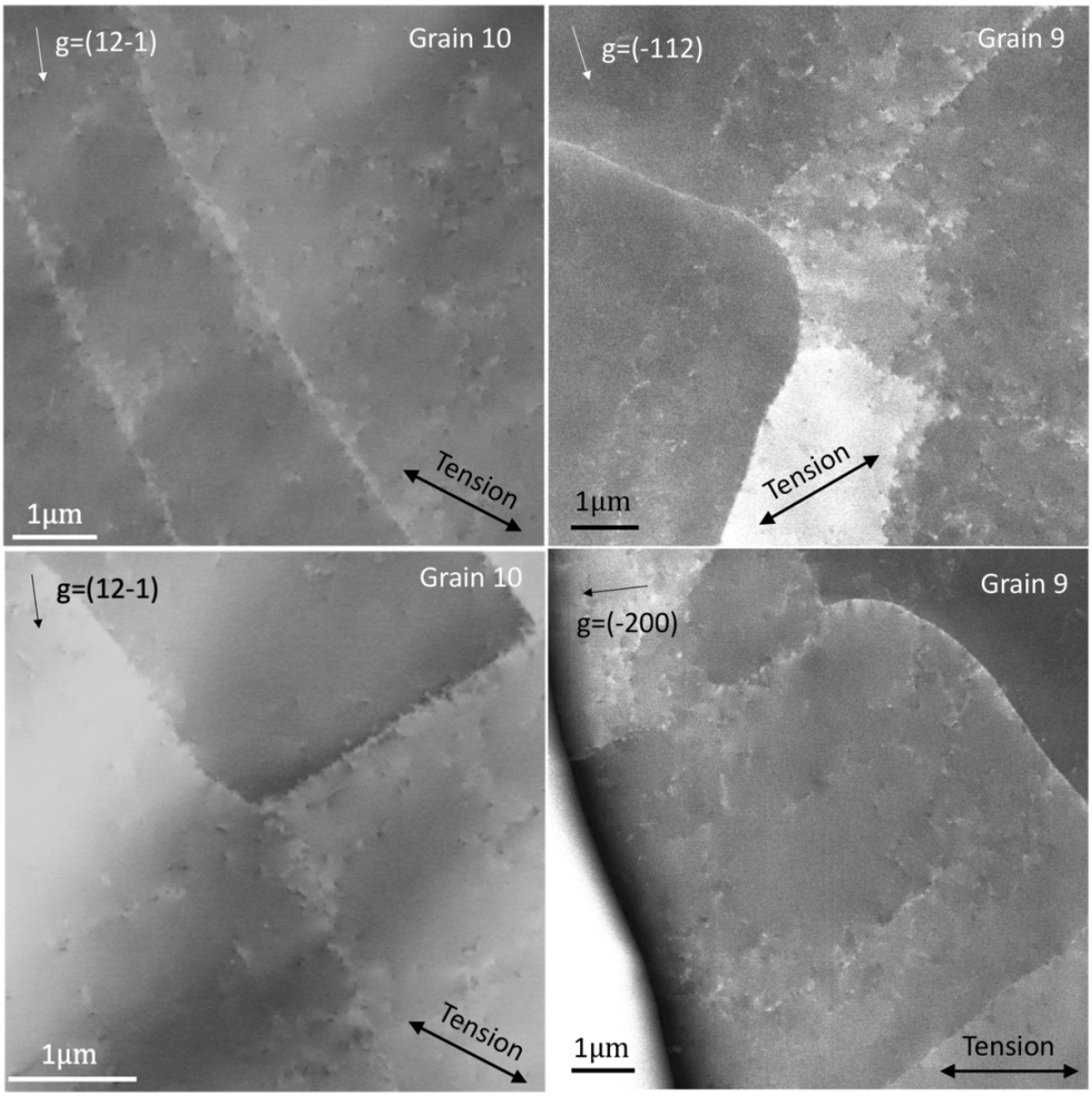

Figure 63. Representative ECC images of two regions in Grain 10 (left) and grain 9 (right) of Sample NX10-9HT. Both high density dislocations (white and dark features) and low angle grain boundaries could be observed.

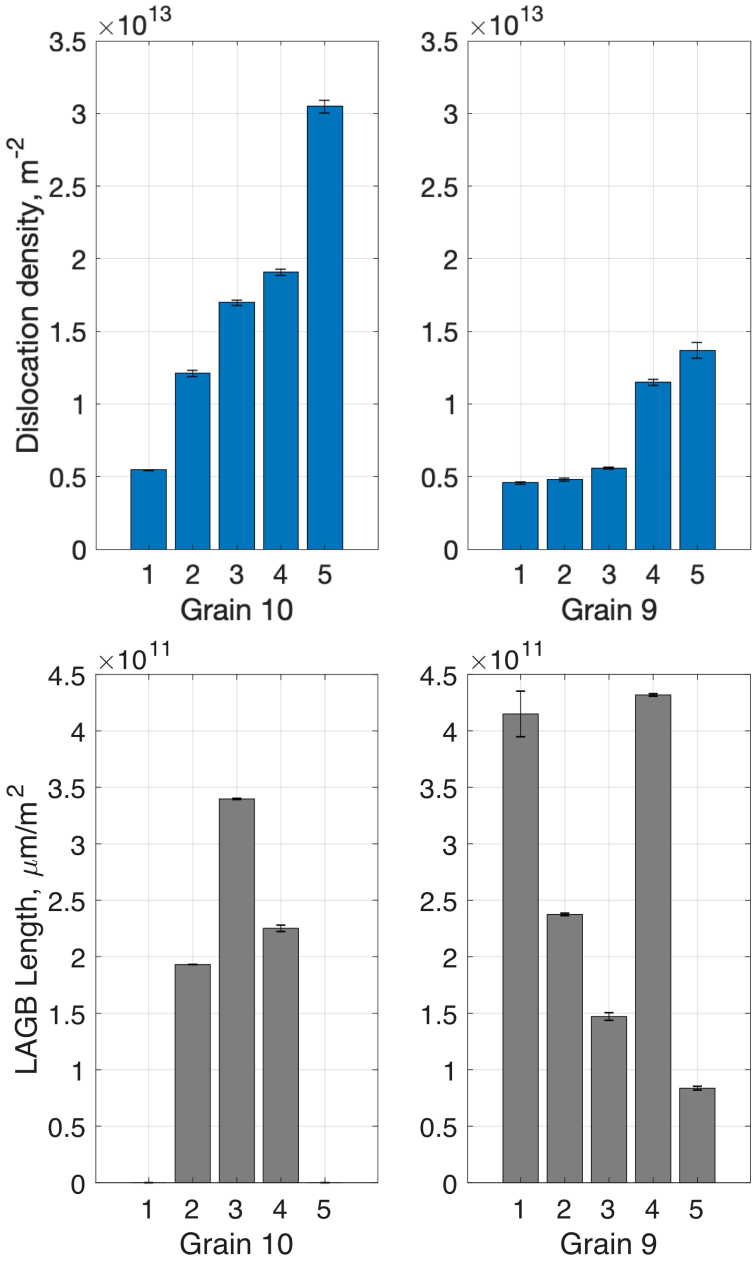

Figure 64. Bar-plots of dislocation density measurement from ECCI images (top) and LAGB length per area measured using ImageJ (bottom) in five regions. Two regions in grain 10 contain no visible LAGBs. Grain 10 has a higher density of dislocations and a shorter LAGB length. Details of dislocation density and LAGB length measurements are presented in APPENDIX B.

LAGBs were observed in regions near the HAGB after 5% strain in Figure 63. During the deformation, dislocations were generated and organized to form low-energy dislocation walls, or LAGBs. Comparison of BSE images of the same region in Grain 9 near the HAGB-LAGB

junction before (Figure 65a) and after (Figure 65b) the deformation clearly showed the trend of subgrain development. Dislocation slip during plastic deformation leads to crystal rotation, and hence, local crystal orientation changes leading to local misorientation, which can be measured using EBSD analysis. The GROD angle maps before (Figure 65c) and after (Figure 65d) deformation show a lower orientation deviation after deformation, suggesting that the dislocations could exit the sample or accumulate in LAGBs after deformation. GROD axis maps (Figure 65e and f) suggest that local regions rotate about particular rotation axes during deformation, consistent with subgrain development observed in Figure 65b. The LAGB marked in Figure 65d and f existed before deformation, and should not be confused with the developed LAGBs (with smaller misorientations) near the HAGB (Figure 65b).

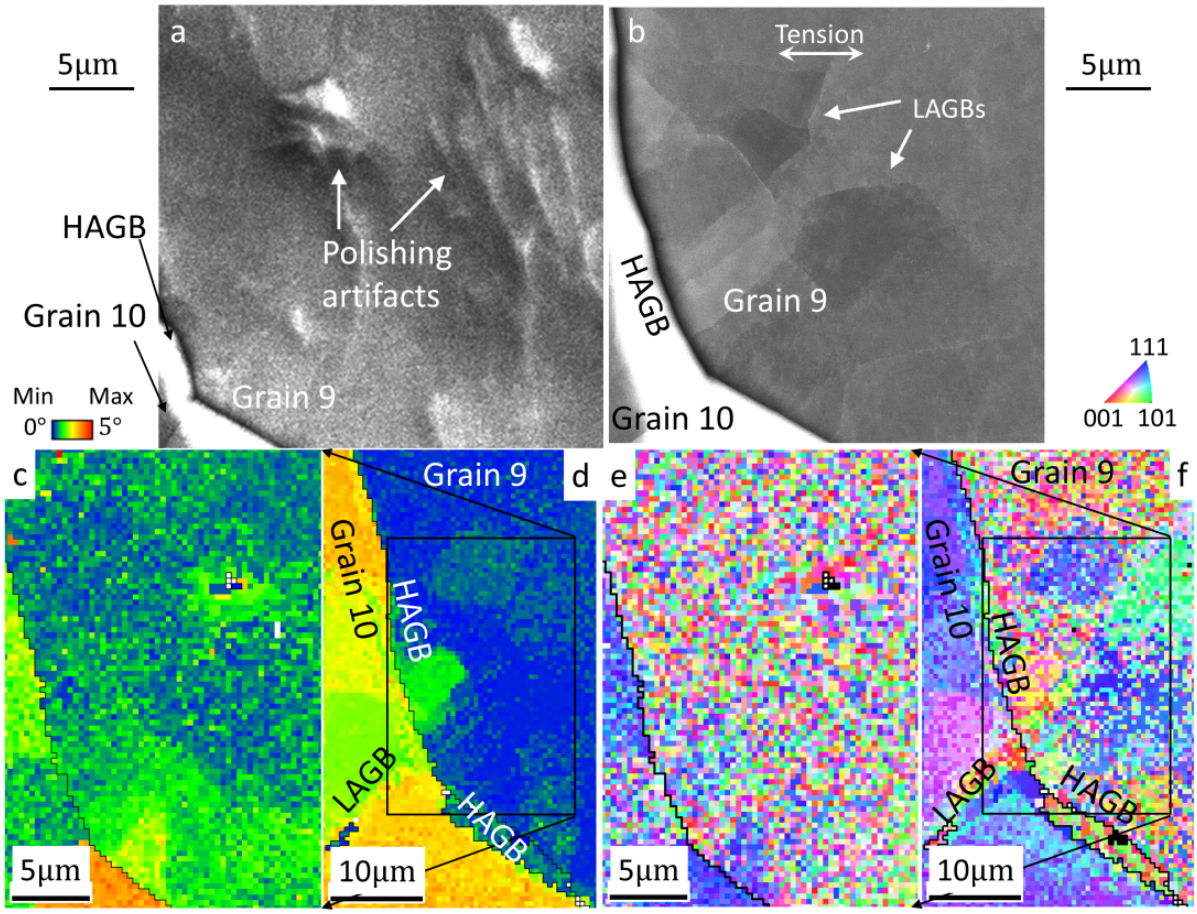

Figure 65. NX10-9HT BSE images of the same region before (a) and after (b) deformation show a trend of subgrain development; GROD angle maps before (c) and after (d) deformation show distinct regions with specific orientations and sharper boundaries after deformation; GROD axis maps after (f) deformation also show regions with distinct misorientation axes that were not observed before (e) deformation.

The bottom surface of deformed NX10-9HT was also observed and the BSE image and EBSD maps are shown in Figure 66, where the HAGB and pre-existing LAGB can still be observed and consistent with the top surface (Figure 65). The surface topography in the BSE image was caused by a 150 µm chemical polishing to improve surface quality for imaging. The IPF+IQ map shows the LAGB (white line) in Grain 10 and many small subgrains near the HAGB that divides Grain 10 and Grain 9. The KAM map shows the pre-existing LAGB in Grain 10 with about a 4° misorientation along with many short LAGBs that later developed near the HAGB in both grains. There was also a region in Grain 9 with higher KAM about 20 µm to the right of the

HAGB, indicating high dislocation content. The GROD-axis map clearly shows particular regions having different rotation axes (regions with different colors), suggesting the development of subgrains, consistent with observations on the top surface (Figure 65).

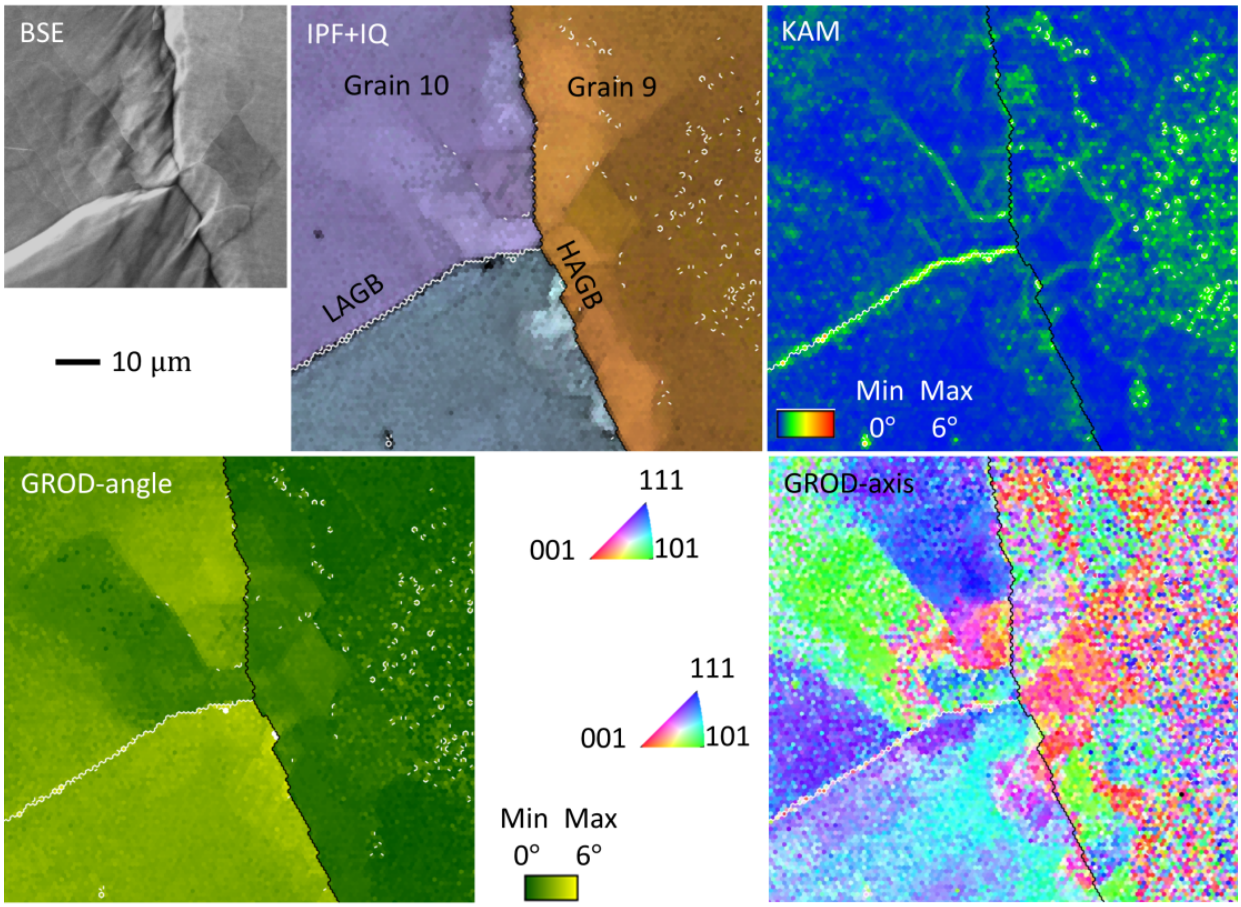

Figure 66. NX10-9HT (deformed) BSE image and EBSD scans of the bottom surface (~1.5 mm beneath) of approximately the same area shown in Figure 65. The EBSD maps were flipped to provide a consistent view with the maps in Figure 65.

3. TD3-0 and TD0-7: EBSD analysis before and after deformation

a. Sample TD3-0

EBSD analysis was performed on Sample TD3-0 (both grains in hard orientations), before and after the 5% tensile deformation, in the same three regions (scan area = 200 × 200 μm) along

the grain boundary. Figure 67 shows the favored slip systems in each grain (Column 1) and the KAM map before (Column 2) and after (Column 3) the 5% deformation for all three scanned areas.

The three slip systems with the highest Schmid factors are indicated for each grain using prisms that have slip planes (shaded) and Burgers vectors (turquoise lines) (Figure 67 Column 1). The highest Schmid factor is 0.40 for Grain 0 and 0.32 for Grain 3 (highlighted in red font). These favored slip systems are the same for all three scanned areas, with a slight change in the Schmid factors. For the KAM maps, the upper region (Figure 67 Row 1) showed no apparent change after deformation, while the center region (Row 2) showed a slight decrease of KAM in the right grain and an increase of KAM in the left grain. The lower region (Row 3) showed a slight decrease of KAM in both grains. Dislocations may exit the sample after the deformation, leading to a lower misorientation in the area.

To track the grain rotation after deformation, the average orientations (Euler angles) of Grain 0 and Grain 3 for all three regions (upper, center, and lower) are summarized in Table 11. The orientation change is calculated from the orientations (Euler angles) before and after deformation, as listed in Table 11. It shows that both grains had about the same 3-4° rotation after 5% deformation. Note that the samples were taken out from the SEM chamber for tensile deformation between EBSD scans of the same regions before and after the deformation, therefore, the orientation change of the same region could also be caused by mounting errors (1–2°). If so, then the two grains in Sample TD3-0 show little orientation rotation after deformation. This grain orientation rotation analysis, combined with the KAM maps that did not show significant changes after deformation, suggest uniform or lack of deformation in regions near the grain boundary for Sample TD3-0, with medium Schmid factor (m~0.4) in Grain 0 and low Schmid factor (m~0.32) in Grain 3.

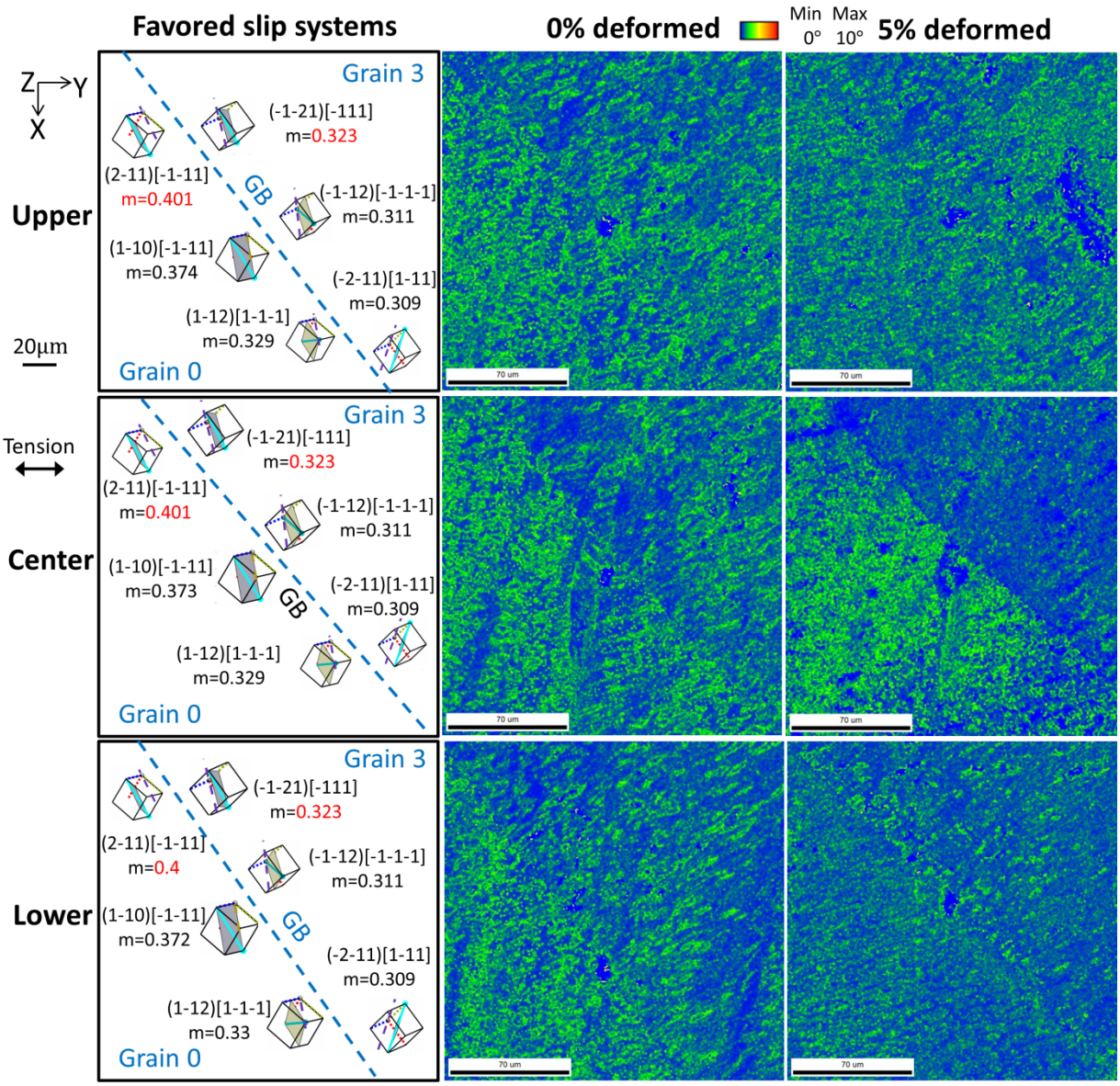

Figure 67. TD3-0 favored slip systems (Column 1) and KAM maps (Columns 2 and 3) of three locations (upper, center, and lower) along the grain boundary before and after 5% deformation. Three slip systems with the highest Schmid factors for each grain are indicated by the prisms with shaded planes and turquoise lines representing slip planes and Burgers vectors, respectively.

Table 11. Sample TD3-0 measured orientations of the upper, center, and lower regions (Figure 67) before and after deformation. (Orientation Euler angles in degrees).

	Grain #	Before deformation (°)	After deformation (°)	Orientation rotation (°)
Upper	Grain 0	(12, 34, 313)	(11, 36, 315)	3.3
	Grain 3	(24, 39, 16)	(22, 43, 20)	4.1
Center	Grain 0	(13, 34, 312)	(13, 36, 313)	3.1
	Grain 3	(24, 39, 16)	(25, 43, 17)	4.1
Lower	Grain 0	(13, 34, 311)	(13, 36, 315)	4.2
	Grain 3	(24, 39, 16)	(25, 41, 18)	3.3

b. Sample TD0-7

A similar EBSD analysis on Sample TD0-7 (with a hard orientation in Grain 0 and a soft orientation in Grain 7) was performed before and after the 5% deformation at three locations (scan area = 200×200 μm) near the grain boundary, and the KAM maps are shown in Figure 68 (second and third column). In contrast to Sample TD3-0, Sample TD0-7 showed significant changes in KAM values after deformation in all three locations observed. The KAM maps before deformation show a slightly higher KAM in the left grain. After deformation, there was a large increase in the KAM in both grains, yet the right grain showed a narrow band of low KAM several microns away from the grain boundary, where there was a higher value of KAM, suggesting heterogeneous deformation near the grain boundary. The indentation used as a landmark was visible in the KAM maps and appeared to affect the local misorientations during the deformation.

Schmid factor analysis shows the favored slip systems for each grain (Figure 68 Column 1). The highest Schmid factor of Grain 0 is 0.33, while the highest Schmid factor in Grain 7 is 0.49. Because Grain 7 is in a soft orientation, it underwent a larger amount of deformation, which is consistent with the more significant changes in the KAM maps of Grain 7. The grain orientation rotation analysis is shown in Table 12, where there is a larger orientation change in Grain 7, consistent with it being softer.

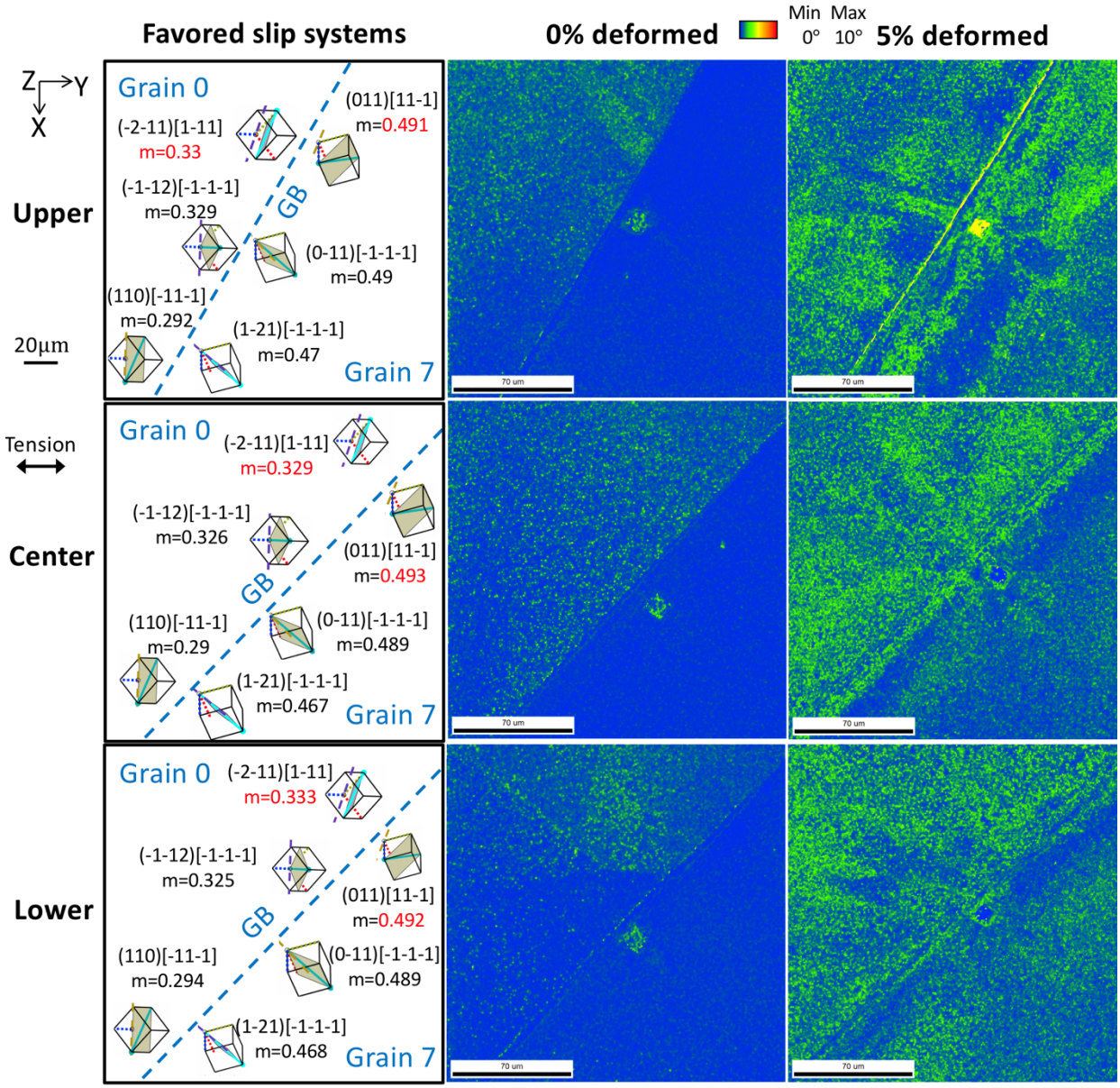

Figure 68. TD0-7 favored slip systems (Column 1) and KAM maps (Columns 2 and 3) of three locations (upper, center, and lower) along the grain boundary before and after 5% deformation. Three slip systems with the highest Schmid factors for each grain are indicated by the prisms. Grain 7, with a soft orientation, shows more significant changes in KAM maps.

Table 12. Sample TD0-7 measured orientations and crystal rotations of the upper, center, and lower regions (Figure 68) before and after deformation. (Orientation Euler angles in degrees).

	Grain #	Before deformation (°)	After deformation (°)	Orientation rotation (°)
Upper	Grain 0	(358, 34, 45)	(359, 35, 45)	0.7
	Grain 7	(90, 40, 289)	(97, 40, 288)	6.1
Center	Grain 0	(359, 34, 45)	(358, 36, 47)	2.1

Table 12 (cont'd)

	Grain 7	(91, 40, 289)	(97, 40, 287)	5.2
Lower	Grain 0	(358, 34, 45)	(357, 35, 47)	1.9
	Grain 7	(91, 40, 288)	(95, 40, 288)	4.0

4. TD3-4 and TD5-0: MO and ECCI results

a. TD3-4

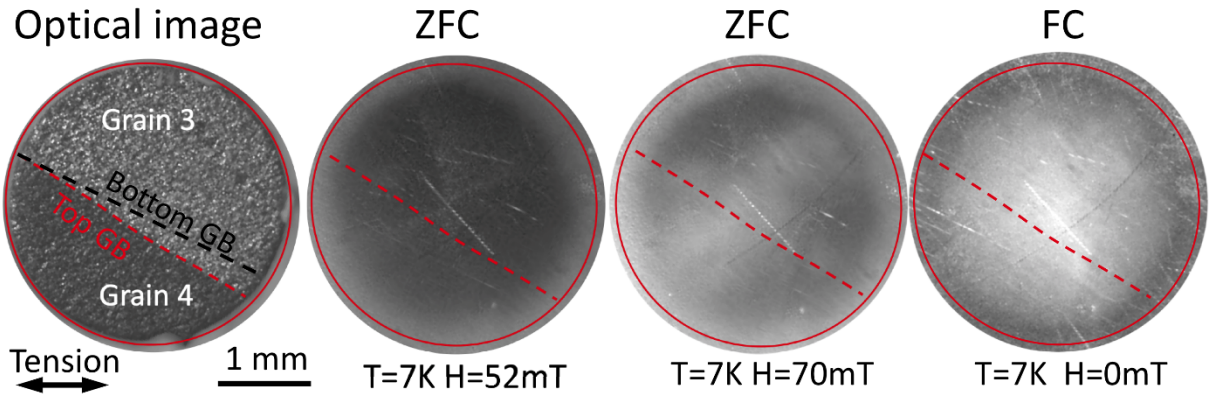

Figure 69. Optical image and MO images of deformed Sample TD3-4 MO, which showed no preferential grain boundary flux penetration.

Figure 69 shows the optical image, ZFC and FC MO images of the MO sample extracted from 5% deformed TD3-4. The ZFC images show central flux penetration, with no GB flux penetration observed. There was no obvious difference in flux penetration in the two grains. The FC image shows similar patterns of flux trapping in the center of the sample. The grain boundary of TD3-4 is a low angle grain boundary, with a misorientation of 11° and GB tilt of 0–13° (Table 3).

EBSD analysis was performed on TD3-4 after deformation and the results are shown in Figure 70. A step size of 0.1 μm was used to reveal details of the orientation gradient. The IPF map shows very uniform orientation in both grains, and the LAGB is marked using a white line. KAM maps show uniform misorientations in the two grains. The EBSD analysis suggests uniform

deformation in the two grains, both of which have soft orientations (Table 3). Sample TD3-4 showed the lowest yield strength (22 MPa) and hardening in tensile tests, as shown in Figure 55.

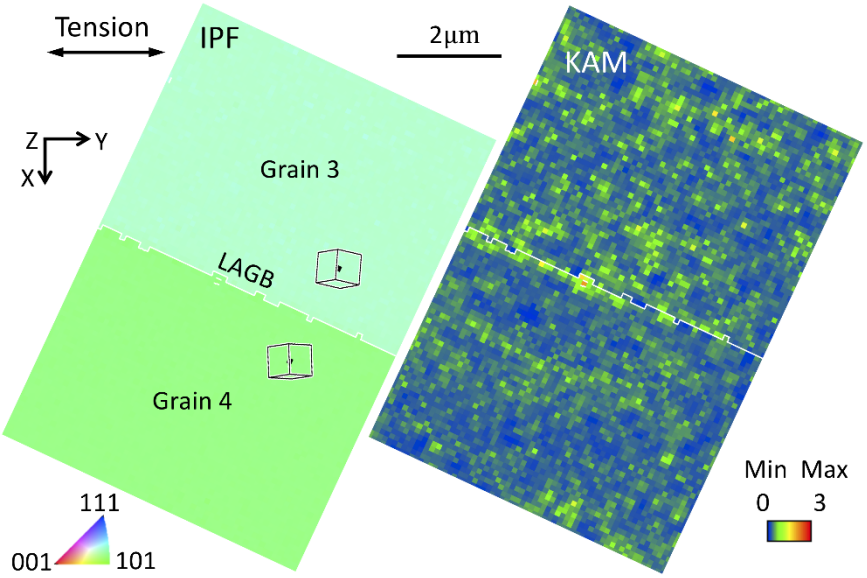

Figure 70. Sample TD3-4 IPF and KAM maps from an EBSD scan with a step size of 0.1 µm after deformation show uniform orientation in both grains.

Figure 71 shows ECC images for Grain 3 (left) and Grain 4 (right) after deformation. Individual dislocations in the LAGB can be observed. Grain 3 appeared to have a higher density of dislocations. However, this could not be substantiated from the limited number of ECCI observations.

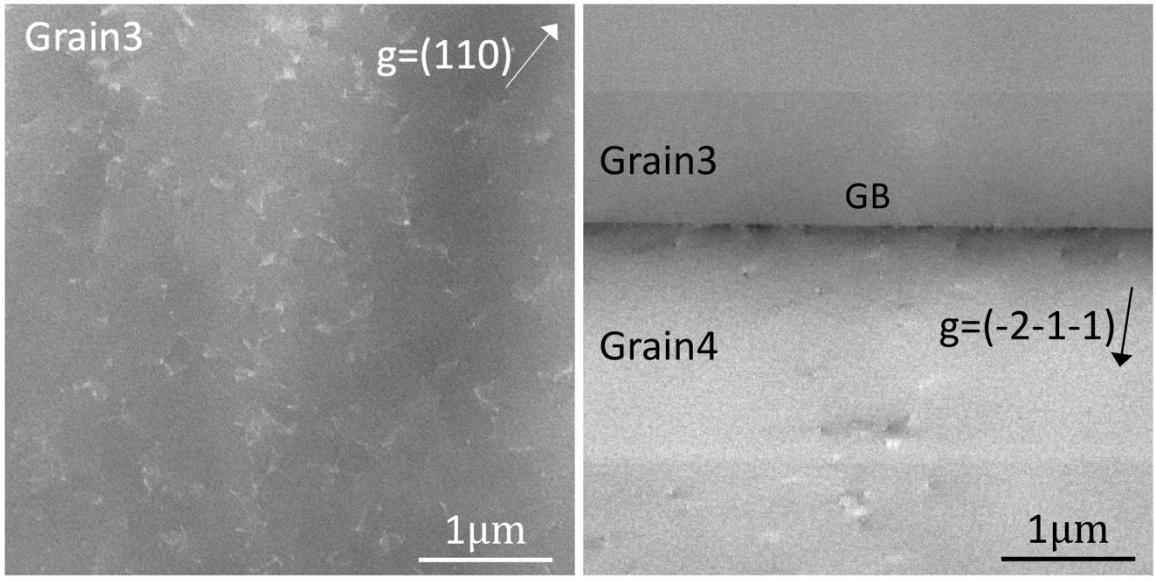

Figure 71. Representative ECC images of Grain 3 with $\boldsymbol{g}$ = (110) and Grain 4 with $\boldsymbol{g}$ = (-2-1-1) after deformation of TD3-4. Grain 3 appeared to have a higher dislocation density than Grain 4. However, more data are needed to be conclusive about the dislocation density difference in the two grains.

b. TD5-0

Sample TD5-0 has a grain boundary with a 36° misorientation and 0–4° GB tilt angle. Figure 72 shows the MO imaging results of the MO sample extracted from the deformed Sample TD5-0. The red dashed line and the red circle represent the grain boundary and the edge of the MO sample, respectively. The ZFC MO images show central flux penetration starting at T = 7 K, H = 40 mT, and the center was completely penetrated at T = 7 K, H = 48 mT, without any observed difference in the penetration in the two grains. While the FC image in Figure 72 shows slightly more trapped flux in Grain 5.

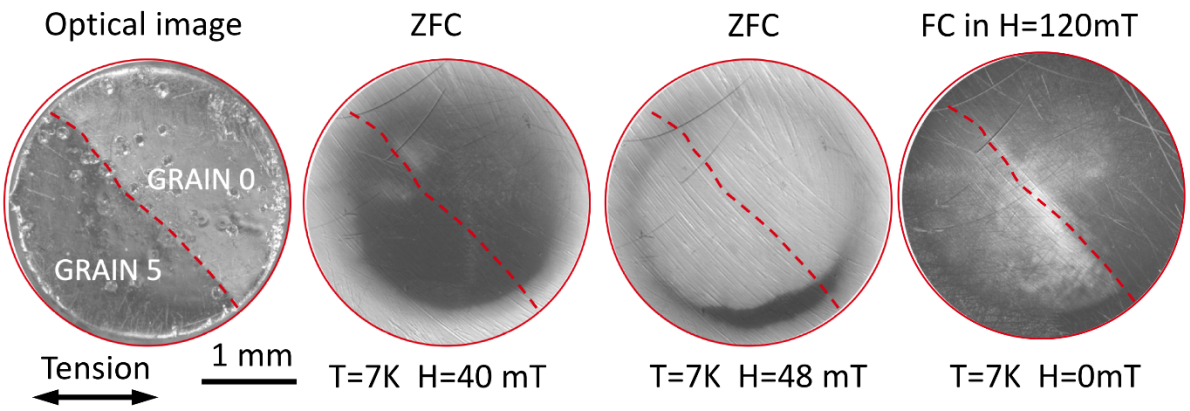

Figure 72. Optical image and ZFC MO images of deformed Sample TD5-0 at $T = 7$ K, $H = 40$ mT and 48 mT and FC MO image at $T = 7$ K, $H = 0$ mT.

Sample TD5-0 was deformed to 13% engineering strain by accident (instead of 5% strain). The deformed sample is shown in Figure 73. The red circle indicates the location of the grain boundary, which is also where the MO sample was extracted. The side view (Figure 73b) clearly showed more deformation in Grain 5 than in Grain 0, corresponding to more trapped flux in Grain 5 (FC image in Figure 72).

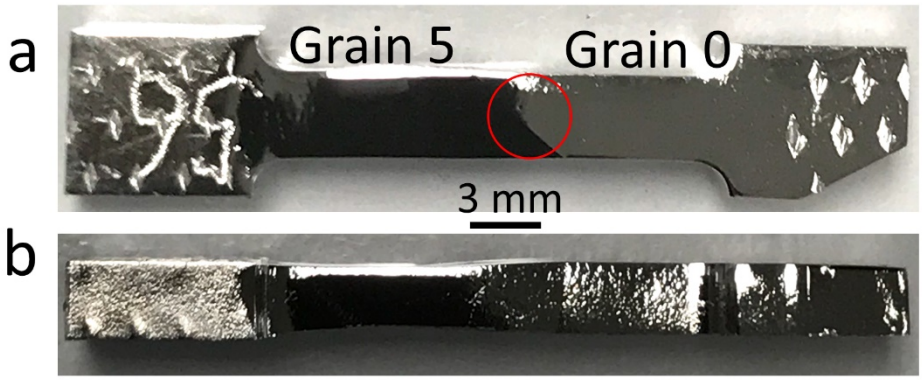

Figure 73. Top view (a) and side view (b) of Sample TD5-0 after it was accidentally deformed to ~13% engineering strain show more deformation in Grain 5. The red circle indicates the location of the grain boundary and the location of the MO sample extraction.

C. Discussion

1. Cold work and flux trapping

Cold work is heavily involved in the fabrication process of Nb cavities and the understanding of its effect on magnetic flux trapping in Nb is desirable.

Deformed Sample NX6-10AE showed more trapped flux in Grain 6 (Figure 56), which appeared to have a higher dislocation density than Grain 10 according to the ECCI analysis. The MO imaging of deformed NX10-9HT clearly showed more trapped flux in Grain 10 (Figure 62), which had a higher density of dislocations than Grain 9. NX10-9HT also showed sub-grain development in areas near the grain boundary (Figure 65 and Figure 66). Similarly, TD5-0 showed slightly more trapped flux in Grain 5 (Figure 72), which experienced a larger amount of deformation than Grain 0, as shown in Figure 73. All these results suggest that cold work, which causes dislocation multiplication and substructure development, increases magnetic flux trapping.

Posen [24], [25] examined how cold work and dislocations affect flux trapping and expulsion in SRF grade Nb. He found that high-temperature heat treatment (900–1000 ℃) could significantly improve the flux expulsion property of Nb due to the reduction of grain boundaries and dislocations [24]. In another study [25], two single-cell Nb cavities were fabricated from rolled (more deformed) and as-received (less deformed) Nb sheets. The magnetic flux trapping measurements suggested that the cavity made from the rolled Nb sheet showed nearly full flux trapping, while the cavity made from the as-received Nb sheet showed much less flux trapping. The results from this chapter are consistent with Posen's findings.

Although three of the five MO imaged bicrystal samples showed different trapped flux in the two adjacent grains, deformed Sample NX10-9AE (Figure 61) and Sample TD3-4 (Figure 69) showed no difference in flux penetration/trapping in the two adjacent grains, possibly due to the

uniform deformation in the two adjacent grains of both samples. This suggests that uniformly distributed dislocations are not as effective as organized dislocation substructures in trapping flux. The results of MO imaging of the five bicrystal samples are summarized in Table 13

Table 13. The flux trapping behavior and amount of deformation of the five MO imaged bicrystal Nb samples.

Sample ID	Flux trapping behavior	Amount of deformation
NX6-10AE	More trapping in Grain 6	Higher dislocation density in Grain 6
NX10-9AE	Central flux pepentration	Uniform deformation
NX10-9HT	More trapping in Grain 10	Higher dislocation density in Grain 10
TD3-4	Central flux penetration	Uniform deformation
TD5-0	More trapping in Grain 5	More deformation in Grain 5

2. Effect of 800 ℃ 2-hour heat treatment

The Samples NX6-10AE, NX6-10HT, NX10-9AE, and NX10-9HT were used to evaluate the effect of the 800 ℃ pre-heat treatment on the deformation behavior in 5% strained bicrystal Nb. ECCI analysis of the heat treated NX6-10HT before deformation showed pre-existing dislocations and LAGBs that were not removed by the heat treatment (Figure 58), while the after deformation ECCI analysis showed a trend of subgrain development and heterogeneous deformation in areas near the grain boundary, as shown in Figure 59 and Figure 60. This subgrain development was not observed in ECCI analysis of the as-extracted sample NX6-10AE. It is surprising to note that the heat treated sample NX6-10HT showed a higher yield strength (32 MPa) and hardening in the tensile test than the as-extracted Sample NX6-10AE (26 MPa) (Figure 55). As subgrain boundaries provide barriers to dislocations, it is possible that anneal led to the generation of stable low angle boundaries in Sample NX6-10HT.

The heat-treated sample NX10-9HT showed a lower yield strength (28 MPa) than as-extracted Sample NX10-9AE (33 MPa), possibly due to the reduced pre-existing dislocations

during the 800 ℃ heat treatment. Similar to NX6-10HT, NX10-9HT also showed the development of subgrains after deformation in the areas near the pre-existing LAGB-HAGB junction, as shown in the EBSD maps of both the top and bottom surface in Figure 65 and Figure 66. In contrast, no LAGBs or subgrains were observed in the as-extracted samples (NX6-10AE and NX10-9AE). This suggests that the development of subgrains during deformation is possibly related to the 800 ℃ heat treatment.

3. Effect of 600 ℃ 10-hour heat treatment

A 600 ℃ heat treatment was performed for all MO samples before cooling down for MO imaging, such that the hydrogen can be mostly removed from the bulk. No hydride scars were observed on the sample surface after the cryogenic MO cycle, suggesting that hydrogen concentration was significantly reduced. The 600 ℃ heat treatment prevents formation of hydrides in grain boundaries of cavities.

The undeformed bicrystals discussed in Chapter VI show obvious preferential flux penetration along the hydrogen contaminated grain boundaries (Figure 44 and Figure 49). However, in this chapter, without hydride precipitation, no grain boundary related flux penetration was observed in the five MO imaged samples. This provides more evidence that intrinsic characteristics of grain boundaries possibly do not have a substantial effect on flux trapping as significant as hydrides and dislocations do. Instead, hydrides may be the major contributor to flux trapping.

4. Deformation behavior of bicrystal Nb

The strategy of sample design in this chapter is to achieve focused deformation near the grain boundaries (NX6-10, NX10-9) or cause different orientation combinations (hardness) in

neighboring grains (TD3-0, TD0-7, TD3-4, and TD5-0) based on orientation and Schmid factor analysis.

Significant LAGB development and heterogeneous deformation near the grain boundaries were observed from ECCI and EBSD analysis of the deformed bicrystal Samples NX6-10HT (Figure 59and Figure 60) and NX10-9HT (Figure 65and Figure 66), which suggests focused shear near the grain boundaries and is consistent with the sample design of these two samples from the Ningxia Nb disk. However, direct observation of the effect of these LAGBs near the HAGBs on flux trapping was not achieved.

The stress-strain curves in Figure 55 showed that TD3-0 and TD0-7, with hard-hard and hard-soft orientation combinations, had the highest yield strength (43 MPa and 40 MPa) and hardening, while TD3-4, with soft-soft orientation combination, showed the lowest yield strength (22 MPa). This is consistent with the sample design of the TD Nb disk. These different combinations of orientation hardness led to different amounts of deformation in the two adjacent grains, which could be responsible for the different magnetic flux trapping in the two adjacent grains that was observed in NX6-10AE, NX10-9HT, and TD5-0.

D. Summary

The results suggest some correlations between the amount of cold work, development of dislocation substructure, and flux trapping in Nb. Samples with larger amounts of deformation or higher dislocation densities in the grain tend to cause more trapped flux than the adjacent grain. This conclusion is also supported by Posen's work on the effect of dislocations and cold work on flux repulsion properties of Nb cavities. Uniformly distributed dislocations probably do not trap flux as effectively as organized dislocation substructures, such as LAGBs.

Significant development of LAGBs near grain boundaries in the previously heat treated samples suggests that focused deformation occurred near grain boundaries; however, the effect of these LAGBs on flux trapping was not observed in the MO experiments. MO results from this chapter also provide evidence that grain boundaries probably do not play a significant role in flux penetration/trapping.

Chapter VIII. DISCUSSION

This chapter is an integrated discussion based on Chapters IV, V, VI, and VII to summarize the findings of the relationships between plastic deformation, dislocations, grain boundaries, hydrogen, heat treatment, cryogenic cycles, and flux trapping/penetration in high purity Nb single crystal and bicrystal samples. The five hypotheses proposed in Chapter II are evaluated in this discussion, and new hypotheses based on the overall results are proposed for future work.

Hypothesis 1: HAGBs are transport channels, while LAGBs and dislocation substructures are traps, for hydrogen.

Formation of normal conducting Nb hydrides during cryo-cooling causes a 12% volume increase and leads to deformation accommodation, hence hydride scars, in the Nb matrix [96], [148], [149]. Room temperature observation of hydride scars on the sample surface can indirectly reveal the distribution of hydrogen near grain boundaries, as well as the interaction of hydrogen with LAGBs and HAGBs. Hypothesis 1 can be supported by the evidence presented below.

Large hydride scars were observed at both LAGBs and HAGBs. In Chapter IV, hydride scars along LAGBs and within grains (Figure 28) and a 20–60 μm hydrogen depleted zone on either side of the LAGBs were observed after the MO cooling. These results suggest that the hydrogen atoms diffuse from the grain interiors towards the LAGBs, which could be segregation sites or traps for hydrogen, resulting in preferential precipitation of hydrides at LAGBs and hydride free zones near the LAGBs. In contrast, hydride scars observed on Sample II in Chapter VI showed decreasing sizes of hydride scars with the distance from the high angle grain boundary, suggesting that HAGBs are a source of hydrogen that diffuses into the grain, and HAGBs act as transport channels for hydrogen in Nb.

Hypothesis 2: Hydride precipitation may be favored at grain boundaries and dislocation substructures along specific crystallographic directions related to dislocation arrangements.

As shown in Chapter VI (Figure 46), hydride scars showed different morphologies in different grains, with similar shapes within the same grain. This indicates the morphologies of hydride precipitates is orientation dependent. Large hydrides were observed at both HAGBs and LAGBs on both the surface and the subsurface, suggesting grain boundaries are preferred hydride nucleation sites.

Dislocation observations within and near hydride scars in Chapter VI revealed an apparently higher dislocation density of hydride scars in Sample II with multiple MO cycles than in Sample I that experienced only one MO cycle. This suggests that hydrides formed in locations where previous hydrides had formed. If so, dislocation networks can act as nucleation sites for hydrides that can trap flux.

These results support the first half of Hypothesis 2, while the effect of dislocation arrangements is still unclear. Further study of the hydride nucleation and growth is needed to clarify the effect of dislocation arrangement on hydride formation.

Hypothesis 3: Hydrides and dislocation substructures (including LAGBs) are the main sources of flux trapping or premature flux penetration, while the effect of HAGBs on flux trapping/penetration is not as significant.

Hypothesis 3 can be supported by the results summarized below. Premature magnetic flux penetration and flux trapping indicate local suppression of superconductivity. Preferential flux penetration was observed at both LAGBs and HAGBs, but with different flux penetration behaviors.

In the deformed single crystal Nb sample discussed in Chapter IV, some LAGBs decorated with hydrides appeared to cause premature magnetic flux entry along the LAGBs, but hydrides

distributed within the grain interior did not cause any apparent flux penetration, as shown in Figure 30and Figure 31. This suggests that the combination of normal conducting hydrides and the dislocation substructures in LAGBs might be necessary to cause early flux entry. LAGBs combined with Nb hydrides locally reduce the superconducting order parameter, leading to the breakdown of the superconductivity at LAGBs. The 800 ℃ anneal removed most of the hydrogen, and the MO imaging showed significant restoration of the bulk superconductivity; however, LAGB weakness was still present after the anneal. A small amount of remaining hydrogen could not be removed by the heat treatment [16], resulting in nanometer scale hydrides that were beyond the resolution of MO imaging. These small hydrides could cause LAGB weakness after anneal.

For HAGBs studied in Chapter VI, MO imaging showed that only grain boundaries parallel to the magnetic field showed preferential flux penetration. This is consistent with the work done by Polyanskii [27]. The samples in Polyanskii's study were directly cut from a Nb slice and no heat treatment was done before MO imaging. Therefore, those samples were also contaminated with hydrogen, similar to the sample conditions in Chapter VI. While the samples in Polyanskii's work were only studied using MO without heat treatment, the current work studied the grain boundary flux penetration before and after heat treatment that removed most of the hydrogen in the samples.

Sample II (fork flux sample) in Chapter VI (Figure 25) showed preferential HAGB flux penetration; however, the fork flux penetration could be turned off by removing hydrogen, and then restored when hydrogen was reintroduced. This suggests that hydrogen is the enabling factor of the preferential HAGB flux penetration in Sample II, while the HAGB itself may not have as significant of an effect on flux penetration, except that HAGBs provide transport paths for hydrogen. In hydrogen contaminated samples the HAGBs contain hydrogen that can precipitate

during cooldown, and hence, become susceptible to early flux entry or retained trapped flux. This is supported by MO studies in Chapter VII, where samples heat treated to remove hydrogen did not cause apparent HAGB related flux penetration.

Hypothesis 4: Patterns of flux penetration are related to the arrangements of dislocation substructures.

The sample designs based on Schmid factor analysis were used to deform single crystal samples to introduce dislocations with different orientations with respect to the surface; however, the effect on flux penetration/trapping was not evident in the MO observations in Chapter IV. Further study using higher resolution magnetic flux characterization methods is necessary to answer this question.

Hypothesis 5: The amount of trapped flux is proportional to the density of dislocations in cold worked Nb samples. Compared with randomly distributed dislocations, more organized dislocation substructures (such as LAGBs) are more effective at trapping magnetic flux.

Dislocations are pinning centers for magnetic flux due to the elastic energy interaction between a dislocation and a flux line. This was supported by the results in Chapter VII, where a strategic design was made based on crystal orientation analysis and Schmid factor calculation to deform the samples so that dislocations with desired arrangements could be introduced. MO and ECCI analyses suggested that samples with a larger amount of deformation or a higher dislocation density cause more trapped flux. There was evidence that uniformly distributed random dislocations were less effective at trapping flux than organized dislocation substructures (LAGBs).

Heterogeneous deformation and significant LAGB development near the grain boundaries were observed in both NX6-10HT (Figure 60) and NX10-9HT (Figure 66). The effect of these observed dislocation substructures on magnetic flux behavior was sought, but no apparent correlation could be found in the current study, except for sample NX10-9HT that showed a larger

length of LAGB trace in grain 9 that had less trapped flux, compared with the adjacent grain 10 (Figure 64). Due to the resolution limitation of MO imaging technique, the effect of dislocation orientation with respect to the applied field on flux penetration was not examined in the MO study of the deformed single crystals in Chapter IV.

New hypotheses

Based on the results of this work and the evaluation of the five hypotheses, new hypotheses can be proposed for future work. They are summarized below.

1. LAGBs are worse than HAGBs. HAGBs may not favor hydride nucleation that traps flux as much as LAGBs do. The random structure of HAGBs may not be as likely to provide favorable hydride nucleation sites as a network of dislocations (LAGBs) with repetitive defect structures that may provide a larger critical size for hydride nucleation.

2. Random dislocations are worse than LAGBs. Sample NX10-9HT was deformed and annealed. It showed a larger amount of trapped flux in grain 10, which has a higher dislocation density and a shorter length of LAGB trace, than grain 9 with a lower dislocation density and longer length of LAGB trace. This suggests the possibility that trapped flux is more dominated by random dislocations than organized dislocations (LAGBs), although this contradicts Hypothesis 5. This could be a path to follow for future work to further understand the difference between free dislocations and organized dislocations.

3. Recrystallization is an effective way to remove dislocations and LAGBs, which were found to facilitate hydride nucleation and premature flux penetration. If so,

recrystallized samples should be less sensitive to hydride contamination and flux trapping. Future work can examine if recrystallization processing leads to less trapped flux.

Chapter IX. CONCLUSION AND FUTURE WORK

A. Conclusion

Previous studies on flux trapping in Nb either did not control hydrogen contamination or did not use characterization methods that can resolve spatial distribution of flux trapping and dislocations. In the current work, both ECCI and MO imaging were used to achieve direct observation of dislocations and flux trapping in Nb samples. Heat treatments were used to control the hydrogen content, and Schmid factor analysis was performed to choose tensile axes to introduce dislocations with special arrangements.

Hydrogen contamination is detrimental to Nb cavity performance and should be strictly controlled by pre-cooling heat treatment to remove hydrogen from the material. The interaction of hydrogen with LAGBs and HAGBs leads to preferential hydrides precipitation, which can cause flux penetration and trapping. HAGBs act as transport channels for hydrogen, which tends to diffuse from HAGBs towards the grain interiors, while hydrogen atoms may diffuse from the grain interiors towards the LAGBs, which are hydrogen traps. The diffusion of hydrogen from grain interiors to LAGBs leads to preferential hydride precipitation at LAGBs and hydride free zones near the LAGB. On the other hand, HAGBs act as hydrogen sources, which is consistent with decreasing hydride sizes with distance from the HAGB.

Both low angle and high angle grain boundaries can show preferential flux penetration and trapping when contaminated with hydrogen, but the two have different effects on flux penetration/trapping. The dislocation substructures in LAGBs, combined with hydrides, reduce superconducting order parameter and cause local suppression of superconducting, resulting in flux penetration. The LAGB related flux trapping was still present after the heat treatment that removed most of the hydrogen contamination. By contrast, the flux penetration at a HAGB can be turned

off by removing hydrogen and then restored by reintroducing hydrogen. This suggests that it is the hydrides in the HAGB that cause the flux penetration, while the intrinsic characteristics of the HAGBs may not have a significant influence on flux penetration.

There is some correlation between cold work and the flux trapping in SRF grade Nb. Larger amounts of deformation or higher dislocation densities in a grain tend to cause more trapped flux than in an adjacent grain with fewer dislocations. The effect of dislocation orientation, with respect to the applied field, on flux penetration, however, was not observed in the MO experiments. Magnetic flux characterization methods with higher resolution and sensitivity are necessary to understand details of the effect of dislocation arrangements.

There is a high density (~$10^{12}\ m^{-2}$) of pre-existing dislocations in Nb ingot that were caused by the thermal strains during ingot cooling. Subsequent small (5%) plastic deformation leads to a significant development of subgrains, which are stable and cannot be removed by 800 ℃ anneal. Therefore, recrystallization processing needs to be considered to remove as many dislocations and LAGBs as possible to achieve high performance of Nb cavities.

B. Future work

Three of the deformed bicrystal samples (GB3-0, GB0-7, and GB6-10HT) are waiting to be measured using MO imaging. This work should be continued and finished so that the MO results can be compared with the microstructure characterization (EBSD and ECCI characterizations of these samples are already finished). This can provide more data, which can be used to evaluate the new hypothesis that LAGBs cause more damage than HAGBs in flux trapping.

Compression experiments of two single crystal Nb samples extracted from Ningxia Nb disk have started, and the EBSD measurements of three regions after 0%, 5%, 10%, 15%, and 20% compression were performed to track the orientation evolution with compression. The samples were sent to National High Magnetic Field Lab-Applied Superconductivity Center for magnetization measurements using a vibrating sample magnetometer (VSM) to study the effect of cold work on flux trapping. This work is still in progress and should be continued and finished. It can help explain how compression affects flux trapping in single crystal Nb.

Due to the resolution of MO imaging, there are still many open questions to be answered, such as the effect of dislocation arrangements and LAGBs on flux trapping, which cannot be resolved using MO imaging. Advanced methods should be explored to obtain a deeper understanding of the mechanism of flux trapping. Possible options include AC susceptibility, superconducting quantum interface device (SQUID), vibrating sample magnetometer (VSM), and magnetic writer probe to detect local flux in Nb. This can help understand whether random dislocations cause more damage than LAGBs.

Since recrystallization is an effective process the remove dislocations and LAGBs, studies of conditions leading to recrystallized Nb cavities should be performed in the future. Magnetic flux characterization needs to be performed to test if recrystallized samples trap less flux.

APPENDICES

APPENDIX A: Sample preparation for ECCI

1. Mechanical grinding and polishing

All Nb samples were extracted using electron discharge machining performed by technicians at the Department of Physics and Astronomy Machine Shop on campus.

The surfaces to be observed were then ground using sandpapers, in a sequence of Grit 600, 800, and 1200, for 2–6 minutes for each sandpaper, using a polishing machine. The samples were held by hand and a gentle pressure was applied to the samples while keeping the sample flat on the sample paper. Before moving to the next sandpaper with finer grit particles, the ground surface was observed under an optical microscope to make sure that all scratches were about the size of the grit particle size of the current sandpaper.

Mechanical polishing was then performed on cloth using 9 μm, 3 μm, and 1 μm diamond suspensions, followed by a final polishing using 0.05 μm OP-S (colloidal silica suspension). Each polishing step lasted about 5–10 minutes. The sample surface was then prepared using either electropolishing or chemical polishing to remove some surface material in order to remove the damaged layer.

2. Electropolishing

The procedures of electropolishing below were reproduced from procedures from Derek Baars (a former PhD student).

The setup of the electropolishing is summarized in Figure 74. 180 mL sulfuric acid and 20 mL hydrofluoric acid were mixed in a plastic bicker that was set into a metal bowl filled with methanol bath. Liquid nitrogen was added to the methanol bath to maintain a bath temperature of -30 ℃. This whole setup was placed on top of the plate of a stirrer, and a stir bar was used to stir the acid mixture gently. A tungsten rod covered with a Teflon mesh was used as the cathode, and a Nb sample was the anode with the surface to be observed facing the tungsten rod. The sample and the tungsten rod were submerged in the flowing acid mixture, and the polishing kept going for 8–10 minutes with a voltage of 15 V.

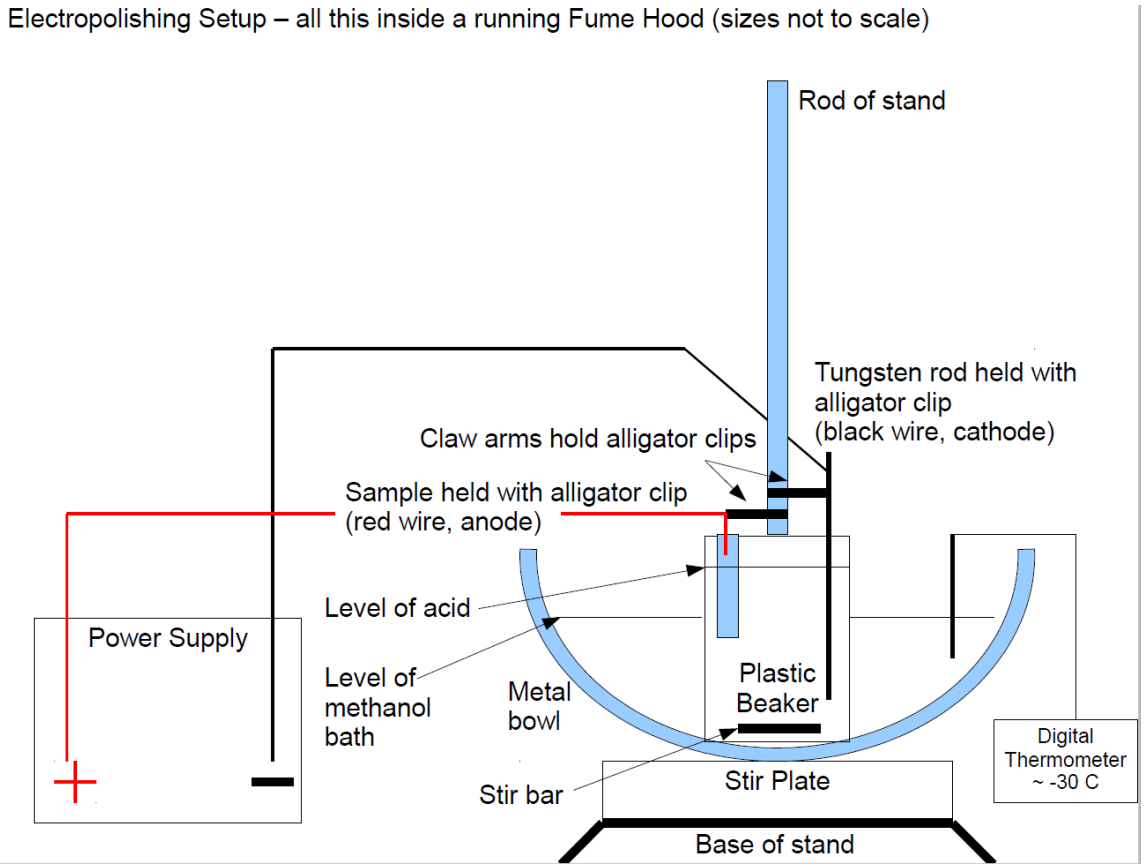

Figure 74. Setup of electropolishing. (after Derek Baars).

3. Chemical polishing

Chemical polishing was an alternative method to remove damaged surface material. The recipe is the same as buffered chemical polishing, consisting of one part of hydrofluoric acid, one part of sulfuric acid, and two parts of phosphoric acid. A plastic bicker containing the acid mixture was put on a stir plate, and a stir bar was used to gently stir the acid mixture. The Nb sample was submerged in the acid mixture for 5–15 minutes, surface to be observed facing against the flow direction of the acid mixture. Some samples with small dimensions (diameter < 3 mm, thickness < 1.5 mm) were directly dropped into the acid mixture. Finally, the sample was rinsed in methanol. A few etch pits would appear on the sample surface, but this did not affect ECCI observations.

APPENDIX B: Dislocation density measurement in sample NX10-9HT (Chapter VII)

Dislocation density was measured in five areas in each grain near the grain boundary of sample NX10-9HT. A correction factor of 1/cos(60◦) was multiplied by the measured dislocation density values, assuming that the dislocations were at random orientations. The results of dislocation density measurement of grain 10 and grain 9 are shown in Table 14 and Table 15. The ECCI images used for dislocation counting in grain 10 and grain 9 are shown in Figure 75 and Figure 76.

Table 14. Dislocation density measurement of grain 10.

Grain 10		**Grain 10 (geometry correction)**		
density(m^{-2})	standard deviation	density(m^{-2})	standard deviation	standard error
2.73E+12	3.24E+10	5.47E+12	6.48E+10	2.16E+10
6.05E+12	3.43E+11	1.21E+13	6.86E+11	2.29E+11
8.52E+12	2.82E+11	1.70E+13	5.64E+11	1.88E+11
9.56E+12	3.09E+11	1.91E+13	6.19E+11	2.06E+11
1.52E+13	6.70E+11	3.05E+13	1.34E+12	4.47E+11

Table 15. Dislocation measurement in grain 9.

Grain 9		**Grain 9 (geometry correction)**		
density(m^{-2})	standard deviation	density(m^{-2})	standard deviation	standard error
2.28E+12	1.41E+11	4.57E+12	2.83E+11	9.42E+10
2.40E+12	1.62E+11	4.79E+12	3.24E+11	1.08E+11
2.79E+12	8.58E+10	5.58E+12	1.72E+11	5.72E+10
5.77E+12	3.38E+11	1.15E+13	6.77E+11	2.26E+11
6.85E+12	8.27E+11	1.37E+13	1.65E+12	5.51E+11

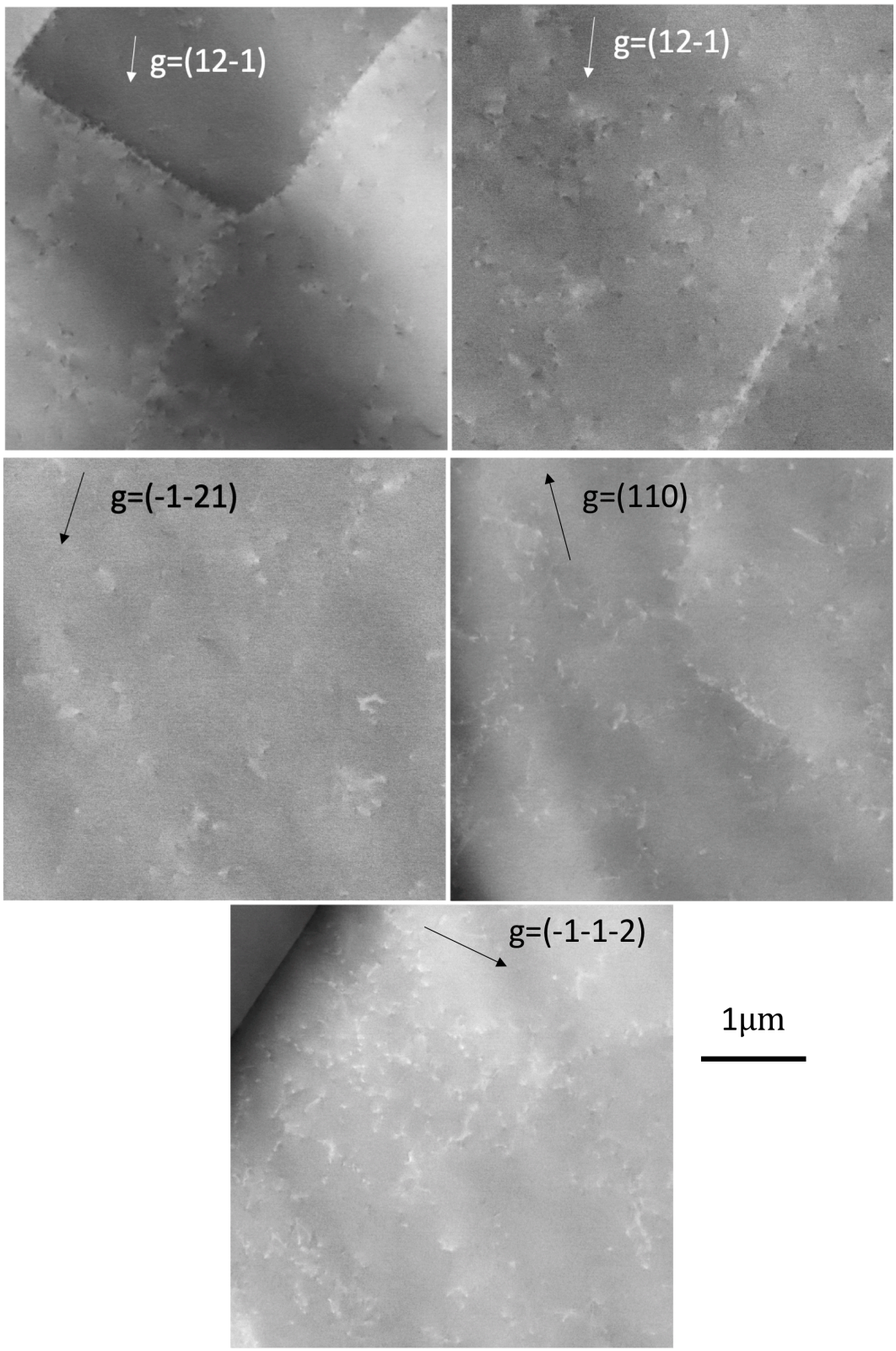

Figure 75. ECCI images of five regions in grain 10 for dislocation density measurement of sample NX10-9HT.

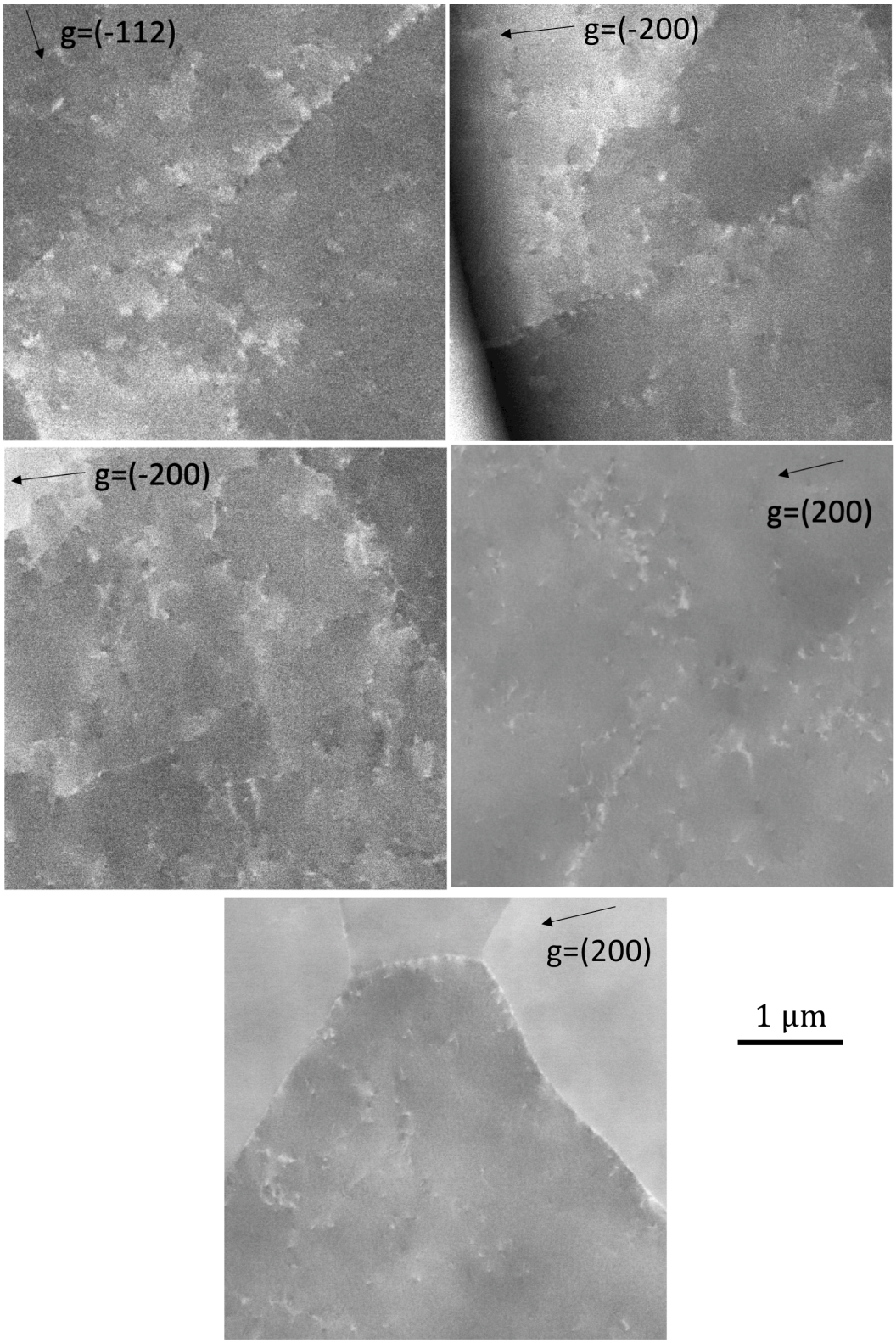

Figure 76. ECCI images of five regions in grain 9 for dislocation density measurement of sample NX10-9HT.

APPENDIX C: Published work on MO study of deformed single-crystal Nb samples

Mingmin Wang is the second author and contributed to much of the original work including the experimental and sample design, MO sample extraction, result analyses, and discussion.

Development of Low Angle Grain Boundaries in Lightly Deformed Superconducting Niobium and their influence on Hydride Distribution and Flux Perturbation

Z-H Sung[1*], M. Wang[2], A. A. Polyanskii[1], C. Santosh[1], S Balachandran[1], C. Compton[3], D. C. Larbalestier[1], T. R. Bieler[2], and P. J. Lee[1]

[1]National High Magnetic Field Laboratory-Applied Superconductivity Center, Tallahassee, FL, 32310

[2]Chemical Engineering and Materials Science, Michigan State University, East Lansing, MI, 48824

[3]Facility for Rare Isotope Beams, Michigan State University, East Lansing, MI, 48824

ABSTRACT: This study shows that low angle grain boundaries (LAGBs) can be created by small 5% strains in high purity (RRR ≥ 200) SRF-grade single crystalline niobium (Nb) and that these boundaries act as hydrogen traps as indicated by the distribution of niobium hydrides ($Nb_{1-x}H_x$). $Nb_{1-x}H_x$ is detrimental to superconducting radio frequency (SRF) Nb cavities due to its normal conducting properties at cavity operating temperatures. By designing a single crystal tensile sample extracted from a large grain (>5 cm) Nb ingot slice for preferred slip on one slip plane, LAGBs and dense dislocation boundaries developed. With chemical surface treatments following standard SRF cavity fabrication practice, $Nb_{1-x}H_x$ phases were densely precipitated at the LAGBs upon cryogenic cooling (8-10 K/min). Micro-crystallographic analysis confirmed heterogeneous hydride precipitation, which included significant hydrogen atom accumulation in LAGBs. Magneto-optical imaging (MOI) analysis showed that these sites can then act as sites for both premature flux penetration and eventually flux trapping. However, this hydrogen related degradation at LAGBs did not completely disappear even after a 800°C/2hrs anneal typically used for hydrogen removal in SRF Nb cavities. These findings suggest that hydride precipitation at a LAGB is facilitated by a non-equilibrium concentration of vacancy-hydrogen (H) complexes aided by mechanical deformation and the hydride phase interferes with the recovery process under 800°C annealing.

1. INTRODUCTION

Niobium (Nb) is the most well developed material for the fabrication of superconducting radio frequency (RF) cavities, which are the enabling core structures of linear particle accelerator such as SNS, CEBAF, FRIB, and Project X [1, 2]. The advantages of Nb derive from both its superconducting and mechanical properties. It has a relatively high lower critical field ($\mathbf{H}_{c1}$), which

allows RF magnetic fields up to 180-200 mT at 2 K [3], and is very ductile, which makes it easy to fabricate cavity shapes by a variety of techniques [1]. Achieving high accelerating gradients with a constant high quality factor, Q_0, (a measure of energy efficiency) while increasing accelerating fields ($\mathbf{H}_{RF} \approx$ 120-150mT) is a major goal for SRF cavity research. RF performance degradation, commonly known as 'Q-disease' and 'high field Q slope (HFQS)' are strongly related to surface contamination by oxygen (O) and hydrogen (H) [1, 4, 5, 6, 13, 20]. The presence of surface oxides and hydrides are inevitable with the final chemical treatment steps to produce a damage-free smooth surface after cavity shape fabrication. The two available surface treatments are electropolishing (EP) and buffered chemical polishing (BCP). The strong passivity of Nb leaves dense multilayers of oxide (Nb_2O_5-Nb_2O-NbO, ~ 2-3 nm thick) on the surface [7, 8, 9] and substantial uptake of hydrogen occurs in the bulk of SRF Nb during these chemical processes [4, 5].

To reduce the aforementioned RF performance degradation, heat treatments in two different temperature ranges under ultrahigh vacuum ($\geq 10^{-6}$ Torr) condition, ~100-120°C for 48h ("mild bake") and 600°C/10h - 800°C/2h ("anneal"), are effective. The former is for HFQS and the latter for 'Q-disease'. These heat treatments lead to; a) modification of the oxide layers [10, 11], b) reduction of hydrogen density from the bulk [12, 13], and c) reduction in the defect density introduced by the cavity forming process [14]. Of the surface oxides, the pentoxide (Nb_2O_5) is thought to be mainly responsible for the thermal breakdown of RF superconductivity due to its insulating (dielectric) property [4, 6], and the development of magnetic moments is also possible if there are oxygen vacancies [15]. During mild baking, the Nb_2O_5 layer decomposes and O diffuses into the Nb matrix so that the surface (~100 nm) is in the "dirty limit" condition [10]. However, an understanding of the influence of the mild bake thermal process on hydrogen and hydride formation and their effect on surface RF superconductivity is still not fully developed.

The ubiquitous presence, size, and high mobility of H leads to a Nb-H solid solution [17]. As the cavity is cooled down, the hydride phase ($Nb_{1-x}H_x$) precipitates from a super-saturated solution around 100-130 K [13, 17, 18]. Nb hydride leads to significant RF loss during the cavity operation since its critical superconducting temperature, $T_c \sim 1.5$ K, is lower than the cavity operation temperature of 2-4 K [6, 17]. Romanenko proposed that the 120°C bake significantly reduces hydride formation and correspondingly indicated a sharp reduction in the dislocation density [13] as well as reduction in near surface vacancy-H complexes [19]. In the Romanenko model, it is suggested that vacancy-H complexes are preferential hydride precipitation sources, and the 120°C bake reduces the numbers of vacancy complexes leading to dissociation of vacancy-H. Although the number of free H atoms are now increased they are not precipitated due to absence of favorable traps, and high hydrogen mobility in the Nb lattice. Elastic recoil detector experiments indicated that the hydrogen content does not vary with the range and time period of thermal treatments [20] and there may still remain the appearance of small size (< 100 nm) hydrides after heat treatments, which might be responsible for HFQS [20, 21]. Using a cryogenic laser confocal microscope, Barkov [18, 22] observed in-situ hydride formation on an SRF-grade Nb coupon whose surface was mechanically damaged with conventional mechanical polishing and chemical treated with BCP or EP. However, the hydride phase did not precipitate within the resolution of this technique (> ~ 120 nm) after 120°C /24h bake or 800°C /3h anneal treatment. Kim [23] and Tao [24] investigated regions in the vicinity of 'hot spots' (the areas identified by thermometry during cavity testing), using atom probe tomography in conjunction with cryogenic scanning transmission electron microscopy. This atomic scale study showed that hot spot regions have high

hydrogen content, and hydrogen atoms naturally accumulate at the interface between the surface oxide layer and the Nb metal matrix. This is consistent with the findings of secondary ion mass spectroscopy (SIMS) investigations [4, 25]. The dense Nb oxide phase is a protective layer that blocks transport of H into SRF Nb. This local enrichment of H atoms at the interface of Nb and Nb oxides leads to favorable conditions for hydride precipitation. Using cryogenic TEM, Trenikhina [26] also showed that the 120 °C bake can reduce the number of hydrides by ~40-50 % on an EP'ed cavity surface.

From these detailed studies, there is clear evidence of defect related hydride formation and RF performance improvement when "H" contamination is modified by thermal treatments. From a fundamental microstructure point of view, a determination of the interactions between commonly occurring defects and hydrogen is desirable in high purity Nb. The commonly occurring defects in bulk Nb that are relevant to changes in the surface superconducting properties are vacancies, dislocations, impurities, and low and high angle grain boundaries. Thus, understanding of the effect of plastic deformation of Nb on hydride precipitation is very relevant to development of better cavity processing techniques. Mechanical deformation for cavity shape fabrication causes dislocation multiplication [14], a non-equilibrium vacancy concentration [27], and formation of dense dislocation walls like planar grain boundaries or low angle grain boundaries (LAGBs) [28, 29]. It is well known that the core of dislocations is of concern because an "H" rich site (Cottrell cloud) [13, 30] and vacancies also facilitate the formation of hydrides [19, 20].

In this study, the dislocation content of a high purity SRF-grade Nb single crystal was increased in particular planes by applying 5% tensile strain to a selected single crystal SRF Nb coupon sample with a well characterized crystallographic orientation. The sample was then polished to provide a favorable environment for Nb hydride precipitation at planar defects such as dense dislocation walls or low angle grain boundaries (LAGBs). Magnetic flux behavior perturbed by local $Nb_{1-x}H_x$ segregation is evaluated using magneto-optical imaging (MOI) after the chemical treatment and a subsequent 800°C heat treatment. The presences of Nb hydride formation is observed by comparing surface topological features before and after the cryogenic cooling. Defects that might be favorable for hydride segregation were investigated using transmission electron microscopy (TEM) and electron backscattered diffraction (EBSD). This study seeks to help clarify the relationships between plastic deformation induced dislocations and hydride precipitation and their effect on superconductivity of SRF Nb.

2. EXPERIMENTAL DETAIL

2.1. SELECTION OF THE SAMPLE

An SRF-grade, high purity (RRR: residual resistivity ratio ≥ 200), large grain (grain diameter > 50 mm), niobium ingot slice fabricated by Tokyo Denkai using multiple electron beam melting (EBM) [31] was provided by FRIB for this study. The left optical image in Fig. 77 shows an overview of this Nb ingot slice, having ~ 10 single grains at the center and ~ 30 small grains along the circumference, with a diameter of 270 mm and a thickness of 3 mm. Surface normal orientations of the seven largest single grains were characterized by Laue X-ray diffraction and indexed using OrientExpress software [32]. The right color map in Fig. 77 shows the obtained crystal orientations and the cubic lattices orientation for each grain, based upon defining the Y axis as horizontal and Z out of the page.

The Schmid factor describes the likelihood of activating a slip system based upon uniaxial deformation and the crystal orientation. For uniaxial deformation, the value of the Schmid factor is between 0 and 0.5 (where 0.5 represents a soft orientation where the resolved shear stress on a slip system is as high as it can be) [14]. The direction of tensile strain was chosen to maximize activation of slip on a {112} plane. Using a MATLAB code [32, 33], the Schmid factors were computed based on the measured grain orientation (Bunge Euler angles φ_1, Φ, φ_2 = 167° 141° 108°). Figure 2 shows all possible Schmid factors for each of the 24 slip systems as a function of the first Euler angle. A rotation of the sample by 37.1° or rotating the tensile sample orientation 37.1° gives the $[1\bar{1}1]$ (121) and the $[1\bar{1}1]$ (110) slip systems their maximum Schmid factor (dashed red line). Thus, the sample was extracted using electrical discharge machining (EDM) with this extra 37.1° rotation, as illustrated in Fig. 77a.

The tensile sample was uni-axially strained to reach a level of 5 % strain. For magneto-optical imaging (MOI) analysis, each deformed sample was cut into four small pieces (3 × 3 × 1.5 mm), making tilted cuts to align dislocation Burgers vectors to be parallel or perpendicular to the sectioned surface (not shown in Fig. 78). The tilted cuts were determined so that the slip plane was parallel to the cut surface for the "left" samples (c & d), and so that the "right" samples (a & b) have the slip plane perpendicular to the surface. Thus, the dislocation Burgers vectors are perpendicular in these two different types of the sample surfaces. As screw dislocations are expected to predominate (due to their lower mobility than edge dislocations) then both edge and screw line directions are parallel to the surface in the "left" slices (c & d), and screw dislocations are perpendicular to the surface in the "right" slices (a & b). Thus, these samples were designed to examine how the magnetic field would interact with screw dislocations perpendicular to the magnetic field (left) or parallel to the magnetic field (right).

2.2. MAGNETO-OPTICAL IMAGING (MOI)

Magneto optical imaging (MOI) uses the strong Faraday effect in bismuth doped yttrium iron garnet (B-YIG) to measure the change of the vertical magnetic field component (H_z) above a superconducting sample using a standard polarized light microscope. The technique is able to resolve fields of the order of 1 mT with ~ 5-10 μm spatial resolution [34]. Three different MOI operation modes, ZFC (Zero Field Cooled), RF (Remnant Fielded), and FC (Field Cooled), were used to observe the local redistribution of the magnetic flux in these coupons, when cooled below the T_c of Nb ~ 9.2 K. ZFC MO imaging shows perturbation of the surface superconducting properties on the sample after cooling well below T_c and then applying an increasing external magnetic field until the sample is fully penetrated. For RF mode the procedure for ZFC is followed, but after the sample is significantly penetrated, the external magnetic field is removed so that magnitude and distribution of the remnant magnetic flux can be obtained. For FC mode MO imaging, the sample is cooled below T_c while in the presence of an externally applied magnetic field and then the external field is removed; this mode is more sensitive to the bulk superconducting properties because the field was fully penetrated. In this FC mode, normal conducting artifacts such as bulk defects, impurities, and grain boundaries are often visible as dark features because they are preferential routes for flux trapping. In this mode, a homogeneous defect-free square sample would exhibit a perfect "rooftop" pattern of diagonal bright lines crossing from the four corner.

2.3. MICROSTRUCTURE AND MICROCRYSTALLOGRAPHIC ANALYSIS

The microstructural properties of the selected 5% tensile deformed sample were characterized using a JEOL ARM 200F transmission electron microscope (TEM). TEM thin foils were prepared by slicing the remaining central part (triangle) of the deformed sample (Fig. 78) with a precision diamond saw so that the TEM sample normal was parallel to the tensile strain direction. Sliced samples were initially mechanical thinned to ~ 150-200 μm thickness by diamond lapping and then subsequently reduced to ~80-100 μm in central thickness by a dimple grinder. To observe pristine cold-work deformed structure, thinned specimen were finalized for electron transparency using a Struers Tenupol-5 Twin-Jet polishing system with a solution of 6-8 vol% H_2SO_4 in methanol. This electric jet polishing is preferred over the focused ion beam (FIB) technique in TEM sample preparation for observation of dislocation morphology in soft metals like Nb because the heavy Ga ions of the FIB can easily disturb the lattice structures of the soft metal surface, which leaves point defects on the TEM sample surface. Electron backscattered diffraction (EBSD) - orientation imaging microscopy (OIM) was used to characterize the micro-crystallographic features on the sample surface. The OIM was performed in a Zeiss 1540 EsB field emission scanning electron microscope (FESEM) equipped with an EDAX-Hikari high speed OIM camera. Using a 15 keV electron beam energy, we were able to scan the surface with a small (50-100 nm) step size which can identify the crystallographic orientation at a sub-micrometer-scale with a precision of better than 0.1 degree.

3. RESULTS

The 30 minute BCP revealed low angle grain boundaries (LAGBs: <1-5 degree) on the gently polished single crystal Nb samples, as shown in the optical images (top left) in Fig. 80 and Fig. 81, which have either screw dislocation lines out or in the viewing plane, respectively. These LAGBs were apparently produced during the 5 % tensile strain cold work deformation. Chemical polishing produced grooves at LAGBs that are similar to those typically produced at high angle grain boundaries (HAGBs > 15 degree). ZFC and RF mode MO images in Fig. 80 and Fig. 81 show magnetic flux behavior on the samples below the 9.2 K T_c of Nb. During MO imaging, external magnetic fields were applied normal to the sample surface, so that the activated dislocation slip plane was aligned parallel to the direction of the magnetic field. The external magnetic flux clearly penetrates into the LAGBs earlier than into the grains, as indicated by the red arrows in both images. Likewise, RF MO images show distinct contrast variations at LAGBs, as indicated by the blue arrows, which implies significant disturbance of circulating superconducting currents at LAGBs. However, not all LAGBs are responsible for this magnetic flux perturbation. Flux penetration occurs only on the upper part of the LAGB in Fig. 80, and only some LAGBs are involved in the flux penetration, as indicated by the blue and green dotted lines in Fig. 81. In addition, no distinguishable difference is found with regards to dislocation morphology. Since the cooling temperature and magnetic field were carefully chosen for optimum monochromatic contrasts for MO imaging, the difference in the amount of penetration from the edges between two samples might not directly implicate any difference in superconducting properties.

Bright field (BF) transmission electron microscope (TEM) images in Fig. 83 show the microstructure of the 5% deformed Nb samples having cell structures with dense dislocations walls. The cell block structure is typical of a metal with medium to high stacking fault energy after plastic

deformation [35]. A high density of dislocation networks is observed in planar boundaries, as indicated by the red arrows. These boundaries are low angle grain boundaries (LAGBs) due to their low lattice misorientation angle (< 1-5 degree) between cell blocks. The sketch depicting two dislocation sources on a (101) and a (121) plane on either side of a boundary shows how dislocation walls may develop between two sources. If they operate at unequal rates, the number of dislocations from each would lead to an accumulating misorientation. The inclination of dislocations walls would be 45º from the slip plane, as (nearly) opposite signed dislocations have stable positions that would lead to walls that are either parallel or perpendicular to the tensile axis, resulting in roughly square tubes of dislocation walls perpendicular to the Burgers vector and perpendicular to the tensile axis. A more detailed study is needed to precisely describe the dislocation substructure, but these images clearly show development of low angle boundaries consistent with Figs. 4-6.

To conduct the MOI analysis, the samples were cooled below the 9.2 K T_c of Nb at a rate of 8-10 K/min from ambient temperature under a ~10^{-2}-10^{-3} Torr vacuum. Figure 6 compares the surface morphological features of the samples before and after the cryogenic cooling. Many blister-like surface relief structures appeared on the surface after cooling. This topological change is consistent with the observation of a laser confocal microscopy study [18, 22], and these structures are attributed to hydride precipitations that occurred between T ~ 100-130 K. The hydrides are believed to be stable during MOI, but after MOI, when the sample temperature is ramped back up above the saturation temperature, the hydrides decompose and leave residual scars on the surface. Most interestingly, the hydride phases preferentially precipitate along the LAGBs in this sample, as indicated by the surface topography. Even some LAGBs that had not previously been identified from surface grooving after BCP were revealed by hydride precipitation. These topological features are more easily observed in the enlarged area images (the rightmost) of Fig. 82.

Micro-crystallographic structures at the vicinity of the LAGB where premature magnetic flux penetration occurred (Fig. 81, “left” sample, d) was characterized using FESEM/EBSD-OIM. An FESEM secondary electron image (Fig. 84b) shows further details of the hydride scars resulting from hydride segregation both along the LAGB and within the grains. Most interestingly, ~ 20-60 μm width of clean areas appeared at either side of the LAGB, as marked with the blue arrows, which suggests a strongly reduced hydride concentration or size in those areas. To further investigate these features, a local average misorientation map (Fig. 84c) is reconstructed based on the EBSD scan [36]. The map shows that the hydride scars are misoriented by 5-9º from the surrounding crystal. This is also consistent with the fact that hydride precipitates form as islands on the sample surface [19]. There appear to be two distinct sizes of the hydride scars, a 1 μm size closer to the LAGB and 10 μm features more than 50 μm away from the LAGB. Near the LAGB, there is no evidence of hydrides within 10 μm to left of the LAGB and 50 μm to the right of the LAGB. The shapes of the hydride scars suggest an orientation sensitivity to the distribution of hydrogen or hydride precipitates. A misorientation profile across a LAGB hydride scars is plotted in Fig. 84c and shows the intrinsic crystallographic misorientation features related to the hydride scars that we have observed. This plot also shows that the LAGB offset is only about 1/2°, *i.e.* at the angular resolution limit of our EBSD analysis. At the bottom of the map, a nearly horizontal boundary also has hydrides decorating the line, but the angle of misorientation decreases from right to left, such that the boundary misorientation is apparently too low to support hydride nucleation close to the vertical boundary.

To determine the effect of the standardized cavity thermal treatment on "H" contamination at LAGBs, the small Nb samples were annealed at 800°C for 2h under ultrahigh vacuum (10^{-6} Torr) after the first MO imaging analysis, and then re-analyzed using MOI. It is empirically known that 600°C for 10h or 800°C for 2-3h anneal can expel most of the H atoms from the bulk of SRF Nb [12, 22] and no additional micron sized hydride relief after temperature cycling of the annealed samples was observed. Figure 9 shows both ZFC and FC mode MO images of the two samples having different dislocation morphology (see Fig. 79) after 800°C annealing. The flux penetration into the samples is not markedly different, although local penetration is observed, as indicated by the red arrows, and this penetration is coincidently associated with the same vertical LAGB in the left (d) and right (b) samples observed prior to heat treatment. They appear to initially penetrate from the top surface rather than the edges. The penetrated regions also appear broader and additional locations are observed. The FC mode images also show some contrast changes for trapped magnetic flux at the "weak" LAGBs, marked by the blue arrows. However, similar to the initial MO imaging, not all of entire LAGBs are responsible for the magnetic flux perturbations, as represented with the small offset blue and green dotted lines. Contrary to the first MOI, a clear rooftop pattern contrast appears on the surface. This rooftop pattern is created when strong superconducting currents circulate in the bulk of the material. These results suggest that the 800°C anneal likely recovered most of bulk properties affected by H contamination, but was not fully effective at the LAGBs.

4. DISCUSSION

With precise evaluation of grain crystallographic orientation for the maximum shear stress, we were able to successfully induce the formation of low angle grain boundaries (LAGBs) in a high purity SRF-grade single crystalline niobium by applying only a 5% tensile deformation. Through buffer chemical polishing (BCP) following with hydrofluoric acid (HF) rinsing, significant hydrogen upload was demonstrated to occur, leading to favorable environments for Nb hydride ($Nb_{1-x}H_x$) segregation. Surface topological and microstructural analysis confirmed the appearance of preferential hydride precipitation along the LAGBs upon cryogenic cooling. MO imaging suggests that this LAGB segregation could be a contributor to premature magnetic flux penetration and magnetic flux trap, observed for some of the LAGBs. Subsequent annealing at 800°C/2h significantly changed the mode of flux perturbation but areas of weakness remained.

4.1. DEVELOPMENT OF LAGBS AT LOW TENSILE STRAIN IN NIOBIUM

The effect of strain on the microstructure of SRF Nb is important because mechanical deformation is used to form the cavity shapes and additional post-fabrication deformation is used to tune multi-cell cavities. Compared to other BCC metals, dislocations in pure Nb are stable because the interaction forces for driving dislocations in slip systems are small, and dislocation entanglements lead to much smaller internal stress [14]. Dislocation slip occurs when the resolved shear stress exceeds the critical resolved shear stress, which can be quantitatively estimated with Schmid factor [32]. In this study, a minimal cold work deformation of only 5% led to the formation of cell structure consisting of dislocations, as shown in the BF TEM images of Fig 7. In metallic deformation, such cell structures result from one of two mechanisms; dislocation accumulation between regions with different strain patterns or mutual trapping of dislocations into low energy

configuration [28]. These two different systems induce two different boundary conditions, i.e., geometrical necessary boundaries (GNBs) or incidental dislocation boundaries (IDBs), respectively. Dislocation slip with different strain patterns accommodates the lattice orientation, so that GNBs show a higher misorientation angle across the cell blocks, compared to the IDBs [28, 29]. To form these planar boundaries, external activation energy either by heat treatment or high cold work deformation (> 20%) is typically required to rearrange dislocations, especially in cavity grade Nb [33, 37]. However, this sample formed LAGBs with only 5% tensile deformation followed by BCP chemical treatment and hydride precipitates resulting from subsequent cryogenic cooling. Thus, it appears that preferentially activating one slip direction on two planes could lead to rearrangement of statistically stored dislocations into a low energy substructure as illustrated in Figure 7. Alternatively, pre-existing subgrain boundaries may have provided a site for accumulation of dislocations during the deformation. At this time, we cannot distinguish an already existing sub grain boundary from a newly created GNB during deformation from an analysis of misorientation angle [28]. It is also possible that Nb hydride phase formation or transformation during the cooling process might locally provide a driving force for creation of dislocation structure. Formation of β-phase hydride increases molar volume of Nb matrix by ~ 12 %, resulting in locally increased dislocation densities around hydride-Nb interface [38, 39].

However, to clarify these possible mechanisms for the formation of planar boundaries in a single crystal of Nb, multiple batches of samples having similar slip system would need to be deformed in strategically chosen orientations and would then need to be characterized by the same method, and identify the misorientation angle between cells using TEM diffraction analysis. The misorientation angle is a key parameter to understand the formation mechanism of LAGBs as well as homogeneity in mechanical deformation of a single grain. Heterogeneous deformation characteristics of single grain Nb has impeded efficient use of large grain Nb ingot slices to fabricate cavities; for example, bulging and irregularity of thickness after molding [14].

In the TEM study in Fig. 83, attempts to measure the misorientation angle between dislocation cell blocks was hampered by the high angled wedge shape of the thin foils, which restricted the available range of tilt. Thus, further TEM investigation will be following as a future work in conjunction with multiple sample batch study.

4.2. FLUX PERTURBATION AT LAGBS

The MOI investigations show that magnetic flux preferentially penetrates both low and high angle grain boundaries, and coupling this with the observation of preferential precipitation of hydrides at the same boundaries suggests a link between the two. Although hydride precipitates are also distributed across the grain interiors (see Fig. 82), they apparently did not have the same effect on flux-penetration as LAGBs in the MOI observation (see MO images in Fig. 80 and Fig. 81). Nb hydrides combined with dislocation networks locally reduce the superconducting order parameter and superconducting gap at LAGB, thereby leading to breakdown of superconductivity. Hydride precipitates at LAGBs also act as normal conductors to trap magnetic vortices while cooling down. Such trapped vortices are vibrated during RF operation of an SRF Nb cavity and this induces local heating. As a result, local thermal breakdown of RF superconductivity can occur on the surface [3, 40]. In this study, cooling rate was constant across T_c of Nb ~ 9.2K from the room temperature at a rate of 8-10 K/min, so there is probably no significant cooling rate related flux trapping effect on the MO imaging, as presented in Ref 40.

Even though many of the hydride scars are large enough to be within spatial resolution limits in the MOI technique, the observed MO contrast is dominated by the collective influence of the defects at the boundaries (our previous MO studies show that this contrast requires close alignment between the applied magnetic field and the boundary plane [41]). LAGBs in this study seem to be not planar boundaries having small misorientation against external magnetic field, thus more detailed study is needed to clarify why only some of LAGBs are highly responsible for the magnetic flux perturbations. However, because MO imaging reflects more of a bulk than surface condition and the extensive hydride formation occurs primarily on the surface, this study suggests that nanometer size (< 100 nm) hydride segregation at grain boundaries [20, 21] can cause a similar magnetic flux disturbance, leading to GB weakness [41, 42].

4.3. HYDRIDE DISTRIBUTION IN THE VICINITY OF LAGBS

EBSD micro-crystallographic analysis (see Fig. 84) shows that a hydrogen depleted zone of ~ 20-60 μm width emerged on either side of the LAGBs after cryogenic cooling. The local average misorientation map suggests that a substantial amount of hydrogens migration toward the boundary occurred during the cooling. According to grain boundary segregation models in metal alloys [43, 44], GB segregation is known to be the result of dragging solute atoms to the GB in the form of vacancy-complexes. When plastic deformation is applied, non-equilibrium vacancy concentrations can be produced in the metal by dragging jogs in screw dislocations. The supersaturated vacancies can interact with hydrogen atoms and create supersaturated vacancy-solute complexes. The propensity of vacancies to sink to the GB gives rise to non-equilibrium grain boundary segregation with the solute atoms [27]. The schematic in Fig. 86 illustrates a proposed mechanism of hydrogen transport to a LAGB due to vacancies: (a) at ambient condition, the equilibrium vacancy concentration exist in bulk Nb. (b) a tensile stress is applied, and the boundary is created by dislocation propagation and migration, with increased vacancy density. (c) with the boundary acting as a sink for vacancies, a non-equilibrium vacancy gradient and a concurrent transport of solute “H” atoms to the boundary occurs. (d) during cryogenic cooling, the H enriched complexes in the boundary preferentially nucleate hydrides at ~ 100-130 K. In this way, preferential hydride segregation at LAGB results from the vacancy sink. Romanenko [19] has previously described how hydride precipitation within top surface sheath of ~ 100 nm depth of a SRF Nb cavity can be initiated from the formation of vacancy-H complexes, and the number of V-H complexes determine the density of hydride precipitates. Typical cooldown between 150 K and 2 K during SRF Nb cavity operation allows hydrogen atoms to diffuse up to a length of ~ 30 μm (L_{diff}), enabling segregation [22]. This diffusion distance is comparable to the width of the observed hydride depleted zone.

4.4. EFFECT OF 800°C ANNEAL

After the 800°C/2h anneal the pattern of flux penetration into the sample was substantially altered; while still suggesting some residual weakness at the LAGBs, the bulk properties are mostly recovered (see Fig. 85). A plausible explanation is that residual hydrides at LAGBs beyond the resolution of MOI perturb the circulating superconducting currents and produce the very different magnetic flux penetration pattern that appear to be initiated from the surface. This surface initiated flux penetration has also been observed in a prior MO investigation [45] on a polycrystalline Nb

coupon subjected to a series of surface treatments based on a previous cavity processing sequence (in that case, the 750°C anneal was followed by the + 120°C bake). The complicated treatments produced severe surface irregularity, so that flow of magnetic flux applied normal to the sample surface was significantly disturbed. However, the very shallow (few micrometer depth) of the surface groove at LAGB in this sample had much less severe topographic relief. The 800°C/2h anneal may be insufficient to remove all hydrogen atoms segregated at the LAGBs and the resulting formation of hydrides precipitated at LAGBs during cool-down may still locally degrade superconductivity; this would be consistent with a recent surface susceptibility study [46]. In this study, the 800°C heat treatment did not remove the very low angle boundaries which have a very low interfacial energy.

4.5. EFFECT OF CRYSTAL ORIENTATION

Although the mechanical deformation of the sample was designed to favor the production of a specific kind of dislocation geometry, visual evidence of this effect on magnetic field penetration is suggested by the lesser amount of flux penetration in the "right" sample in Figs. 4 and 5. However, highly sensitive superconducting characterizations like AC susceptibility [46] or superconducting quantum interface device (SQUID) or vibrating sample magnetometer (VSM) [47] would be necessary to clearly understand the effect of dislocation structural morphology. These superconductivity characterizations require more specific sample preparation with a suitable size for measurements that would differ from current cavity processing techniques.

5. CONCLUSION

This study shows direct evidence of preferential hydride segregations at low angle grain boundaries (LAGBs) in SRF-grade high purity single crystal niobium through imaging of pits resulting from their decomposition. This segregated hydride phase correlates to a significant suppression of superconductivity at low angle grain boundaries produced by a low tensile strain (5%). These planar LAGBs were decorated with dense dislocations entanglements, since the tensile deformation was employed in parallel to the maximum shear stress. The low hydride concentration zone adjacent to the boundaries suggests that the LAGB segregation results from substantial "H" diffusion with the local non-equilibrium concentration of vacancy-H complexes. The MO imaging shows that 800°C annealing process has a substantial effect on the magnetic flux perturbation of the sample but there is still some weakness of the LAGBs perhaps through a residual concentration of trapped H. Thus it is likely that higher temperature or longer thermal treatments would be required to completely eliminate the effect of the plastic deformation relative "H" contaminations in SRF-grade Nb. This is the first observation of cold work deformation induced superconducting degradation in SRF-grade Nb in terms of hydride precipitation and additional experiments are underway to study the effect of annealing temperature and nitrogen (N) and titanium (Ti) surface doping. While these results are relevant for large-grain cavities, similar phenomena probably occur in polycrystals, but it is not clear or easy to determine if the low angle boundaries within the grains affects hydride formation and flux trapping more than the plentiful high angle gain boundaries.

ACKNOWLEDGEMENT

This work was supported by the US DOE under awards DE-FG02-13ER41973 and DE-SC0009960 and by the State of Florida. The EBSD-OIM and HR TEM facilities at FSU are funded and supported by the Florida State University Research Foundation, and the National High Magnetic Field Laboratory, which is supported in part by the National Science Foundation Cooperative Agreement DMR-1157490.

REFERENCES

[1] H. Padamsee, "RF Superconductivity vol II: Science, Technology and Application" (Weinheim: Wiley-VCH) (2009)
[2] A Yamamoto, M Ross, N Walker, "Advances in SRF development for ILC", in the proceedings of the 15th SRF workshop, Chicago, IL, USA, MOIOA02 (2011)
[3] A Gurevich, "Multiscale mechanisms of SRF breakdown", Physica C 441, pp38-43 (2006)
[4] C. Z. Antoine, A. Aspart, J. P. Charrier, H. Safa, and B. Visentin, "Alternative approaches for surface treatment of Nb superconducting cavities" in the proceedings of the 9th SRF workshop, Santa Fe, USA, TAU008 (1999)
[5] J. Knobloch, "The Q disease" in superconducting niobium RF cavities" AIP Conf. Proc., 671, pp133-150 (2003)
[6] C. Z. Antoine, B. Aune, B. Bonin, J. M. Cavedon, M. Juillard, A. Godin, C. Henriot, P. Leconte, H. Safa, A. Veyssiere, A. Chevarier, and B. Roux, "The role of atomic hydrogen in Q-degradation of niobium superconducting RF cavities: analytical point of view" in the proceedings of the 5th SRF workshop (DESY, Hamburg), pp616-34, srf91f01 (1991)
[7] J. Halbritter, "Transport in superconducting niobium films for radio frequency application", J. Appl. Phys., 97, 083904 (2005)
[8] J. Halbritter, "On the oxidation and on the superconductivity of niobium", Appl. Phys. Solid Surface, 43, 1, pp1–28 (1987)
[9] M. Delheusy, A. Stierle, N. Kasper, R. P. Kurta, A. Vlad, H. Dosch, C. Antoine, A. Resta, E. Lundgren, and J. Andersen, "X-ray investigation of subsurface interstitial oxygen at Nb/oxide interfaces", Appl. Phys. Lett., 92, 101911 (2008)
[10] G. Ciovati, "Improved oxygen diffusion model to explain the effect of low-temperature baking on high field losses in niobium superconducting cavities", Appl. Phys. Lett., 89, 022507 (2006)
[11] T. Proslier, J. F. Zasadzinski, L. Cooley, C. Antoine, J. Moore, J. Norem, M. Pellin, and K. E. Gray, "Tunneling study of cavity grade Nb; Possible magnetic scattering at the surface", Appl. Phys. Lett., 92, 212505 (2008)
[12] P. Kneisel, G. Ciovati, P. Dhakal, K. Saito, W. Singer, X. Singer, and G. R. Myneni, "Review of ingot niobium as a material for superconducting radio frequency accelerating cavities," Nucl. Instr. Meth. Phys. Res.: Accelerators, Spectrometers, Detectors and Associated Equipment, vol 774, pp133-150 (2015)
[13] A. Romanenko and H. Padamsee, "The role of near-surface dislocations in the high magnetic field performance of superconducting niobium cavities," Supercond. Sci. Technol., 23, 045008 (2010)
[14] T. R. Bieler, N. T. Wright, F Pourbohrat, C. Compton, K. T. Hartwig, D. Baars, A. Zamiri, S. Chandrasekaran, P. Darbandi, H. Jiang, E. Skoug, S. Balachandran, G. E. Ice, and W. Liu,

"Physical and mechanical metallurgy of high purity Nb for accelerator cavities", Phys. Rev. ST Accel. Beams, 13, 031002 (2010)
[15] R. J. Cava, B. Batlogg, J. J. Krajewski, H. F. Poulsen, P. Gammel, W. F. Peck, Jr., and L. W. Rupp, Jr., "Electrical and magnetic properties of $Nb_2O_{5-\delta}$ crystallographic shear structures, Phys. Rev. B, 44, 6973 (1991)
[16] H. Padamsee, Open discussion on Hot Topic: What is the best surface treatment for high Q and medium gradient?, SRF2013, 16th International conference on RF superconductivity, Sep 23-27, Paris, France (2013)
[17] S. Isagawa, "Hydrogen absorption and its effect on low-temperature electric properties of niobium", J. Appl. Phys., 51, 8 (1980)
[18] F. Barkov, A. Romanenko, and A. Grassellino, "Direct observation of hydrides formation in cavity-grade niobium", Phys. Rev. ST Accel. Beams, 15, 122001 (2012)
[19] A. Romanenko, F. Barkov, L. D. Cooley, and A. Grassellino, "Proximity breakdown of hydrides in superconducting niobium cavities" Supercond. Sci. Technol., 26, 035003 (2013)
[20] A. Romanenko, and L. V. Goncharova, "Elastic recoil detection studies of near-surface hydrogen in cavity-grade niobium" Supercond. Sci. Technol., 24, 105017 (2011)
[21] A. Romanenko, C. J. Edwardson, P. G. Coleman, and P. J. Simpson, "The effect of vacancies on the microwave surface resistance of niobium revealed by positron annihilation spectroscopy", Appl. Phys. Lett., 102, 232601 (2013)
[22] F. Barkov, A. Romanenko, Y. Trenikhina, and A. Grassellino, "Precipitation of hydrides in high purity niobium after different treatments", J. Appl. Phys., 114, 164904 (2013)
[23] Y-J Kim, R Tao, R. F. Klie, and D. N. Seidman, "Direct atomic-scale imaging of hydrogen and oxygen interstitials in pure niobium using atom-probe tomography and aberration-corrected scanning transmission electron microscopy, *ACS Nano,*7(1), pp732-739 (2012)
[24] R. Tao, A. Romanenko, L. D. Cooley, and R. F. Klie, "Low temperature study of structural phase transitions in niobium hydrides" J. Appl. Phys., 114, 044306 (2013)
[25] P. Maheshwari, F. A. Steviea, G. Myenenib, G. Ciovatib, J. M. Rigsbeec, and D. P. Griffisa, "Analysis of interstitial elements in niobium with secondary ion mass spectrometry (SIMS)", AIP Conf. Proc., 1352, 151 (2011)
[26] Y. Trenikhina, A. Romanenko, J. Kwon, J-M. Zuo, and J. F. Zasadzinski, "Nanostructural features degrading the performance of superconducting radio frequency niobium cavities revealed by transmission electron microscopy and electron energy loss spectroscopy", J. Appl. Phys., 117, 154507 (2015)
[27] X. Tingdong, "Creating and destroying vacancies in solids and non-equilibrium grain boundary segregation", Philos. Mag., 83, 7, pp889-899 (2003)
[28] D. Kuhlmann-Wilsdorf, and N Hansen, "Geometrically necessary, Incidental and Subgrain boundaries" Scripta Metallugica, 25, pp1557-1562 (1991)
[29] D. A. Hughes, N. Hasen, and D. J. Bammann, "Geometrically necessary boundaries, Incidental dislocation boundaries, and Geometrically necessary dislocations" Scripta Metallugica, 48, pp147-153 (2003)
[30] J. A. Rodrigues and R. Kirchheim, "More evidence for the formation of a dense Cottrell cloud of hydrogen (hydride) at dislocations in niobium and palladium", Scripta Metallurgica, 17, pp159-164 (1983)
[31] W. Singer, "SRF Cavity Fabrication and Material". arXiv preprint arXiv:1501.07142 (2015)
[32] M. Wang, D. Kang, T.R. Bieler, C.C. Compton, Z. H. Sung, P. J. Lee, and A. A. Polyanskii, "Introduction of precisely controlled microstructural defects into SRF cavity niobium sheets and

impact on local superconducting properties", in the proceedings of the 17th SRF workshop, MOPB018, Sep 13-18, Whistler, BC, Canada (2015)
[33] D. Baars, PhD Dissertation, "Investigation of active slip systems in high purity single crystal niobium", Michigan State University (2013)
[34] A. A. Polyanskii, X. Y. Cai, D. M. Feldmann, and D. C. Larbalestier, "Visualization of magnetic flux in magnetic materials and high temperature superconductors uing the faraday effect in ferrimagnetic garnet films," in Nano-Crystalline and Thin Film Magnetic Oxides, I. Nedkov and M. Ausloos, Eds. Springer Netherlands, pp353-370 (1999)
[35] R. Srinivansan, G. B. Viswanathan, V. I. Levit, and H. L. Fraser, "Orientation effect on recovery and recrystallization of cold rolled niobium single crystals" Mater. Sci. Eng. A, 507, pp179-189 (2009)
[36] S. I. Wright, M. M. Nowell, D. P. Field, "A review of strain analysis using electron backscatter diffraction" Microsc. Microanal., 17, pp316-329 (2011)
[37] D. Baars, H. Jiang, T. R. Bieler, A. Zamiri, F. Pourboghart, and C. Compoton, "Application of Texture Analysis: Ceramic Transactions (Wiley, New York) vol 201, p391 (2008)
[38] C. Wainwright, A. J. Cook, and B. E. Hopkins, "The structures of niobium-hydride alloys", J Less-Common Met., 6, 362 (1964)
[39] M. Amano ad Y. Sasaki, "Dislocation structure in dehydrogenated niobium" Phys. Status Solidi A, 19, 405 (1973)
[40] S. Posen, M. Checchin, A. C. Crawford, A. Grassellino, M. Martinello, O. S. Melnychuk, A. Romanenko, D. A. Sergatskov, and Y. Trenikhina, "Efficient expulsion of magnetic flux in superconducting radiofrequency cavities for high Q_0 applications", J. Appl. Phys., 119, 213903 (2016)
[41] P. J. Lee, A. A. Polyanskii, A. Gurevich, A. A. Squitieri, D. C. Larbalestier, P. C. Bauer, C. Boffo, and H. T. Edwards, "Grain boundary flux penetration and resistivity in large grain niobium sheet," Physica C, vol 441, pp126-129 (2006)
[42] Z-H Sung, PhD Dissertation, "The influence of grain boundaries on the properties of superconducting radio frequency cavity" University of Wisconsin – Madison (2010)
[43] P. Lejček, "Grain boundary Segregation in Metals", Springer series in materials science (2010)
[44] P. E. J. Flewitt and R. K. Wild, "Grain boundaries: Their Microstructure and Chemistry" (2001)
[45] A. Polyanskii, P. Bauer, P. J. Lee, C. Boffo, L. Bellantoni, H. Edwards, A. Gurevich, M. Jewell, D. C. Larbalestier , G. K. Perkins, and A. Squitieri, "Inhomogeneous flux penetration in niobium sheet sampled across the cavity production route: An Investigation of the properties of BCP niobium for superconducting RF Cavities" in the proceedings of the 12th SRF workshop, TUP55, Ithaca, New York, USA (2005)
[46] Z-H. Sung, A. Dzyuba, P. J. Lee, D. C. Larbalestier, and L. D. Cooley, "Evidence of incomplete annealing at 800°C and the effects of 120°C baking on the crystal orientation and the surface superconducting properties of cold-worked and chemically polished Nb," Supercond. Sci. Technol., 28, 075003 (2015)
[47] S. B. Roy, G. R. Myneni, and V. C. Sahni, "On the reliable determination of the magnetic field for first flux-line penetration in technical niobium materials", Supercond. Sci. Technol. 21, 065002 (2008)

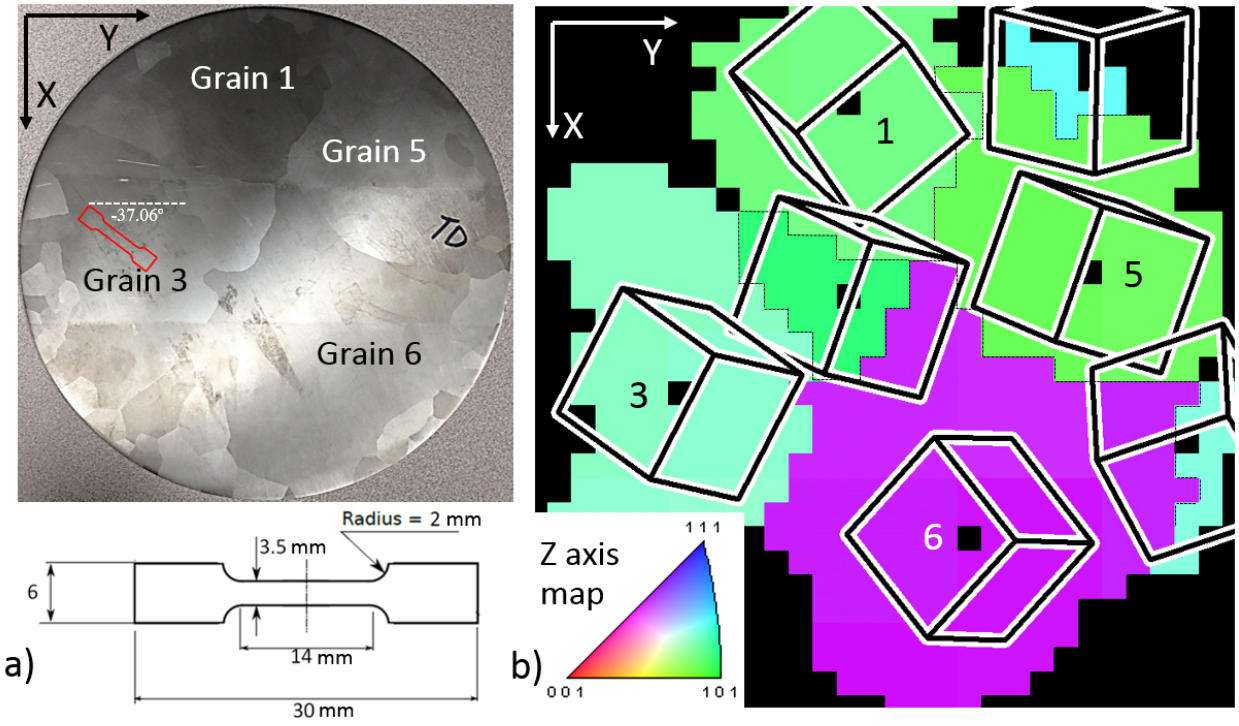

Figure 77. (a) (top) SRF-grade, high purity (RRR ≥ 200), large grain (> 5-10 cm), niobium ingot slice with a diameter of 270 mm and a thickness of 3 mm, manufactured by Tokyo Denkai and (bottom) the dimension of the tensile strain test coupon. The red outline represents the ~37.1° angular rotation of EDM extraction for the test coupons at Grain 3. (b) Grain crystallographic orientation normal to the slice surface, characterized with Laue X-ray diffraction and OrientExpress indexing program [32]. The inset shows the orientation color legend, and the unit cells indicate the crystal orientation of each grain.

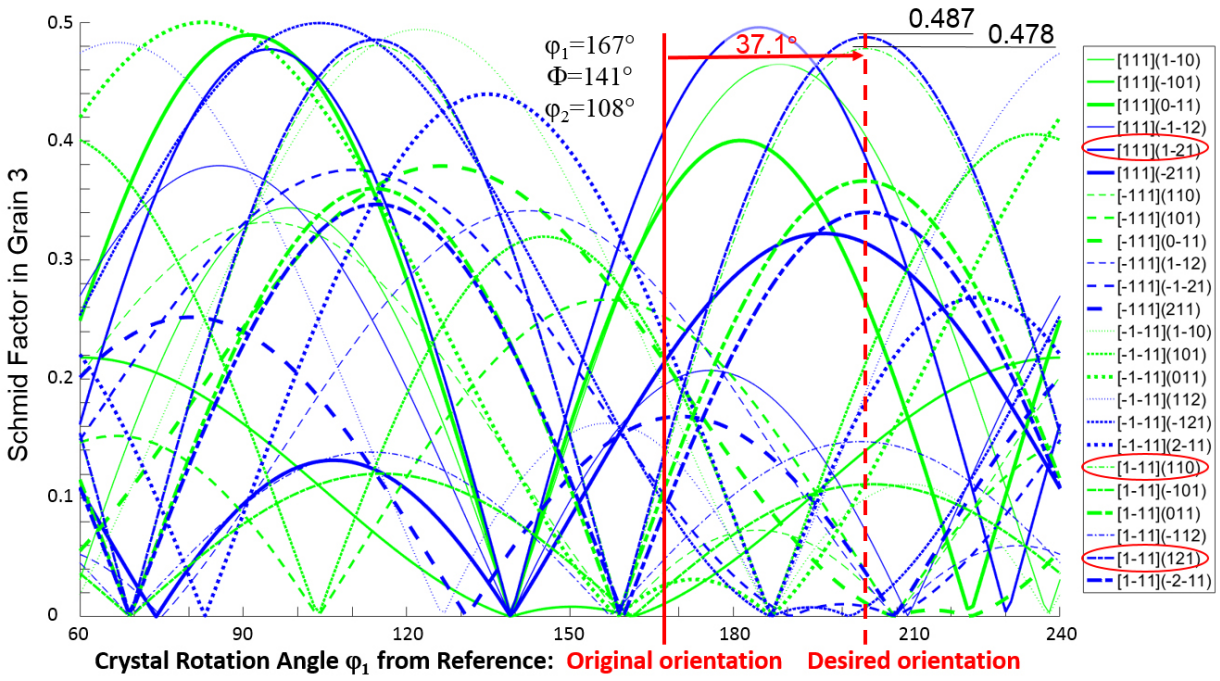

Figure 78. Absolute value of Schmid factor calculated for all slip systems in grain # 3 (Fig. 77) with the red solid line representing the reference orientation and the dashed line indicating the desired orientation to favor $[1\bar{1}1]$ slip system on (121) and (101) plane.

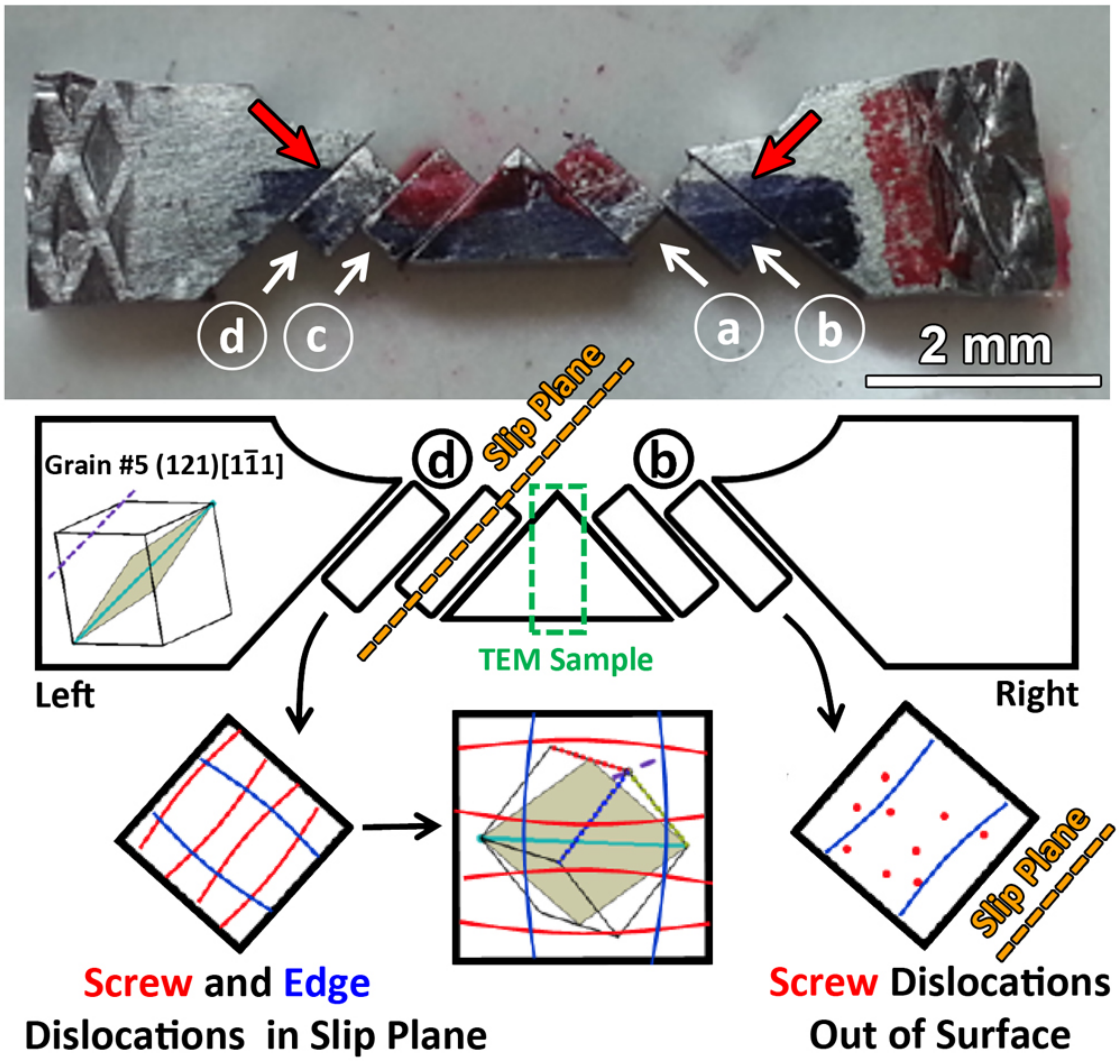

Figure 79. [Top] Optical image of the test coupon of single grain #3 (Fig. 77) after 5% tensile strain deformation and EDM sectioning (sample ID of four small pieces: a to d). The red arrows indicate the direction of magneto-optical (MO) imaging, which is the opposite direction of the externally applied magnetic field during MOI. [Bottom] A schematic diagram showing the estimated direction of the slip plane and the anticipated screw and edge dislocation morphology in a MOI viewing plane. The unit cell illustrates the gray (121) slip plane and the blue [1$\bar{1}$1] slip direction vector (screw line direction). In the left sample (c & d), edge and screw dislocation lines are parallel to the MOI viewing plane (slip plane); in the right sample (a & b), screw dislocation lines are perpendicular to the MOI view direction.

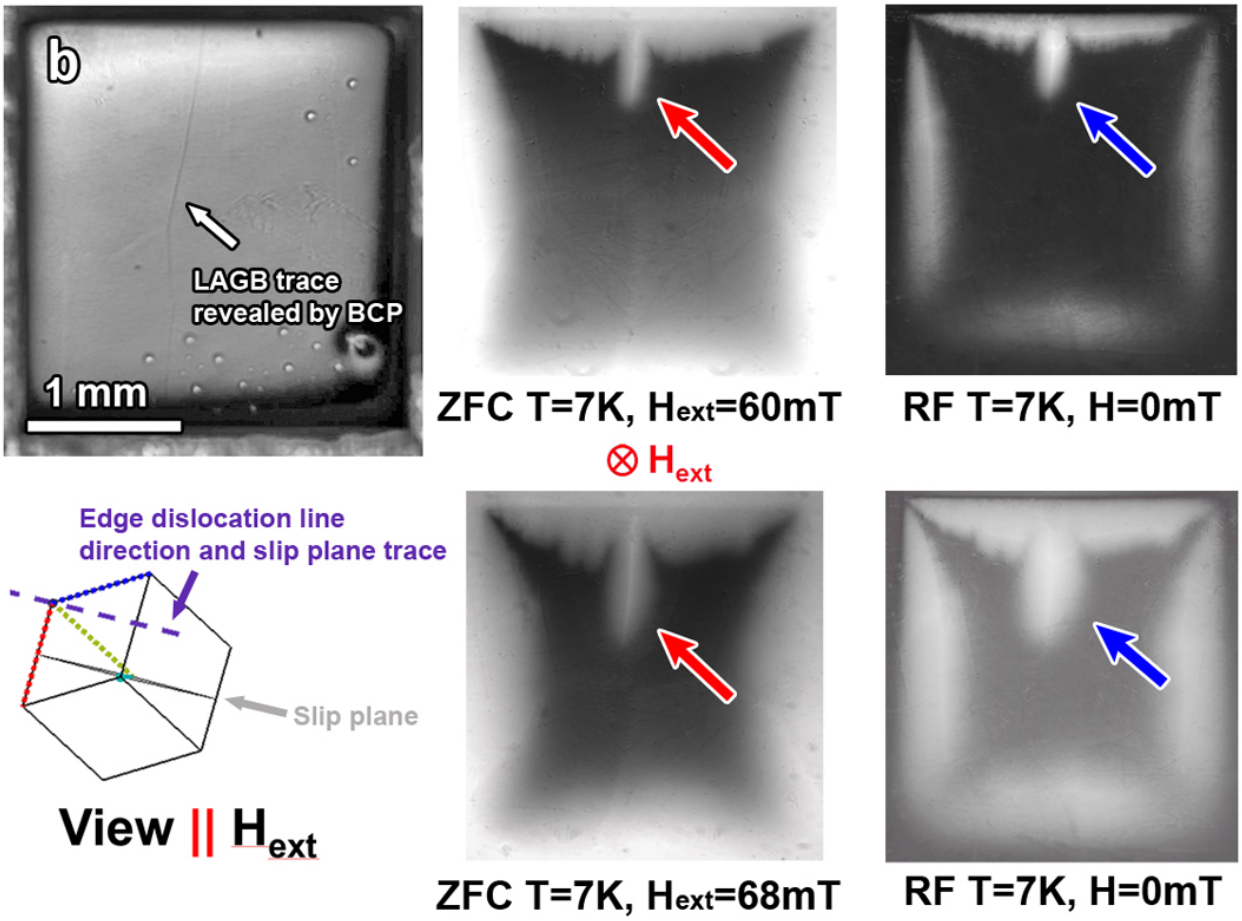

Figure 80. ZFC and RF mode MO images of the "right" sample (b, Fig. 79) with the orientation of the slip plane (perpendicular to page) with screw dislocation lines out of the viewing plane/slip plane and the edge directions line direction indicated by the violet dotted line.

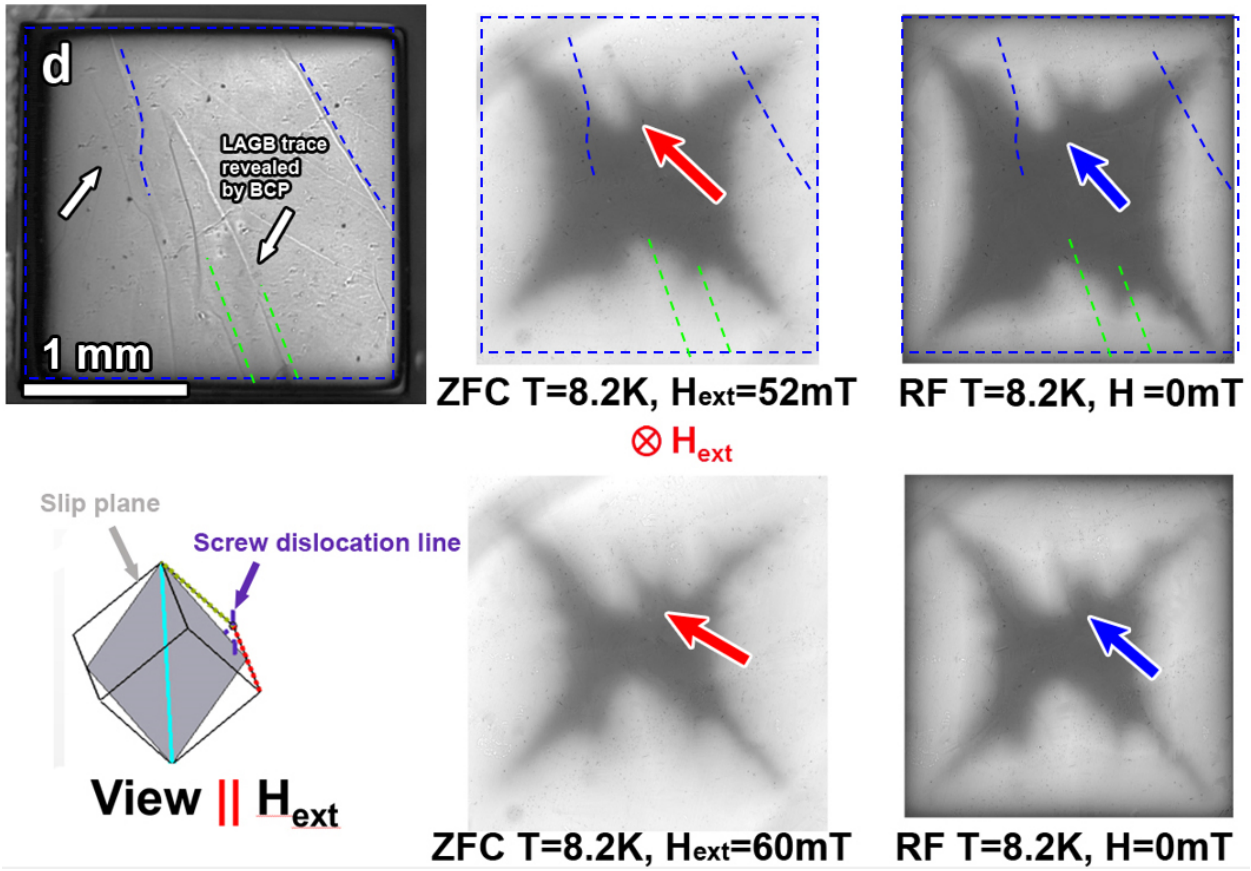

Figure 81. ZFC and RF mode MO images for the "left" sample (d, Fig. 79); the configuration of the gray (121) slip lane and the screw dislocation line direction (violet dotted line and teal line) screw dislocation line direction is in the viewing plane/slip plane. In the upper images, small offset blue and green dotted lines are applied for easy recognition of the GB locations.

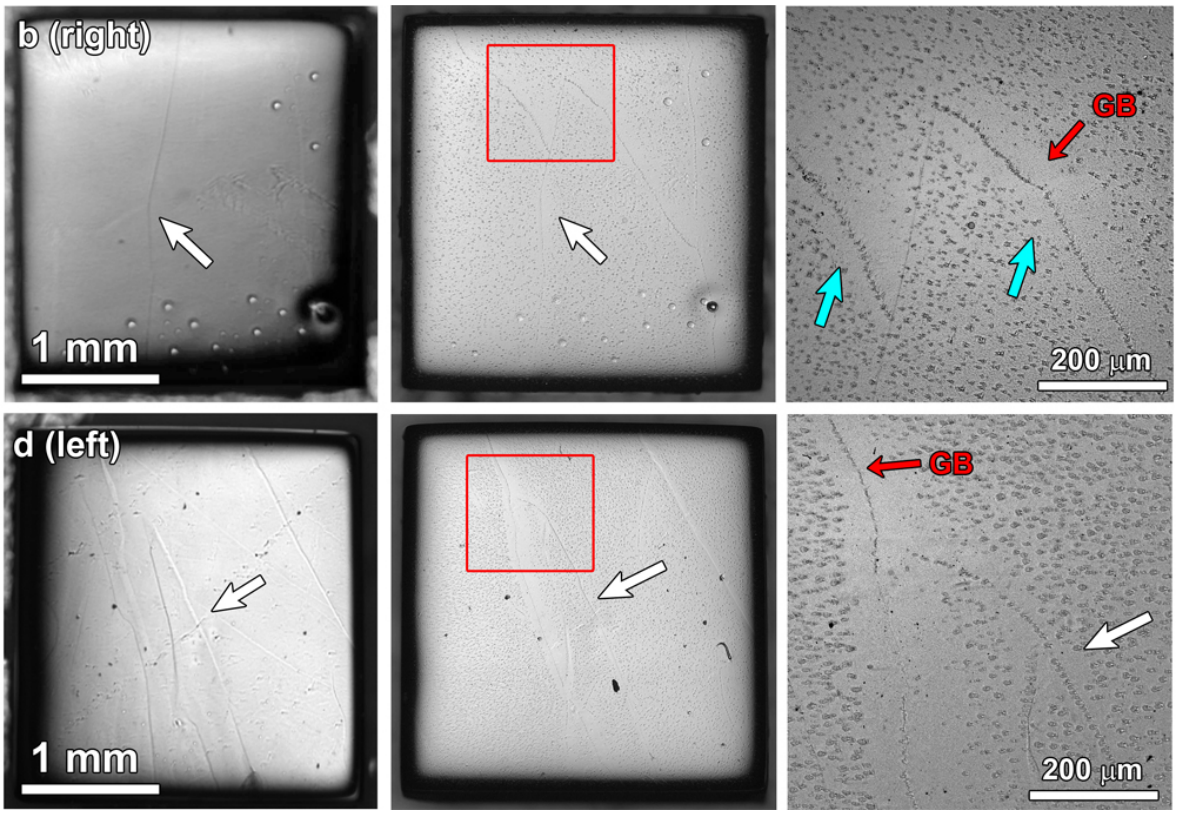

Figure 82. Surface optical images of the “right” sample (b, upper) and the “left” sample (d, lower) before (the leftmost) and after (the middle) cryogenic cooling below T_c of Nb ~ 9.2 K for MO imaging. The rightmost images that show enlarged areas in the vicinity of LAGBs, as indicated with red rectangles clearly show surface scar features resulting from hydride precipitation.

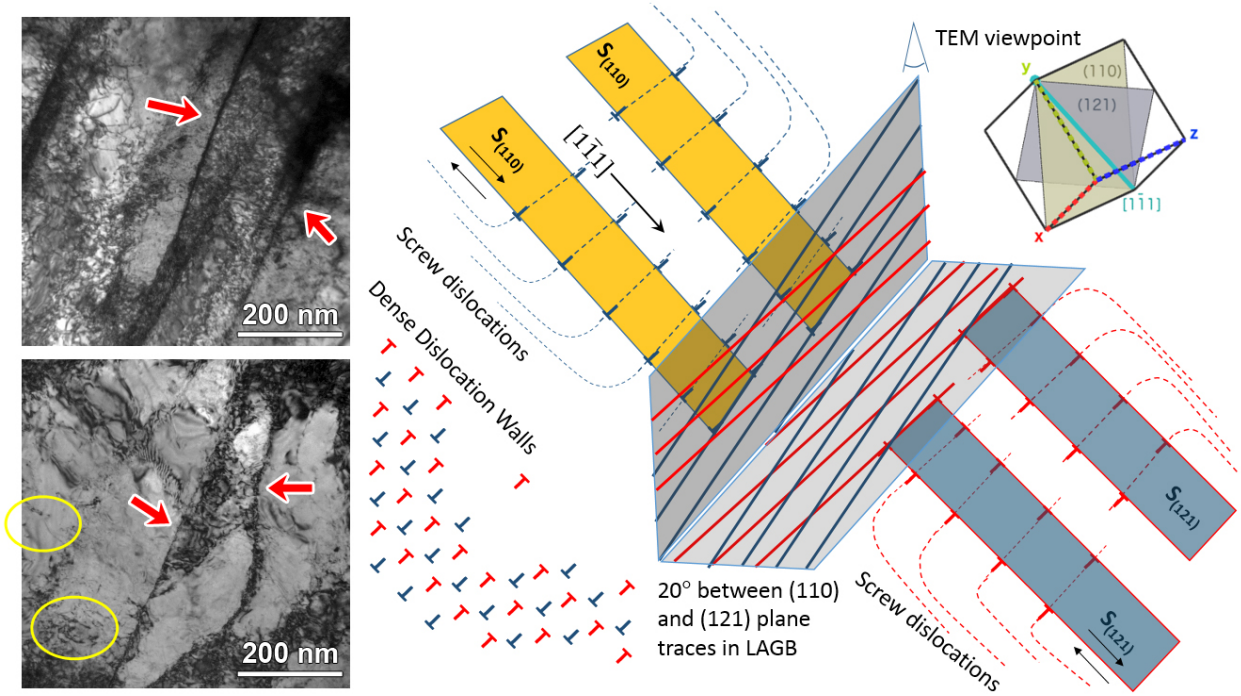

Figure 83. Bright field (BF) transmission electron microscope (TEM) images of cross sectional microstructure (normal to the tensile direction) of the 5% tensile strained grain # 3 (Fig. 79), and a schematic of the possible dislocation arrangement on sub-boundaries parallel and perpendicular to the tensile axis.

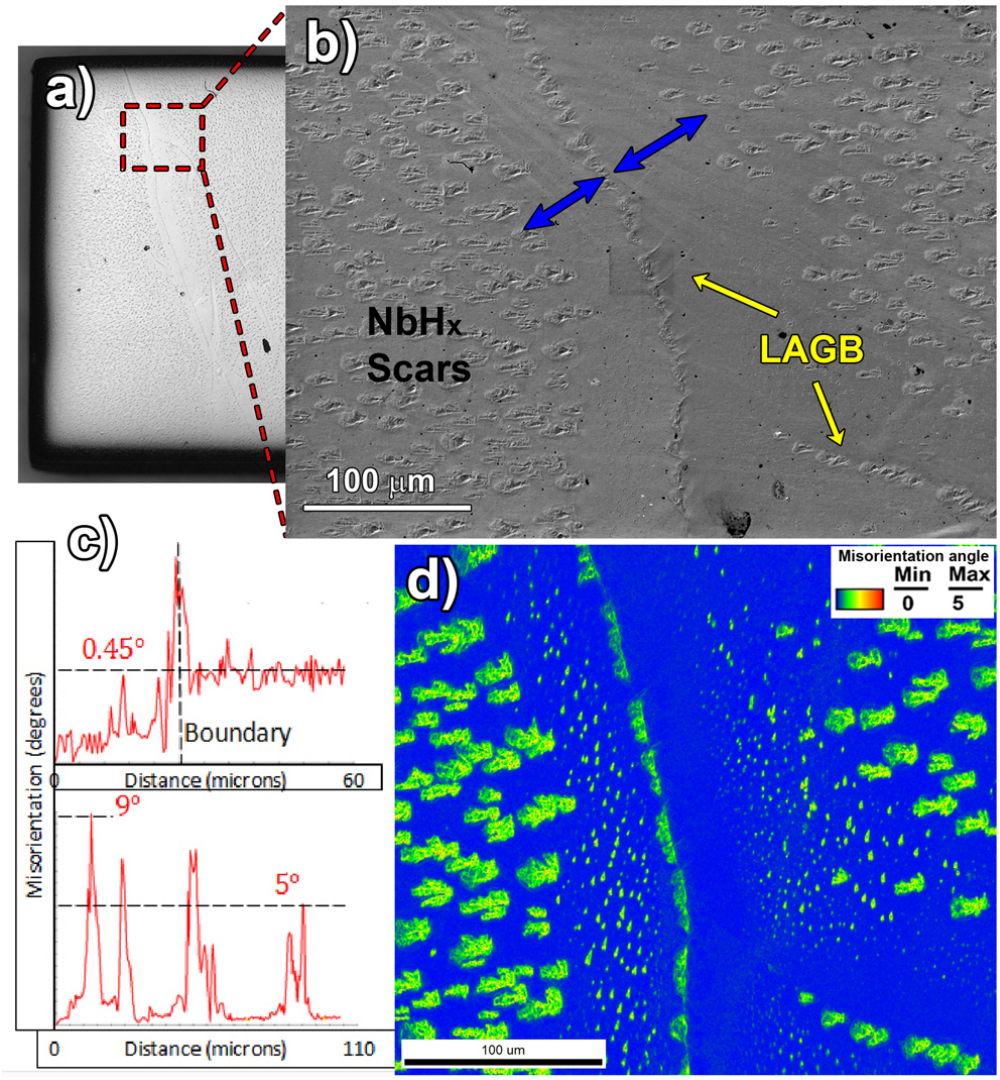

Figure 84. (a) Light microscopy image of the LAGB where premature magnetic flux penetration occurs in MOI analysis (Fig. 81, the "left" sample, d) with (b) higher magnification scanning electron microscope secondary electron image of the area indicated by the dotted rectangle in the optical image, (d) local average misorientation map with misorientation profiles (c) along two line traces and through several hydride scars (top) and across the LAGB (bottom), from electron backscattered diffraction (EBSD) data.

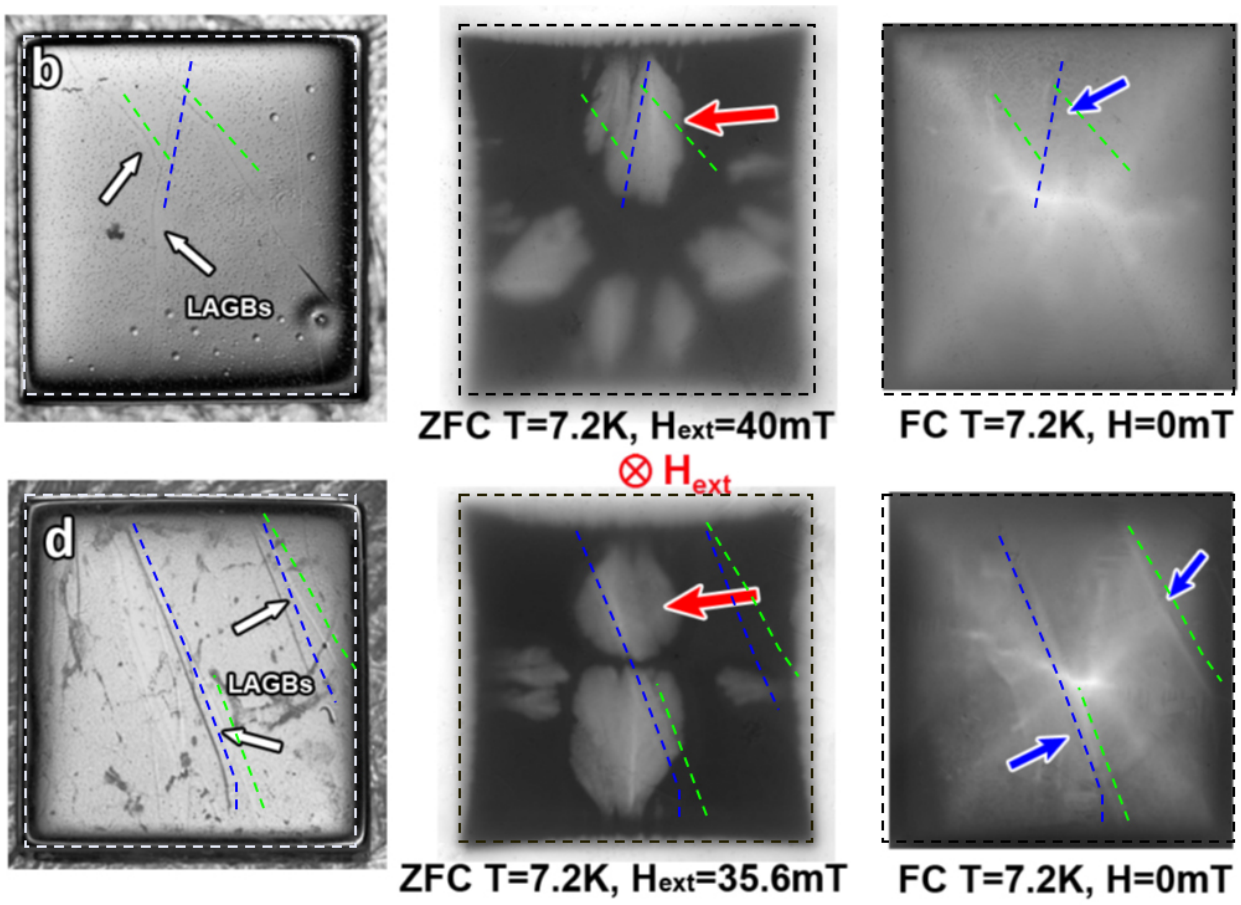

Figure 85. ZFC and FC mode MO images of the "right" (upper images, b) and "left" (lower images, d) samples after 800°C/2hrs anneal under ultrahigh vacuum (≥ 10^{-6} torr). Small offset blue and green dotted lines are applied for easy recognition of the GB locations.

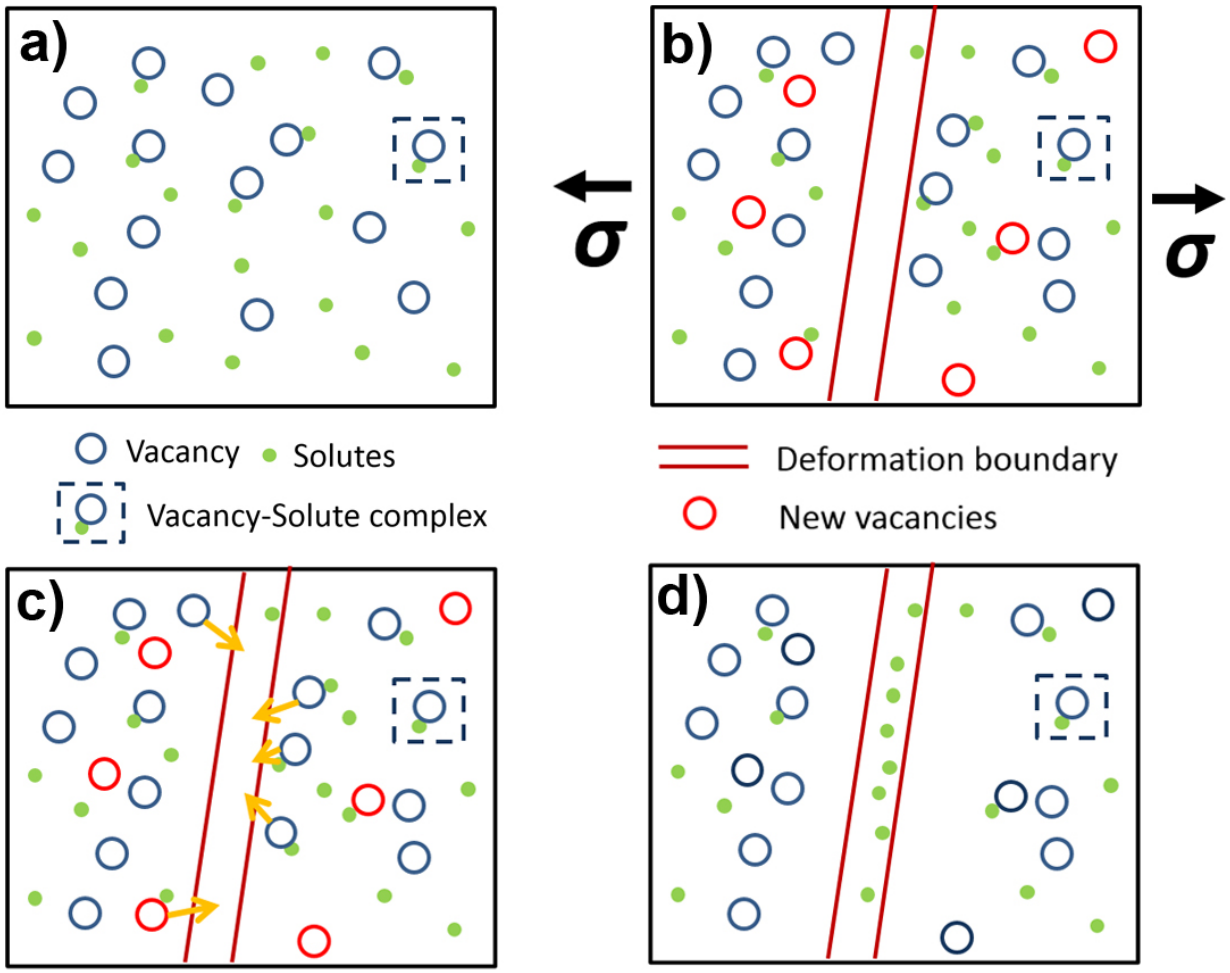

Figure 86. Schematic of $Nb_{1-x}H_x$ accumulation and precipitation at low angle grain boundaries (LAGBs) based on stressed induced non-equilibrium vacancies and their absorption into GB with concurrent transport of H to the boundary via vacancies [27, 43, 44].

BIBLIOGRAPHY

BIBLIOGRAPHY

[1] O. Barbalat, “Applications of particle accelerators,” 1990.

[2] M. Silari, “Applications of particle accelerators in medicine,” *Radiat. Prot. Dosimetry*, vol. 146, no. 4, pp. 440–450, 2011.

[3] L. Rodriguez-Fernandez, “Particle Accelerator Applications: Ion and Electron Irradiation in Materials Science, Biology and Medicine,” in *AIP Conference Proceedings*, 2010, vol. 1271, no. 1, pp. 159–179.

[4] H. Padamsee, J. Knobloch, and T. Hays, *RF Superconductivity for Accelerators*, vol. 206. New York: Wiley, 1998.

[5] W. Singer, “SRF Cavity Fabrication and Materials,” in *arXiv*, 2015, vol. 1501.07142, no. May 2013, pp. 171–207.

[6] C. Antoine, “Materials and surface aspects in the development of SRF Niobium cavities,” 2012.

[7] H. Padamsee, “The science and technology of superconducting cavities for accelerators,” *Supercond. Sci. Technol.*, vol. 14, no. 4, p. R28, 2001.

[8] F. Furuta *et al.*, “Experimental comparison at KEK of high gradient performance of different single cell superconducting cavity designs,” in *EPAC06*, 2006.

[9] A. Romanenko, A. Grassellino, A. C. Crawford, D. A. Sergatskov, and O. Melnychuk, “Ultra-high quality factors in superconducting niobium cavities in ambient magnetic fields up to 190 mG,” *Appl. Phys. Lett.*, vol. 105, no. 23, p. 234103, 2014.

[10] T. R. Bieler *et al.*, “Physical and mechanical metallurgy of high purity Nb for accelerator cavities,” *Phys. Rev. Spec. Top. - Accel. Beams*, vol. 13, no. 3, p. 31002, 2010.

[11] G. Ciovati and A. Gurevich, “Measurement of RF losses due to trapped flux in a large grain niobium cavity,” in *13th International Workshop on RF Superconductivity*, 2007, pp. 132–136.

[12] T. Matsushita, *Flux pinning in superconductors*, vol. 164. New York: Springer, 2007.

[13] G. Ciovati and A. Gurevich, “Evidence of high-field radio-frequency hot spots due to trapped vortices in niobium cavities,” *Phys. Rev. Spec. Top. - Accel. Beams*, vol. 11, no. 12, p. 122001, 2008.

[14] A. Dasgupta, C. C. Koch, D. M. Kroeger, and Y. T. Chou, “Flux pinning by grain boundaries in niobium bicrystals,” *Philos. Mag. Part B*, vol. 38, no. 4, pp. 367–380, 1978.

[15] G. Zerweck, “On pinning of superconducting flux lines by grain boundaries,” *J. Low*

Temp. Phys., vol. 42, no. 1–2, pp. 1–9, 1981.

[16] Z.-H. Sung *et al.*, "Development of low angle grain boundaries in lightly deformed superconducting niobium and their influence on hydride distribution and flux perturbation," *J. Appl. Phys.*, vol. 121, no. 19, p. 193903, 2017.

[17] M. Checchin, M. Martinello, A. Grassellino, A. Romanenko, and J. F. Zasadzinski, "Electron mean free path dependence of the vortex surface impedance," *Supercond. Sci. Technol.*, vol. 30, no. 3, p. 34003, 2017.

[18] M. Martinello *et al.*, "Effect of interstitial impurities on the field dependent microwave surface resistance of niobium," *Appl. Phys. Lett.*, vol. 109, no. 6, p. 62601, 2016.

[19] S. Posen, A. Grassellino, A. Romanenko, and O. Melnychuk, "Flux expulsion variation in SRF cavities," in *17th International Conference on RF Superconductivity*, 2015, pp. 404–408.

[20] M. Wang, D. Kang, and T. R. Bieler, "Direct observation of dislocation structure evolution in SRF cavity niobium using electron channeling contrast imaging," *J. Appl. Phys.*, vol. 124, no. 15, 2018.

[21] S. Aull, O. Kugeler, and J. Knobloch, "Study of trapped magnetic flux in superconducting niobium samples," in *15th International Conference on RF Superconductivity*, 2011.

[22] C. Z. Antoine, "Influence of crystalline structure on rf dissipation in superconducting niobium," *Phys. Rev. Accel. Beams*, vol. 22, no. 3, p. 34801, 2019.

[23] A. Romanenko and H. Padamsee, "The role of near-surface dislocations in the high magnetic field performance of superconducting niobium cavities," *Supercond. Sci. Technol.*, vol. 23, no. 4, p. 45008, 2010.

[24] S. Posen *et al.*, "Efficient expulsion of magnetic flux in superconducting radiofrequency cavities for high Q0 applications," *J. Appl. Phys.*, vol. 119, no. 21, p. 213903, 2016.

[25] S. Posen *et al.*, "The Effect of Mechanical Cold Work on the Magnetic Flux Expulsion of Niobium," *arXiv Prepr. arXiv1804.07207*, 2018.

[26] Z.-H. Sung *et al.*, "Large grain CBMM Nb ingot slices: An ideal test bed for exploring the microstructure-electromagnetic property relationships relevant to SRF," in *AIP Conference Proceedings*, 2015, vol. 1687, no. 1, p. 20004.

[27] A. A. Polyanskii *et al.*, "Magneto-Optical Study High-Purity Niobium for Superconducting RF Application," in *AIP Conference Proceedings-American Institute of Physics*, 2011, vol. 1352, no. 1, pp. 186–202.

[28] P. J. Lee *et al.*, "Grain boundary flux penetration and resistivity in large grain niobium sheet," *Phys. C Supercond.*, vol. 441, no. 1–2, pp. 126–129, 2006.

[29] M. Wang, T. Bieler, C. Compton, and D. Kang, “Characterization of Microstructural Defects in SRF Cavity Niobium using Electron Channeling Contrast Imaging,” in *18th Int. Conf. on RF Superconductivity (SRF’17), Lanzhou, China, July 17-21, 2017*, 2018, pp. 792–796.

[30] P. Dieter, “Superconducting cavities for accelerators,” *REPORTS Prog. Phys.*, vol. 61, no. 5, p. 431, 1998.

[31] D. Kang, D. C. Baars, A. Mapar, T. R. Bieler, F. Pourboghrat, and C. C. Compton, “Study of slip and deformation in high purity single crystal nb for accelerator cavities,” in *17th International Conference on RF Superconductivity*, 2015, pp. 191–195.

[32] B. Barish and J. E. Brau, “The International Linear Collider,” *Int. J. Mod. Phys. A*, vol. 28, no. 27, p. 1330039, 2013.

[33] J. Galayda, “The new LCLS-II project: Status and challenges,” 2014.

[34] K. Saito, “State-of-the-Art and Future Prospects in RF Superconductivity,” in *Proceedings of IPAC2012, New Orleans, Louisiana, USA*, 2012, pp. 11–15.

[35] A. Chandra, G. S. Frankel, and M. D. Sumption, “Electropolishing of niobium to obtain defect free surfaces,” in *15th International Conference on RF Superconductivity*, 2011.

[36] D. Gonnella, J. Kaufman, and M. Liepe, “Impact of nitrogen doping of niobium superconducting cavities on the sensitivity of surface resistance to trapped magnetic flux,” *J. Appl. Phys.*, vol. 119, no. 7, p. 73904, 2016.

[37] P. H. E. Meijer, “Kamerlingh Onnes and the discovery of superconductivity,” *Am. J. Phys.*, vol. 62, no. 12, pp. 1105–1108, 1994.

[38] D. Van Delft and P. Kes, “The discovery of superconductivity,” *Phys. Today*, vol. 63, no. 9, pp. 38–43, 2010.

[39] B. W. Maxfield and W. L. McLean, “Superconducting penetration depth of niobium,” *Phys. Rev.*, vol. 139, no. 5A, p. A1515, 1965.

[40] L. D. Landau and V. L. Ginzburg, “On the theory of superconductivity,” *J. Exp. Theor. Phys.*, vol. 20, p. 1064, 1950.

[41] B. Rosenstein and D. Li, “Ginzburg-Landau theory of type II superconductors in magnetic field,” *Rev. Mod. Phys.*, vol. 82, no. 1, pp. 109–168, 2010.

[42] J. Vogt, O. Kugeler, and J. Knobloch, “High Q research: the dynamics of flux trapping in superconducting niobium,” in *16th International Conference on RF superconductivity*, 2013.

[43] O. S. Romanenko and H. Padamsee, “SURFACE CHARACTERIZATION OF NB CAVITY SECTIONS - UNDERSTANDING THE HIGH FIELD Q-SLOPE,” Cornell

University, 2009.

[44] A. B. Pippard, “Trapped Flux in Superconductors,” *Philos. Trans. R. Soc. London. Ser. A, Math. Phys. Sci.*, vol. 248, no. 941, pp. 97–129, 1955.

[45] E. J. Kramer, “Fundamental Fluxoid-Defect Interactions in Irradiated Superconductors,” *J. Nucl. Mater.*, vol. 72, no. 1–2, pp. 5–33, 1978.

[46] C. Meingast and D. C. Larbalestier, “Quantitative description of a very high critical current density Nb-Ti superconductor during its final optimization strain. II. Flux pinning mechanisms,” *J. Appl. Phys.*, vol. 66, no. 12, pp. 5971–5983, 1989.

[47] L. Fang *et al.*, “Huge critical current density and tailored superconducting anisotropy in SmFeAsO0.8F0.15 by low-density columnar-defect incorporation,” *Nat Commun*, vol. 4, 2013.

[48] M. Wang *et al.*, “Investigation of the Effect of Strategically Selected Grain Boundaries on Superconducting Properties of SRF Cavity Niobium,” in *18th Int. Conf. on RF Superconductivity (SRF’17), Lanzhou, China, July 17-21, 2017*, 2018, pp. 787–791.

[49] A. M. Campbell and J. E. Evetts, “Flux vortices and transport currents in type II superconductors,” *Adv. Phys.*, vol. 21, no. 90, pp. 199–428, 1972.

[50] M. Peach and J. S. Koehler, “The forces exerted on dislocations and the stress fields produced by them,” *Phys. Rev.*, vol. 80, no. 3, p. 436, 1950.

[51] J. P. Hirth and J. Lothe, *Theory of dislocations*, 2nd ed. Malabar, Florida: Krieger Publishing Company, 1982.

[52] D. Hull and D. J. Bacon, *Introduction to dislocations*. Butterworth-Heinemann, 2001.

[53] E. Orowan, “Zur kristallplastizität. i,” *Zeitschrift für Phys.*, vol. 89, no. 9–10, pp. 605–613, 1934.

[54] M. Polanyi, “Über eine Art Gitterstörung, die einen Kristall plastisch machen könnte,” *Zeitschrift für Phys.*, vol. 89, no. 9–10, pp. 660–664, 1934.

[55] G. I. Taylor, “The mechanism of plastic deformation of crystals. Part I.—Theoretical,” *Proc. R. Soc. London. Ser. A, Contain. Pap. a Math. Phys. Character*, vol. 145, no. 855, pp. 362–387, 1934.

[56] V. Bulatov and W. Cai, *Computer simulations of dislocations*, vol. 3. Oxford University Press on Demand, 2006.

[57] G. Simmons and H. Wang, “Single crystal elastic constants and calculated aggregate properties,” 1971.

[58] G. I. Taylor and C. F. Elam, “The distortion of iron crystals,” *Proc. R. Soc. London. Ser.*

A, Contain. Pap. a Math. Phys. Character, vol. 112, no. 761, pp. 337–361, 1926.

[59] H. Gough, "The behaviour of a single crystal of $α$-iron subjected to alternating torsional stresses," *Proc. R. Soc. London. Ser. A, Contain. Pap. a Math. Phys. Character*, vol. 118, no. 780, pp. 498–534, 1928.

[60] M. S. Duesbery, R. A. Foxall, and P. B. Hirsch, "The plasticity of pure niobium single crystals," *Le J. Phys. Colloq.*, vol. 27, no. C3, pp. C3--193, 1966.

[61] T. Maiti, "PHYSICS-BASED CRYSTAL PLASTICITY MODELING OF SINGLE CRYSTAL NIOBIUM," Michigan State University, 2017.

[62] E. Furubayashi, "Behavior of dislocations in Fe-3% Si under stress," *J. Phys. Soc. Japan*, vol. 27, no. 1, pp. 130–146, 1969.

[63] F. Louchet, L. P. Kubin, and D. Vesely, "In situ deformation of bcc crystals at low temperatures in a high-voltage electron microscope Dislocation mechanisms and strain-rate equation," *Philos. Mag. A*, vol. 39, no. 4, pp. 433–454, 1979.

[64] A. Seeger, "Peierls barriers, kinks, and flow stress: Recent progress: Dedicated to Professor Dr. Haël Mughrabi on the occasion of his 65th birthday," *Zeitschrift für Met.*, vol. 93, no. 8, pp. 760–777, 2002.

[65] D. Kuhlmann-Wilsdorf and N. Hansen, "Geometrically necessary, incidental and subgrain boundaries," *Scr. Metall. Mater.*, vol. 25, no. 7, pp. 1557–1562, 1991.

[66] B. Bay, N. Hansen, D. A. Hughes, and D. Kuhlmann-Wilsdorf, "Overview no. 96 evolution of fcc deformation structures in polyslip," *Acta Metall. Mater.*, vol. 40, no. 2, pp. 205–219, 1992.

[67] N. Hansen, "Deformation microstructures," *Scr. Metall. Mater.*, vol. 27, no. 11, pp. 1447–1452, 1992.

[68] R. D. Doherty *et al.*, "Current issues in recrystallization: a review," *Mater. Sci. Eng. A*, vol. 238, no. 2, pp. 219–274, 1997.

[69] E. Schmid and W. Boas, "Kristallelastizität," in *Kristallplastizität*, Springer, 1935, pp. 15–24.

[70] J. W. Christian, "Some surprising features of the plastic deformation of body-centered cubic metals and alloys," *Metall. Trans. A*, vol. 14, no. 7, pp. 1237–1256, 1983.

[71] G. I. Taylor, "Section A.-Mathematical and physical sciences.-The deformation of crystals of $β$-brass," *Proc. R. Soc. London. Ser. A, Contain. Pap. a Math. Phys. Character*, vol. 118, no. 779, pp. 1–24, 1928.

[72] R. A. Foxall, M. S. Duesbery, and P. B. Hirsch, "The deformation of niobium single crystals," *Can. J. Phys.*, vol. 45, no. 2, pp. 607–629, 1967.

[73] D. K. Bowen, J. W. Christian, and G. Taylor, “Deformation properties of niobium single crystals,” *Can. J. Phys.*, vol. 45, no. 2, pp. 903–938, 1967.

[74] P. J. Sherwood, F. Guiu, H. C. Kim, and P. L. Pratt, “Plastic anisotropy of tantalum, niobium, and molybdenum,” *Can. J. Phys.*, vol. 45, no. 2, pp. 1075–1089, 1967.

[75] D. F. Stein, “The effect of orientation and impurities on the mechanical properties of molybdenum single crystals,” *Can. J. Phys.*, vol. 45, no. 2, pp. 1063–1074, 1967.

[76] D. Hull, J. F. Byron, and F. W. Noble, “Orientation dependence of yield in body-centered cubic metals,” *Can. J. Phys.*, vol. 45, no. 2, pp. 1091–1099, 1967.

[77] M. S. Duesbery and R. A. Foxall, “A detailed study of the deformation of high purity niobium single crystals,” *Philos. Mag.*, vol. 20, no. 166, pp. 719–751, 1969.

[78] M. S. Duesbery, “The dislocation core and plasticity,” *Elsevier Sci. Publ. Dislocations Solids.*, vol. 8, pp. 67–173, 1989.

[79] V. Vitek, “Core structure of screw dislocations in body-centred cubic metals: relation to symmetry and interatomic bonding,” *Philos. Mag.*, vol. 84, no. 3–5, pp. 415–428, 2004.

[80] H. Saka and G. Taylor, “Slip systems in a body-centred-cubic Li—Mg alloy,” *Philos. Mag. A*, vol. 43, no. 6, pp. 1377–1392, 1981.

[81] A. Mapar, *Crystal Plasticity Modeling of the Deformation of BCC Iron and Niobium Single Crystals*. Michigan State University, 2017.

[82] D. Kang, “Characterization of Microstructure and Slip Behavior of Niobium Used to Fabricate Accelerator Cavities,” Michigan State University, 2019.

[83] D. Baars, “Investigation of active slip systems in high purity single crystal niobium,” Michigan State University, 2013.

[84] J. F. Smith, “The H- Nb (Hydrogen-Niobium) and D- Nb (Deuterium-Niobium) systems,” *Bull. Alloy Phase Diagrams*, vol. 4, no. 1, pp. 39–46, 1983.

[85] A. Kimura and H. K. Birnbaum, “Hydrogen induced grain boundary fracture in high purity nickel and its alloys—enhanced hydrogen diffusion along grain boundaries,” *Acta Metall.*, vol. 36, no. 3, pp. 757–766, 1988.

[86] H. K. Birnbaum and P. Sofronis, “Hydrogen-enhanced localized plasticity—a mechanism for hydrogen-related fracture,” *Mater. Sci. Eng. A*, vol. 176, no. 1–2, pp. 191–202, 1994.

[87] R. A. Oriani, “The diffusion and trapping of hydrogen in steel,” *Acta Metall.*, vol. 18, no. 1, pp. 147–157, 1970.

[88] J. Č\’\ižek *et al.*, “Hydrogen-induced defects in bulk niobium,” *Phys. Rev. B*, vol. 69, no. 22, p. 224106, 2004.

[89] J. Knobloch, “The ‘Q Disease’ in superconducting niobium rf cavities,” in *AIP Conference Proceedings*, 2003, vol. 671, no. 1, pp. 133–150.

[90] A. Romanenko, F. Barkov, L. D. Cooley, and A. Grassellino, “Proximity breakdown of hydrides in superconducting niobium cavities,” *Supercond. Sci. Technol.*, vol. 26, no. 3, p. 035003, Mar. 2013.

[91] A. Romanenko and L. V Goncharova, “Elastic recoil detection studies of near-surface hydrogen in cavity-grade niobium,” *Supercond. Sci. Technol.*, vol. 24, no. 10, p. 105017, 2011.

[92] F. Barkov, A. Romanenko, and A. Grassellino, “Direct observation of hydrides formation in cavity-grade niobium,” *Phys. Rev. Spec. Top. Beams*, vol. 15, no. 12, p. 122001, 2012.

[93] K. Faber and H. Schultz, “Hydrogen contamination in tantalum and niobium following UHV-degassing,” *Scr. Metall.*, vol. 6, no. 11, pp. 1065–1070, 1972.

[94] C. Z. Antoine *et al.*, “The role of atomic hydrogen in Q-degradation of niobium superconducting rf cavities: analytical point of view,” in *Proc. of 5th Workshop on RF Superconductivity, DESY, Hamburg, Germany*, 1991, pp. 616–634.

[95] T. Tajima *et al.*, “Q Disease : Insights From 350 Mhz Spoke Cavities Tests and Erd Analyses of Hydrogen in Niobium *,” in *this workshop*, 2003, pp. 655–657.

[96] B. J. Makenas and H. K. Birnbaum, “Phase changes in the niobium-hydrogen system I: Accommodation effects during hydride precipitation,” *Acta Metall.*, vol. 28, no. 7, pp. 979–988, 1980.

[97] H. K. Birnbaum, M. L. Grossbecr, and M. Amano, “Hydride precipitation in Nb and some properties of NbH,” *J. Less Common Met.*, vol. 49, pp. 357–370, 1976.

[98] R. Balasubramaniam, “Accommodation effects during room temperature hydrogen transformations in the niobium-hydrogen system,” *Acta Metall. Mater.*, vol. 41, no. 12, pp. 3341–3349, 1993.

[99] K. Nörthemann and A. Pundt, “Coherent-to-semi-coherent transition of precipitates in niobium-hydrogen thin films,” *Phys. Rev. B*, vol. 78, no. 1, p. 14105, 2008.

[100] J. Tien, A. W. Thompson, I. M. Bernstein, and R. J. Richards, “Hydrogen transport by dislocations,” *Metall. Trans. A*, vol. 7, no. 6, pp. 821–829, 1976.

[101] M. Pitaval, P. Morin, J. Baudry, E. Vicario, and G. Fontaine, “Advances in crystalline contrast from defects,” *Scanning Electron Microsc. IIT Res. Institute, Chicago, Ill. 1977, 439-444*, 1976.

[102] P. Morin, M. Pitaval, D. Besnard, and G. Fontaine, “Electron--channelling imaging in scanning electron microscopy,” *Philos. Mag. A*, vol. 40, no. 4, pp. 511–524, 1979.

[103] J. T. Czernuszka, N. J. Long, E. D. Boyes, and P. B. Hirsch, “Imaging of dislocations using backscattered electrons in a scanning electron microscope,” *Philos. Mag. Lett.*, vol. 62, no. 4, pp. 227–232, 1990.

[104] D. C. Joy, “Direct defect imaging in the high resolution SEM,” *MRS Online Proc. Libr. Arch.*, vol. 183, 1990.

[105] B. A. Simkin and M. A. Crimp, “An experimentally convenient configuration for electron channeling contrast imaging,” *Ultramicroscopy*, vol. 77, no. 1–2, pp. 65–75, 1999.

[106] M. A. Crimp, “Scanning electron microscopy imaging of dislocations in bulk materials, using electron channeling contrast,” *Microsc. Res. Tech.*, vol. 69, no. 5, pp. 374–381, 2006.

[107] S. Zaefferer and N.-N. Elhami, “Theory and application of electron channelling contrast imaging under controlled diffraction conditions,” *Acta Mater.*, vol. 75, pp. 20–50, 2014.

[108] M. A. Crimp, J. T. Hile, T. R. Bieler, and M. G. Glavicic, “Dislocation density measurements in commercially pure titanium using electron channeling contrast imaging,” *TMS Lett.*, vol. 1, pp. 15–16, 2004.

[109] M. A. Crimp, B. A. Simkin, and B. C. Ng, “Demonstration of the g·bxu= 0 edge dislocation invisibility criterion for electron channelling contrast imaging,” *Philos. Mag. Lett.*, vol. 81, no. 12, pp. 833–837, 2001.

[110] S. Zaefferer, “New developments of computer-aided crystallographic analysis in transmission electron microscopy,” *J. Appl. Crystallogr.*, vol. 33, no. 1, pp. 10–25, 2000.

[111] S. Zaefferer, “Computer-aided crystallographic analysis in the TEM,” *Adv. Imaging Electron Phys.*, vol. 125, pp. 355–XII, 2003.

[112] H. Kriaa, A. Guitton, and N. Maloufi, “Fundamental and experimental aspects of diffraction for characterizing dislocations by electron channeling contrast imaging in scanning electron microscope,” *Sci. Rep.*, vol. 7, no. 1, p. 9742, 2017.

[113] P. N. Schatz and A. J. McCaffery, “The faraday effect,” *Q. Rev. Chem. Soc.*, vol. 23, no. 4, pp. 552–584, 1969.

[114] A. A. Polyanskii, D. M. Feldmann, and D. C. Larbalestier, “Magneto-optical characterization techniques,” *Handb. Supercond. Mater. Ed. by David Cardwell David Ginley, Inst. Phys. UK*, vol. 1551, 2003.

[115] A. A. Polyanskii, X. Y. Cai, D. M. Feldmann, and D. C. Larbalestier, “Visualization of magnetic flux in magnetic materials and high temperature superconductors using the Faraday effect in ferrimagnetic garnet films,” in *Nano-Crystalline and Thin Film Magnetic Oxides*, Springer, 1999, pp. 353–370.

[116] O. Kugeler, J. Vogt, and J. Knobloch, “Influence of the cooldown at the transition

temperature on the SRF cavity quality factor," in *16th International Conference on RF Superconductivity*, 2013.

[117] A. V Narlikar and D. Dew-Hughes, "The effect of dislocation configuration on the superconducting properties of niobium and vanadium," *Phys. status solidi*, vol. 6, no. 2, pp. 383–390, 1964.

[118] H. U. Habermeier, W. Klein, R. Aoki, and H. Kronmüller, "Magneto-optical investigation of flux penetration in plastically deformed niobium monocrystals," *Phys. Status Solidi*, vol. 53, no. 1, pp. 225–235, 1979.

[119] J. Köszegi, O. Kugeler, D. Abou-Ras, J. Knobloch, and R. Schäfer, "A magneto-optical study on magnetic flux expulsion and pinning in high-purity niobium," *J. Appl. Phys.*, vol. 122, no. 17, p. 173901, 2017.

[120] Z. H. Sung, P. J. Lee, A. Gurevich, and D. C. Larbalestier, "Evidence for preferential flux flow at the grain boundaries of superconducting RF-quality niobium," *Supercond. Sci. Technol.*, vol. 31, no. 4, p. 45001, 2018.

[121] S. Posen *et al.*, "Role of magnetic flux expulsion to reach Q 3 10 10 in superconducting rf cryomodules," *Phys. Rev. Accel. Beams*, vol. 22, no. 3, p. 32001, 2019.

[122] R. P. Huebener and A. Seher, "Nernst effect and flux flow in superconductors. I. Niobium," *Phys. Rev.*, vol. 181, no. 2, p. 701, 1969.

[123] A. Romanenko, A. Grassellino, O. Melnychuk, and D. A. Sergatskov, "Dependence of the residual surface resistance of superconducting radio frequency cavities on the cooling dynamics around Tc," *J. Appl. Phys.*, vol. 115, no. 18, p. 184903, 2014.

[124] D. Kang, D. C. Baars, T. R. Bieler, and C. C. Compton, "Characterization of large grain Nb ingot microstructure using EBSP mapping and Laue camera methods," in *AIP Conference Proceedings*, 2011, vol. 1352, no. 1, pp. 90–99.

[125] T. E. Everhart and R. F. M. Thornley, "Wide-band detector for micro-microampere low-energy electron currents," *J. Sci. Instrum.*, vol. 37, no. 7, p. 246, 1960.

[126] V. Randle, "Microtexture Determination and Its Applications,(1992)," *London, Inst. Mater.*

[127] D. J. Dingley and V. Randle, "Microtexture determination by electron back-scatter diffraction," *J. Mater. Sci.*, vol. 27, no. 17, pp. 4545–4566, 1992.

[128] F. J. Humphreys, Y. Huang, I. Brough, and C. Harris, "Electron backscatter diffraction of grain and subgrain structures—resolution considerations," *J. Microsc.*, vol. 195, no. 3, pp. 212–216, 1999.

[129] G. Nolze, "Image distortions in SEM and their influences on EBSD measurements," *Ultramicroscopy*, vol. 107, no. 2–3, pp. 172–183, 2007.

[130] A. J. Schwartz, M. Kumar, B. L. Adams, and D. P. Field, *Electron backscatter diffraction in materials science*. Springer, 2000.

[131] P. Kneisel *et al.*, "Review of ingot niobium as a material for superconducting radiofrequency accelerating cavities," *Nucl. Instruments Methods Phys. Res. Sect. A Accel. Spectrometers, Detect. Assoc. Equip.*, vol. 774, pp. 133–150, 2015.

[132] P. Lejcek, *Grain boundary segregation*. Springer, 2010.

[133] P. E. J. Flewitt and R. K. Wild, "Grain boundaries: their microstructure and chemistry," *Grain Boundaries Their Microstruct. Chem. by PEJ Flewitt, RK Wild, pp. 338. ISBN 0-471-97951-1. Wiley-VCH, April 2001.*, p. 338, 2001.

[134] X. Tingdong, "Creating and destroying vacancies in solids and non-equilibrium grain-boundary segregation," *Philos. Mag.*, vol. 83, no. 7, pp. 889–899, 2003.

[135] F. Barkov, A. Romanenko, Y. Trenikhina, and A. Grassellino, "Precipitation of hydrides in high purity niobium after different treatments," *J. Appl. Phys.*, vol. 114, no. 16, p. 164904, 2013.

[136] Z. H. Sung, A. Dzyuba, P. J. Lee, D. C. Larbalestier, and L. D. Cooley, "Evidence of incomplete annealing at 800 C and the effects of 120 C baking on the crystal orientation and the surface superconducting properties of cold-worked and chemically polished Nb," *Supercond. Sci. Technol.*, vol. 28, no. 7, p. 75003, 2015.

[137] S. B. Roy, G. R. Myneni, and V. C. Sahni, "On the reliable determination of the magnetic field for first flux-line penetration in technical niobium material," *Supercond. Sci. Technol.*, vol. 21, no. 6, p. 65002, 2008.

[138] D. Kang, D. C. Baars, A. Mapar, T. R. Bieler, F. Pourboghrat, and C. C. Compton, "Study of slip and deformation in high purity single crystal nb for accelerator cavities," in *17th International Conference on RF Superconductivity*, 2015, pp. 20–40.

[139] A. Mapar, T. Bieler, D. Kang, C. Compton, and F. Pourboghrat, "Crystal plasticity modeling of single crystal Nb," 2015.

[140] G. Naresh-Kumar *et al.*, "Rapid nondestructive analysis of threading dislocations in wurtzite materials using the scanning electron microscope," *Phys. Rev. Lett.*, vol. 108, no. 13, p. 135503, 2012.

[141] C. A. Schneider, W. S. Rasband, and K. W. Eliceiri, "NIH Image to ImageJ: 25 years of image analysis," *Nat. Methods*, vol. 9, no. 7, p. 671, 2012.

[142] J.-Y. Kim, D. Jang, and J. R. Greer, "Insight into the deformation behavior of niobium single crystals under uniaxial compression and tension at the nanoscale," *Scr. Mater.*, vol. 61, no. 3, pp. 300–303, 2009.

[143] F. F. Csikor, C. Motz, D. Weygand, M. Zaiser, and S. Zapperi, "Dislocation avalanches,

strain bursts, and the problem of plastic forming at the micrometer scale," *Science (80-.).*, vol. 318, no. 5848, pp. 251–254, 2007.

[144] N. Friedman *et al.*, "Statistics of dislocation slip avalanches in nanosized single crystals show tuned critical behavior predicted by a simple mean field model," *Phys. Rev. Lett.*, vol. 109, no. 9, p. 95507, 2012.

[145] J. Antonaglia *et al.*, "Tuned critical avalanche scaling in bulk metallic glasses," *Sci. Rep.*, vol. 4, p. 4382, 2014.

[146] T. R. Bieler, P. Eisenlohr, C. Zhang, H. J. Phukan, and M. A. Crimp, "Grain boundaries and interfaces in slip transfer," *Curr. Opin. Solid State Mater. Sci.*, vol. 18, no. 4, pp. 212–226, 2014.

[147] M. A. Crimp, J. T. Hile, T. R. Bieler, and M. G. Glavicic, "Dislocation density measurements in commercially pure titanium using electron channeling contrast imaging," *TMS Lett*, vol. 1, pp. 15–16, 2004.

[148] C. Wainwright, A. J. Cook, and B. E. Hopkins, "The structures of niobium-hydride alloys," *J. Less Common Met.*, vol. 6, no. 5, pp. 362–374, 1964.

[149] M. Amano and Y. Sasaki, "Dislocation structure in dehydrogenated niobium," *Phys. status solidi*, vol. 19, no. 2, pp. 405–414, 1973.